Title
Advances in Surface Patterning and Next-Generation Electronic Biosensors

Author
Cheung, Kevin

Publication Date
2019

Peer reviewed|Thesis/dissertation

UNIVERSITY OF CALIFORNIA

Los Angeles

Advances in Surface Patterning and Next-Generation Electronic Biosensors

A dissertation submitted in partial satisfaction of the

requirements for the degree Doctor of Philosophy

in Chemistry

by

Kevin Cheung

2019

ABSTRACT OF THE DISSERTATION

Advances in Surface Patterning and Next-Generation Electronic Biosensors

by

Kevin Cheung

Doctor of Philosophy in Chemistry

University of California, Los Angeles, 2019

Professor Paul S. Weiss, Co-Chair

Professor Anne M. Andrews, Co-Chair

Chemical lift-off lithography (CLL) is a subtractive soft-lithographic technique used to pattern self-assembled monolayers (SAMs) containing functional alkanethiolates on Au surfaces. Alkanthiolate molecules, along with a single monolayer of Au, are removed in this process by oxygen-plasma activated polydimethysiloxane (PDMS) stamps. Monolayers patterned *via* CLL are robust, in contrast to conventional soft lithography, enabling high-fidelity patterning over a dynamic range of feature sizes (millimeter to nanometer). Recently, I have advanced CLL to pattern additional surfaces, including other coinage metals (*e.g.*, Pt, Pd, Ag, Cu), reactive and transition metals (*e.g.*, Ni, Ti, Al), and semiconductors (*e.g.*, Ge). This process has a wide range of applications, including patterning of bioactive molecules and supported metal monolayers, as well as the simple, convenient fabrication of field-effect transistors (FETs).

I have designed and developed FET biosensors coupled to rationally designed and chemically synthesized oligonucleotide sequences with molecular recognition capabilities, termed aptamers, for the detection of a diverse range of biologically important small-molecule targets (*e.g.*, neurotransmitters, amino acids, sugars, lipids). Upon target capture, aptamers undergo conformational changes that redistribute charge densities on FET surfaces resulting in measurable changes in transconductance. These aptamer-FET sensors detected targets in full ionic strength biological fluids, with high specificity and selectivity, over large concentration ranges with low detection limits.

Using this platform, I have developed sensors for the direct detection of the amino acid phenylalanine for potential point-of-care use for patients with phenylketonuria (PKU), a common genetic disorder that results in elevated and potentially harmful levels of phenylalanine in the blood and brain. Phenylalanine aptamer-FETs showed high sensitivity and selectivity towards phenylalanine *versus* similarly structured molecules, and were able to differentiate physiological phenylalanine concentrations in serum from mice treated with a phenylalanine hydroxylase inhibitor (*i.e.*, a PKU mouse model). In parallel, I have extended this FET biosensor platform for the detection and discrimination of single base-pair mismatches in oligonucleotides towards electronic single-nucleotide polymorphism genotyping. I demonstrated the ability of DNA-functionalized FETs to distinguish hybridization between fully complementary DNA sequences, and analogous sequences with different types and locations of mismatches. Performing FET measurements under physiologically relevant conditions and elucidating sensing mechanisms is necessary for ultimate use in disease diagnostics and clinical point-of-care applications.

This dissertation of Kevin Cheung is approved.

Dino Di Carlo

Xiangfeng Duan

Paul S. Weiss, Committee Co-Chair

Anne M. Andrews, Committee Co-Chair

University of California, Los Angeles

2019

For my family, my friends, and my mentors

Table of Contents

List of Abbreviations and Symbols

Acronyms and Symbols

1D	one-dimensional
2D	two-dimensional
2-PEA	2-phenylethylamine
A	adenine
aCSF	artificial cerebral spinal fluid
APD	avalanche photodiode
AFM	atomic force microscopy
Ag	silver
AgCl	silver chloride
Al	aluminum
Au	gold
CLL	chemical lift-off lithography
C	carbon
C	cytosine
C18	octanethiol
C8-dithiol	1,8-octanedithiol
$CaCl_2$	calcium chloride
CCD	charge-coupled device
CD	circular dichroism
CI	confidence intervals
CLS	core level shifts

CNT carbon nanotube

COOH carboxyl

Cp*Rh pentamethylcyclopentadienyl rhodium(III)

Cr chromium

Cu copper

CVD chemical vapor deposition

DC direct current

DCM 4-(dicyanomethylene)-2-methyl-6-(4-dimethylaminostyryl)-4*H*-pyran

DNA deoxyribonucleic acid

dsDNA double-stranded DNA

EAB electrochemical aptamer-based

EBL electron-beam lithography

EDTA ethylenediaminetetraacetic acid

fcc face-centered cubic

$FeCl_3$ iron(III) chloride

$FeNO_3$ iron(III) nitrate

FESEM field-emission scanning electron microscope

FET field-effect transistor

FIB focused ion-beam lithography

FQM fluorescence quenching microscopy

G guanine

Ge germanium

GPAW grid-based projector augmented wave

***h*-PDMS**	hard polydimethylsiloxane
H_2O_2	hydrogen peroxide
H_2SO_4	sulfuric acid
H_3PO_4	phosphoric acid
HCl	hydrochloric acid
HF	hydrofluoric acid
HNO_3	nitric acid
HPLC	high performance liquid chromatography
I	current
I-V	current-voltage
I_{DS}	source-drain current
$In(NO_3)_3$	indium(III) nitrate
In_2O_3	indium oxide
$K_2Cr_2O_7$	potassium dichromate
KCl	potassium chloride
K_d	dissociation constant
KOH	potassium hydroxide
LBL	layer-by-layer
μ	electron mobility
μCIP	microcontact insertion printing
μCP	microcontact printing
μDP	microdisplacement printing
MBS	3-maleimidobenzoic acid *N*-hydroxysuccinimide ester

$MgCl_2$ magnesium chloride

MIFE metal-induced fluorescence enhancement

miRNA microRNA

mRNA messenger ribonucleic acid

MUDA 11-mercapto-1-undecanoic acid

MUO 11-mercapto-1-undecanol

N sample size

N_2 nitrogen

NaCl sodium chloride

NH_2 amino

NH_4OH ammonium hydroxide

Ni nickel

NIH National Institutes of Health

NMR nuclear magnetic resonance

ns not significant

O oxygen

O_2 oxygen

OH hydroxyl

OPA-S *o*-phthalaldehyde-sulfite

P *p*-value

P postnatal day

PAH phenylalanine hydroxylase

PBS phosphate-buffered saline

PCPA *para*-chlorophenylalanine

PCR polymerase chain reaction

Pd palladium

PDMS poly(dimethylsiloxane)

PEPA *para*-Ethynylphenylalanine

PEW Perdew-Burke-Ernzerhof

PF-AFM peak-force atomic force microscopy

Phe phenylalanine

PKU phenylketonuria

PMMA poly(methyl methacrylate)

PNA peptide nucleic acid

PPA phenylypyruvic acid

PPCLL polymer-pen chemical lift-off lithography

PPL polymer-pen lithography

Pt platinum

R_a average roughness

RFU relative fluorescence units

R_q root mean square roughness

RIE reactive-ion etching

RNA ribonucleic acid

S sulfur

S1P sphingosine-1-phosphate

SAM self-assembled monolayer

SELEX systematic evolution of ligands by exponential enrichment

SEM scanning electron microscopy

SERT serotonin transporter

Si silicon

SiNW silicon nanowire

SiO_2 silicon dioxide

SNP single-nucleotide polymorphism

ssDNA single-stranded DNA

T thymine

Tht Thioflavin T

Ti titanium

TPH tryptophan hydroxylase

Tph2 tryptophan hydroxylase 2

Tris tris(hydroxymethyl)aminomethane

tRNA transfer ribonucleic acid

Trp tryptophan

Tyr tyrosine

U uracil

UV ultraviolet

V_{GS} gate voltage

VP-SEM variable pressure scanning electron microscopy

XPS X-ray photoelectron spectroscopy

ZT Zeitgeber time

Units

Å	Ångström
C	Celsius
cm	centimeter
cm^2	square centimeter
eV	electron volt
fM	femtomolar
fs	femtosecond
g	gram
h	hour
Hz	hertz
kV	kilovolt
lb	pound
µA	microampere
µL	microliter
µM	micromolar
µm	micrometer
M	molar
m	meter
mA	milliampere
mer	repeat unit
mol	mole
mg	milligram

min	minute
mL	milliliter
mM	millimolar
mm	millimeter
MΩ·cm	milliohm-centimeter
ms	millisecond
mV	millivolt
mW	milliwatt
N	newton
nM	nanomolar
nm	nanometer
Pa	pascal
pN	piconewton
ps	picosecond
psi	pound per square inch
s	second
V	volt
W	watt

Acknowledgments

I would like to first thank my advisors Professors Paul Weiss and Anne Andrews, without whom none of this would have been possible. Throughout my time working with Paul, he always encouraged and supported me, and gave me the freedom to grow and develop my own independent research and scientific ideas. I learned how to take a project from conception to publication, and also how to translate my research to a broad audience. I had the particular pleasure of working with Anne during the second half of my graduate career. I am very grateful to have been able to join her research group and have her as my co-advisor. Anne taught and encouraged me to improve the quality of the science that I worked on, both in research and in writing. With her support I was able to push myself to grow as a scientist. Also, I appreciate our mutual love of desserts. I would also like to thank my other committee members Professors Dino Di Carlo and Xiangfeng Duan for their support.

Dr. Liane Slaughter was the first person that I worked with in the Weiss group. I thank her for taking me under her mentorship and helping me to get started in the group. I remember fondly the scientific discussions we would always have, and her guidance helped to define my initial years in graduate school. I would particularly like to thank my good friend, colleague, and mentor Dr. Nako Nakatsuka. Nako is someone I know that I can always turn to for help and for honest advice. She has helped me to grow as a person and a scientist both in and out of the lab. I owe a lot of my successes to her friendship, support, and guidance. I have worked together with Chuanzhen Zhao on several different projects and have always been impressed by his work ethic. I thank him for his continued assistance throughout graduate school over many different research projects, and I look forward to seeing what comes next for him after I leave. I am glad to have worked with Dr. John Abendroth who I

respect and look up to both as a person and as a scientist. I sincerely appreciate his advice and friendship over the years. Also, I would like to thank Drs. Alexandra Mendoza and Natcha Wattanatorn for their friendship and support both inside and outside of graduate school. I am glad to have started graduate school together with Taylor Aubry-Komin. Although we ended up in different research groups, I enjoyed our time as roommates and I am thankful to have remained friends throughout the years.

Next, I would like to thank some current and former members of the Weiss group, specifically, Professors Mary Elizabeth Anderson and Xiaobin Xu, Drs. Dominic Goronzy, Jeffrey Schwartz, Andrew Serino, and Qing Yang, Jason Belling, Dominik Stemer, and Thomas Young, for their friendship and scientific contributions. I would also like to thank my friends Drs. Cathy Tan and Erika Kang, Eric Ting, Jonathan Chu, Dr. Srijita Sarkar, and Tiffany Pan for sticking with me and supporting me during my long journey through graduate school. Finally, I would like to thank my family, specifically my parents Yim and Peter, and my sister Alice, for all of their love and support. It was my parents that introduced me to science at a young age. They have given me so many opportunities that I am grateful for. I would have never been able to pursue a graduate education if it was not for continued support throughout my life.

Additionally, my dissertation work was supported by the U.S. Department of Energy (DE-SC-1037004), the W. M. Keck Foundation, the National Science Foundation (CMMI-1636136), Hewlett Packard, Nantworks, Aptatek Biosciences, and the National Institute on Drug Abuse (DA045550). I personally acknowledge support from a SG fellowship awarded by the Department of Chemistry and Biochemistry at the University of California, Los Angeles.

Vita

I received my Bachelors of Science in Chemistry, with honors, at the University of California, Santa Barbara (UCSB). At UCSB, I pursued research in the lab of Professor Norbert Reich. There I conducted research on the spatiotemporal controlled release of siRNA from Au nanoshells *via* pulsed near-infrared laser irradiation for targeted gene knockdown in cancer and stem cells. In 2013, I was one of three US students chosen through the Cooperative International Science and Engineering Internships program for a research internship at the Department of Materials at the University of Oxford. At Oxford, I performed research in the lab of Professor Kyriakos Porfyrakis on the synthesis and purification of endohedral metallofullerenes for applications in quantum computing. Upon graduation from UCSB in 2014, I was awarded the prestigious Phi Lamda Upsilon award.

I began my graduate studies in 2014 at the University of California, Los Angeles (UCLA), under the mentorship of Professors Paul Weiss and Anne Andrews. In their groups, I performed research on advancing a subtractive soft lithographic patterning technique, termed chemical lift-off lithography, used to pattern self-assembled monolayers of functional alkanethiols on metal surfaces. I also designed and developed field-effect transistor sensors functionalized with nucleic acid receptors for the electronic detection of biologically relevant molecules. In 2019, I was accepted into the National Institutes of Health, National Cancer Institute, Graduate Student Recruiting Program. I was also awarded a best poster award at the Aptamers 2019 conference, outstanding student talk at the Southern California Biomedical Sciences Graduate Student Research Symposium, a SG fellowship and ACS research showcase fellowship from the Department of Chemistry and Biochemistry at UCLA, and a National Research Council postdoctoral fellowship.

Publications

1. **Cheung, K. M.**; Stemer, D. M.; Zhao, C.; Young, T. D.; Belling, J. N.; Andrews, A. M.; Weiss, P. S. Chemical Lift-Off Lithography of Metal and Semiconductor Surfaces *ACS Mater. Lett.* **2019**, *2*, 76–83.

2. **Cheung, K. M.**; Yang, K.-A.; Nakatsuka, N.; Zhao, C.; Ye, M.; Jung, M. E.; Yang, H.; Weiss, P. S.; Stojanović, M. N.; Andrews, A. M. Phenylalanine Monitoring *via* Aptamer-Field-Effect Transistor Sensors. *ACS Sens.* **2019**, in press. DOI: 10.1021/acssensors.9b01963

3. Lau, J.; Trojniak, A. E.; Maraugha, M. J.; VanZanten, A. J.; Osterbaan, A. J.; Serino, A. C.; Ohnsorg, M. L.; **Cheung, K. M.**; Ashby, D. S.; Weiss, P. S.; Dunn, B. S.; Anderson, M. E. Conformal Ultrathin Film MOF Analogs: Characterization of Growth, Porosity, and Electronic Transport. *Chem. Mater.* **2019**, *31*, 8977–6121.

4. Abendroth, J. M.; **Cheung, K. M.**; Stemer, D. M.; El Hadri, M. S.; Zhao, C.; Fullerton, E. E.; Weiss, P. S. Spin-Dependent Ionization of Chiral Molecular Films. *J. Am. Chem. Soc.* **2019,** *141*, 3863–3974.

5. Nakatsuka, N.; Yang, K.-A.; Abendroth, J. M.; **Cheung, K. M.**; Xu, X.; Yang, H.; Zhao, C.; Zhu, B.; Rim, Y. S.; Yang, Y.; Weiss, P. S.; Stojanović, M. N.; Andrews, A. M. Aptamer–Field-Effect Transistors Overcome Debye Length Limitations for Small-Molecule Sensing. *Science* **2018,** *362*, 319–324.

6. Zhao, C.; Xu, X.; Bae, S.-H.; Yang, Q.; Liu, W.; Belling, J. N.; **Cheung, K. M.**; Rim, Y. S.; Yang, Y.; Andrews, A. M.; Weiss, P. S. Large-Area, Ultrathin Metal-Oxide Semiconductor Nanoribbon Arrays Fabricated by Chemical Lift-Off Lithography. *Nano Lett.* **2018,** *18*, 5590–5595.

7. Nakatsuka, N.; Hasana-Sadrabadi M. M.; **Cheung, K. M.**; Young, T. D.; Bahlakeh, G.; Moshaverinia, A.; Weiss, P. S.; Andrews, A. M. Polyserotonin Nanoparticles as Multifunctional Materials for Biomedical Applications *ACS Nano* **2018***, 12*, 4761–4774.

8. Slaughter, L. S.; **Cheung, K. M.**; Kaappa, S.; Cao, H. H.; Yang, Q.; Young, T. D.; Serino, A. C.; Malola, S.; Olson, J. M.; Link, S.; Häkkinen, H.; Andrews, A. M.; Weiss, P. S. Patterning of Supported Gold Monolayers *via* Chemical Lift-Off Lithography. *Beilstein J. Nanotechnol.* **2017,** *8*, 2648–2661.

9. Xu, X.; Yang, Q.; **Cheung, K. M.**; Zhao, C.; Wattanatorn, N.; Belling, J. N.; Abendroth, J. M.; Slaughter, L. S.; Mirkin, C. A.; Andrews, A. M.; Weiss, P. S. Polymer-Pen Chemical Lift-Off Lithography. *Nano Lett.* **2017,** *17*, 3302–3311.

10. Stemer, D. M.; Abendroth, J. M.; **Cheung, K. M.**; Ye M.; El Hadri, M. S.; Fullerton, E. E.; Weiss, P. S. Differential Charging in Photoemission from Mercurated DNA Monolayers on Ferromagnetic Films. *Nano Lett.* **2019**, in revision.

CHAPTER I

Advances in Surface Patterning

and Next-Generation Electronic Biosensors

I.A. Chemical Patterning of Self-Assembled Monolayers

Self-assembled monolayers (SAMs) of alkanethiolate molecules on Au surfaces are a widely studied and versatile system for probing and controlling surface, interfacial, and environmental properties and interactions.[1-3] The ability to pattern SAMs spatially on surfaces imparts additional control over the placement of SAM molecules, which has led to a multitude of applications in surface science.[4-9] Self-assembled monolayers are commonly patterned using high-throughput, economical, and large-area soft-lithographic techniques (*e.g.*, microcontact printing, μCP),[5,6,8-11] in which patterned polydimethylsiloxane (PDMS) stamps "inked" with alkanethiols are brought into contact with metal surfaces (**Figure I.1**). However, patterns created by μCP are limited in resolution and fidelity due to lateral diffusion of molecules during and after the printing process, broadening feature sizes (**Figure I.1B,C**).[6,9,11-13]

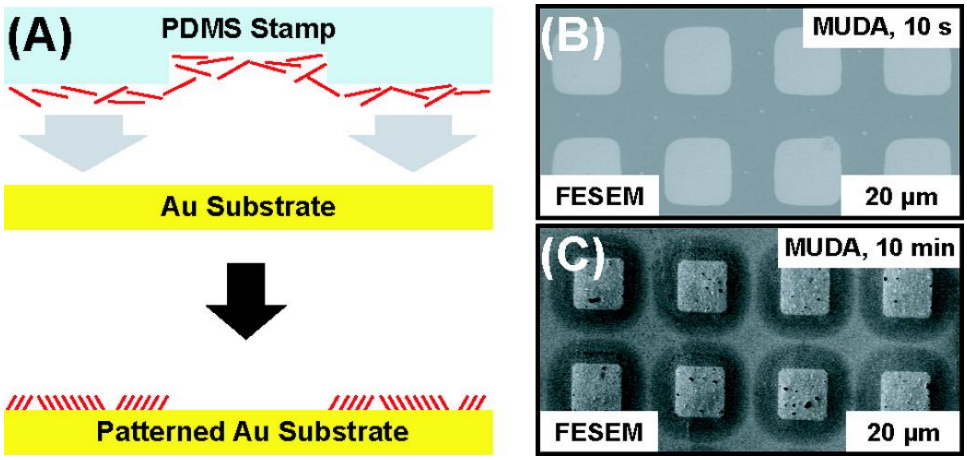

Figure I.1. (A) Schematic of microcontact printing, where a polydimethylsiloxane (PDMS) stamp inked with alkanethiols is brought into contact with an Au substrate, additively patterning the surface. **(B)** Field-emission scanning electron microscope (FESEM) image of a patterned self-assembled monolayer (SAM) of mercaptoundecanoic acid (MUDA) on Au after 10 s of stamp contact. **(C)** Field-emission scanning electron microscope image of a patterned SAM of MUDA after 10 min of stamp contact. Darker regions surrounding the patterned features are indicative of broadening *via* lateral diffusion. Reprinted (adapted) with permission from *ACS Nano*. Copyright 2007, American Chemical Society.

There have been various advances to improve pattern fidelity and features sizes attainable *via* soft lithography. For example, by using more complex stamp geometries or patterning processes (*e.g.*, dip-pen nanolithography,[14] polymer-pen lithography,[15] beam-pen lithography),[16] nanoscale features are attainable. Additionally, methods to preserve feature resolution *via* printing into preexisting monolayers have previously been developed and studied. Monolayers composed of labile molecules can be displaced *via* patterned stamps (*i.e.*, microdisplacement printing, μDP).[17,18] Printing into SAMs of *not* easily displaced molecules results in *insertion* of molecules isotropically into intrinsic defect sites of the existing monolayer (*i.e.*, microcontact insertion printing, μCIP), resulting in dilute patterns of inserted molecules (ideal for biorecognition applications).[19-21] However, requiring preformed monolayers of displaceable molecules or only patterning into native defects limits the types and densities of molecules that can be patterned *via* μDP and μCIP respectively.

I.B. Chemical Lift-Off Lithography

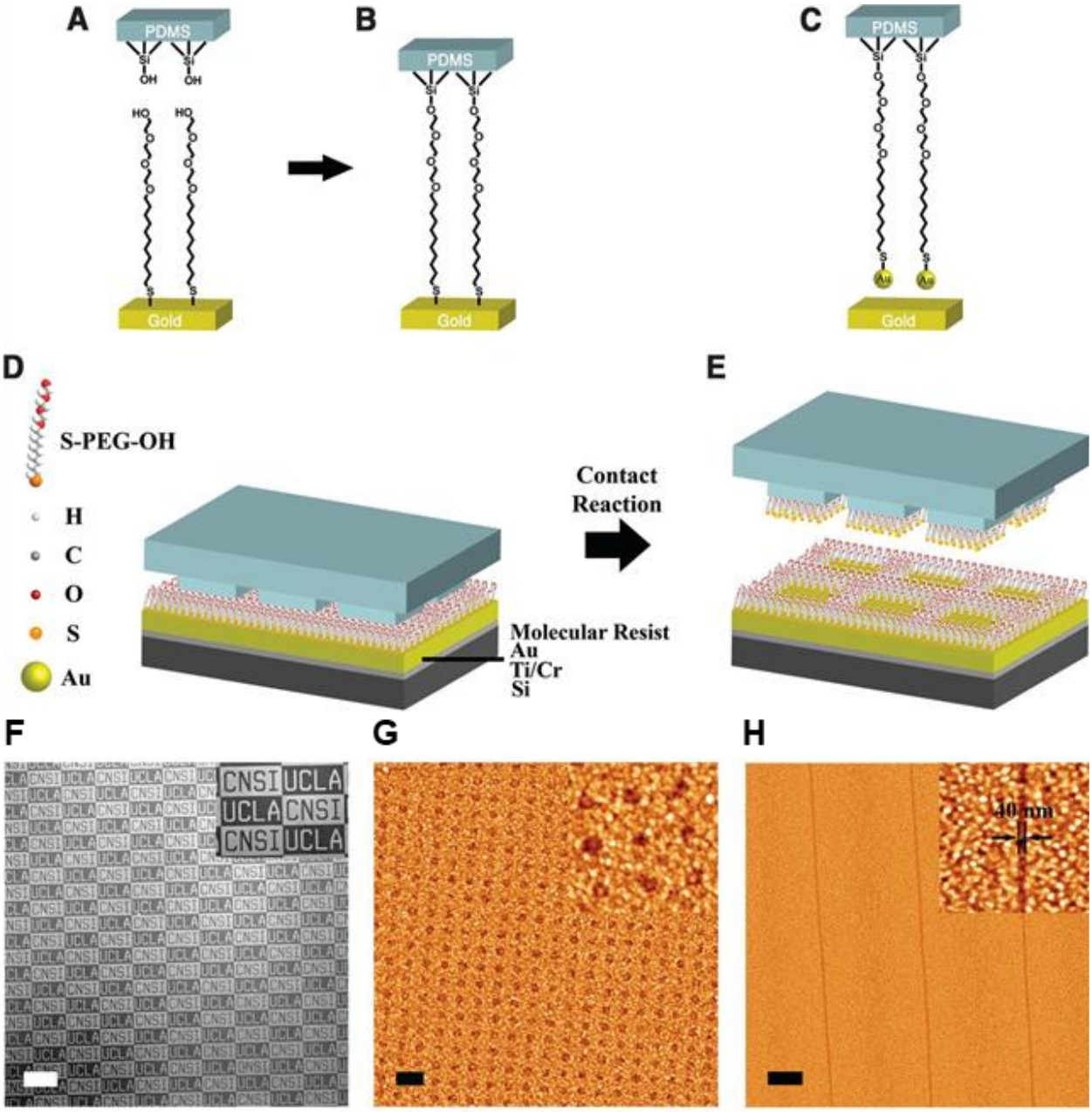

Figure I.2. Chemical lift-off lithography (CLL). (A,B) An oxygen-plasma activated polydimethylsiloxane (PDMS) stamp is brought into contact with a self-assembled monolayer (SAM) of functional alkanethiols. **(C)** "Lift-off" of the PDMS stamp from the surface removes contacted SAM molecules and a monolayer of Au atoms. **(D,E)** Schematic demonstrating the subtractive patterning of a SAM of alkanethiols on a Au surface *via* CLL. **(F)** Fluorescence microscope and **(G,H)** atomic-force microscope images of SAMs patterned on Au *via* CLL over a dynamic range of feature sizes (micrometer to nanometer). Reprinted (adapted) with permission from *Science*. Copyright 2012, American Association for the Advancement of Science.

The first half of my dissertation builds upon work started by Liao *et al.* on an alternative surface patterning technique termed chemical-lift-off lithography (CLL).[22] Chemical lift-off lithography is a *subtractive* soft-lithographic method used to pattern SAMs of functional alkanethiolates on Au surfaces *via* contact and subsequent removal of O_2-plasma activated PDMS stamps (**Figure I.2A-E**).[22,23] In the CLL process, covalent linkages are formed between the stamp and certain types of functional tail groups of the contacted molecules (**Figure I.2A-E**).[22,23] Removal of stamps removes SAM molecules, along with a monolayer of Au, in the contacted regions (**Figure I.2C**).[22-24] In contrast to conventional soft-lithographic techniques, features created *via* CLL are robust (*i.e.*, no observable lateral diffusion), enabling patterning over a dynamic range of feature sizes (millimeter to nanometer, **Figure I.2F-H**).[22,23,25] The yield of a single CLL step on Au is *ca.* 70%,[22] and the molecules remaining in lifted-off regions have been demonstrated as an advantageous matrix for small-molecule patterning towards biorecognition applications.[26-33]

In addition to small-molecule patterning, CLL has inspired a variety of applications, including the patterning of biomolecules,[26,31,32] supported Au monolayers,[24] and the facile fabrication of field-effect transistor (FET) arrays.[34,35] Using polymer-pen arrays[25] or advanced patterning strategies (*i.e.*, roof collapse),[36] in conjunction with CLL, large-area and high-fidelity nanoscale features can be straightforwardly produced. Insertion of thiolated DNA into artificial defect-rich regions created *via* CLL was shown as a straightforward method of DNA patterning with controllable DNA density.[26] Notably, DNA patterning using CLL had superior hybridization efficiency compared to conventional alkanethiol backfilling methods.[26] Patterning of DNA *via* CLL has been used to investigate spin-selective DNA-

mediated charge transfer,[27] and also for wafer-scale bioactive patterning towards a variety of analytical applications.[31-33,37]

Motivated by insights gained from previous studies on CLL, Slaughter *et al.* devised fabrication, characterization, and simulation strategies to interrogate the nanoscale structure and chemical functionality of the Au removed during the CLL process.[24] Lifting off from patterned Au surfaces onto featureless PDMS stamps enabled the patterning of supported Au monolayers on flexible and transparent polymer supports (*i.e.*, PDMS).[23,24] These supported Au monolayers had sub-nanometer apparent heights, consistent with removal of a single monolayer of Au.[24] The optical properties of these Au monolayers were dissimilar from those of bulk Au (*i.e.*, they were optically transparent), however, they retained the chemical functionality of Au (*e.g.*, Au-thiol chemistry).[24] The ability to encode chemical functionality of supported Au monolayers spatially has potential applications for the development of flexible and transparent sensor technologies.

I have advanced and extended CLL to pattern a variety of surfaces, including other coinage metal, transition and reactive metal, and semiconductor surfaces.[38] For all surfaces tested, high-fidelity patterns of alkanethiolates were achieved and (mono)layers of substrate atoms were removed onto PDMS stamps, analogous to CLL with Au. Performing multiple CLL steps with the same PDMS stamp enabled the fabrication of atomically blended supported bimetallic monolayers. Additionally, I demonstrated that lifting-off molecules that form more pristine and defect-free monolayers compared to those of alkanethiols (*i.e.*, isomers of carboxylic-acid-functionalized carboranethiolates)[39,40] may increase the yield of CLL and the fidelity of the resulting supported Au monolayers. Patterning isomers of carboranethiolates

that are chemically and physically identical but have different dipole moments, enabled local tuning of substrate work functions for band alignment purposes.[41,42]

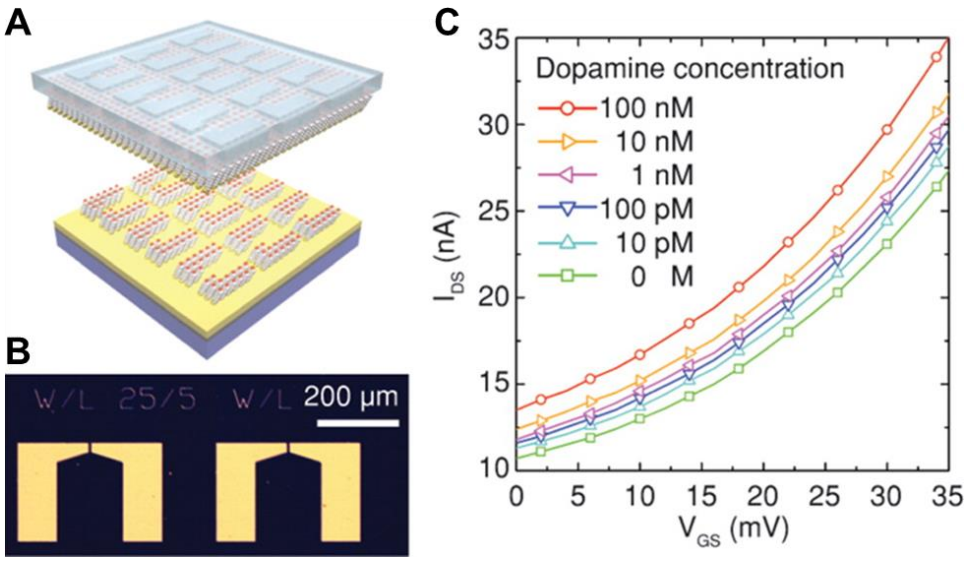

Figure I.3. (A) Schematic of the patterning of self-assembled monolayers of alkanethiols *via* CLL as chemical resists for the generation of arrays of Au electrodes for field-effect transistors (FETs). **(B)** Optical microscope image of etched Au electrodes on an indium oxide semiconducting layer patterned *via* CLL. **(C)** Transfer (I-V) curves of dopamine-specific aptamer-functionalized FETs measured after exposure to different dopamine concentrations demonstrating dopamine detection down to picomolar concentrations. Reprinted (adapted) with permission from *ACS Nano*. Copyright 2015, American Chemical Society.

Patterned SAMs formed *via* CLL can be used as molecular resists during chemical wet etching processes for the generation of Au micro/nanostructures.[22,24,34-36] In particular, work led by Kim *et al.* demonstrated this strategy to pattern Au electrodes on top of metal oxide semiconductors (*e.g.*, indium oxide) for the straightforward fabrication of FET arrays with tunable channel sizes (*i.e.*, by varying the spacing between the Au electrodes, **Figure I.3A,B**).[34] Zhao *et al.* also demonstrated by performing sequential wet etching steps using Au structures generated *via* CLL as masks, that underlying layers of indium oxide could be patterned.[35] Transistors fabricated *via* CLL were functionalized with an artificial nucleic acid

receptor (*i.e.*, aptamer) that recognizes the neurotransmitter dopamine.[34,43] These aptamer-FETs were used to detect dopamine down to picomolar concentrations (**Figure I.3C**).[34] While sufficient for proof-of-concept biosensing, these particular FET sensors were only operated in dilute buffers and were *not* highly selective due to the inherent cross-reactivity of the dopamine aptamer towards norepinephrine,[34,43] a similarly structured small-molecule neurotransmitter.

I.C. Field-Effect Transistor Biosensors

Inspired by this work, the second half of my dissertation focuses on the design and development of next-generation electronic biosensors based on field-effect transistors functionalized with nucleic acid receptors for applications in point-of-care and disease diagnostics. Field-effect transistors with biological receptors have been widely studied and developed for the rapid, electronic, and label-free detection of biological targets.[34,44-52] Recognition of charged targets, or target-mediated changes in receptor conformation can gate underlying semiconductor layers, resulting in measurable changes in transconductance. Conventional FET biosensors based on protein or antibody receptors are unable to sense in biological fluids (*i.e.*, high ionic-strength solutions) due to the large sizes of these receptors (*ca.* 10 nm) relative to the charge screening distance near transistor surfaces (*i.e.*, the Debye length, <1 nm in physiological conditions).[45,53]

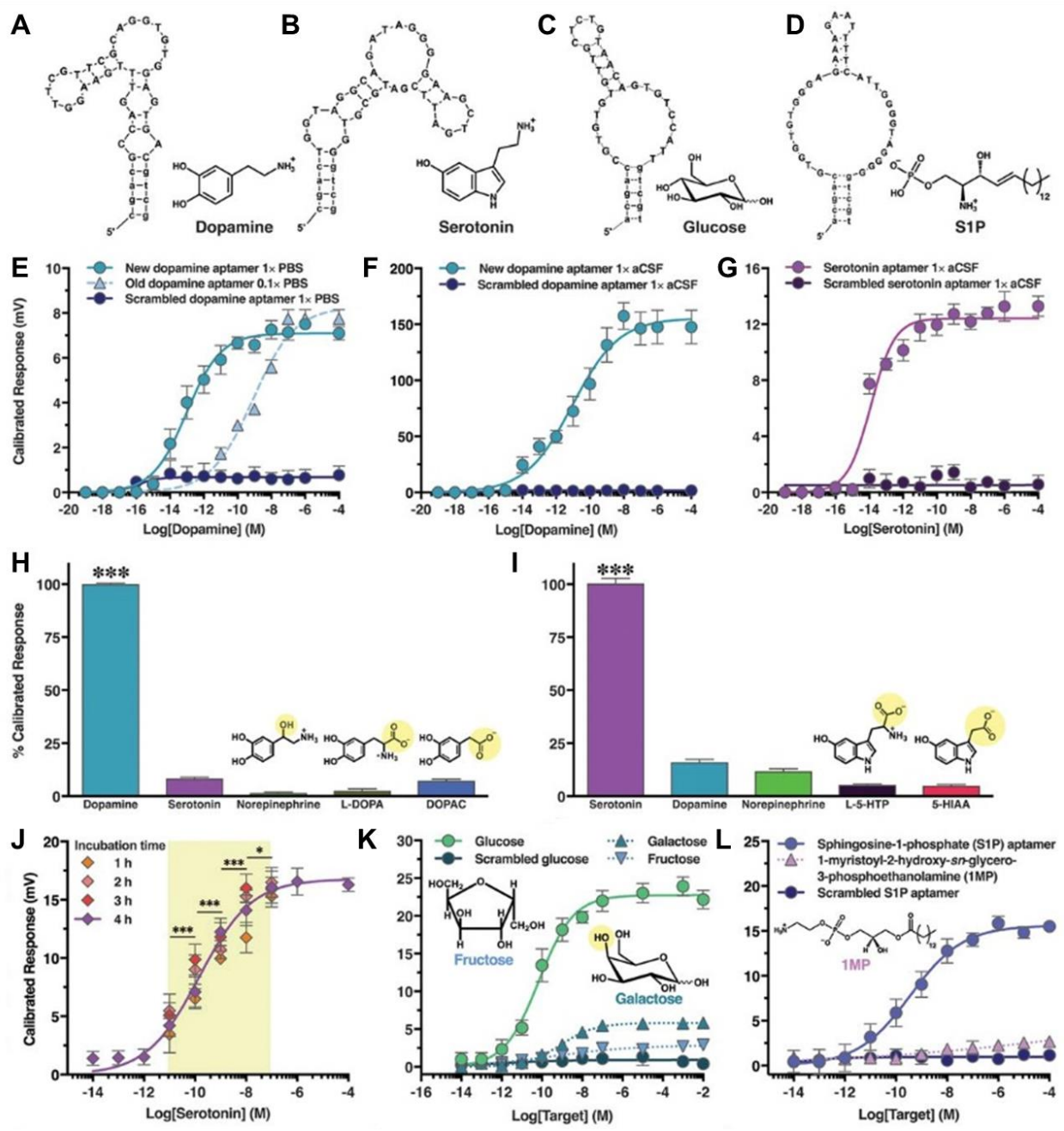

Figure I.4. (A-D) Aptamer sequences specific for dopamine, serotonin, glucose, and sphingosine-1-phosphate (S1P). Aptamer-field-effect transistor (FET) sensing of dopamine in **(E)** 1× phosphate-buffered saline (PBS) and **(F)** 1x artificial cerebral spinal fluid (aCSF), and **(G)** sensing of serotonin in 1× aCSF. **(H)** Dopamine and **(I)** serotonin aptamer-FET responses to similarly structured molecules showing minimal cross-reactivity. **(J)** Aptamer-FET sensing of serotonin in brain tissue homogenates from *Tph2* null mice. Detection of neutral targets **(K)** glucose and **(L)** S1P using aptamer-FETs. Reprinted (adapted) with permission from *Science*. Copyright 2018, American Association for the Advancement of Science.

Recently, Nakatsuka *et al.* integrated newly isolated high-affinity aptamers with ultrathin-film In_2O_3 FETs for the detection of a diverse range of biologically relevant small molecules (*e.g.*, neurotransmitters, sugars, lipids, **Figure I.4**).[45] Aptamers were isolated *via* solution phase *in vitro* systematic evolution of ligands by exponential enrichment (SELEX);[54,55] nucleic acid libraries were designed to lead to conformational changes upon target binding.[56,57] Rearrangement of a portion of the negatively charged oligonucleotide backbones (and solution counterions) of aptamers upon target capture occurs close enough to semiconductor surfaces to circumvent Debye-length limitations in physiological conditions.[45,58] Aptamer-FETs demonstrated selective detection of small-molecule targets, including neutral targets, over a dynamic concentration range in full ionic strength buffers and complex biological matrices (*e.g.*, brain tissue homogenates, whole blood, serum, **Figure I.4**).[45,58]

Investigation into the mechanism of detection revealed that aptamer backbones can rearrange closer to or further away from transistor surfaces upon target capture.[45] Additionally, FETs were able to detect target binding to aptamers that underwent large rearrangements in secondary structure, as well as subtler conformational changes (*i.e.*, adaptive binding with preformed structural motifs).[45] The ability to transduce modest conformational changes into measurable signals generalizes this approach when compared to other aptamer-based sensing strategies (*e.g.*, electrochemical aptamer-based sensors)[59-62] where measured signals are contingent upon large target-induced structural rearrangements.

Using an aptamer-FET biosensor platform, I developed sensors for the direct detection of the amino acid phenylalanine for potential point-of-care use for patients with

phenylketonuria (PKU), a common genetic disorder that results in elevated and potentially harmful levels of phenylalanine in the blood and brain.[58,63] There are currently no point-of-care or at-home options for measuring blood phenylalanine to assist with the management of PKU.[63] By integrating phenyalanine-specific aptamers onto thin-film In_2O_3 FET platforms, I showed highly sensitive phenylalanine detection under high ionic-strength, physiological conditions with negligible cross-reactivity to similarly structured interferents.[58] Using these sensors, I measured modest yet physiologically relevant differences in phenylalanine concentrations in serum from mice treated with a phenylalanine hydroxylase inhibitor (*i.e.*, a PKU mouse model), demonstrating potential use for rapid, serum phenylalanine determination.[58]

In parallel, I advanced FET biosensors to detect specific oligonucleotide sequences towards differentiating single nucleotide polymorphisms (SNPs), which are associated with genetic diseases (*e.g.*, sickle cell disease), as well as susceptibility to different types of cancer.[64] In this case, FETs were chemically functionalized with single-stranded DNA probes to test selectivity towards complementary target sequences *versus* target sequences that differed by single bases. By taking advantage of differences in stabilities of sequences with different base-pair mismatches, I demonstrated the ability of DNA-functionalized FETs to distinguish hybridization between fully complementary DNA and RNA sequences, and analogous sequences with different types and locations of mismatches. The development and implementation of biosensors that can sense and differentiate oligonucleotide sequences without amplification presents new opportunities in the fields of disease diagnostics and precision medicine.

In the following four chapters, I discuss advances and contributions that I have made using CLL, such as improving feature resolution, investigating supported Au monolayers, extending this technique to different substrates and molecules, and ultimately for the fabrication of FETs. In the subsequent two chapters, I explore the use of nucleic-acid-functionalized FETs as biosensors for the detection of the amino acid phenylalanine and specific nucleic acid sequences for potential point-of-care and personalized healthcare applications. I conclude by discussing prospects of the supported Au monolayer material fabricated *via* CLL as a platform for further characterization and structural growth, as well as structure-function relationships in aptamer-FETs towards the ultimate goal of measuring chemical signaling *in vivo*.

I.D. References

(1) Love, J. C.; Estroff, L. A.; Kriebel, J. K.; Nuzzo, R. G.; Whitesides, G. M. Self-Assembled Monolayers of Thiolates on Metals as a Form of Nanotechnology. *Chem. Rev.* **2005,** *105*, 1103–1170.

(2) Claridge, S. A.; Liao, W.-S.; Thomas, J. C.; Zhao, Y.; Cao, H. H.; Cheunkar, S.; Serino, A. C.; Andrews, A. M.; Weiss, P. S. From the Bottom Up: Dimensional Control and Characterization in Molecular Monolayers. *Chem. Soc. Rev.* **2013,** *42*, 2725–2745.

(3) Vericat, C.; Vela, M. E.; Corthey, G.; Pensa, E.; Cortés, E.; Fonticelli, M. H.; Ibañez, F.; Benitez, G. E.; Carro, P.; Salvarezza, R. C. Self-Assembled Monolayers of Thiolates on Metals: A Review Article on Sulfur-Metal Chemistry and Surface Structures. *RSC Advances* **2014,** *4*, 27730–27754.

(4) Mrksich, M.; Whitesides, G. M. Patterning Self-Assembled Monolayers Using Microcontact Printing: A New Technology for Biosensors? *Trends Biotechnol.* **1995,** *13*, 228–235.

(5) Wilbur, J. L.; Kumar, A.; Biebuyck, H. A.; Kim, E.; Whitesides, G. M. Microcontact Printing of Self-Assembled Monolayers: Applications in Microfabrication. *Nanotechnology* **1996,** *7*, 452–457.

(6) Xia, Y.; Whitesides, G. M. Extending Microcontact Printing as a Microlithographic Technique. *Langmuir* **1997,** *13*, 2059–2067.

(7) Smith, R. K.; Lewis, P. A.; Weiss, P. S. Patterning Self-Assembled Monolayers. *Prog. Surf. Sci.* **2004,** *75*, 1-68.

(8) Quist, A. P.; Pavlovic, E.; Oscarsson, S. Recent Advances in Microcontact Printing. *Anal. Bioanal. Chem.* **2005,** *381*, 591–600.

(9) Alom Ruiz, S.; Chen, C. S. Microcontact Printing: A Tool to Pattern. *Soft Matter* **2007,** *3*, 168–177.

(10) Jackman, R. J.; Wilbur, J. L.; Whitesides, G. M. Fabrication of Submicrometer Features on Curved Substrates by Microcontact Printing. *Science* **1995,** *269*, 664–666.

(11) Perl, A.; Reinhoudt, D. N.; Huskens, J. Microcontact Printing: Limitations and Achievements. *Adv. Mater.* **2009,** *21*, 2257–2268.

(12) Srinivasan, C.; Mullen, T. J.; Hohman, J. N.; Anderson, M. E.; Dameron, A. A.; Andrews, A. M.; Dickey, E. C.; Horn, M. W.; Weiss, P. S. Scanning Electron Microscopy of Nanoscale Chemical Patterns. *ACS Nano* **2007,** *1*, 191-201.

(13) Schwartz, J. J.; Hohman, J. N.; Morin, E. I.; Weiss, P. S. Molecular Flux Dependence of Chemical Patterning by Microcontact Printing. *ACS Appl. Mater. Interfaces* **2013,** *5*, 10310–10316.

(14) Piner, R. D.; Zhu, J.; Xu, F.; Hong, S.; Mirkin, C. A. "Dip-Pen" Nanolithography. *Science* **1999,** *283*, 661–663.

(15) Huo, F.; Zheng, Z.; Zheng, G.; Giam, L. R.; Zhang, H.; Mirkin, C. A. Polymer Pen Lithography. *Science* **2008,** *321*, 1658–1660.

(16) Huo, F.; Zheng, G.; Liao, X.; Giam, L. R.; Chai, J.; Chen, X.; Shim, W.; Mirkin, C. A. Beam Pen Lithography. *Nat. Nanotechnol.* **2010,** *5*, 637–640.

(17) Dameron, A. A.; Hampton, J. R.; Smith, R. K.; Mullen, T. J.; Gillmor, S. D.; Weiss, P. S. Microdisplacement Printing. *Nano Lett.* **2005,** *5*, 1834-1837.

(18) Dameron, A. A.; Hampton, J. R.; Gillmor, S. D.; Hohman, J. N.; Weiss, P. S. Enhanced molecular patterning via microdisplacement printing. *J. Vac. Sci. Technol., B: Microelectron. Process. Phenom.* **2005,** *23*, 2929-2932.

(19) Mullen, T. J.; Srinivasan, C.; Hohman, J. N.; Gillmor, S. D.; Shuster, M. J.; Horn, M. W.; Andrews, A. M.; Weiss, P. S. Microcontact Insertion Printing. *Appl. Phys. Lett.* **2007,** *90*, 063114.

(20) Vaish, A.; Shuster, M. J.; Cheunkar, S.; Weiss, P. S.; Andrews, A. M. Tuning Stamp Surface Energy for Soft Lithography of Polar Molecules to Fabricate Bioactive Small-Molecule Microarrays. *Small* **2011,** *7*, 1471-1479.

(21) Shuster, M. J.; Vaish, A.; Cao, H. H.; Guttentag, A. I.; McManigle, J. E.; Gibb, A. L.; Martinez, M. M.; Nezarati, R. M.; Hinds, J. M.; Liao, W. S.; Weiss, P. S.; Andrews, A. M. Patterning small-molecule biocapture surfaces: microcontact insertion printing vs.photolithography. *Chem. Commun.* **2011,** *47*, 10641-10643.

(22) Liao, W.-S.; Cheunkar, S.; Cao, H. H.; Bednar, H. R.; Weiss, P. S.; Andrews, A. M. Subtractive Patterning *via* Chemical Lift-Off Lithography. *Science* **2012,** *337*, 1517.

(23) Andrews, A. M.; Liao, W.-S.; Weiss, P. S. Double-Sided Opportunities Using Chemical Lift-Off Lithography. *Acc. Chem. Res.* **2016,** *49*, 1449-1457.

(24) Slaughter, L. S.; Cheung, K. M.; Kaappa, S.; Cao, H. H.; Yang, Q.; Young, T. D.; Serino, A. C.; Malola, S.; Olson, J. M.; Link, S.; Häkkinen, H.; Andrews, A. M.; Weiss, P. S. Patterning of Supported Gold Monolayers *via* Chemical Lift-Off Lithography. *Beilstein J. Nanotechnol.* **2017,** *8*, 2648–2661.

(25) Xu, X.; Yang, Q.; Cheung, K. M.; Zhao, C.; Wattanatorn, N.; Belling, J. N.; Abendroth, J. M.; Slaughter, L. S.; Mirkin, C. A.; Andrews, A. M.; Weiss, P. S. Polymer-Pen Chemical Lift-Off Lithography. *Nano Lett.* **2017,** *17*, 3302-3311.

(26) Cao, H. H.; Nakatsuka, N.; Serino, A. C.; Liao, W.-S.; Cheunkar, S.; Yang, H.; Weiss, P. S.; Andrews, A. M. Controlled DNA Patterning by Chemical Lift-Off Lithography: Matrix Matters. *ACS Nano* **2015,** *9*, 11439-11454.

(27) Abendroth, J. M.; Nakatsuka, N.; Ye, M.; Kim, D.; Fullerton, E. E.; Andrews, A. M.; Weiss, P. S. Analyzing Spin Selectivity in DNA-Mediated Charge Transfer *via* Fluorescence Microscopy. *ACS Nano* **2017,** *11*, 7516-7526.

(28) Cao, H. H.; Nakatsuka, N.; Liao, W.-S.; Serino, A. C.; Cheunkar, S.; Yang, H.; Weiss, P. S.; Andrews, A. M. Advancing Biocapture Substrates *via* Chemical Lift-Off Lithography. *Chem. Mater.* **2017,** *29*, 6829-6839.

(29) Cao, H. H.; Nakatsuka, N.; Deshayes, S.; Abendroth, J. M.; Yang, H.; Weiss, P. S.; Kasko, A. M.; Andrews, A. M. Small-Molecule Patterning *via* Prefunctionalized Alkanethiols. *Chem. Mater.* **2018,** *30*, 4017-4030.

(30) Chen, C.-Y.; Li, H.-H.; Chu, H.-Y.; Wang, C.-M.; Chang, C.-W.; Lin, L.-E.; Hsu, C.-C.; Liao, W.-S. Finely Tunable Surface Wettability by Two-Dimensional Molecular Manipulation. *ACS Appl. Mater. Interfaces* **2018,** *10*, 41814–41823.

(31) Chen, C.-Y.; Wang, C.-M.; Chen, P.-S.; Liao, W.-S. Surface Functional DNA Density Control by Programmable Molecular Defects. *Chem. Commun.* **2018,** *54*, 4100–4103.

(32) Chen, C.-Y.; Wang, C.-M.; Chen, P.-S.; Liao, W.-S. Self-Standing Aptamers by an Artificial Defect-Rich Matrix. *Nanoscale* **2018,** *10*, 3191–3197.

(33) Chen, C.-Y.; Wang, C.-M.; Li, H.-H.; Chan, H.-H.; Liao, W.-S. Wafer-Scale Bioactive Substrate Patterning by Chemical Lift-Off Lithography. *Beilstein J. Nanotechnol.* **2018,** *9*, 311–320.

(34) Kim, J.; Rim, Y. S.; Chen, H.; Cao, H. H.; Nakatsuka, N.; Hinton, H. L.; Zhao, C.; Andrews, A. M.; Yang, Y.; Weiss, P. S. Fabrication of High-Performance Ultrathin In2O3 Film Field-Effect Transistors and Biosensors Using Chemical Lift-Off Lithography. *ACS Nano* **2015,** *9*, 4572-4582.

(35) Zhao, C.; Xu, X.; Bae, S.-H.; Yang, Q.; Liu, W.; Belling, J. N.; Cheung, K. M.; Rim, Y. S.; Yang, Y.; Andrews, A. M.; Weiss, P. S. Large-Area, Ultrathin Metal-Oxide Semiconductor Nanoribbon Arrays Fabricated by Chemical Lift-Off Lithography. *Nano Lett.* **2018,** *18*, 5590-5595.

(36) Zhao, C.; Xu, X.; Yang, Q.; Man, T.; Jonas, S. J.; Schwartz, J. J.; Andrews, A. M.; Weiss, P. S. Self-Collapse Lithography. *Nano Lett.* **2017,** *17*, 5035-5042.

(37) Chen, C.-Y.; Wang, C.-M.; Liao, W.-S. A Special Connection between Nanofabrication and Analytical Devices: Chemical Lift-Off Lithography. *Bull. Chem. Soc. Jpn.* **2019,** *92*, 600-607.

(38) Cheung, K. M.; Stemer, D. M.; Zhao, C.; Young, T. D.; Belling, J. N.; Andrews, A. M.; Weiss, P. S. Chemical Lift-Off Lithography of Metal and Semiconductor Surfaces. *ACS Mater. Lett.* **2019,** *2*, 76-83.

(39) Thomas, J. C.; Schwartz, J. J.; Hohman, J. N.; Claridge, S. A.; Auluck, H. S.; Serino, A. C.; Spokoyny, A. M.; Tran, G.; Kelly, K. F.; Mirkin, C. A.; Gilles, J.; Osher, S. J.; Weiss, P. S. Defect-Tolerant Aligned Dipoles within Two-Dimensional Plastic Lattices. *ACS Nano* **2015,** *9*, 4734-4742.

(40) Thomas, J. C.; Boldog, I.; Auluck, H. S.; Bereciartua, P. J.; Dušek, M.; Macháček, J.; Bastl, Z.; Weiss, P. S.; Baše, T. Self-Assembled *p*-Carborane Analogue of *p*-Mercaptobenzoic Acid on Au{111}. *Chem. Mater.* **2015,** *27*, 5425-5435.

(41) Kim, J.; Rim, Y. S.; Liu, Y.; Serino, A. C.; Thomas, J. C.; Chen, H.; Yang, Y.; Weiss, P. S. Interface Control in Organic Electronics Using Mixed Monolayers of Carboranethiol Isomers. *Nano Lett.* **2014,** *14*, 2946-2951.

(42) Serino, A. C.; Anderson, M. E.; Saleh, L. M. A.; Dziedzic, R. M.; Mills, H.; Heidenreich, L. K.; Spokoyny, A. M.; Weiss, P. S. Work Function Control of Germanium through Carborane-Carboxylic Acid Surface Passivation. *ACS Appl. Mater. Interfaces* **2017,** *9*, 34592-34596.

(43) Walsh, R.; DeRosa, M. C. Retention of function in the DNA homolog of the RNA dopamine aptamer. *Biochem. Biophys. Res. Commun.* **2009,** *388*, 732-735.

(44) Rim, Y. S.; Bae, S.-H.; Chen, H.; Yang, J. L.; Kim, J.; Andrews, A. M.; Weiss, P. S.; Yang, Y.; Tseng, H.-R. Printable Ultrathin Metal Oxide Semiconductor-Based Conformal Biosensors. *ACS Nano* **2015,** *9*, 12174-12181.

(45) Nakatsuka, N.; Yang, K.-A.; Abendroth, J. M.; Cheung, K. M.; Xu, X.; Yang, H.; Zhao, C.; Zhu, B.; Rim, Y. S.; Yang, Y.; Weiss, P. S.; Stojanović, M. N.; Andrews, A. M. Aptamer–Field-Effect Transistors Overcome Debye Length Limitations for Small-Molecule Sensing. *Science* **2018,** *362*, 319.

(46) Allen, B. L.; Kichambare, P. D.; Star, A. Carbon Nanotube Field-Effect-Transistor-Based Biosensors. *Adv. Mater.* **2007,** *19*, 1439–1451.

(47) Curreli, M.; Zhang, R.; Ishikawa, F. N.; Chang, H.; Cote, R. J.; Zhou, C.; Thompson, M. E. Real-Time, Label-Free Detection of Biological Entities Using Nanowire-Based FETs. *IEEE Trans. Nanotechnol.* **2008,** *7*, 651–667.

(48) Green, N. S.; Norton, M. L. Interactions of DNA with Graphene and Sensing Applications of Graphene Field-Effect Transistor Devices: A Review. *Anal. Chim. Acta* **2015,** *853*, 127–142.

(49) Li, B.-R.; Hsieh, Y.-J.; Chen, Y.-X.; Chung, Y.-T.; Pan, C.-Y.; Chen, Y.-T. An Ultrasensitive Nanowire-Transistor Biosensor for Detecting Dopamine Release from Living PC12 Cells Under Hypoxic Stimulation. *J. Am. Chem. Soc.* **2013,** *135*, 16034–16037.

(50) Lung Khung, Y.; Narducci, D. Synergizing Nucleic Acid Aptamers with 1-Dimensional Nanostructures as Label-Free Field-Effect Transistor Biosensors. *Biosens. Bioelectron.* **2013,** *50*, 278–293.

(51) Schöning, M. J.; Poghossian, A. Recent Advances in Biologically Sensitive Field-Effect Transistors (BioFETs). *Analyst* **2002,** *127*, 1137–1151.

(52) So, H.-M.; Won, K.; Kim, Y. H.; Kim, B.-K.; Ryu, B. H.; Na, P. S.; Kim, H.; Lee, J.-O. Single-Walled Carbon Nanotube Biosensors Using Aptamers as Molecular Recognition Elements. *J. Am. Chem. Soc.* **2005,** *127*, 11906–11907.

(53) Vacic, A.; Criscione, J. M.; Rajan, N. K.; Stern, E.; Fahmy, T. M.; Reed, M. A. Determination of Molecular Configuration by Debye Length Modulation. *J. Am. Chem. Soc.* **2011,** *133*, 13886–13889.

(54) Ellington, A. D.; Szostak, J. W. In Vitro Selection of RNA Molecules that Bind Specific Ligands. *Nature* **1990,** *346*, 818-822.

(55) Tuerk, C.; Gold, L. Systematic Evolution of Ligands by Exponential Enrichment: RNA Ligands to Bacteriophage T4 DNA Polymerase. *Science* **1990,** *249*, 505.

(56) Yang, K.-A.; Pei, R.; Stefanovic, D.; Stojanović, M. N. Optimizing Cross-Reactivity with Evolutionary Search for Sensors. *J. Am. Chem. Soc.* **2012,** *134*, 1642–1647.

(57) Yang, K.-A.; Pei, R.; Stojanović, M. N. *In Vitro* Selection and Amplification Protocols for Isolation of Aptameric Sensors for Small Molecules. *Methods* **2016,** *106*, 58–65.

(58) Cheung, K. M.; Yang, K.-A.; Nakatsuka, N.; Zhao, C.; Ye, M.; Jung, M. E.; Yang, H.; Weiss, P. S.; Stojanovic, M.; Andrews, A. M. Phenylalanine Monitoring via Aptamer-Field-Effect Transistor Sensors. *ACS Sensors* **2019**, DOI:10.1021/acssensors.9b01963.

(59) Idili, A.; Gerson, J.; Parolo, C.; Kippin, T.; Plaxco, K. W. An Electrochemical Aptamer-Based Sensor for the Rapid and Convenient Measurement of L-Tryptophan. *Anal. Bioanal. Chem.* **2019,** *411*, 4629-4635.

(60) Kent, A. D.; Spiropulos, N. G.; Heemstra, J. M. General Approach for Engineering Small-Molecule-Binding DNA Split Aptamers. *Anal. Chem.* **2013,** *85*, 9916-9923.

(61) White, R. J.; Rowe, A. A.; Plaxco, K. W. Re-Engineering Aptamers to Support Reagentless, Self-Reporting Electrochemical Sensors. *Analyst* **2010,** *135*, 589-594.

(62) Xiao, Y.; Uzawa, T.; White, R. J.; DeMartini, D.; Plaxco, K. W. On the Signaling of Electrochemical Aptamer-Based Sensors: Collision- and Folding-Based Mechanisms. *Electroanalysis* **2009,** *21*, 1267–1271.

(63) Blau, N.; van Spronsen, F. J.; Levy, H. L. Phenylketonuria. *Lancet* **2010,** *376*, 1417–1427.

(64) Wang, D. G.; Fan, J.-B.; Siao, C.-J.; Berno, A.; Young, P.; Sapolsky, R.; Ghandour, G.; Perkins, N.; Winchester, E.; Spencer, J.; Kruglyak, L.; Stein, L.; Hsie, L.; Topaloglou, T.; Hubbell, E.; Robinson, E.; Mittmann, M.; Morris, M. S.; Shen, N.; Kilburn, D.; Rioux, J.; Nusbaum, C.; Rozen, S.; Hudson, T. J.; Lipshutz, R.; Chee, M.; Lander, E. S. Large-Scale Identification, Mapping, and Genotyping of Single-Nucleotide Polymorphisms in the Human Genome. *Science* **1998,** *280*, 1077–1082.

CHAPTER II

Polymer-Pen Chemical Lift-Off Lithography

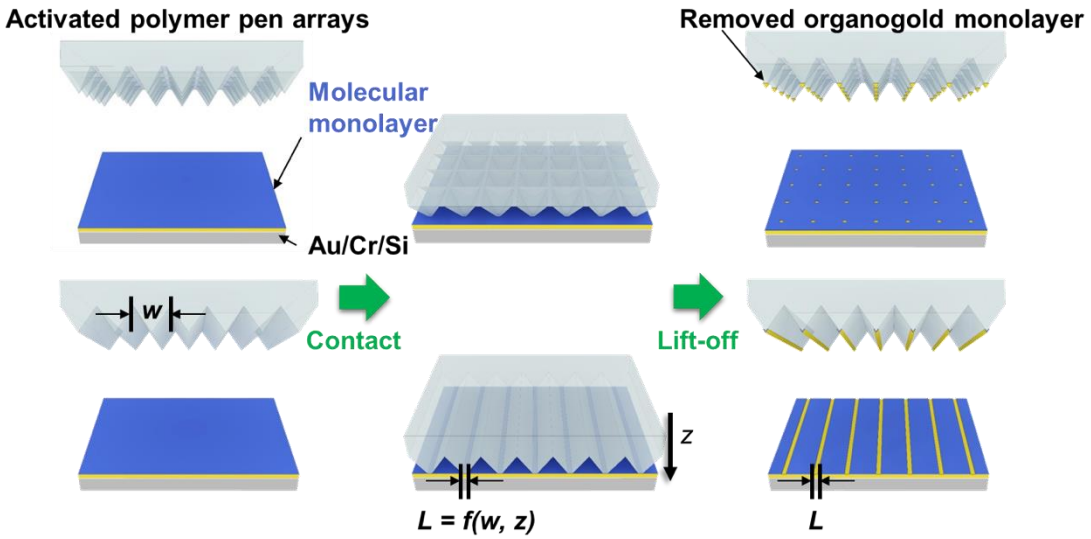

The information in this chapter was published in
Nano Letters **2017**, *17*, 3302–3311
and has been reproduced here with permission.

Authors: Xu, X.[#]; Yang, Q.[#]; **Cheung, K. M.**; Zhao, C.; Wattanatorn, N.; Belling, J. N.; Abendroth, J. M.; Slaughter, L. S.; Mirkin, C. A.; Andrews, A. M.; Weiss, P. S.

([#]indicates equal contribution)

II.A. Introduction

Substantial progress has been made in chemical patterning methods to push resolution from micron to nanometer scales for applications in electronics,[1-7] optics,[8,9] energy,[10,11] and biology,[12,13] *e.g.*, integrated circuits,[14-16] displays,[17-19] ultrasensitive biosensors,[20-25] nanomotors,[26] biomolecule micro-/nano-arrays,[27-31] wearable sensors,[32-35] and other advanced metamaterials.[36] Nano- and microfabrication are dominated by patterning methods based on energetic beams, such as light, electrons, ions, and X-rays. Conventional photolithography can be used to fabricate structures over large areas, however, resolution is limited and costs of the masks are high. Advanced lithography techniques, such as liquid immersion/multiple patterning photolithography,[37,38] X-ray lithography,[39,40] or extreme ultraviolet photolithography[41-43] can push resolution to nanometer scales but availability is limited due to high set-up and maintenance costs. Direct-write techniques, such as electron-beam lithography (EBL)[44-50] and focused ion-beam lithography (FIB)[51,52] are used to generate nanoscale patterns, but time-consuming serial writing processes limit their throughput.[53]

Without using energetic beams, microcontact printing (μCP) is a high-throughput, straightforward molecular printing technique for chemical patterning at the micro- and nanometer scales.[54,55] Microcontact printing involves elastomeric stamps with molecular "inks" such as organic molecules, proteins, or DNA that enables ink transfer to planar or curved substrates composed of metals, glass, or polymers to produce patterns. Organic ink molecules, such as alkanethiols, serve as molecular resists in successive wet etching steps to transfer patterns to underlying substrates, *e.g.*, metals.[56,57] Nonetheless, ink molecules are

known to diffuse laterally beyond the contact areas during printing, resulting in resolution limited to ~100 nm for μCP.[58-60]

We have developed strategies to minimize or to eliminate lateral diffusion of ink molecules *via* modified μCP methods.[61-66] For example, microdisplacement printing[67,68] and microcontact insertion printing[59,69] are used to print molecules on alkanethiol self-assembled monolayer (SAM) -modified substrates through displacement or insertion processes, respectively. The SAMs in the unpatterned regions prevent ink molecules from diffusing beyond the contact areas.[59,70] We also developed a "subtractive" stamping process called chemical lift-off lithography (CLL),[60,71] in which oxygen plasma-activated polydimethylsiloxane (PDMS) stamps selectively remove hydroxyl- (-OH) (or other sufficiently reactive groups such as amine-) terminated alkanethiols only in the contact areas with high pattern fidelity and without observable lateral diffusion. The remaining molecules of the SAM in the non-lifted-off regions act as resists for selective etching of exposed gold in the patterned regions. High-fidelity chemical patterns with linewidths as narrow as 40 ± 2 nm were achieved using CLL, with features reaching 20 nm *via* double patterning[60] and even 5 nm (corresponding to patterns *ca*. ten molecules across).[71] However, for CLL, like μCP, the fabrication of masters with nanometer-scale resolution relies on low-throughput, high-cost EBL/FIB limiting applicability.

Dip-pen lithography can write chemical patterns directly on substrates at sub-50 nm resolution by using atomic force microscopy with tip-coated molecular "inks", *e.g.*, alkanethiols, but again, throughput is low due to time-consuming serial writing.[72] Polymer-pen lithography (PPL)[73-77] combines high-resolution dip-pen lithography[72,78] and μCP by using a scanning stage equipped with massively parallel polymer-pen arrays (with sub-

80 nm tip diameters) to write patterns with ink molecules directly at ~100 nm resolution with high throughput.[73] Reusable masters for producing polymer pens are fabricated by conventional photolithography at micron-scale resolution *via* anisotropic etching of Si{100}.[73] The use of a scanning stage enables nanometer-scale control of polymer pens in the *x, y,* and *z* planes. Another advantage of PPL is that feature sizes can be tuned from 80 nm to >10 μm by varying dwell times and vertical pen compression in a single stamp.[76] However, lateral diffusion of ink molecules persists, limiting the resolution of PPL similar to issues with μCP.

To advance feature resolution in chemical patterning in highly multiplexed and facile directions, we developed a hybrid method termed polymer-pen chemical lift-off lithography (PPCLL) that combines the advantages of PPL (massively parallel polymer pens with nanometer-scale tips for high-throughput patterning and feature size tunability by controlling vertical compression distances) and CLL (high-fidelity patterning without lateral diffusion) to enable large-area, low-cost, and sub-20-nm resolution patterning capabilities simultaneously.

II.B. Experimental Methods

II.B.1. Materials

Prime quality 4″ Si{100} wafers (P/B, 1-10 ohm-cm) were purchased from University Wafer Inc. (Boston, MA, USA). 11-Mercapto-1-undecanol was purchased from Sigma-Aldrich (St. Louis, MO, USA). Sylgard 184® silicone elastomer kit was purchased from Ellsworth Adhesives (Germantown, WI, USA). The 32-mer DNA molecules thiolated at the 5′ end (5′-/5ThioMC6-D/GAC TGA CCT CGG ACG CGA CTG ACC TCG GAC GA-3′ with molecular

weight 10148.8 g/mol and melting temperature 70.1 °C) and Alexa 488 fluorophore-labeled complementary DNA (5′-/5Alex488N/TCG TCC GAG GTC AGT CGC GTC CGA GGT CAG TC-3′ with molecular weight 10529.0 g/mol and melting temperature 70.1 °C) were purchased from Integrated DNA Technologies (Coralville, IA, USA). The DNA stock solutions were diluted to 1 μM with TE buffer (10 mM Tris and 0.1 mM EDTA). The ZEP 520A e-beam resist, SPR700-1.2 photoresist, MF-26A developer, and 30 wt% potassium hydroxide (KOH) solutions were obtained from the Integrated Systems Nanofabrication Cleanroom (ISNC) at UCLA.

II.B.2. Characterization

Scanning electron microscopy (SEM) images were taken using a Zeiss Supra 40VP scanning electron microscope (SEM). The PDMS stamps were made conductive by sputtering 5-nm Au for SEM imaging. ImageJ (https://imagej.nih.gov/ij/) was used to quantify the dimensions of the micro/nanostructures and chemical patterns in the SEM images. Surface roughness was characterized using a Bruker Dimension Icon Scanning Probe Microscope.

II.B.3.Fabrication of Si Masters and PDMS Stamps

Fabrication of Si masters and PDMS stamps are shown in **Scheme II.S1.** A 500-nm-thick SiO_2 film was thermally grown on piranha-cleaned Si{100} wafers. The pattern in the photomask was designed using AutoCAD software (Autodesk, Inc.). Photomasks for fabricating Si masters composed of a 2D array of squares or lines whose linewidths were >1 μm were fabricated by conventional photolithography. The designed linewidths were equal to the base linewidths of the polymer pens. Positive photoresist SPR700-1.2 was spin-coated on SiO_2/Si wafer surfaces, followed by a 90 s soft bake at 90 °C on a hotplate. A Karl Suss contact aligner was used to expose the photoresist on the wafers selectively with the pattern from

photomask with an optimal exposure time of 16.5 sec (UV wavelength = 365 nm, intensity = 8.5 mW/cm^2). The exposed wafers were baked post-exposure at 110 °C for 90 s, immersed in MF-26A developer for 1 min (development), rinsed with deionized water, and blown dry with N_2 gas.

For a proof of concept of PPCLL, we designed a line array pattern with a series of linewidths in sequence from 3500 nm to 4000 nm, as listed in **Table II.1**, with neighbor center-to-center distances of 14 μm. Between each two neighboring lines, we inserted a line with a 6 μm linewidth, which served as the pattern for the support elements. All of the lines had the same 200 μm length. Positive electron-beam resist ZEP 520A was spin-coated (3000 RPM, 30 sec) on a (2 cm × 2 cm) Si{100} wafer with a 500-nm-thick SiO_2 coating. The edge of the Si{100} wafer was pre-cut to be parallel to the Si<110> direction. A pre-bake was performed at 180 °C for 2 min. An electron-beam writer (Vistec EBPG 5000+ ES) was used to write the designed patterns on the substrate with repeated line arrays with an overall area of 1 cm × 1 cm. One min of development in ZED-N50 was used to expose the SiO_2 pattern.

After patterning by photolithography or EBL, the exposed SiO_2 was selectively etched by RIE (Oxford 80 Plus) using a gas mixture of CHF_3 (25-sccm) and Ar (25 sccm) at 35 mTorr. Anisotropic etching of Si{100} took place in a mixture of 4:1 KOH (30%) and isopropanol at 75 °C with variable times depending on the feature sizes. The fabrication of the Si master was completed by removing the remaining SiO_2 and resist in a 25% HF solution for 5 min. A 10:1 mass ratio of Sylgard® 184 elastomer silicone elastomer base and curing agent were thoroughly mixed and then degassed in a vacuum desiccator. This mixture was poured onto the Si master and cured overnight at 65 °C. After curing, PDMS stamps were carefully removed from the Si master.

II.B.4. Surface Functionalization of Au/Cr/Si Substrates for PPCLL

The 5-nm Cr and 100-nm Au films were deposited on clean silicon wafers in a CHA Solution E-Beam Evaporator at high vacuum (10^{-8} Torr) with evaporation rates of 0.1 nm/s. The Cr/Au/Si wafers were annealed in a hydrogen flame for 5-10 sec to create Au{111} surfaces and then immersed into a 0.5 mM 11-mercapto-1-undecanol ethanolic solution overnight for SAM formation on the Au surface.

II.B.5. Activation of PDMS Stamps

Clean PDMS stamps were treated in oxygen plasma (Harrick Plasma, Ithaca, NY) for 40 s at a power of 18 W and a pressure of 10 to generate hydrophilic surfaces.

II.B.6. DNA Insertion and Fluorescence Microscopy

Substrates after PPCLL were incubated in a 1 μm solution of thiolated DNA in 0.01 M PBS (pH = 7.4) for ~17 h to insert the DNA into the lifted-off areas. The substrates were then rinsed with deionized water and blown dry with N_2 gas. The inserted DNA was hybridized by incubating the substrates with a 1 μm solution of Alexa 488-labeled complementary DNA in 0.01 M PBS (pH = 7.4) for 30 min. Samples were imaged using an inverted fluorescence microscope (Axio Observer.D1, Carl Zeiss MicroImaging, Inc., Thornwood, NY, USA) with excitation and emission wavelengths of 470 ± 20 nm and 525 ± 25 nm, respectively.

II.C. Results and Discussion

Fabrication of polymer pens with nanometer-sized tip diameters is described (**Scheme II.S1**). Films of 500-nm-thick SiO_2 were grown on 4" Si{100} wafers *via* thermal oxidation, followed by spin coating with photoresist (SPR700-1.2). Conventional photolithography was then used to create micron-scale square or line array patterns on photoresist-coated

SiO_2/Si{100} wafers. The linewidths of the masters govern the *base* linewidths of the polymer pens. Overall areas are 1.5 cm × 1.5 cm for each square or line array pattern. It is critical to align edge axes of the square/line features on each photomask such that they are parallel with the primary flat edge of each Si{100} wafer, which is parallel to the <110> direction of Si{100}. Imperfect alignment resulted in blunt pen tips.

Next, reactive ion-etching (RIE) was used to etch exposed SiO_2 selectively to reveal the underlying Si{100}. Subsequently, a solution with a 4:1 ratio of 30% KOH and isopropanol was used to etch Si{100} wafers anisotropically to generate recessed pyramidal or v-shaped structure arrays having base dimensions matched to the designed patterns in the photomasks.[77] The Si master fabrication was completed by removing remaining SiO_2 in 25% HF solution for 5 min. Finally, PDMS stamps containing arrays of polymer pens were produced from the masters. Both the masters and stamps can be reused many times.

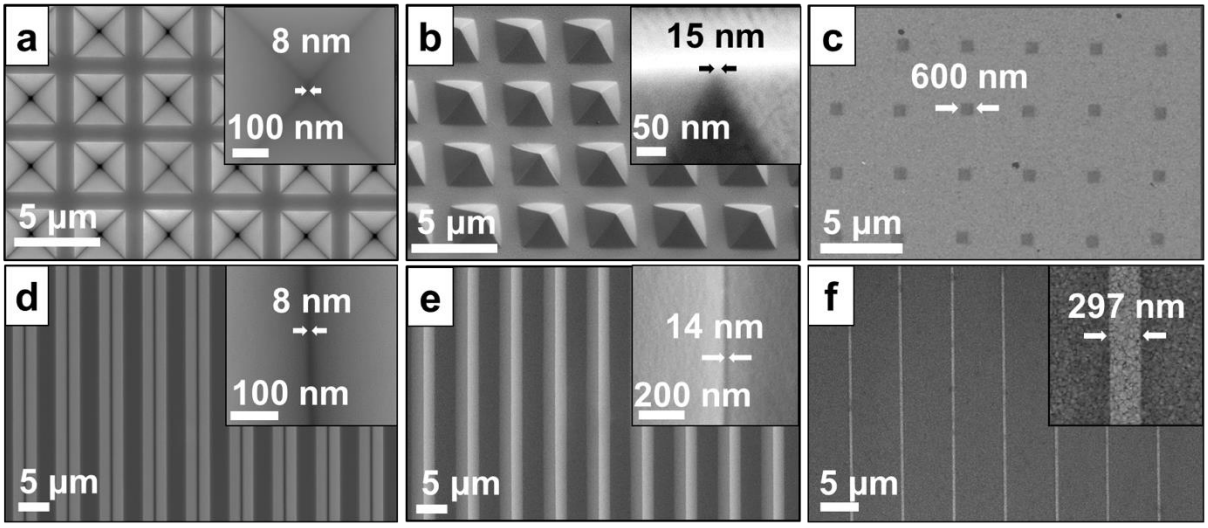

Figure II.1. Scanning electron microscopy (SEM) images of: **(a)** Si master with recessed pyramidal structures having base linewidths of 3 µm and a periodicity of 4 µm; **(b)** polydimethylsiloxane (PDMS) stamp with pyramidal polymer-pen arrays replicated from the master in **(a)**; **(c)** polymer-pen chemical lift-off lithography (PPCLL) pattern produced using the stamp in **(b)** without external compression; **(d)** Si master with recessed v-shaped structures with base linewidths of 3.8 µm and a periodicity of 7 µm; **(e)** PDMS stamp with v-shaped polymer pen arrays replicated from the master in **(d)**; **(f)** typical PPCLL pattern produced using the stamp in **(b)** without external compression. (Insets: high magnification SEM images) (The images **(c)** and **(f)** are processed to visualize the patterns better; the unprocessed images are shown in **Figure II.S3**).

As shown in the scanning electron microscopy (SEM) images in **Figure II.1**, high-quality Si masters containing large arrays of recessed pyramidal or v-shaped structures and stamps containing large arrays of protruding pyramidal/v-shaped polymer pens were fabricated using this method. The recessed pyramids or v-shaped structures of the masters had typical tip diameters d_{tip} of 8 nm, whereas protruding pyramids and v-shaped polymer pens had average measured tip diameters d_{tip} of 19 ± 2 nm and 15 ± 2 nm, respectively. Typical polymer pen tips with d_{tip} of 15 nm and 14 nm are shown in the insets of **Figure II.1.** The larger tip diameters of the features on the PDMS stamps compared to those of the masters were likely due to tip-rounding effects caused by the high surface tension of PDMS when it is applied to the masters (and before curing).[79] The sub-20-nm tip-diameters d_{tip} of

the polymer pens are comparable to the smallest features fabricated using EBL,[48] however, polymer pens produced by the method described above avoid EBL and thus, the need to produce each set of pens serially. Average tip diameters of the polymer pens fabricated here are smaller than most reported polymer pens (usually >50 nm),[73] because the square or narrow rectangular features on the photomasks have small widths (<6 μm) and their edges were perfectly aligned to Si<110> directions to allow Si{111} facets to converge into sharp points or sharp lines during the anisotropic etching of Si{100}.

As-fabricated PDMS stamps with polymer pen arrays were used in PPCLL as illustrated in **Scheme II.1.** Step 1: a 40-sec O_2 plasma-treatment-generated hydrophilic siloxy (Si-OH) groups on PDMS stamp surfaces containing pyramidal/v-shaped polymer pens. This step is called "activation".[80] Step 2: activated PDMS stamps were brought into conformal contact with Au/Cr/Si substrates (Au: 100 nm over Cr: 5 nm) functionalized with hydroxyl-terminated alkanethiol SAM molecules. 11-Mercapto-1-undecanol SAM molecules were used throughout this study, but alkanethiols with other backbones, chain lengths, and terminal functional groups can be used.[31,60] A condensation reaction occurs between Si-OH groups on activated PDMS stamps and the terminal hydroxyl groups of the self-assembled alkanethiol molecules to form covalent bonds, *i.e.*, Si-O-SAM thereby enabling lift-off.[60] Step 3: the PDMS stamps were removed to lift-off SAM molecules only in the contact areas producing complementary patterns of SAMs on the Au/Cr/Si substrates. Note that in this lift-off process, a layer of Au adatoms is removed along with the lifted SAM molecules. We hypothesize that this occurs because weaker Au-Au bonds in the top layer of the substrate surfaces are preferentially broken during lift-off, rather than the Au-S bonds between the substrate and alkanethiols.[60]

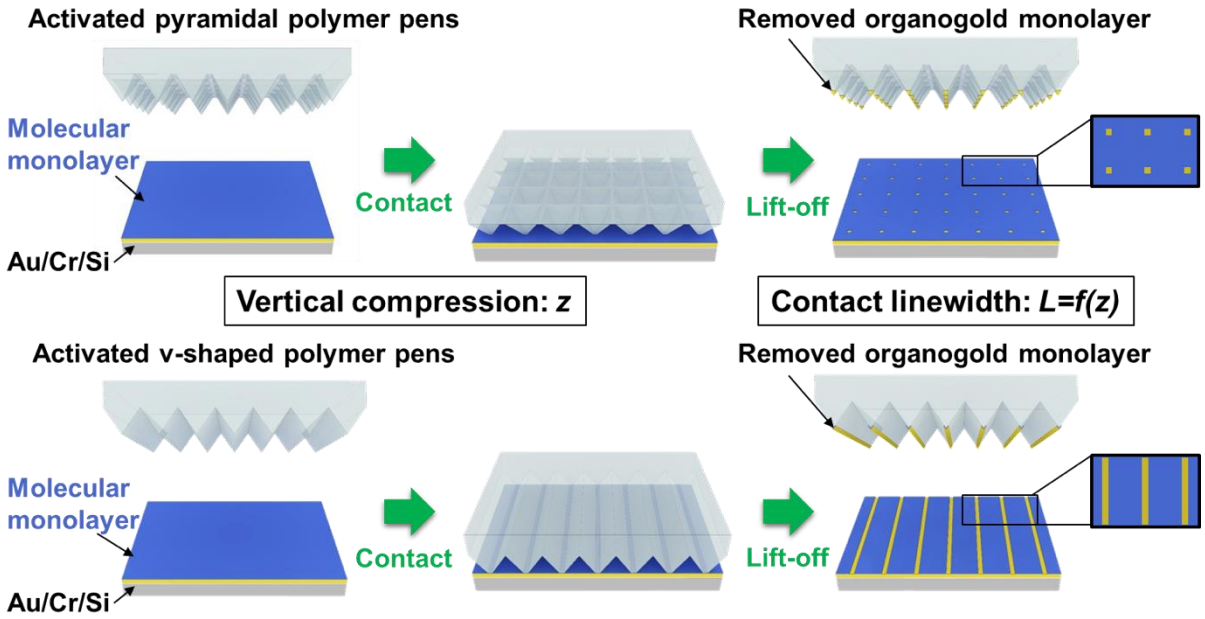

Scheme II.1. Schematic illustrations of polymer-pen chemical lift-off lithography (PPCLL) using pyramidal (top) and v-shaped (bottom) polymer pen arrays. In both cases, in the first step, hydroxyl-terminated alkanethiol molecules form self-assembled monolayers (SAMs) on Au/Cr/Si substrates. The polydimethylsiloxane (PDMS) stamps carrying the polymer-pen arrays are then activated with oxygen plasma treatment. In the second step, an activated PDMS stamp is brought into conformal contact with the SAM on a Au/Cr/Si substrate using a known vertical compression distance. Condensation reactions occur between the hydroxyl-terminated SAM molecules and the activated PDMS stamp to form strong covalent bonds. In the third step, the PDMS stamp is lifted off of the substrate, removing a portion of SAM molecules (~70%) together with Au adatoms from the contact areas to produce a complementary pattern on the substrate and an organogold monolayer on the stamp in the regions of contact. The contact/feature linewidth (L) is controlled by the vertical compression distance (z) of the stamp during contact *via* the relationship $L = f(z)$.

As previously reported,[76,77] deformation of polymer pens and thus, the areas contacted by each pen can be controlled in PPL by compressing the polymer pens onto the substrates using a scanning stage with vertical compression-distance control. For example, square features can be obtained with linewidths ranging from 500-2000 nm by controlled vertical compression with sub-micron increments.[76] However, time-dependent lateral diffusion results in larger feature sizes than actual contact areas in PPL. By contrast, in PPCLL, patterned features and contact areas are *identical* in size. If the vertical compression

distance is controlled at the nanometer-scale, then presumably contact areas can be correspondingly controlled. However, in practice, nanometer-scale differences in deformation and contact areas are challenging.

Alternately, computational simulations can be used to predict deformation at the nanometer scale. Here, we simulated compression of v-shaped polymer pens, in addition to the more well-studied pyramidal polymer pens.[76,81] Zheng *et al*. simulated deformation of pyramidal polymer pens and found that contact radii increased linearly with vertical compression distances from sub-100-nm to sub-micron with nanometer-scale resolution.[81] To simulate the vertical compression-distance dependent deformation of v-shaped polymer pens at the nanometer scale, we constructed a 2D *Mooney-Rivlin* model using a finite-element method *via* ANSYS software (Ansys Inc., Canonsburg, PA). We simulated vertical compression distances (z) from 0 nm to 560 nm with a minimum step size in z of 2 nm for v-shaped polymer pens having a base linewidth (w) = 4000 nm and a tip diameter of 22 nm. An element size of 8 nm was used to model polymer-pen tips (from the tip to 400 nm in height). For the remainder of the polymer-pen height, an element size of 40 nm was used.

The initial contact was set to occur at a vertical compression distance of z = 10 nm. As shown in **Figure II.2**, as z increased, the v-shaped polymer pen tips flattened and the contact linewidths (L) increased. After fitting, we found a quadratic dependence between z and L at w = 4000 nm:

$$L = f(z) = a + bz + cz^2 \quad \textbf{Eq. (II.1)}$$

where a = 0 nm, b = 0.444, c = 5.72 × 10^{-4} nm^{-1}, z > 10 nm, with L in nm. According to **Eq. (II.1)**, we can precisely and robustly control the feature size by controlling z. Note, that the standard deviation of the difference between the simulation results and fitted curve is

only 1.4 nm, and can be further reduced by decreasing the element size and step size in the simulations. Therefore, **Eq. (II.1)** accurately represents the relationship between z and L.

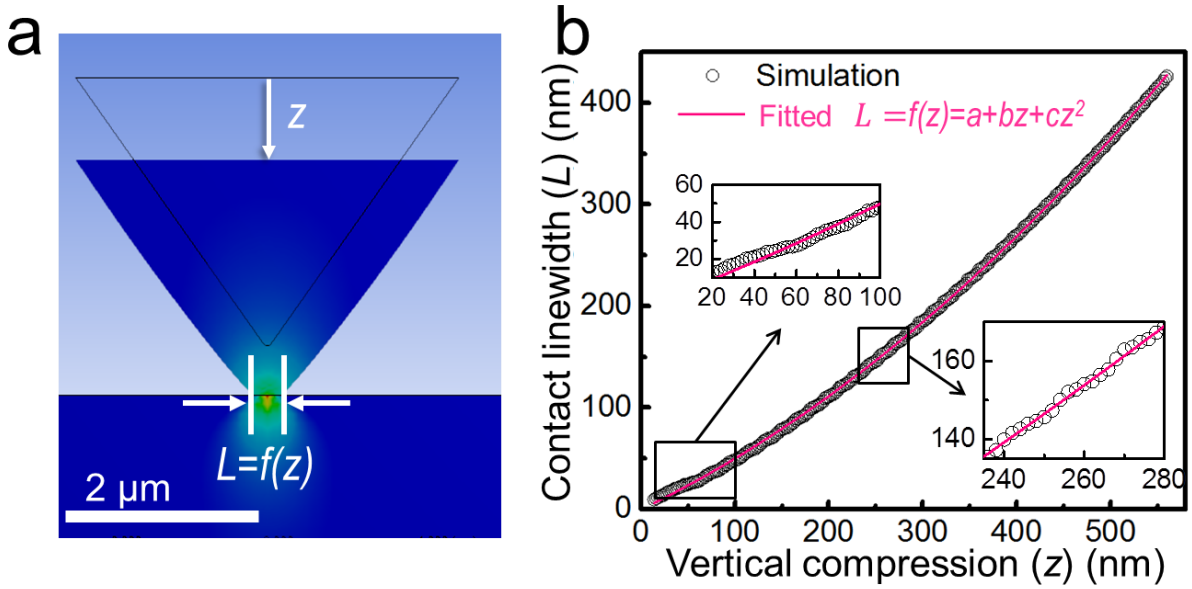

Figure II.2. (a) Simulation: cross-sectional view of a v-shaped polymer pen (base linewidth: 4-μm) vertically compressed onto a rigid Au surface with a vertical compression distance of z and a resulting contact linewidth of $L = f(z)$. **(b)** Simulation results: increasing the vertical compression distance z leads to increased contact linewidth (L). The relationship between vertical compression distance z and L is fitted using the quadratic equation $L = f(z) = a + bz + cz^2$, where a, b, and c are constants.

The above simulations demonstrate that feature-size resolution can be tuned at the nanometer scale in PPCLL. However, in practical experiments, resolution is affected by the following additional factors: (a) precision of vertical compression distance, which relies solely on the resolution of the scanning stage – typically, a piezoelectric stage has a resolution <1 nm; and (b) surface smoothness of the polymer pens and substrates. As shown in **Figure II.S1**, atomic force microscopy characterization shows that the surfaces used here have an arithmetic average roughness (R_a) of 0.4 ± 0.1 nm for a recessed structure in the master and 1.1 ± 0.1 nm for a polymer pen. The value of R_a for the Au/Cr/Si substrate is ~1 nm (data not shown).

The integration of a piezoelectric scanning stage[75,77] and a high-quality leveling technique into PPCLL, such as an optical- or force-feedback leveling system, would enable an ultimate theoretical resolution of <2 nm to be reached.[75] Without using these advanced equipment-intensive techniques, we nevertheless demonstrate nanometer-scale feature size control in PPCLL by designing and implementing a support-arm array system and polymer pen arrays with height gradients, as described in the following experiments and simulations.

In the first experiment, activated PDMS stamps containing large arrays (3750 × 3750 and 1 × 2150) of pyramidal (w = 3 μm, period = 4 μm) or v-shaped polymer pens (w = 3.8 μm, period = 7 μm) were placed on substrates without external compression. Stamps conformally contacted substrates without the need for a leveling system. The contact time was set to 4-6 h to ensure high-quality pattern transfer. Our previous CLL work showed features could be transferred with contact times as short as 1 min; however, shorter contact times resulted in poorer features after wet etching.

The PPCLL patterns were imaged by SEM. The different intensities observed in SEM images were due to different chemical components on the surfaces.[59] As shown in **Figure II.1c,f**, a square-dot array pattern (~600 nm linewidth) and a line-array pattern (~300 nm linewidth) were achieved. Moreover, the lateral diffusion of ink molecules was avoided in PPCLL, otherwise much enlarged features would have been observed after such long contact times.[59,76] The periodicities of the dot/line arrays were consistent with the stamp patterns. The enlarged feature sizes, compared to the original 20 nm tip diameters, was the result of polymer pen deformation caused by the weight of the stamps, which increased the contact linewidth to >20 nm. However, features were still 1-2 orders of magnitude smaller than the base linewidths of the polymer pens in the photomask. Without

using sophisticated fabrication techniques, we achieved sub-micron feature scales over large areas simply by this "contact & lift" process. Our results demonstrate that PPCLL is an economical and high-throughput method for producing sub-micron features over large areas.

We learned from the first set of experiments that the stamp weight deforms the tips such that no leveling is necessary. The height of each pyramidal/v-shaped polymer pen (h) is determined by its base linewidth (w) using the equation: $h = \frac{w}{2} \cdot tan\ tan\ \theta\ = \frac{w}{\sqrt{2}}$, here θ is the angle between the Si{100} and Si{111} facets. Thus, polymer pens with a series of different base linewidths (w_i) have different heights (h_i) by design. As illustrated in **Figure II.3a**, the distances ($D_i = D_0 - h_i$) from the tip of each polymer pen to the surface are different, where the subscript i ($i > 0$) is used to distinguish different polymer pens, and D_0 ($D_0 > h_i$) is the initial vertical distance from the base of the polymer pens to the surface of each substrate before contact. Under conformal contact, all of the polymer pens have the same initial vertical compression distance, z. However, upon initial contact with the substrate and due to their height differences, each polymer pen has a *different* effective vertical compression distance, $z_i' = z - D_i$. Contact only occurs when $z_i' > 0$, *i.e.*, $z > D_i$. Each contacted polymer pen has a contact linewidth, $L = f(z_i')$. We hypothesize that this process would be similar to vertical compression distances in PPCLL controlled using a piezoelectric scanning stage system.

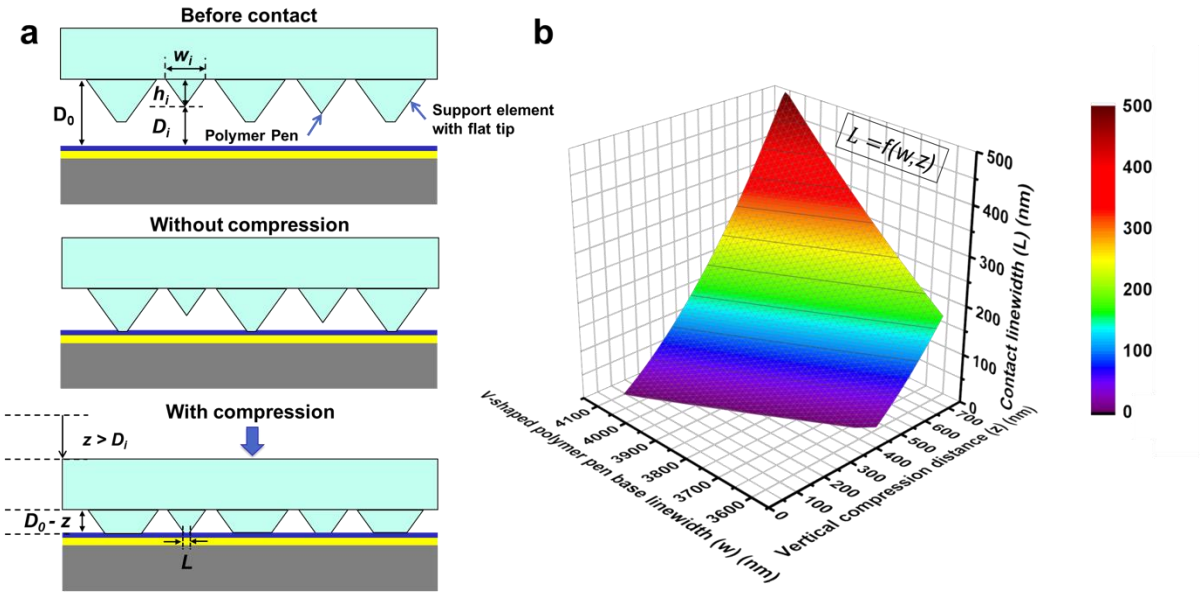

Figure II.3. (a) Illustration of a polydimethylsiloxane (PDMS) stamp used in polymer-pen chemical lift-off lithography (PPCLL) having support elements (taller v-shaped polymer pens with flat tips) interleaved with v-shaped polymer pens (sharp tips with designed base linewidths w_i): before contact, after placement on a substrate but with no vertical compression, and after vertical compression. Here, D_0 ($D_0 > h_i$) is the initial vertical distance from the base of the polymer pens to the surface of each substrate before contact; h_i is the height of a polymer pen; D_i is distance from the polymer pen tip to the substrate, $D_i = D_0 - h_i$; z is the vertical compression distance and L is resulting contact linewidth. **(b)** Simulation of results where v-shaped polymer pen base linewidths (w) and vertical compression distances (z) were varied to control contact-dependent linewidths (L), *i.e.*, $L = f(w, z)$.

To test this hypothesis, we added the base linewidth w as another variable in our simulations, in addition to the vertical compression distance z, *i.e.*, $L = f(w, z)$. In this simulation, we designed a series of w values ranging from 3500 to 4000 nm in increments of 25 nm. The initial vertical distance from the base of all of the v-shaped polymer pens to the surfaces of substrates was set at D_0 = 3000 nm, which is a reasonable distance to keep all of the v-shaped polymer pens from contacting the substrates. Then, vertical compression distances z, ranging from 0 to 700 nm with a step size of 5 nm, were applied in the contact simulation between each v-shaped polymer pen and the substrate. After fitting the simulation results for all of the polymer pens with $L = f(z)$, we derived a series of fitted curves.

We plotted and connected all the fitted curves in the same 3D space to form a curved surface. The curved surface was well fit by:

$$L = f(z, w) = a + bz + cw + dzw + ez^2 + fw^2 \quad \textbf{Eq. (II.2)}$$

where a = 2783, b = -2.786, c = -1.602, d = 7.572 × 10^{-4}, e = 5.729 × 10^{-4}, f = 2.232 × 10^{-4} (the fitted curved surface is plotted in **Figure II.3b**. The **Eq. (II.2)** is a universal equation wherein we can design and control desired contact linewidths L either through w or z. Furthermore, when z is fixed, w becomes the only variable influencing L. Under these conditions, **Eq. (II.2)** is reduced to:

$$L = f(w) = a'' + b''w + c''w^2 \quad \textbf{Eq. (II.3)}$$

Based on the above simulation results, in the second experiment, we added two components in PPCLL, *i.e.*, a stamp support system and polymer pens with height gradients. The supporting elements are taller polymer pens with flat tips (obtained by incomplete anisotropic etching of Si{100}) distributed between the polymer pens used for pattering, as illustrated in **Figure II.3a**. Here, the support elements have fixed base linewidths of 6 μm (**Figure II.4a**). These support elements serve as weight-bearing pillars to support the stamp[56] and the flat tips further serve as a low-cost leveling system. Properly designed support elements can either keep the patterning-purpose polymer-pen arrays away from the substrate by fully cancelling the weight of the stamp or they can control the degree of tip deformation of the patterning-purpose polymer pens by partially offsetting the stamp weights. The support elements can also be integrated into other PPL designs as an initial contact indicator to estimate how much extra vertical compression distance or force is needed to obtain desired contact areas.[75,77]

For the second component, a series of v-shaped polymer pen arrays was designed with base linewidths from 3500 to 4000 nm, as listed in **Table II.1.** The support elements were designed with linewidth increments of 25, 50, and 100 nm. For the 25-nm increment (shown in bold in **Table II.1**), the corresponding height increment of the polymer pens was $\frac{25\ nm}{\sqrt{2}} = 18\ nm$. As shown in **Figure II.4a,** the v-shaped polymer pens were separated by the support elements. Electron-beam lithography was used to produce base linewidths with small increments (25 to 100 nm) for proof-of-concept purposes (details of EBL are in Materials and Methods). The differences between the designed base linewidths (w_{design}) and the measured base linewidths ($w_{measured}$) of the v-shaped polymer pens were 100 nm, as listed in **Table II.1.**

Using this stamp design, a PPCLL experiment *without* an extra compression force beyond the weight of the stamp was performed. As seen in the SEM image in **Figure II.4**, v-shaped polymer pens with larger base linewidths generated larger PPCLL feature linewidths, which indicated larger contact areas, as expected. A full set of SEM images are shown in **Figure II.S4**. As listed in **Table II.1**, we obtained a series of linewidths of 31 ± 4 nm, 48 ± 4 nm, 67 ± 4 nm, 81 ± 7 nm, 101 ± 7 nm, and 120 ± 5 nm, 134 ± 7 nm, 141 ± 5 nm, 156 ± 8 nm, 169 ± 8 nm, 202 ± 5 nm, 223 ± 9 nm, 248 ± 6 nm, and 309 ± 9 nm. Among these, the smallest linewidth was 31 ± 4 nm. For w_{design} from 3550 to 3750 nm, the designed base linewidth increment Δw_{design} was fixed at 25 nm resulting in an average measured base linewidth increment of $\Delta w_{measured}$ = 26 ± 6 nm, and an average calculated height increment of $\Delta h_{calculated}$ = 18 ± 4 nm based on $\Delta w_{measured}$ increment (shown in bold in **Table II.1**). Such small increments resulted in average measured pattern linewidth increments $\Delta L_{measured}$ at the sub-20-nm scale, 15 ± 4 nm. Both the sub-40-nm linewidth and the sub-20-nm linewidth

increments are comparable to the critical dimensions and resolutions of many vacuum-based nanolithography techniques.[44-52]

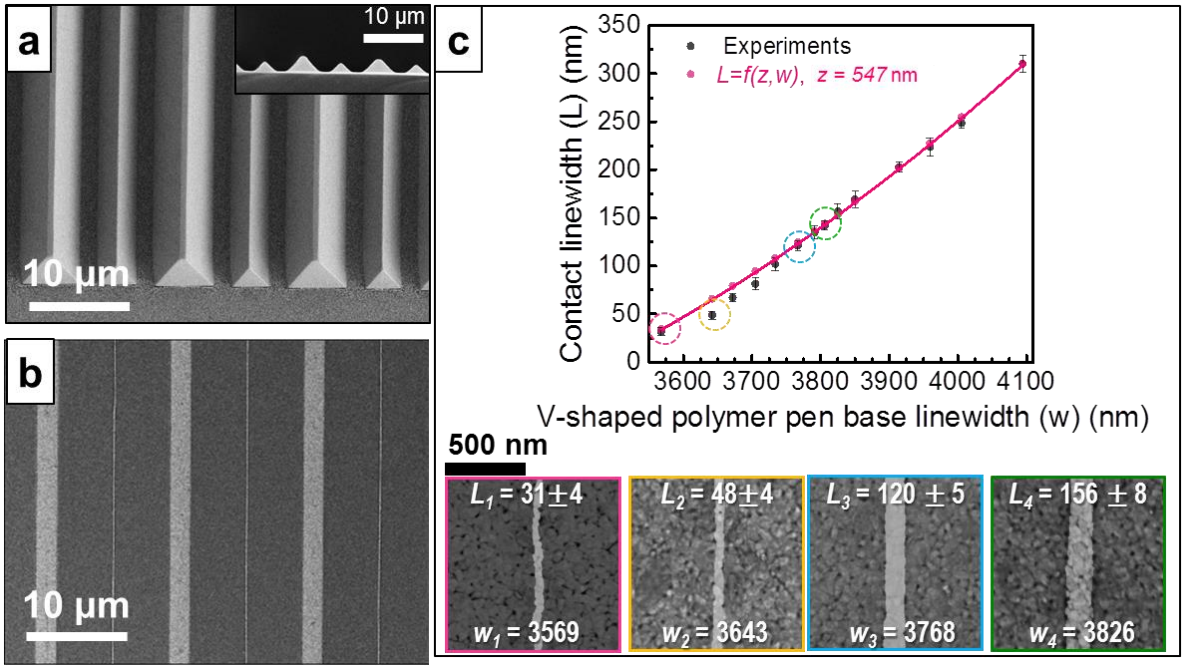

Figure II.4. (a) A scanning electron microscope (SEM) image of a polymer-pen array having designed height gradients and a stamp support system; Inset: cross-sectional view to show height differences. **(b)** A SEM image of a polymer-pen chemical lift-off lithography (PPCLL) pattern produced by the stamp in **(a)**. **(c)** A plot of experimental and simulation results of the relationship between the linewidths of the PPCLL patterns and the v-shaped polymer pen base linewidths. Below are four SEM images of typical PPCLL patterned lines corresponding to the four data points circled in different colors. Note, L_1, L_2, L_3, and L_4 are measured linewidths; w_1, w_2, w_3, and w_4 are the corresponding base linewidths in nm. (The images **(b)** and insets of **(c)** are processed to visualize the patterns better; the unprocessed images are shown in **Figures II.S3** and **II.S4**.)

Table II.1. Measured and simulated patterning results of polymer-pen chemical lift-off lithography using stamp support elements and v-shaped polymer pens over a series of designed base linewidths. All values are in nm.

w_{design}	$w_{measured}$	$L_{measured}$	$L_{simulated}$	Δw_{design}	$\Delta w_{measured}$	$\Delta h_{calculated}$	$\Delta L_{measured}$
3500	3569	31 ± 4	34	-	-	-	-
3550	3643	48 ± 4	65	50	74	52	17
3575	3673	67 ± 4	79	**25**	**30**	**21**	**18**
3600	3706	81 ± 7	94	**25**	**33**	**23**	**14**
3625	3735	101 ± 7	108	**25**	**29**	**21**	**20**
3650	3768	120 ± 5	124	**25**	**33**	**23**	**19**
3675	3792	134 ± 7	136	**25**	**24**	**17**	**14**
3700	3807	141 ± 5	143	**25**	**15**	**11**	**7**
3725	3826	156 ± 8	153	**25**	**19**	**13**	**15**
3750	3851	169 ± 8	166	**25**	**25**	**18**	**13**
3800	3915	202 ± 5	201	50	64	45	33
3850	3960	223 ± 9	227	50	45	32	21
3900	4006	248 ± 6	254	50	46	32	25
4000	4095	309 ± 9	309	100	89	63	61

Footnote: w_{design} is the designed base linewidth of the v-shaped polymer pens; $w_{measured}$ is the measured linewidth of each PPCLL line pattern; $L_{simulated}$ is the simulated contact linewidth based on **Eq. (II.3)** $L = f(w, z)$, for $w = w_{measured}$ and z = 547 nm;Δw_{design}, $\Delta w_{measured}$, and $\Delta L_{measured}$ are the increments corresponding to w_{desgin}, $w_{measured}$, and $L_{measured}$;$\Delta h_{calculated}$ is the height increment of v-shaped polymer pen calculated from$\Delta h_{calculated} = \frac{1}{\sqrt{2}}\Delta w_{measured}$.

Next, we compared the measured results with the universal equation **Eq. (II.2)** from the simulation results. The measured feature linewidths $L_{measured}$ and the measured base linewidths $w_{measured}$ of the corresponding v-shaped polymer pens are plotted in **Figure II.4c**. To calculate the corresponding vertical compression distance z in **Eq. (II.2)**, we first applied the largest measured $w_{measured}$ = 4095 nm and $L_{measured}$ = 309 nm in **Eq. (II.2)** to get z =

547 nm. Then, by fixing z at 547 nm, we obtained **Eq. (II.3)**, where a'' = 1431 nm, b'' = -1.188, and c'' = 2.232 × 10^{-4} nm^{-1}. We plotted **Eq. (II.3)** in **Figure II.4c** and found that the calculated data fit the experimental data well. Based on $w_{measured}$, we calculated $L_{simulated}$. The almost negligible differences (~5 nm average) between the $L_{measured}$ and $L_{simulated}$ could be due to imperfect estimates of the PDMS properties used in the simulations.

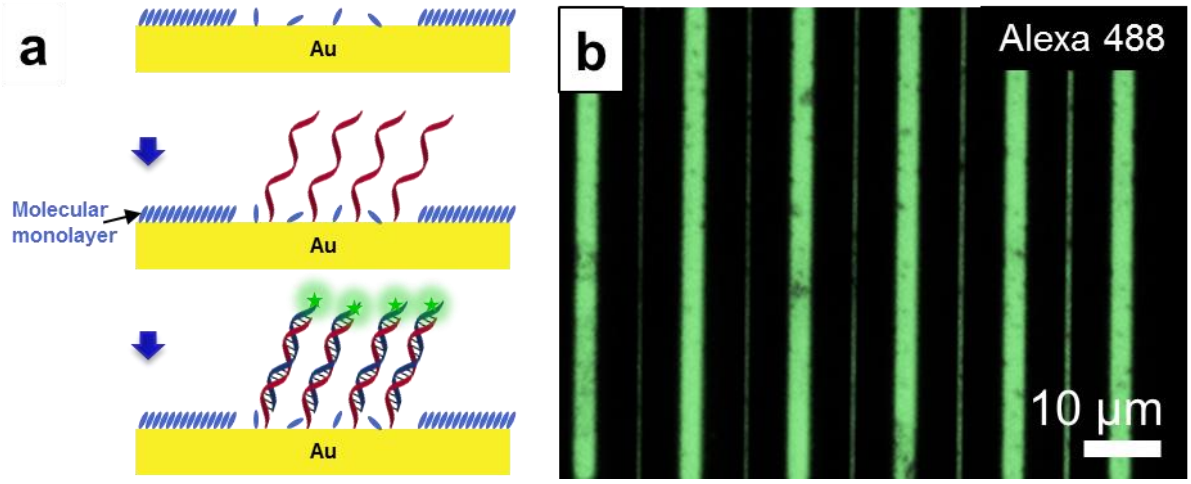

Figure II.5. (a) After polymer-pen chemical lift-off lithography (PPCLL) patterning, thiolated DNA molecules are inserted into the patterned regions and fluorescently labeled complementary target DNA is hybridized on the substrate. **(b)** A typical fluorescence microscopy image after hybridization. (False color (green) is used to enhance pattern image.)

To visualize the fabricated patterns, to test the applicability of PPCLL, and to demonstrate the potential for biological patterning applications, DNA hybridization experiments were performed. We have demonstrated that CLL can be used to produce DNA patterns with high hybridization efficiencies.[7] Using PPCLL to pattern DNA in a similar fashion represents an economical and high-throughput avenue for fabricating functional DNA micro/nano arrays.[7,23,60,82] As shown in the scheme in **Figure II.5a**, SAM molecules were removed from the contacted regions by PPCLL and thiolated single-stranded DNA molecules were inserted into the patterned regions through Au-S bonding.

Single-stranded patterned DNA was hybridized with fluorescently labeled complementary DNA enabling visualization of the chemical lift-off patterns *via* fluorescence microscopy. In **Figure II.5b**, an image of a PPCLL pattern is shown illustrating regions (lines of varying widths) of patterned, hybridized DNA. The patterns are consistent with SEM data, which provides additional confirmation that PPCLL has indeed occurred. The DNA hybridization experiments show that PPCLL can be used to pattern biomolecules that retain functionality, *i.e.*, hybridization in this case. Being able to adjust pattern sizes and to create large-area substrates with binding sites and bioactive species illustrates that PPCLL might be used to fabricate biological devices, such as, biosensors, nucleotide arrays, and selective capture substrates.

II.D. Conclusions and Prospects

In summary, we demonstrated and tested PPCLL through simulation and experiments. Polymer-pen chemical lift-off lithography offers high pattern fidelity, low-cost, large-area, nanometer-scale resolution patterning capabilities by combining the advantages of polymer-pen lithography and chemical lift-off lithography. Through the use of stamp support elements and polymer pens with designed size gradients, we demonstrated sub-40-nm feature patterning and sub-20-nm feature linewidth increments without a piezoelectric scanning stage or a leveling system used in many conventional nanolithography techniques. Nonetheless, we plan to couple PPCLL with a piezoelectric scanning stage system to realize higher resolution patterning. Polymer-pen chemical lift-off lithography is a promising nanofabrication technique for a broad range of applications in electronics, optics, energy, and biology.

II.E. Supplementary Material

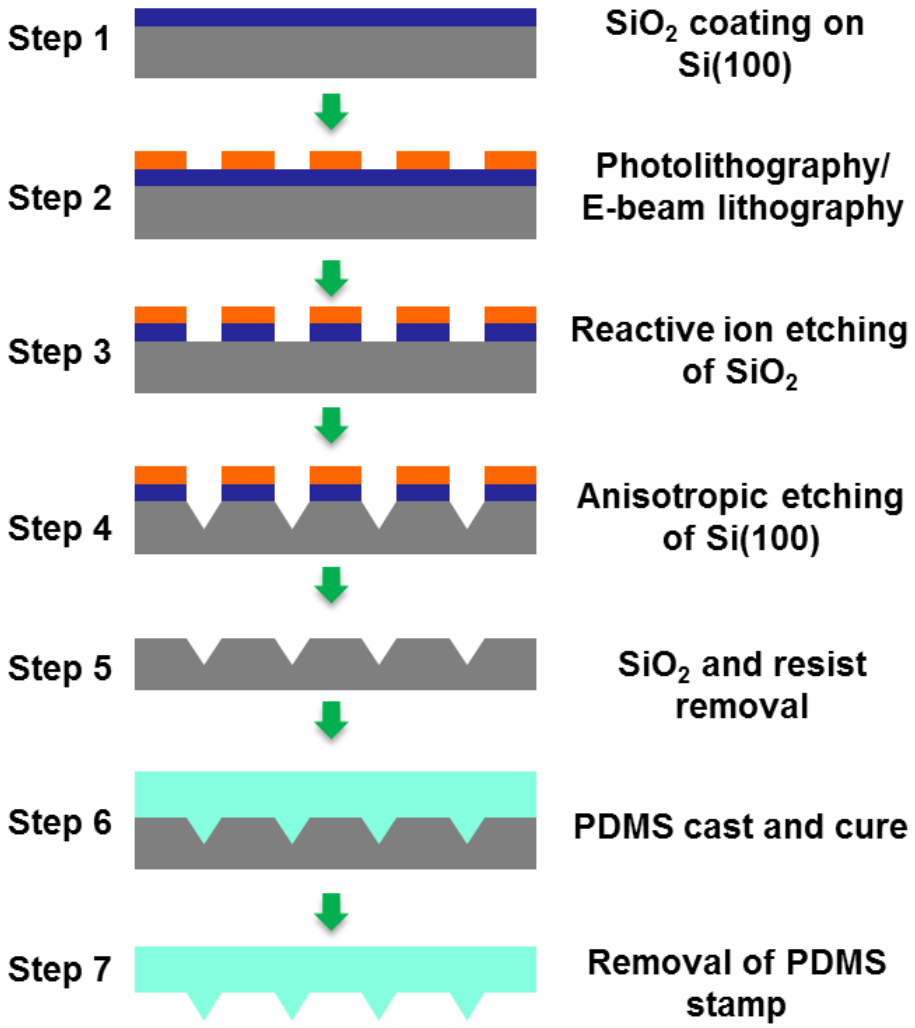

Scheme II.S1. The fabrication scheme of silicon masters and polydimethylsiloxane (PDMS) stamps.

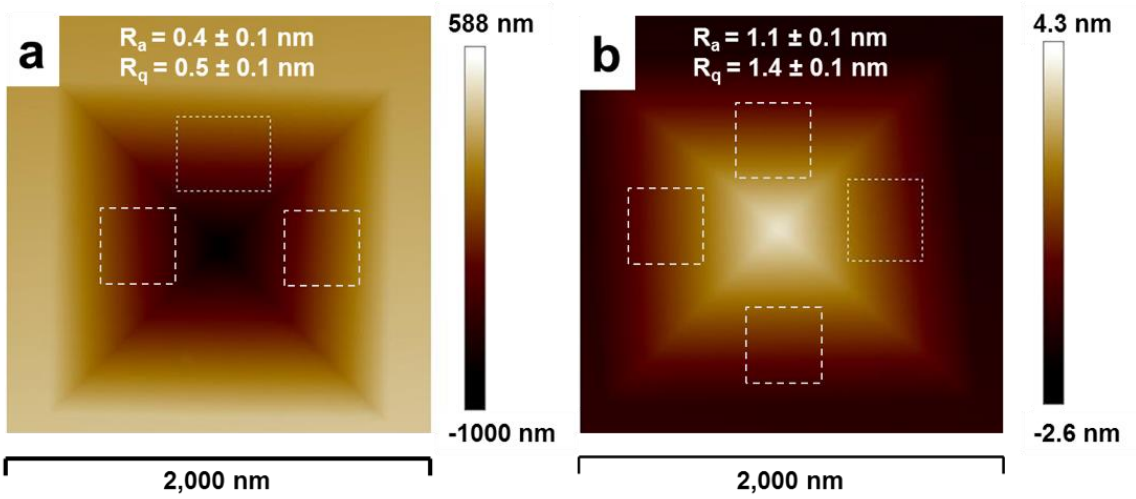

Figure II.S1. Atomic force microscope (AFM) height images of **(a)** inverted pyramid on a silicon master and **(b)** protruding pyramid on a polydimethylsiloxane (PDMS) stamp. The AFM data were collected using a Bruker Dimension Icon Scanning Probe Microscope. Surface roughness was measured inside the square dashed-line areas for each image using the instrument software, Nanoscope Analysis. The R_a is the arithmetic average of absolute values and R_q is the root mean square of the data points.

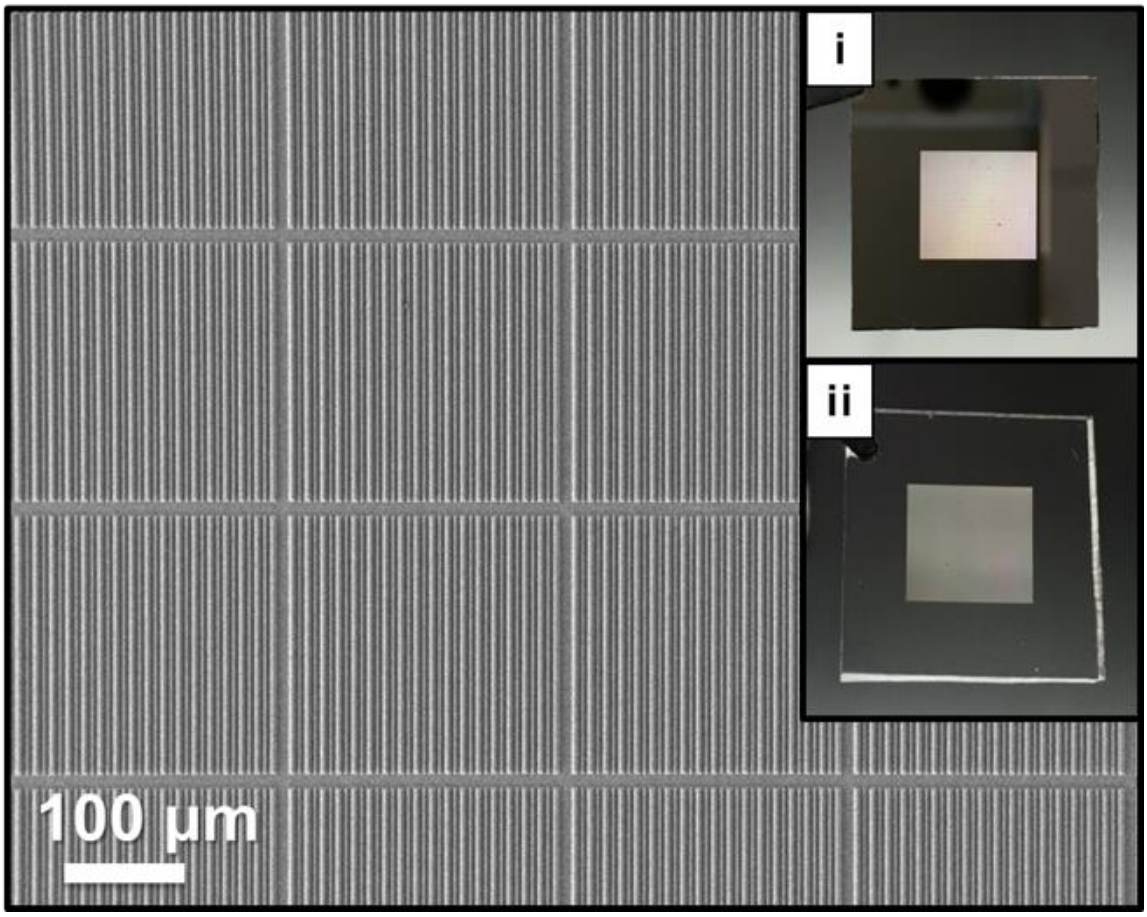

Figure II.S2. A scanning electron microscope image of a polydimethylsiloxane (PDMS) stamp with gradient arrays. Insets: photographs of **(i)** a silicon master and **(ii)** a PDMS stamp.

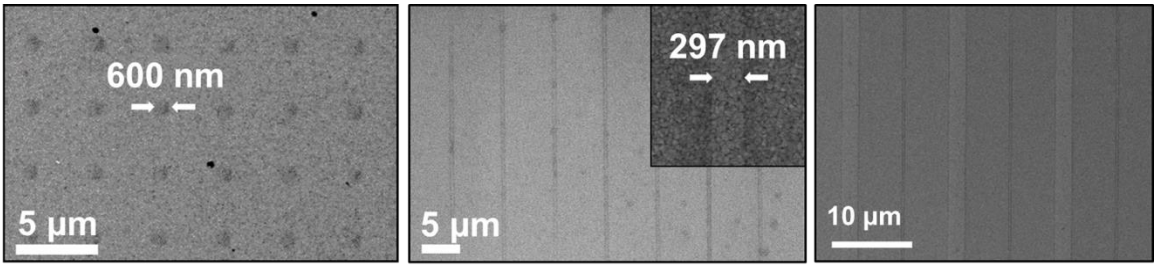

Figure II.S3. Unprocessed images of **Figures II.1c**, **II.1f**, and **II.4b**.

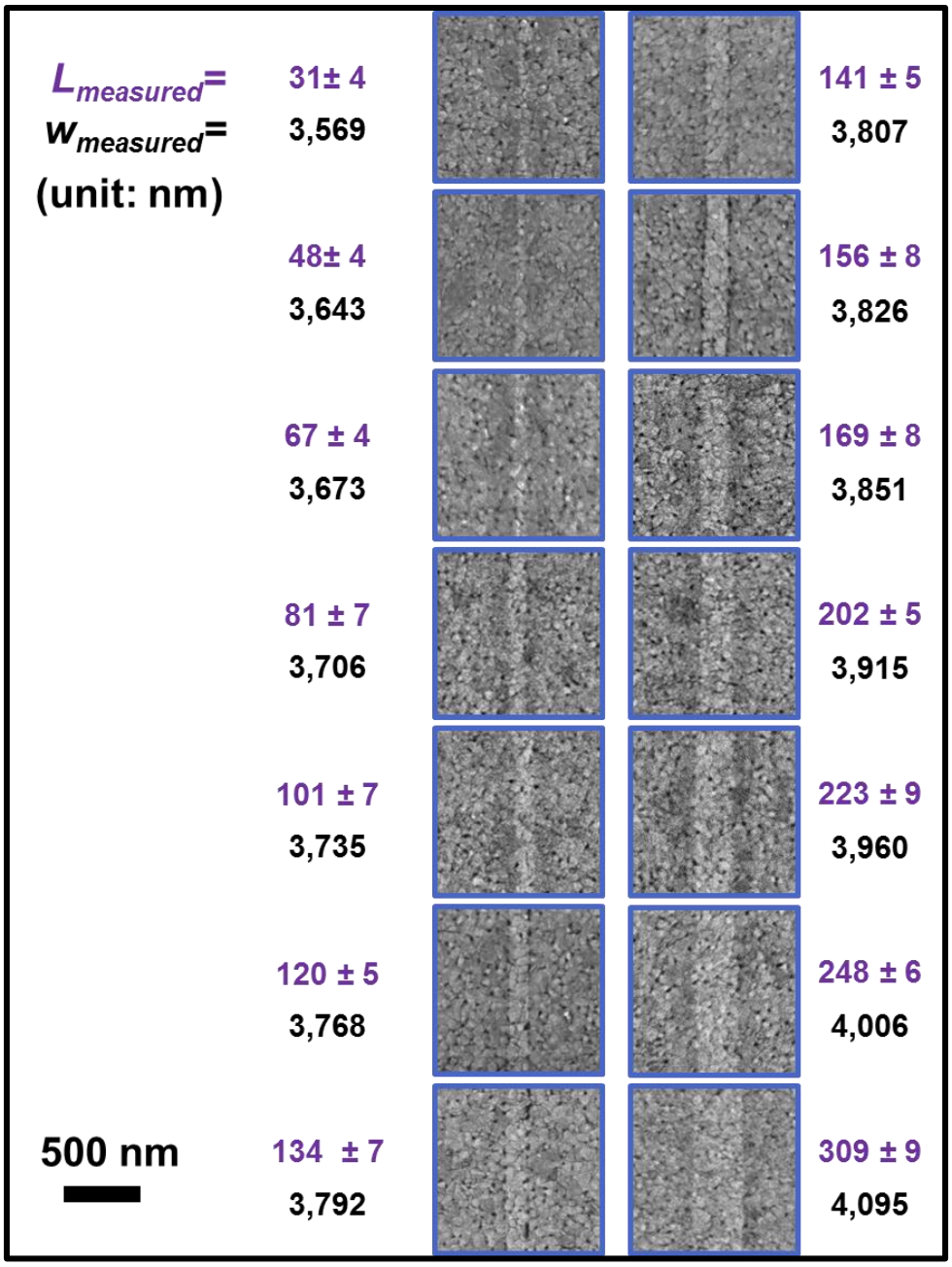

Figure II.S4. A full set of scanning electron microscope images of line patterns with a series of different linewidths ($L_{measured}$) patterned from a series of corresponding v-shaped polymer pens with linewidths ($w_{measured}$) as listed in Table II.1.

II.F. References

(1) Jeon, H.-J.; Kim, K. H.; Baek, Y.-K.; Kim, D. W.; Jung, H.-T. New Top-Down Approach for Fabricating High-Aspect-Ratio Complex Nanostructures with 10 nm Scale Features. *Nano Lett.* **2010**, *10*, 3604–3610.

(2) Pires, D.; Hedrick, J. L.; De Silva, A.; Frommer, J.; Gotsmann, B.; Wolf, H.; Despont, M.; Duerig, U.; Knoll, A. W. Nanoscale Three-Dimensional Patterning of Molecular Resists by Scanning Probes. *Science* **2010**, *328*, 732–735.

(3) Carlson, A.; Bowen, A. M.; Huang, Y.; Nuzzo, R. G.; Rogers, J. A. Transfer Printing Techniques for Materials Assembly and Micro/Nanodevice Fabrication. *Adv. Mater.* **2012**, *24*, 5284–5318.

(4) Smith, J. T.; Franklin, A. D.; Farmer, D. B.; Dimitrakopoulos, C. D. Reducing Contact Resistance in Graphene Devices through Contact Area Patterning. *ACS Nano* **2013**, *7*, 3661–3667.

(5) Priolo, F.; Gregorkiewicz, T.; Galli, M.; Krauss, T. F. Silicon Nanostructures for Photonics and Photovoltaics. *Nat. Nanotechnol.* **2014**, *9*, 19–32.

(6) Tsai, H.; Pitera, J. W.; Miyazoe, H.; Bangsaruntip, S.; Engelmann, S. U.; Liu, C.-C.; Cheng, J. Y.; Bucchignano, J. J.; Klaus, D. P.; Joseph, E. A.; Sanders, D. P.; Colburn, M. E.; Guillorn, M. A. Two-Dimensional Pattern Formation Using Graphoepitaxy of PS-b-PMMA Block Copolymers for Advanced Finfet Device and Circuit Fabrication. *ACS Nano* **2014**, *8*, 5227–5232.

(7) Kim, J.; Rim, Y. S.; Chen, H.; Cao, H. H.; Nakatsuka, N.; Hinton, H. L.; Zhao, C.; Andrews, A. M.; Yang, Y.; Weiss, P. S. Fabrication of High-Performance Ultrathin In_2O_3 Film Field-Effect Transistors and Biosensors Using Chemical Lift-Off Lithography. *ACS Nano* **2015**, *9*, 4572–4582.

(8) Ozbay, E. Plasmonics: Merging Photonics and Electronics at Nanoscale Dimensions. *Science* **2006**, *311*, 189–193.

(9) Henzie, J.; Lee, M. H.; Odom, T. W. Multiscale Patterning of Plasmonic Metamaterials. *Nat. Nanotechnol.* **2007**, *2*, 549–554.

(10) Kung, S.-C.; Van Der Veer, W. E.; Yang, F.; Donavan, K. C.; Penner, R. M. 20 Ms Photocurrent Response from Lithographically Patterned Nanocrystalline Cadmium Selenide Nanowires. *Nano Lett.* **2010**, *10*, 1481–1485.

(11) Fan, F.-R.; Lin, L.; Zhu, G.; Wu, W.; Zhang, R.; Wang, Z. L. Transparent Triboelectric Nanogenerators and Self-Powered Pressure Sensors Based on Micropatterned Plastic Films. *Nano Lett.* **2012**, *12*, 3109–3114.

(12) Ul-Haq, E.; Patole, S.; Moxey, M.; Amstad, E.; Vasilev, C.; Hunter, C. N.; Leggett, G. J.; Spencer, N. D.; Williams, N. H. Photocatalytic Nanolithography of Self-Assembled Monolayers and Proteins. *ACS Nano* **2013**, *7*, 7610–7618.

(13) Moxey, M.; Johnson, A.; El-Zubir, O.; Cartron, M.; Dinachali, S. S.; Hunter, C. N.; Saifullah, M. S. M.; Chong, K. S. L.; Leggett, G. J. Fabrication of Self-Cleaning, Reusable Titania Templates for Nanometer and Micrometer Scale Protein Patterning. *ACS Nano* **2015**, *9*, 6262–6270.

(14) Cao, Q.; Kim, H.-S.; Pimparkar, N.; Kulkarni, J. P.; Wang, C.; Shim, M.; Roy, K.; Alam, M. A.; Rogers, J. A. Medium-Scale Carbon Nanotube Thin-Film Integrated Circuits on Flexible Plastic Substrates. *Nature* **2008**, *454*, 495–500.

(15) Hwang, J. K.; Cho, S.; Dang, J. M.; Kwak, E. B.; Song, K.; Moon, J.; Sung, M. M. Direct Nanoprinting by Liquid-Bridge-Mediated Nanotransfer Moulding. *Nat. Nanotechnol.* **2010**, *5*, 742–748.

(16) Cheong, L. L.; Paul, P.; Holzner, F.; Despont, M.; Coady, D. J.; Hedrick, J. L.; Allen, R.; Knoll, A. W.; Duerig, U. Thermal Probe Maskless Lithography for 27.5 nm Half-Pitch Si Technology. *Nano Lett.* **2013**, *13*, 4485–4491.

(17) Kim, T.-H.; Cho, K.-S.; Lee, E. K.; Lee, S. J.; Chae, J.; Kim, J. W.; Kim, D. H.; Kwon, J.-Y.; Amaratunga, G.; Lee, S. Y.; Choi, B. L.; Kuk, Y.; Kim, J. M.; Kim, K. Full-Colour Quantum Dot Displays Fabricated by Transfer Printing. *Nat. Photon.* **2011**, *5*, 176–182.

(18) Jiang, M.; Kurvits, J. A.; Lu, Y.; Nurmikko, A. V.; Zia, R. Reusable Inorganic Templates for Electrostatic Self-Assembly of Individual Quantum Dots, Nanodiamonds, and Lanthanide-Doped Nanoparticles. *Nano Lett.* **2015**, *15*, 5010–5016.

(19) Xie, W.; Gomes, R.; Aubert, T.; Bisschop, S.; Zhu, Y.; Hens, Z.; Brainis, E.; Van Thourhout, D. Nanoscale and Single-Dot Patterning of Colloidal Quantum Dots. *Nano Lett.* **2015**, *15*, 7481–7487.

(20) Liang, X.; Morton, K. J.; Austin, R. H.; Chou, S. Y. Single Sub-20 nm Wide, Centimeter-Long Nanofluidic Channel Fabricated by Novel Nanoimprint Mold Fabrication and Direct Imprinting. *Nano Lett.* **2007**, *7*, 3774–3780.

(21) Stewart, M. E.; Anderton, C. R.; Thompson, L. B.; Maria, J.; Gray, S. K.; Rogers, J. A.; Nuzzo, R. G. Nanostructured Plasmonic Sensors. *Chem. Rev.* **2008**, *108*, 494–521.

(22) Xu, X. B.; Kim, K.; Li, H. F.; Fan, D. L. Ordered Arrays of Raman Nanosensors for Ultrasensitive and Location Predictable Biochemical Detection. *Adv. Mater.* **2012**, *24*, 5457–5463.

(23) Scheible, M. B.; Pardatscher, G.; Kuzyk, A.; Simmel, F. C. Single Molecule Characterization of DNA Binding and Strand Displacement Reactions on Lithographic DNA Origami Microarrays. *Nano Lett.* **2014**, *14*, 1627–1633.

(24) Rim, Y. S.; Bae, S.-H.; Chen, H.; Yang, J. L.; Kim, J.; Andrews, A. M.; Weiss, P. S.; Yang, Y.; Tseng, H.-R. Printable Ultrathin Metal Oxide Semiconductor-Based Conformal Biosensors. *ACS Nano* **2015**, *9*, 12174–12181.

(25) Xu, X. B.; Kim, K.; Fan, D. L. Tunable Release of Multiplex Biochemicals by Plasmonically Active Rotary Nanomotors. *Angew. Chem. Int. Ed.* **2015**, *54*, 2525–2529.

(26) Kim, K.; Guo, J. H.; Xu, X. B.; Fan, D. L. Micromotors with Step-Motor Characteristics by Controlled Magnetic Interactions among Assembled Components. *ACS Nano* **2015**, *9*, 548–554.

(27) Brown, P. O.; Botstein, D. Exploring the New World of the Genome with DNA Microarrays. *Nat. Genet.* **1999**, *21*, 33–37.

(28) Pollack, J. R.; Perou, C. M.; Alizadeh, A. A.; Eisen, M. B.; Pergamenschikov, A.; Williams, C. F.; Jeffrey, S. S.; Botstein, D.; Brown, P. O. Genome-Wide Analysis of DNA Copy-Number Changes Using Cdna Microarrays. *Nat. Genet.* **1999**, *23*, 41–46.

(29) Lickwar, C. R.; Mueller, F.; Hanlon, S. E.; Mcnally, J. G.; Lieb, J. D. Genome-Wide Protein-DNA Binding Dynamics Suggest a Molecular Clutch for Transcription Factor Function. *Nature* **2012**, *484*, 251–255.

(30) Loven, J.; Orlando, D. A.; Sigova, A. A.; Lin, C. Y.; Rahl, P. B.; Burge, C. B.; Levens, D. L.; Lee, T. I.; Young, R. A. Revisiting Global Gene Expression Analysis. *Cell* **2012**, *151*, 476–482.

(31) Cao, H. H.; Nakatsuka, N.; Serino, A. C.; Liao, W. S.; Cheunkar, S.; Yang, H.; Weiss, P. S.; Andrews, A. M. Controlled DNA Patterning by Chemical Lift-Off Lithography: Matrix Matters. *ACS Nano* **2015**, *9*, 11439–11454.

(32) Ko, H. C.; Stoykovich, M. P.; Song, J.; Malyarchuk, V.; Choi, W. M.; Yu, C.-J.; Geddes Iii, J. B.; Xiao, J.; Wang, S.; Huang, Y.; Rogers, J. A. A Hemispherical Electronic Eye Camera Based on Compressible Silicon Optoelectronics. *Nature* **2008**, *454*, 748–753.

(33) Rogers, J. A.; Someya, T.; Huang, Y. Materials and Mechanics for Stretchable Electronics. *Science* **2010**, *327*, 1603–1607.

(34) Windmiller, J. R.; Wang, J. Wearable Electrochemical Sensors and Biosensors: A Review. *Electroanal.* **2013**, *25*, 29–46.

(35) Pang, C.; Lee, C.; Suh, K.-Y. Recent Advances in Flexible Sensors for Wearable and Implantable Devices. *J. Appl. Polym. Sci.* **2013**, *130*, 1429–1441.

(36) Kim, J.; Rim, Y. S.; Liu, Y.; Serino, A. C.; Thomas, J. C.; Chen, H.; Yang, Y.; Weiss, P. S. Interface Control in Organic Electronics Using Mixed Monolayers of Carboranethiol Isomers. *Nano Lett.* **2014**, *14*, 2946–2951.

(37) Switkes, M.; Rothschild, M. Immersion Lithography at 157 nm. *J. Vac. Sci. Technol. B Microelectron. Nanometer Struct.* **2001**, *19*, 2353.

(38) Mason, M. E.; Ghaida, R. S.; Agarwal, K. B.; Liebmann, L. W.; Nassif, S. R.; Gupta, P. A Novel Methodology for Triple/Multiple-Patterning Layout Decomposition. *Proc. SPIE* **2012**, *8327*, 83270M.

(39) Han, S. H.; Doherty, C. M.; Marmiroli, B.; Jo, H. J.; Buso, D.; Patelli, A.; Schiavuta, P.; Innocenzi, P.; Lee, Y. M.; Thornton, A. W.; Hill, A. J.; Falcaro, P. Simultaneous Microfabrication and Tuning of the Permselective Properties in Microporous Polymers Using X-Ray Lithography. *Small* **2013**, *9*, 2277–2282.

(40) Miszta, K.; Greullet, F.; Marras, S.; Prato, M.; Toma, A.; Arciniegas, M.; Manna, L.; Krahne, R. Nanocrystal Film Patterning by Inhibiting Cation Exchange *via* Electron-Beam or X-Ray Lithography. *Nano Lett.* **2014**, *14*, 2116–2122.

(41) Chang, S. W.; Ayothi, R.; Bratton, D.; Yang, D.; Felix, N.; Cao, H. B.; Deng, H.; Ober, C. K. Sub-50 nm Feature Sizes Using Positive Tone Molecular Glass Resists for EUV Lithography. *J. Mater. Chem.* **2006**, *16*, 1470–1474.

(42) Langner, A.; Paivanranta, B.; Terhalle, B.; Ekinci, Y. Fabrication of Quasiperiodic Nanostructures with EUV Interference Lithography. *Nanotechnology* **2012**, *23*, 105303.

(43) Frommhold, A.; Mcclelland, A.; Yang, D. X.; Palmer, R. E.; Roth, J.; Ekinci, Y.; Rosamund, M. C.; Robinson, A. P. G. Towards 11 nm Half-Pitch Resolution for a Negative-Tone Chemically Amplified Molecular Resist Platform for EUV Lithography. *Proc. SPIE* **2015**, *9425*, 942504.

(44) Cumming, D. R. S.; Thoms, S.; Weaver, J. M. R.; Beaumont, S. P. 3 nm NiCr Wires Made Using Electron Beam Lithography and PMMA Resist. *Microelectron. Eng.* **1996**, *30*, 423–425.

(45) Hu, W. C.; Sarveswaran, K.; Lieberman, M.; Bernstein, G. H. Sub-10 nm Electron Beam Lithography Using Cold Development of Poly(Methylmethacrylate). *J. Vac. Sci. Technol. B* **2004**, *22*, 1711–1716.

(46) Chen, S.; Svedendahl, M.; Antosiewicz, T. J.; Kall, M. Plasmon-Enhanced Enzyme-Linked Immunosorbent Assay on Large Arrays of Individual Particles Made by Electron Beam Lithography. *ACS Nano* **2013**, *7*, 8824–8832.

(47) Kim, S.; Marelli, B.; Brenckle, M. A.; Mitropoulos, A. N.; Gil, E. S.; Tsioris, K.; Tao, H.; Kaplan, D. L.; Omenetto, F. G. All-Water-Based Electron-Beam Lithography Using Silk as a Resist. *Nat. Nanotechnol.* **2014**, *9*, 306–310.

(48) Manfrinato, V. R.; Wen, J. G.; Zhang, L. H.; Yang, Y. J.; Hobbs, R. G.; Baker, B.; Su, D.; Zakharov, D.; Zaluzec, N. J.; Miller, D. J.; Stach, E. A.; Berggren, K. K. Determining the

Resolution Limits of Electron-Beam Lithography: Direct Measurement of the Point-Spread Function. *Nano Lett.* **2014**, *14*, 4406–4412.

(49) Bat, E.; Lee, J.; Lau, U. Y.; Maynard, H. D. Trehalose Glycopolymer Resists Allow Direct Writing of Protein Patterns by Electron-Beam Lithography. *Nat. Commun.* **2015**, *6*, 6654.

(50) Gschrey, M.; Thoma, A.; Schnauber, P.; Seifried, M.; Schmidt, R.; Wohlfeil, B.; Kruger, L.; Schulze, J. H.; Heindel, T.; Burger, S.; Schmidt, F.; Strittmatter, A.; Rodt, S.; Reitzenstein, S. Highly Indistinguishable Photons from Deterministic Quantum-Dot Microlenses Utilizing Three-Dimensional in Situ Electron-Beam Lithography. *Nat. Commun.* **2015**, *6*, 7662.

(51) Volkert, C. A.; Minor, A. M. Focused Ion Beam Microscopy and Micromachining. *MRS Bull.* **2007**, *32*, 389–395.

(52) Kalhor, N.; Boden, S. A.; Mizuta, H. Sub-10 nm Patterning by Focused He-Ion Beam Milling for Fabrication of Downscaled Graphene Nano Devices. *Microelectron. Eng.* **2014**, *114*, 70–77.

(53) Pan, L.; Park, Y.; Xiong, Y.; Ulin-Avila, E.; Wang, Y.; Zeng, L.; Xiong, S.; Rho, J.; Sun, C.; Bogy, D. B.; Zhang, X. Maskless Plasmonic Lithography at 22 nm Resolution. *Sci. Rep.* **2011**, *1*, 175.

(54) Kumar, A.; Whitesides, G. M. Features of Gold Having Micrometer to Centimeter Dimensions Can Be Formed through a Combination of Stamping with an Elastomeric Stamp and an Alkanethiol ''Ink'' Followed by Chemical Etching. *Appl. Phys. Lett.* **1993**, *63*, 2002.

(55) Qin, D.; Xia, Y.; Whitesides, G. M. Soft Lithography for Micro- and Nanoscale Patterning. *Nat. Protoc.* **2010**, *5*, 491–502.

(56) Xia, Y.; Whitesides, G. M. Soft Lithography. *Angew. Chem. Int. Ed.* **1998**, *37*, 550–575.

(57) Xia, Y.; Zhao, X.-M.; Kim, E.; Whitesides, G. M. A Selective Etching Solution for Use with Patterned Self-Assembled Monolayers of Alkanethiolates on Gold. *Chem. Mater.* **1995**, *7*, 2332–2337.

(58) Delamarche, E.; Schmid, H.; Bietsch, A.; Larsen, N. B.; Rothuizen, H.; Michel, B.; Biebuyck, H. Transport Mechanisms of Alkanethiols During Microcontact Printing on Gold. *J. Phys. Chem. B* **1998**, *102*, 3324–3334.

(59) Srinivasan, C.; Mullen, T. J.; Hohman, J. N.; Anderson, M. E.; Dameron, A. A.; Andrews, A. M.; Dickey, E. C.; Horn, M. W.; Weiss, P. S. Scanning Electron Microscopy of Nanoscale Chemical Patterns. *ACS Nano* **2007**, *1*, 191–201.

(60) Liao, W.-S.; Cheunkar, S.; Cao, H. H.; Bednar, H. R.; Weiss, P. S.; Andrews, A. M. Subtractive Patterning *via* Chemical Lift-Off Lithography. *Science* **2012**, *337*, 1517–1521.

(61) Xu, S.; Liu, G.-Y. Nanometer-Scale Fabrication by Simultaneous Nanoshaving and Molecular Self-Assembly. *Langmuir* **1997**, *13*, 127–129.

(62) Xu, S.; Miller, S.; Laibinis, P. E.; Liu, G.-Y. Fabrication of Nanometer Scale Patterns within Self-Assembled Monolayers by Nanografting. *Langmuir* **1999**, *15*, 7244–7251.

(63) Li, X.-M.; Péter, M.; Huskens, J.; Reinhoudt, D. N. Catalytic Microcontact Printing without Ink. *Nano Lett.* **2003**, *3*, 1449–1453.

(64) Mclellan, J. M.; Geissler, M.; Xia, Y. Edge Spreading Lithography and Its Application to the Fabrication of Mesoscopic Gold and Silver Rings. *J. Am. Chem. Soc.* **2004**, *126*, 10830–10831.

(65) Sullivan, T. P.; Van Poll, M. L.; Dankers, P. Y. W.; Huck, W. T. S. Forced Peptide Synthesis in Nanoscale Confinement under Elastomeric Stamps. *Angew. Chem. Int. Ed.* **2004**, *43*, 4190–4193.

(66) Wendeln, C.; Ravoo, B. J. Surface Patterning by Microcontact Chemistry. *Langmuir* **2012**, *28*, 5527–5538.

(67) Dameron, A. A.; Hampton, J. R.; Smith, R. K.; Mullen, T. J.; Gillmor, S. D.; Weiss, P. S. Microdisplacement Printing. *Nano Lett.* **2005**, *5*, 1834–1837.

(68) Saavedra, H. M.; Mullen, T. J.; Zhang, P. P.; Dewey, D. C.; Claridge, S. A.; Weiss, P. S. Hybrid Strategies in Nanolithography. *Rep. Prog. Phys.* **2010**, *73*, 036501.

(69) Shuster, M. J.; Vaish, A.; Cao, H. H.; Guttentag, A. I.; Mcmanigle, J. E.; Gibb, A. L.; Martinez, M. M.; Nezarati, R. M.; Hinds, J. M.; Liao, W. S.; Weiss, P. S.; Andrews, A. M. Patterning Small-Molecule Biocapture Surfaces: Microcontact Insertion Printing Vs. Photolithography. *Chem. Commun.* **2011**, *47*, 10641–10643.

(70) Claridge, S. A.; Liao, W. S.; Thomas, J. C.; Zhao, Y.; Cao, H. H.; Cheunkar, S.; Serino, A. C.; Andrews, A. M.; Weiss, P. S. From the Bottom Up: Dimensional Control and Characterization in Molecular Monolayers. *Chem. Soc. Rev.* **2013**, *42*, 2725–2745.

(71) Andrews, A. M.; Liao, W.-S.; Weiss, P. S. Double-Sided Opportunities Using Chemical Lift-Off Lithography. *Acc. Chem. Res.* **2016**, *49*, 1449–1457.

(72) Piner, R. D.; Zhu, J.; Xu, F.; Hong, S.; Mirkin, C. A. "Dip-Pen" Nanolithography. *Science* **1999**, *283*, 661–663.

(73) Huo, F.; Zheng, Z.; Zheng, G.; Giam, L. R.; Zhang, H.; Mirkin, C. A. Polymer Pen Lithography. *Science* **2008**, *321*, 1658–1660.

(74) Zheng, Z.; Daniel, W. L.; Giam, L. R.; Huo, F.; Senesi, A. J.; Zheng, G.; Mirkin, C. A. Multiplexed Protein Arrays Enabled by Polymer Pen Lithography: Addressing the Inking Challenge. *Angew. Chem. Int. Ed.* **2009**, *48*, 7626–7629.

(75) Liao, X.; Braunschweig, A. B.; Mirkin, C. A. "Force-Feedback" Leveling of Massively Parallel Arrays in Polymer Pen Lithography. *Nano Lett.* **2010**, *10*, 1335–1340.

(76) Liao, X.; Braunschweig, A. B.; Zheng, Z.; Mirkin, C. A. Force- and Time-Dependent Feature Size and Shape Control in Molecular Printing *via* Polymer-Pen Lithography. *Small* **2010**, *6*, 1082–1086.

(77) Eichelsdoerfer, D. J.; Liao, X.; Cabezas, M. D.; Morris, W.; Radha, B.; Brown, K. A.; Giam, L. R.; Braunschweig, A. B.; Mirkin, C. A. Large-Area Molecular Patterning with Polymer Pen Lithography. *Nat. Protoc.* **2013**, *8*, 2548–2560.

(78) Demers, L. M.; Ginger, D. S.; Park, S. J.; Li, Z.; Chung, S. W.; Mirkin, C. A. Direct Patterning of Modified Oligonucleotides on Metals and Insulators by Dip-Pen Nanolithography. *Science* **2002**, *296*, 1836–1838.

(79) Odom, T. W.; Love, J. C.; Wolfe, D. B.; Paul, K. E.; Whitesides, G. M. Improved Pattern Transfer in Soft Lithography Using Composite Stamps. *Langmuir* **2002**, *18*, 5314–5320.

(80) Vaish, A.; Shuster, M. J.; Cheunkar, S.; Weiss, P. S.; Andrews, A. M. Tuning Stamp Surface Energy for Soft Lithography of Polar Molecules to Fabricate Bioactive Small-Molecule Microarrays. *Small* **2011**, *7*, 1471–1479.

(81) Xie, Z.; Shen, Y.; Zhou, X.; Yang, Y.; Tang, Q.; Miao, Q.; Su, J.; Wu, H.; Zheng, Z. Polymer Pen Lithography Using Dual-Elastomer Tip Arrays. *Small* **2012**, *8*, 2664–2669.

(82) Noh, H.; Hung, A. M.; Choi, C.; Lee, J. H.; Kim, J.-Y.; Jin, S.; Cha, J. N. 50 nm DNA Nanoarrays Generated from Uniform Oligonucleotide Films. *ACS Nano* **2009**, *3*, 2376–2382.

CHAPTER III

Patterning of Supported Gold Monolayers

via Chemical Lift-Off Lithography

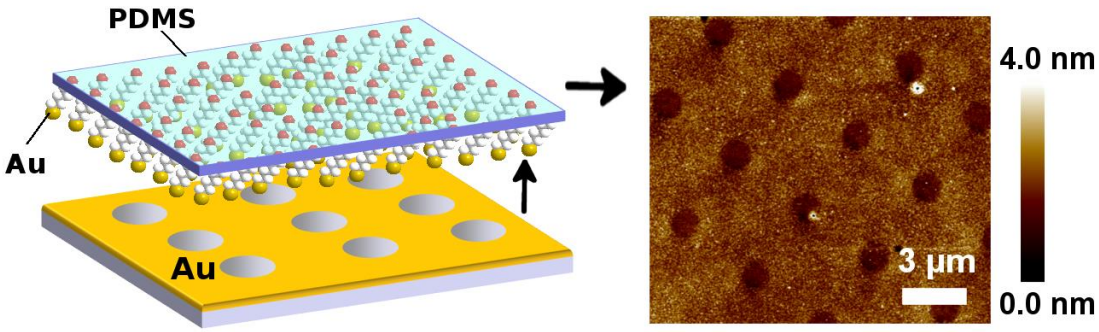

The information in this chapter was published in
Beilstein Journal of Nanotechnology **2017**, *8*, 2648–2661
and has been reproduced here with permission.

Authors: Slaughter L. S.; **Cheung, K. M.**; Kappa, S.; Cao. H. H.; Yang, Q.; Young T. D.; Serino, A. C.; Malola, S.; Olson, J. M.; Link, S.; Häkkinen H.; Andrews, A. M.; Weiss, P. S.

III.A. Introduction

Chemical lift-off lithography (CLL) is a subtractive technique for patterning self-assembled alkanethiol molecules on Au surfaces *via* rupture of Au-Au bonds at the Au-monolayer interface.[1,2] In CLL, hydroxyl-terminated molecules (or other species with reactive termini) in preformed self-assembled monolayers (SAMs) are lifted off Au surfaces through contact with O_2-plasma activated polydimethylsiloxane (PDMS) stamps. Compared with microcontact or transfer printing methods,[3-6] CLL produces crisp, stable patterns with sub-20-nm resolution and areas patterned over square millimeters.[1,7] We have used CLL on gold to control the placement and nanoscale environments around surface-immobilized biomolecules and to simplify patterning steps in device fabrication.[1,2,7-13]

Two-dimensional (2D) materials have proven to be extremely rich in terms of new and potentially useful properties.[14-18] Here, we investigated Au-alkanethiolate layers on PDMS produced during CLL for their 2D material properties. The existence of Au on PDMS following lift-off was initially discovered using X-ray photoelectron spectroscopy (XPS) to investigate post-CLL PDMS stamps.[1] These Au layers had been predicted in a Gedanken experiment by George Whitesides, where he described the strength of the Au-S bond as stronger than the (weakened) bond between the top layer of alkanethiolate-bound Au atoms and the underlying Au substrate. The layers removed during CLL have not yet been well characterized.

In CLL, height differences between the remaining SAMs and the contact regions, where molecules were removed, were the thicknesses of the SAMs plus ~4 Å.[1] This height difference is consistent with one or at most two layers of Au being removed by CLL. Though

not fully elucidated, we refer to the lifted-off species as a (supported) Au-alkanethiolate monolayer (*vide infra*).

Chemical lift-off lithography contrasts with other subtractive or deterministic transfer printing techniques[6,19-23] in that stamp 'inks' during transfer have a different composition than the inks originally deposited onto substrates. While other types of Au thin-films and Au nanoparticles are identified through their measurable geometry- or size-dependent optical and electronic properties (*e.g.*, localized surface plasmons),[24-26] we show that CLL lifted-off monolayers lack significant optical signals distinguishable from the PDMS supporting matrix. By contrast, we determine that the *chemistry* of the supported Au-monolayers remains consistent with that of bulk Au.

We used experimental and computational strategies to characterize the hybrid Au-alkanethiolate 2D material formed at PDMS surfaces *via* lift-off lithography. Chemical lift-off lithography to pattern featureless (flat) PDMS with Au-alkanethiolate monolayers enabled the direct characterization of the nanometer-scale heights of the supported Au monolayers through scanning probe microscopy, as well as the exploration of spatially encoded functionality using fluorescence microscopy. Otherwise, when topographically patterned PDMS stamps are used to pattern Au monolayers, the traits of the latter are overwhelmed by PDMS features that are hundreds of nanometers thick, or are indiscernible on flat PDMS without patterned reference regions, *i.e.*, regions that contain only PDMS adjacent to areas containing monolayers of Au-alkanethiolate complexes.

To gain insight into lift-off lithography removal mechanisms and outcomes of the lift-off process at the atomic scale, we simulated lift-off using molecular dynamics and density functional theory. We determined the energetics of this complex system during lift-off.

Simulations were used to predict the stoichiometry and structure of the lifted-off Au-alkanethiolate monolayers. The calculated stoichiometry provides limits for the structures of the Au-alkanethiolate monolayers, guiding our interpretation of the existence of Au monolayers.

III.B. Experimental Methods

III.B.1. Fabricating Patterned Polydimethylsiloxane Stamps

Stamps with topographic features were prepared as previously described.[27] The Sylgard® 184 silicone elastomer kits were purchased from Dow Corning (Midland, MI, USA). The elastomer base and curing agent were mixed in a 10:1 ratio by weight, stirred for 3-5 min, and degassed in a vacuum dessicator for at least 1 h to remove air bubbles. Degassed mixtures were poured over silicon molds (purchased from KTek Nanotechnology, LLC, Wilsonville, OR, USA or fabricated by photolithography) situated in Petri dishes. After degassing again, PDMS stamps were cured in an oven at 60 ºC for 12 h. The PDMS stamps were separated from silicon masters carefully and cut into desired sizes.

III.B.2. Patterning Au-on-Silicon Masters

Silicon wafers with 100 nm of Au and 5-nm titanium adhesion layers (Platypus, Madison, WI, USA) were trimmed with a diamond scribe to ~1 cm × 1 cm sample sizes. Substrates were annealed with a hydrogen flame and incubated in 1.0 mM ethanolic solutions of mercaptoundecanol overnight at room temperature and ambient pressure to form SAMs. Patterned PDMS stamps were treated with oxygen plasma (Harrick, Ithaca, NY, USA) for 40 s and contacted with SAMs. The stamps were removed from Au substrates after 2 h. Substrates

were then treated with 20 mM iron (III) nitrate and 30 mM thiourea for 10-15 min to etch selectively the Au from the exposed regions.

III.B.3. Fabricating Flat Polydimethylsiloxane Stamps

Stamps were templated using featureless silicon wafers. Silicon wafer pieces (Silicon Quest International, San Jose, CA, USA) were degreased by sonicating sequentially for 5 min in ethanol, 3 min in deionized water, and 5 min in ethanol. Silicon wafer pieces were immediately rinsed with ethanol and blown dry with compressed nitrogen gas. They were then exposed to hexamethyldisilazane vapor for 10 min in a closed chamber to facilitate later removal of PDMS. Glass slides (VWR, Radnor, PA, USA) were trimmed to ~2.5 cm × 2.5 cm squares and sonicated for 20 min in 1% (w/v) Alconox, rinsed with deionized water, and cleaned two additional times. Clean glass pieces were stored in deionized water until they were rinsed and blown dry immediately before use.

Using a plastic spatula with a tapered tip, 1-2 drops of degassed PDMS (10:2 elastomer:curing agent by weight) were placed on the silicon pieces and degassed for an additional 5-10 min. Flat PDMS films were physically attached to glass slide pieces to minimize damage to their surfaces during handling. Dry glass slide pieces were treated with an oxygen plasma for 40 s. Upon removing the silicon pieces with PDMS from the dessicator, a small drop of PDMS was placed on each glass slide, which was then placed gently on top of the PDMS. The 'sandwiches' were cured on a hot plate at 110 °C under a 10 lb. steel-brick weight. After 10 min, the heat was turned off while the 'sandwiches' remained under the weight overnight.

III.B.4. Patterning Flat Polydimethylsiloxane Stamps

Patterned Au-on-Si masters were annealed with a hydrogen flame and then immersed in 1.0 mM mercaptoundecanol overnight to form new SAMs on the patterned Au regions. Prior to performing CLL, masters were sonicated three times for 1 s in fresh ethanol, rinsed, and blown dry. The PDMS on glass pieces were removed from the silicon templates immediately before use, rinsed with ethanol, blown dry with compressed nitrogen, and O_2-plasma treated for 40 s to activate surfaces. The Au-on-Si masters were placed face down on PDMS samples. After initial contact and gently pressing by hand, no additional vertical pressure was applied. Contacted regions were lightly marked on the glass underside with a permanent marker. After contact for 2-24 h, depending on the experiment, Au-on-Si masters were carefully removed from the PDMS. The marked regions were scratched lightly into the PDMS before each sample was rinsed on both sides with ethanol and blown dry.

III.B.5. Peak-Force Atomic Force Microscopy

A Bruker Dimension Icon Scanning Probe Microscope (Bruker Nano, Santa Barbara, CA, USA) was used to map topographies and mechanical properties of flat PDMS stamps patterned with Au-alkanethiolate monolayers. The AFM images of PDMS stamps (flat and patterned) were measured using PeakForce Quantitative Nanomechanical Property Mapping mode. ScanAsyst-Air cantilevers (Bruker, spring constant = 0.4 ± 0.1 N/m) were calibrated with a clean piece of silicon before each measurement. A peak-force set-point between 200 and 400 pN was maintained, except where otherwise indicated. These conditions enabled sufficient contact between tips and samples for imaging, while minimizing the load from the cantilever applied to the PDMS.

III.B.6. Scanning Electron Microscopy of Au-on-Si Masters

Scanning electron microscopy was performed using a JEOL JSM-6700F scanning electron microscope (JEOL, Inc., Tokyo, Japan) with a 750 V DC detector bias and 5 kV accelerating voltage.

III.B.7. Field-Emission Gun Variable Pressure Electron Microscopy of Au on PDMS

Scanning electron micrographs of Au-alkanethiolate monolayers on flat PDMS were imaged with a low vacuum detector in a Nova NanoSEM 230 microscope (FEI, Czech Republic) operating at an accelerating voltage of 5 kV. Samples were affixed to the SEM stub and grounded by conductive carbon and copper tape. Variable pressure SEM (VP-SEM) was performed under 50 Pa of water vapor in the sample chamber to avoid charging insulating PDMS surfaces by the electron beam.

III.B.8. Functional DNA Patterns on Supported Au Monolayers

As-received DNA (Integrated DNA Technologies, Coralville, IA, USA) was diluted in nuclease-free water (QIAGEN, Valencia, CA, USA) to make 100 μM stock solutions. Immediately prior to experiments, DNA stock solutions were diluted 1:100 with 0.01 M phosphate buffered saline (PBS) ([NaCl] = 138 mM, [KCl] = 2.7 mM, and [$MgCl_2$] = 5 mM) pH 7.4 (Sigma-Aldrich, St. Louis, MO, USA) to make 1 μM solutions. Patterns of Au-alkanethiolate monolayers on flat PDMS substrates were functionalized with thiolated single-stranded DNA solutions by pipetting 50-100 μL of 1 μM DNA solutions onto the substrates to cover the patterned regions and incubating for ~20 h at room temperature. The substrates were then rinsed thoroughly with deionized water and blown dry with nitrogen gas. For DNA hybridization on Au-alkanethiolate monolayers on flat PDMS, 50-100 μL of 1 μM AlexaFluor® 488-labeled complementary DNA was pipetted onto the substrates, which were then incubated for 1 h at

room temperature. During incubation, substrates were kept in the dark to minimize photobleaching of fluorescent dyes by ambient light. Substrates were rinsed again with deionized water and blown dry with nitrogen gas.

The DNA duplexes on Au-alkanethiolate monolayers were imaged at an emission wavelength of 517 nm (AlexaFluor® 488; excitation at 492 nm) with an inverted fluorescence microscope (Model: Axio Observer.D1) equipped with an AxioCam MRm charged-coupled device camera (Carl Zeiss MicroImaging, Inc., Thornwood, NY, USA) and a fluorescence filter with excitation and emission wavelengths at 470 ± 20 nm and 525 ± 25 nm, respectively (38 HE/high efficiency, Carl Zeiss MicroImaging, Inc.).

In **Figure III.2A,B**, patterns were formed on an unsupported slab of PDMS. These patterns were functionalized with thiolated single-stranded DNA (5'-TCT CAA GAA TCG GCA TTA GCT CAA CTG TCA ACT CCT CTT T/3ThioMC3-D/-3') using the procedure described above. Thiolated DNA strands were hybridized with dye-labeled complementary strands (5'-AAA GAG GAG TTG ACA GTT GAG CTA ATG CCG ATT CTT GAG A/3AlexF488N/-3'). Samples were then imaged with the patterned side facing down in a drop of deionized water on a clean cover slip. Magnification and exposure times were adjusted appropriately for each patterned region. The same preparation and imaging strategy was employed for samples in **Figure III.S5**.

For patterns in **Figure III.2C,D**, samples were prepared on thin PDMS substrates supported on glass, similar to the sample shown in the photograph in **Figure III.S4**. Thiolated DNA and dye-labeled complementary sequences were 5'-/5-thioMC6-D/ GCA CGA AAC CCA AAC CTG ACC TAA CCA ACG TGC T-3' and 5'-/5-Alex488N/ AGC ACG TTG GTT AGG TCA GGT TTG GGT TTC GTG C-3'. For control experiments, substrates functionalized with

thiolated DNA were incubated with 1 μM AlexaFluor® 488 labeled fully scrambled DNA sequences (5'-/5-Alex488N/ CAT GAA CCA ACC CAA GTC AAC GCA AAC GCA TCA A-3') to test the specificity of DNA hybridization on patterns of Au-alkanethiolate monolayers. In other experiments, substrates were incubated with 0.01 M PBS pH 7.4 without thiolated DNA followed by incubation of 1 μM AlexaFluor® 488 labeled complementary DNA. Each substrate was positioned on the microscope sample holder such that the PDMS side was facing away from the light source and the backside (glass side) of the substrate was facing toward the light source. Images were collected under dry or aqueous conditions. Deionized water drops were pipetted onto the PDMS side of glass substrates to cover the ultrathin Au patterns for imaging under aqueous conditions.

III.B.9. X-Ray Photoelectron Spectroscopy

The XPS spectra were acquired on an AXIS Ultra DLD instrument (Kratos Analytical Inc., Chestnut Ridge, NY, USA) under ultrahigh vacuum (10^{-9} torr) using a monochromatic Al K_α X-ray source (20 mA, 14 kV) with a 200 μm diameter circular spot size. Pass energies were 80 mV for survey spectra and 20 mV for high-resolution spectra of C 1s, S 2p, O 1s, and Au 4f regions. All data points were acquired with 200-ms dwell times. For adequate signal-to-noise, the numbers of scans were adjusted for different regions of the spectrum to account for different relative sensitivity factors and low amounts of Au, ranging from 20 scans for C 1s to 100 scans for Au 4f. Because PDMS is an insulator, a charge neutralizer (flood gun) was used to offset charging of samples that otherwise impedes spectral acquisition. Doing so, however, causes peaks to shift to lower energies compared to their expected energies obtained without using a flood gun.

III.B.10. Chan-Vese Segmentation

In our implementation, AFM topography maps were segmented into foreground regions, which contained lifted-off complexes, and background regions, which contained only PDMS. The algorithm also output a matrix indicating the location of artifacts, which were then excluded from subsequent analysis of both the foreground and background regions (**Figure III.8B**). During post-segmentation analysis, histograms of the two regions were plotted and then fit to Gaussian distributions. Because the data were normally distributed, the apparent heights of the lifted-off layers were calculated through the differences of the means of the foreground and background pixel intensities.

Calculating apparent heights line-by-line along the fast-scan direction, a conventional way of calculating average intensity differences in each line, gave similar values for the apparent heights as those calculated using all image pixels (**Figure III.S9**). The imaging force set-point chosen for use in these studies provided sufficient force for imaging, while minimizing the deformation of Au-alkanethiolate monolayers. Apparent heights were shown to be equally and minimally influenced by the imaging force (**Figure III.S10**).

III.B.11. Molecular Dynamics Simulations

Molecular dynamics simulations were carried out using density functional theory with the Perdew-Burke-Ernzerhof functional[28] using a grid-based projector augmented wave code.[29,30] In total, twelve pulling simulations were performed using a grid basis (with a 0.2 Å grid spacing) and a linear combination of atomic orbitals basis with double-zeta polarized functions. The thermal movement of atoms was simulated using the Langevin thermostat targeting room temperature, implemented in the Atomic Simulation Environment.[31] The thermostat adds both a small, random contribution to the force on the atoms and a small

friction factor that slows them down, aiming for an average total kinetic energy of the atoms that corresponds to the target temperature. The time step for molecular dynamics was 2 fs. To maintain the stabilities of hydrogen atoms on this time scale, their masses were increased to the mass of deuterium.

The unit cell was orthogonal with a size of 8.87 Å in the x-direction and 10.24 Å in the y-direction, in which the unit cell was also set to be periodic. In the z direction, a 10 Å vacuum was set both above and below the structure. In the unit cell, the Au slab consisted of (3, 4, 3) atoms in the (x, y, z) directions, respectively, fulfilling a {111} surface structure with the surface vector pointing in the z-direction. The lattice constant was 4.18 Å corresponding to the theoretical lattice constant of Au in the Perdew-Burke-Ernzerhof approximation. Gamma-points were used in each direction. In addition, four 1-butanethiolates were set on the Au surface forming a $(3 \times 2\sqrt{3})$-rectangular-symmetric structure. Individual thiolates were set to the fcc positions of the Au{111} surface. In the case of the RS-Au-SR units, the Au adatoms were set to bridge positions and the sulfur atoms to positions above the surface and next to adatoms. Butyl was chosen for the alkyl tail as long enough to form the $(3\ \text{Å} \sim 2\sqrt{3})$ rectangular symmetry naturally but short enough to maintain computational costs as low as possible.[32]

Before removal, the system was heated up to room temperature using the Langevin thermostat with a friction parameter of 0.002 s^{-1}; the heating procedure was run for 2 ps in simulated time. The lowest layer of Au was fixed in its initial position to enable the removal of the thiolates. The pulling moved the terminal carbon atoms with constant velocity outward from the Au surface. Typically, a velocity of 0.5 Å/ps was used. The calculation was

continued until thiolate/Au complexes had been completely separated from the surface. The Langevin thermostat was used throughout the calculation to maintain the total energy of the system damping to the energy added due to pulling.

Core level shifts were calculated for the Au atoms in the modeled structures that were removed from surfaces in the simulations. The density functional theory with the PBE functional was used again *via* GPAW to calculate the energies of the structures. The procedure followed the one used by Grönbeck.[33] After relaxing the removed structure to a local energy minimum with residual forces below 0.05 eV/Å on any atom, an electron was removed from the 4f core of a Au atom and the change in the total energy of the system was calculated. To make the results comparable, the energy shift of a bulk Au atom was then subtracted from this energy change.

III.C. Results and Discussion

Master substrates of Au-on-Si were patterned by a first round of CLL. Here, topographically patterned PDMS stamps were used to lift-off hydroxyl-terminated self-assembled alkanethiols (**Figure III.S1**).[1,9] Following this CLL step, Au in the lifted-off (exposed) regions was removed by wet-etching to form Au-features in the noncontact regions. Next, hydroxyl-terminated alkanethiols were self-assembled on the patterned Au masters (**Figure III.1**, left). Topographically flat, activated PDMS was brought into contact with the patterned Au masters to carry out a second round of CLL that resulted in otherwise featureless PDMS patterned only with monolayers of Au-alkanethiolates.

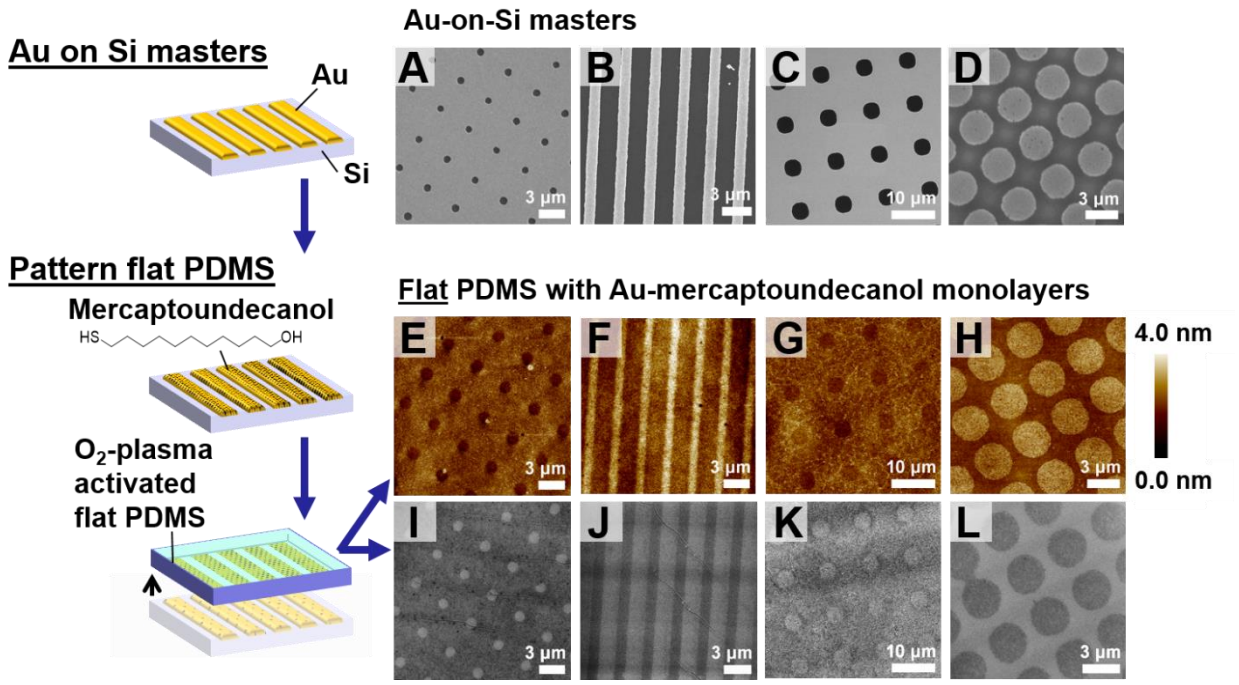

Figure III.1: (Left) Scheme for patterning flat polydimethylsiloxane (PDMS) with Au-mercaptoundecanol monolayers. The Au features (100-nm height) on Au-on-Si masters were functionalized with mercaptoundecanol and contacted with topographically flat PDMS stamps. **(A-D)** Scanning electron micrographs of Au-on-Si masters with **(A)** 1-μm diameter holes, **(B)** 1-μm lines, **(C)** 5-μm diameter holes, and **(D)** 3-μm diameter raised circles. The Au regions appear bright in these images. **(E-H)** Height maps of Au-mercaptoundecanol monolayers on PDMS produced from the Au masters in **(A-D)**, respectively. Images were acquired by peak-force atomic force microscopy. **(I-L)** Variable-pressure scanning electron micrographs of the same Au-alkanethiolate patterns on PDMS visualized in **(E-H)**. Images in **(I-L)** are contrast enhanced to visualize features more clearly. The original images are shown in **Figure III.S2**.

We visualized patterns of Au-alkanethiolate monolayers on PDMS using nanoscale characterization tools. Topographies were measured using peak-force atomic force microscopy (PF-AFM), an intermittent contact mode suitable for interrogating soft samples.[34] The AFM topography map in **Figure III.1E** shows a pattern of recessed circular holes that are each approximately 1 μm in diameter with 4-μm center-to-center separations. These features directly reproduced the lateral dimensions and periodicities of the Au features on the corresponding Au-on-Si master imaged by SEM in **Figure III.1A**. The remaining images in **Figure III.1F-H** demonstrate the same characteristics; protruding

regions in each AFM height map of post-lift-off PDMS corresponded directly to the raised Au features on the related Au-on-Si masters. Thus, PDMS was patterned by *addition* of Au-mercaptoundecanol monolayers from patterned Au regions on Au-on-Si masters, and not by imprinting, as nanoimprinting would result in inverse height topographies from those measured in **Figure III.1E-H**. Notably, after reannealing and self-assembly of new alkanethiol monolayers, Au-on-Si masters were able to be reused a number of times to pattern multiple PDMS samples (**Figure III.S3**).

Patterned lifted-off monolayers were also imaged using variable-pressure scanning electron microscopy (VP-SEM), as shown in **Figure III.1I-L**. Compared with AFM, SEM can be used to image patterns more efficiently as it provides chemical sensitivity and faster image acquisition over larger areas, up to square millimeters.[5,35-37] The VP-SEM modality accommodates non-conducting samples by injecting water vapor into the sample chamber to offset destructive charging of samples. In all cases, the dimensions and feature arrangements on patterned PDMS samples were consistent with those observed by AFM. In the VP-SEM images, functionalized regions consistently appeared less intense than the surrounding regions. We previously observed similar contrast inversion while imaging self-assembled alkanethiols on Au surfaces.[5] In earlier studies, changing the operating voltage (*i.e.*, the primary electron beam voltage) during SEM image acquisition was shown to reverse the contrast for images taken from the same sample. For PDMS, which is not conducting, the accelerating voltage, sample height, and vapor pressure were adjusted so that patterns could be discerned. Contrast in VP-SEM, also depends on the nature of the alkanethiol molecules and SAM disorder (*e.g.*, the orientations and conformations of the molecules in the SAM).[5] The Au-mercaptoundecanol monolayers on PDMS are disordered, as only 60-70% of

alkanethiol molecules are removed during CLL.[1,10,38] The resulting incomplete coverage may also influence the observed contrast. These Au-alkanethiolate monolayers on PDMS are composed of Au atoms bound to the PDMS by organic alkanethiol molecules. Thus, the observed contrast of Au, seen in the SEM images of the Au-on-Si masters (**Figure III.1A-D**), is not necessarily comparable to that of the SEM images of Au-alkanethiolate monolayers (**Figure III.1I-L**).

We were unable to visualize patterned lifted-off monolayers on PDMS using optical extinction spectroscopy (**Figure III.S4**). We attempted to quantify optical extinctions of lifted-off Au monolayers on PDMS using a strategy previously employed to measure extinction from assemblies of Au nanoparticles or nanothin Au films.[39] As shown in **Figure III.S4C**, optical extinction was indistinguishable from instrument noise for visible wavelengths. Furthermore, there were no discernable differences in transmission between regions containing the Au monolayers and unmodified PDMS. Thus, the Au-alkanethiolate hybrid material is transparent at visible wavelengths to within our measurement capabilities.

Although the Au monolayers were not optically detectable, we labeled them with thiolated DNA, using a strategy to detect even minor amounts of species *via* their chemical properties.[40-42] In doing so, we demonstrated the chemical functionality of the Au-alkanethiolate monolayers (**Figure III.2**). Complementary DNA was hybridized to thiolated single-stranded DNA self-assembled on lifted-off Au-containing regions on PDMS. Complementary sequences were fluorescently labeled, enabling indirect visualization of

patterned Au monolayers. Only regions containing Au-alkanethiolates appeared bright in fluorescence microscopy images (**Figure III.2**).

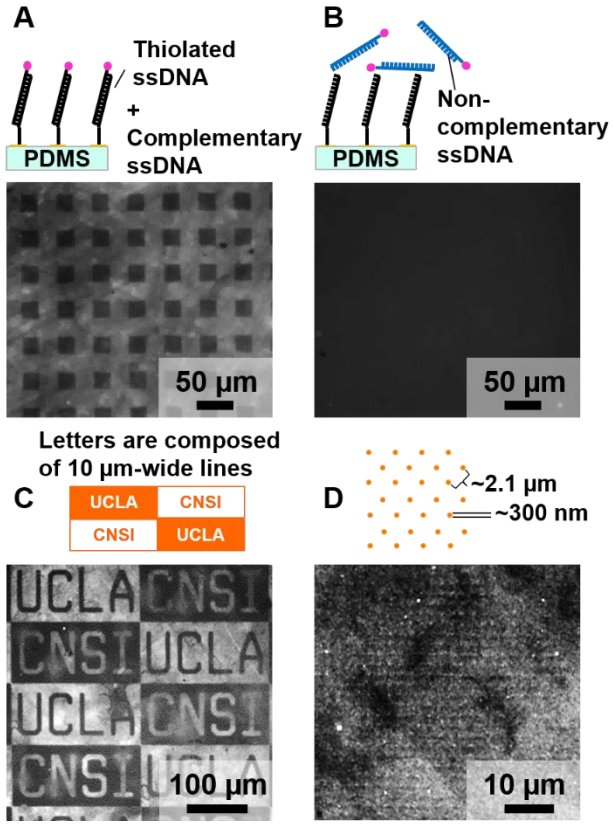

Figure III.2: Fluorescence visualization of patterned lifted-off Au-alkanethiolate monolayers via DNA self-assembly and hybridization. **(A)** (Top) Scheme for complementary DNA hybridization experiments. (Bottom) Fluorescence microscopy image of a Au-alkanethiolate monolayer pattern on flat polydimethylsiloxane (PDMS) after incubation with thiolated single-stranded DNA. Bright (lifted-off) regions between squares are indicative of hybridization of AlexaFluor® 488-labeled complementary DNA. Square regions are dark due to the absence of Au, and therefore, the self-assembled DNA necessary for hybridization. **(B)** (Top) Scheme for non-complementary control experiments. (Bottom) Similar substrate and DNA self-assembly as **(A)** except scrambled, non-complementary fluorescently labeled DNA was used for hybridization. **(C)** Flat PDMS was patterned with Au-alkanethiolate monolayers in the "CNSI" lettered and "UCLA" relief regions. Patterns were then visualized using the same DNA self-assembly and hybridization procedure as panel A. **(D)** A different region of the same PDMS sample shown in **(C)** but patterned with 300-nm dots having 2.1-μm nearest neighbor center-to-center separations.

Using this straightforward functionalization and visualization method, we investigated patterns of lifted-off Au-monolayers on PDMS as substrates for DNA recognition. Upon hybridization of dye-labeled complementary strands, fluorescent patterns were readily observed (**Figure III.2A,C,D**). No measurable fluorescence was detected when DNA-functionalized substrates were exposed to dye-labeled non-complementary DNA (**Figure III.2B**). Thus, the fluorescence patterns observed in **Figure III.2** derive from specific hybridization between thiolated DNA strands and their complementary sequences. Also, no patterns were observed in control experiments investigating nonspecific adsorption of complementary strands to patterned substrates in the absence of self-assembled thiolated DNA, hybridization with non-complementary self-assembled DNA, or self-assembly and hybridization of DNA on unpatterned PDMS (**Figure III.S5**).

Using CLL and fluorescence visualization, we produced images over square-mm areas with lateral feature sizes spanning several orders of magnitude on the same substrates (**Figure III.2C,D**). We have yet to determine the limits of the feature sizes and areas that can be patterned by CLL, with features as small as 5 nm removed from the original monolayer.[2] In addition to a wide range of feature sizes, supported Au monolayer on PDMS patterns were stable for at least six months (**Figure III.S6**). These results suggest that while the optical properties of the lifted-off monolayers are different from those of bulk Au (*i.e.*, the former are optically transparent), lifted-off Au monolayers are chemically similar to bulk Au since they are amenable to self-assembly of thiols, and thus, to forming Au-S bonds. The ability to modify the supported Au monolayers resulting from CLL chemically suggests opportunities for large-scale, transparent, sensor technologies, which could be straightforwardly fabricated under ambient conditions.

Having established characterization modalities to evaluate Au-alkanethiolate monolayers on PDMS, we developed an additional strategy for patterning PDMS with Au-alkanethiolate monolayers that takes advantage of the chemical selectivity associated with CLL. We previously determined that methyl-terminated SAMs do not react with activated PDMS and are therefore inert to lift-off. Terminal functional groups that are 'CLL compatible' include hydroxyl, amino, carboxylate, and phosphonate moieties, such that these groups react with oxidized PDMS and are lifted off.[1,10,11] Performing CLL with flat PDMS stamps and patterned SAMs having regions of reactive *vs.* unreactive molecules on Au was anticipated to yield patterns on PDMS.

The scheme in **Figure III.3A** illustrates this concept. First, CLL was performed using stamps with 7.5-μm diameter wells and mercaptoundecanol SAMs on the Au surfaces, leaving behind SAMs in circular regions. Octadecanethiol (C18) molecules were then inserted into the contact regions resulting in patterned monolayers on Au substrates. Octadecanethiol was selected for study because we hypothesized its chain length would give sufficient contrast in post-CLL AFM imaging, and that it would not displace the remaining mercaptoundecanol monolayer in the circular regions, or prevent it from undergoing CLL with a flat stamp.[43,44] Two-component SAMs on Au having patterned regions distinguished by different terminal groups were then used for a second CLL step involving flat PDMS.

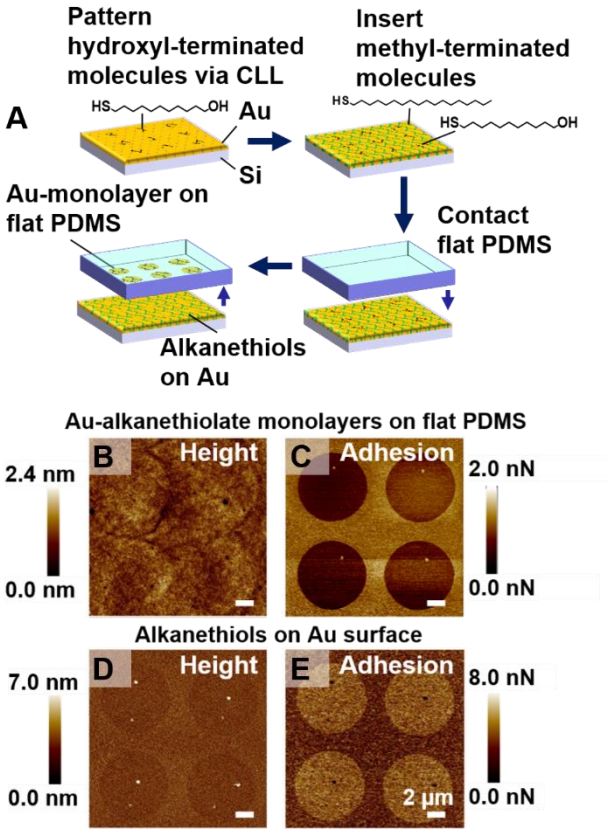

Figure III.3: Chemically selective lift-off onto flat polydimethylsiloxane (PDMS). **(A)** First, chemical lift-off lithography (CLL) was performed with a stamp having recessed circular features and a preformed self-assembled monolayer of mercaptoundecanol. Methyl-terminated alkanethiol molecules were then inserted into the contact regions, resulting in a self-assembled monolayer with patterned terminal functionalities. Performing a second round of CLL using this substrate and flat PDMS resulted in lift-off of Au-alkanethiolate monolayers from regions containing hydroxyl-terminated molecules. **(B)** Height and **(C)** adhesion maps of the Au-alkanethiolate features on PDMS. These maps were simultaneously acquired using peak-force atomic force microscopy. **(D)** Height and **(E)** adhesion maps of the remaining alkanethiols on Au after CLL. The topography and adhesion maps in **(B,C)** show inverted contrast from those in **(D,E)**, respectively.

X-ray photoelectron spectroscopy (XPS) spectra of patterned PDMS illustrated the presence of Au in the regions predominantly containing mercaptoundecanol (noncontact regions associated with the first CLL step), but also in the contact regions dominated by inserted octadecanethiol. Residual mercaptoundecanol in the contact regions is due to the incomplete removal of molecules during the first CLL step. This partial removal has been used to advantage in fabricating tethered DNA for high-efficiency hybridization[10] and for

investigating spin selectivity in electron-transport through DNA.[12] Comparing the XPS peak areas suggested that the amount of Au in the lift-off regions is approximately double the surface concentration of Au in the noncontact regions. We note that the contrast in the topographic AFM map of the Au-alkanethiolate monolayers produced *via* two-component SAMs (**Figure III.3B**) appears lower than that of the monolayers produced *via* Au-on-Si masters (**Figure III.1E-H**). We attribute the low topographic contrast in the height maps in **Figure III.3** to the presence of Au-alkanethiolates in all regions of the patterned PDMS.

In addition to topographic heights, we used PF-AFM to determine adhesion force – the force needed to pull an AFM tip off a surface – to investigate chemical contrast on patterned PDMS.[45] The patterns of circles seen in the AFM adhesion maps in **Figure III.3C,E** are consistent with differential molecular compositions in the lifted-off *vs.* non-lifted-off regions and the chemically selective removal of molecules terminating in hydroxyl *vs*. methyl groups during the second lift-off step whereby patterned PDMS was produced. Collectively, the data in **Figure III.3** demonstrate a CLL-centered strategy for regional control of chemical composition on flat PDMS supporting materials.

To evaluate the Au-alkanethiol-PDMS hybrid material further, we quantified the apparent heights of the regions containing the lifted-off Au monolayers using AFM topography maps of patterned PDMS (**Figure III.1E,F,H**). To recognize and to differentiate systematically regions containing Au-mercaptoundecanol monolayers and PDMS-only background regions, we employed a recently developed image analysis algorithm based on Chan-Vese segmentation.[46-48] This algorithm is an enhanced version of a region-based segmentation method that can be used to detect artifacts and differentiates pattern features from topographically uneven backgrounds, which thresholding strategies cannot

straightforwardly accomplish.[47] Further, this algorithm minimizes user bias inherent in delineating regions of interest and maximizes the number of image data points considered. Details and demonstrations of our implementation are provided in the Experimental section and in **Figures III.S8-III.S10**.

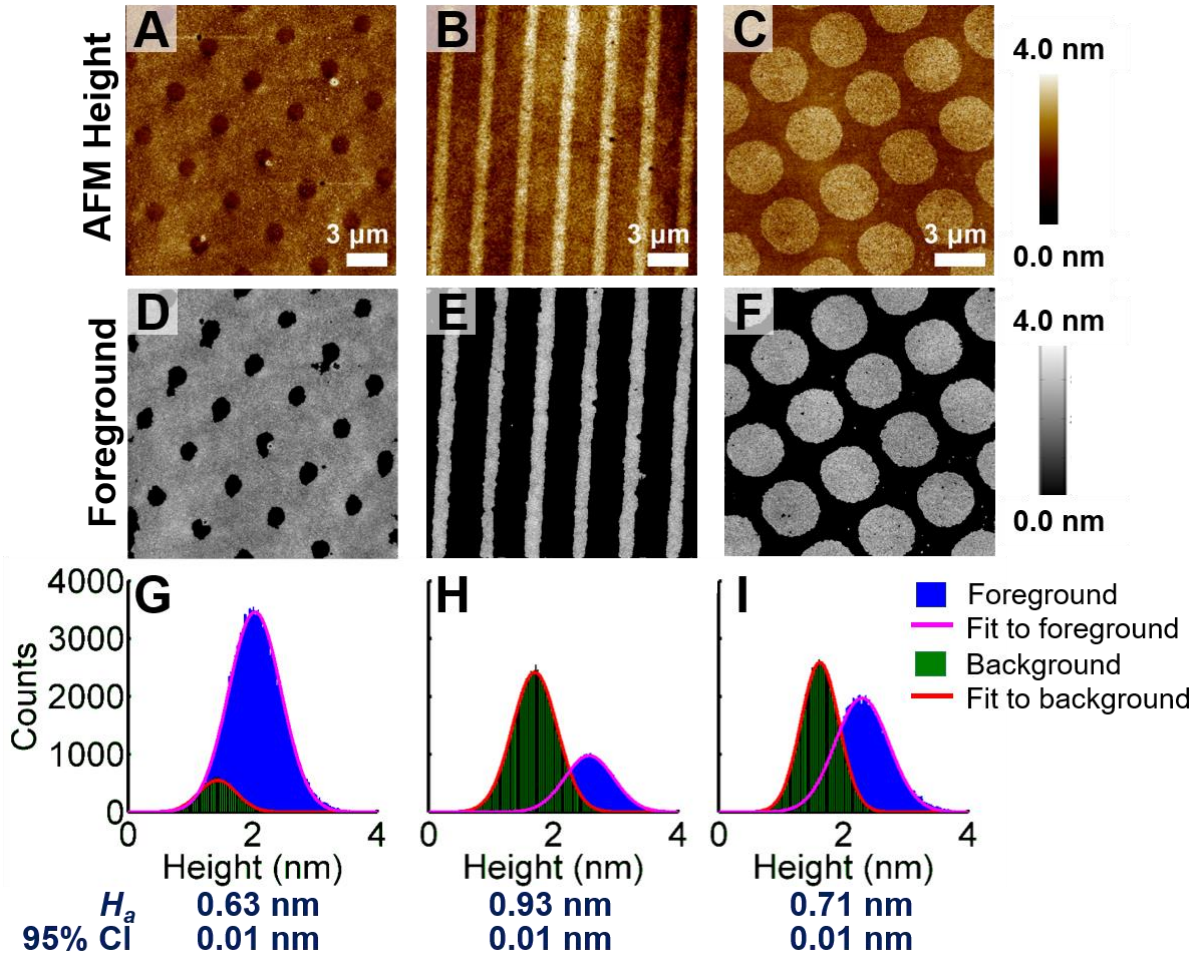

Figure III.4: (A-C) Height maps of three different patterns of Au-mercaptoundecanol monolayers on polydimethylsiloxane (PDMS) acquired using peak-force atomic force microscopy. **(D-F)** Regions classified as 'foreground' are determined using the image segmentation algorithm and contain Au-mercaptoundecanol monolayers corresponding to the images shown in **(A-C)**. **(G-I)** Histograms of the heights represented by the intensities of foreground and background classifications of pixels. Each histogram was fit to a Gaussian distribution and was consistent with a normal distribution. The calculated apparent height, H_a, determined from each image was the difference in the means of the foreground and background pixel intensities. The values for H_a and 95% confidence intervals (95% CI) are shown below each graph.

Monolayers of Au-mercaptoundecanol (**Figure III.4A-C**) were associated with heights ranging from 0.63 ± 0.01 nm to 0.93 ± 0.01 nm determined from the Chan-Vese analyses (**Figure III.4D-I**). These apparent heights are smaller than the height of a SAM of mercaptoundecanol on a Au surface, which is 1.3-1.4 nm with a 30° tilt angle relative to the surface normal.[49-51] Considering an interlayer spacing of Au{111} of 2.35 Å,[52] complete lift-off of alkanethiol SAMs from Au surfaces would yield Au-alkanthiol layers approximately 1.6 nm in height, assuming that the molecules retain their original orientation and each thiol removes one Au atom.

Nonetheless, we know the Au-alkanethiolate monolayers on PDMS from typical CLL experiments are reflective of incomplete lift-off.[1,10,38] Moreover, the dimensions of the Au-alkanethiol complexes that compose the lifted-off monolayer on PDMS are less than the resolution of ambient AFM.[53] As such, an average can be calculated for the apparent heights by multiplying the typical 60-70% yield of CLL with the heights of the full Au-alkanethiolate monolayers calculated above. Doing so yields an apparent height range of 0.96-1.12 nm, which is still greater than the measured heights (**Figure III.4**). The Au-alkanethiolate complexes on PDMS are expected to adopt a variety of orientations relative to the surface, similar to the variety of orientations of self-assembled alkanethiols at incomplete coverage on Au surfaces,[54,55] further reducing our estimate of apparent height. In all, our measured estimates of topographic heights of Au-alkanethiol monolayers on PDMS are consistent with all previous CLL characterizations and with the predicted 1-2 Au atoms lifted-off per alkanethiolate molecule (*vide infra*).

Assumptions made above regarding the structure of Au-alkanethiolate monolayers on PDMS are in agreement with estimates of the stoichiometry of the Au-alkanethiolate

monolayer calculated through molecular dynamics simulations. Atomic rearrangements during the CLL process were modeled using density functional theory and the grid-based projector-augmented wave (GPAW) method.[29] During simulations, a densely packed SAM of chemisorbed butanethiolates was pulled from a Au{111} surface. Details of the initial Au-thiolate surface structure and the pulling speed were varied (see Experimental section). **Figure III.5** shows the initial structures and later snapshots from two representative simulations. Panel A shows the initial structure having RS-Au-SR units (R refers to the butyl chain) on top of a Au{111} surface with defects, while panel B indicates a close-packed layer of butanethiolates on an ideal fcc Au{111} surface.

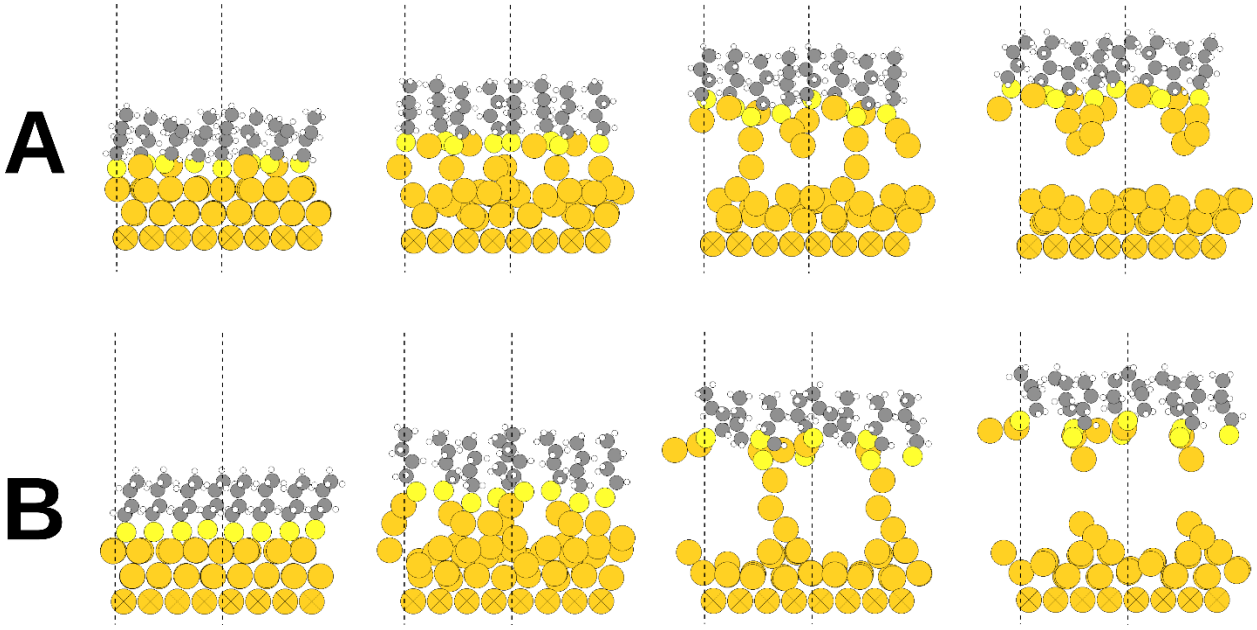

Figure III.5: Configurations calculated from two molecular dynamics simulations of lift-off of a butanethiolate SAM on Au{111}. **(A)** Initially, densely packed RS-Au-SR units occur on Au{111} having surface vacancies. The number of vacancies equals the number of RS-Au-SR units. **(B)** Initially, dense packing of individual butane thiolates occurs at the face-centered cubic sites of a defect-free Au{111} surface. The dashed vertical lines define the borders of each computational unit cell, *i.e.*, in the figure there are two unit cells side by side in each configuration. Atom colors: white, hydrogen; gray, carbon; yellow, sulfur; orange, Au.

We further computationally analyzed the XPS core level shifts (CLS) for each Au atom in the lifted-off complexes (**Figure III.S11**). These calculated spectra are signatures of the predicted structures resulting from CLL of SAMs packed on Au with and without defects. When comparing the spectra and the structures, we found that the shifts are spread ~1.5 eV around the bulk reference value, and similar chemical environments of the Au atoms resulted in similar core level shift energies. These simulations indicate that the CLS of a Au atom in a Au-alkanethiolate monolayer are sensitive to its local environment in the system, and that spectral features would reflect the arrangement of self-assembled molecules on the gold surface at initial and/or intermediate stages of CLL. Our current observations are consistent with the predicted stoichiometries, and these simulations form the basis of work to interrogate the structure and stoichiometry of the lifted-off Au monolayer further.

The potential to lift-off Au *via* PDMS contact is consistent with the discovery that Au-thiolate complexes are the mobile species in SAM diffusion.[2,56] The electronegative sulfur atoms (thiol head groups) withdraw charge from Au atoms, causing measurable changes in the physical properties of Au, including increased binding energies of Au 4f electrons measured by XPS,[57] decreased Au-Au rupture forces in molecular break-junction experiments,[58-60] and shorter Au-S bonds compared with Au-Au bonds measured by electron diffraction.[61,62] At molecular resolution, scanning probe measurements have revealed rearrangements of Au-surface atoms,[63-65] diffusion and alignment of adatom-adsorbate complexes,[56,66] and phase separation of SAMs composed of molecules with different backbones or terminal functionalities.[67-69] Phase separation is driven by stronger intermolecular interactions between one type of SAM molecule *vs.* another in mixed SAMs.

Rearrangements and displacement of molecules in mixed monolayers can also be manipulated by choosing other head groups, such as selenols, in place of thiols.[70,71]

Theorists have investigated the influence of collective interactions among alkanethiol backbones on the removal of clusters of SAM molecules from Au surfaces.[72,73] For example, less force is required to pull a monolayer of heptanethiolates and Au atoms from a Au substrate nanomechanically than a monolayer of propanethiolates. In addition to previously demonstrated lift-off 'compatible' and 'incompatible' terminal groups,[10,11] the head groups and backbones of the SAM molecules themselves are potential parameters for customizing the compositions and chemical states of the lifted-off Au monolayers.

III.D. Conclusions and Prospects

We have devised a suite of fabrication, imaging, and computation strategies to address the structure, functionality, and stoichiometry of Au monolayers lifted-off during chemical lift-off lithography and demonstrate a new 2D Au-hybrid material with unique properties. Using CLL, we produced a functional hybrid material of Au-alkanethiolate monolayers on topographically flat PDMS that spatially encodes chemical functionality at the surface of PDMS, while preserving the transparency and flexibility of the PDMS. The lateral dimensions and periodicity of the lifted-off monolayers were preserved from the Au-on-Si masters when patterning the lifted-off monolayers on PDMS, as imaged by AFM and SEM. These patterns of Au monolayers were recognizable in fluorescence microscopy when functionalized with thiolated DNA hybridized with dye-labeled complementary DNA.

Analysis of the relative heights in AFM images revealed less than a complete monolayer of Au-alkanethiolates on PDMS, consistent with previous findings indicating that

CLL removes ~70% of molecules from contact regions. In agreement with indirect evidence that a monolayer of Au is removed during CLL, molecular dynamics simulations converged on a stoichiometry of ≤1.5 Au atoms per thiol. These simulations also demonstrate that the lifted-off Au atoms are in environments distinct from those at the surface of the bulk Au, and are predicted to be distinguishable in photoelectron spectra.

This body of evidence demonstrates that CLL, an already straightforward method for patterning square centimeter areas of alkanethiol monolayers of Au-on-Si substrates, can also be used to pattern PDMS with Au and to impart encoded chemical functionality without affecting the flexibility or transparency of PDMS. Incorporating chemical functionality onto PDMS will be useful for integrating sensing functions into microfluidic devices.[74-86] Compared with many techniques used to impart submicron features onto PDMS,[80-82] CLL is parallel, high-throughput, and performed under ambient conditions.

Further studies will test the impact of the composition of the supporting molecules on the properties of the lifted-off Au monolayer. The structural and electronic properties of the Au monolayer can be tailored by varying the properties of the supporting molecules.[2] For example, limiting the degrees of freedom of the supporting monolayer by replacing mercaptoundecanol with unsaturated alkanethiols or rigid cage molecules may result in a monolayer that better maintains a planar two-dimensional geometry.[2] Additionally, carboranethiols, which are known to form pristine and nearly defect-free SAMs,[67,87,88] or molecules with additional interactions among the backbones, such as 3-mercapto-*N*-nonylpropionamide, which forms hydrogen-bonding networks,[89,90] are hypothesized to increase the yield of lifted-off molecules during CLL and to produce more complete supported monolayers.[2] Replacing thiol moieties with groups that bind more strongly to

Au,[4,70,71] such as selenolates, will also be investigated. Thus, a rich variety of tunable variables, including stamp geometries, chemical backbones, and anchor groups remain to be explored for CLL.

Ultimately, the resolution of CLL will be defined as the ability to control the separation between individual lifted-off Au-alkanethiolate regions on PDMS (or other supports). It may ultimately be possible by diluting the 'liftable' alkanethiols on gold[8] to reach the ultimate limit of lifting off single molecules. However, the *fidelity* of the features achieved, *i.e.*, the ability to replicate features defined by the alkanethiol monolayers on Au onto the PDMS, will increase with increasing CLL yield. In addition, increasing the CLL yield will improve the fidelity of the patterns of Au-alkanethiols lifted-off on PDMS, and thus presumably more complete and closely packed supported Au monolayers on PDMS.

The computation, fabrication, and visualization strategies established herein form a basic toolbox for interrogating the influence of these variables on CLL and the structure and functionality of the resulting hybrid materials. Further development of CLL has significant potential for fabricating sensors, biocompatible platforms, and other applications that will benefit from flexible, transparent, bio-inert materials combined with the extensive functionalization chemistries of Au.

III.E. Supplementary Material

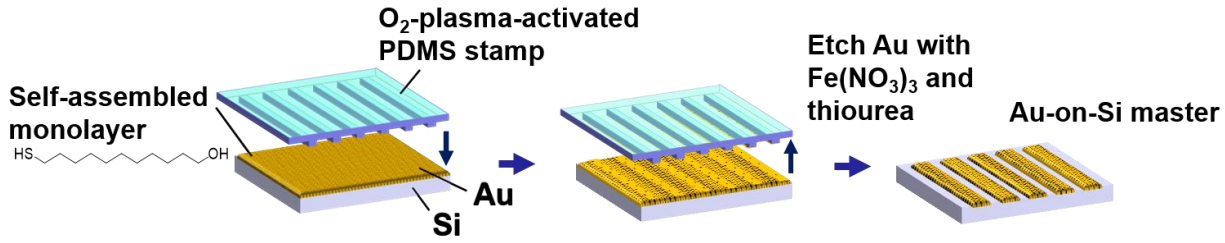

Figure III.S1: Chemical lift-off lithography (CLL) to produce patterned Au-on-Si masters. Topographically patterned polydimethylsiloxane (PDMS) stamps were used to pattern alkanethiol self-assembled monolayers (SAMs) on Au substrates.[1] Alkanethiols were removed from stamp-substrate contact regions as a result of the lift-off process. Solutions of $Fe(NO_3)_3$ and thiourea were then used to remove the exposed Au from the contact regions. The closely packed SAMs remaining in the non-contact regions acted as molecular resists protecting the underlying Au from etching. The resulting Au-on-Si masters were used to pattern flat PDMS, as shown in **Figure III.1**.

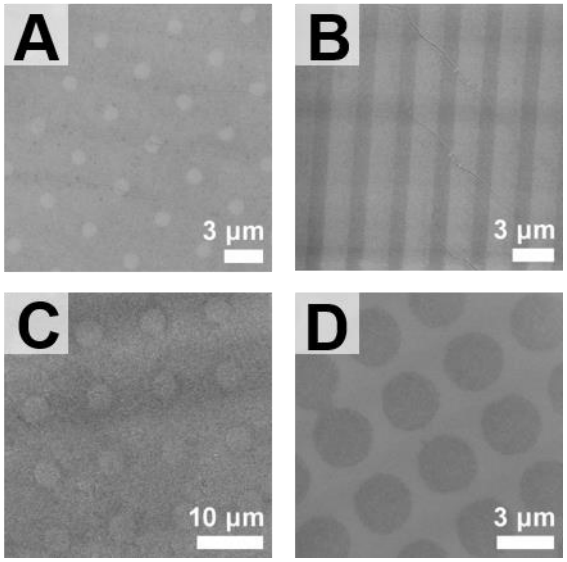

Figure III.S2: (A-D) Unmodified variable-pressure scanning electron micrographs of Au-alkanethiol patterns corresponding to **Figure III.1I-L**, respectively.

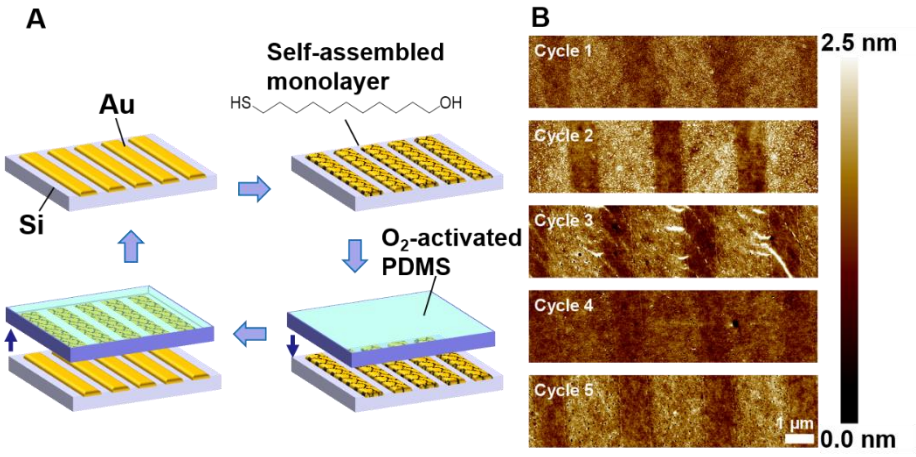

Figure III.S3: Reuse of Au-on-Si masters to pattern multiple polydimethylsiloxane (PDMS) substrates. (A) A patterned Au-on-Si master was functionalized with mercaptoundecanol and used to pattern PDMS by chemical lift-off lithography. After patterning the first PDMS sample, the Au-on-Si master was reannealed, functionalized with a new self-assembled mercaptoundecanol monolayer, and used for lift-off lithography to pattern a second PDMS sample. **(B)** Atomic force microscopy height maps of patterned Au-mercaptoundecanol monolayers on PDMS after five consecutive patterning cycles using the same Au-on-Si master.

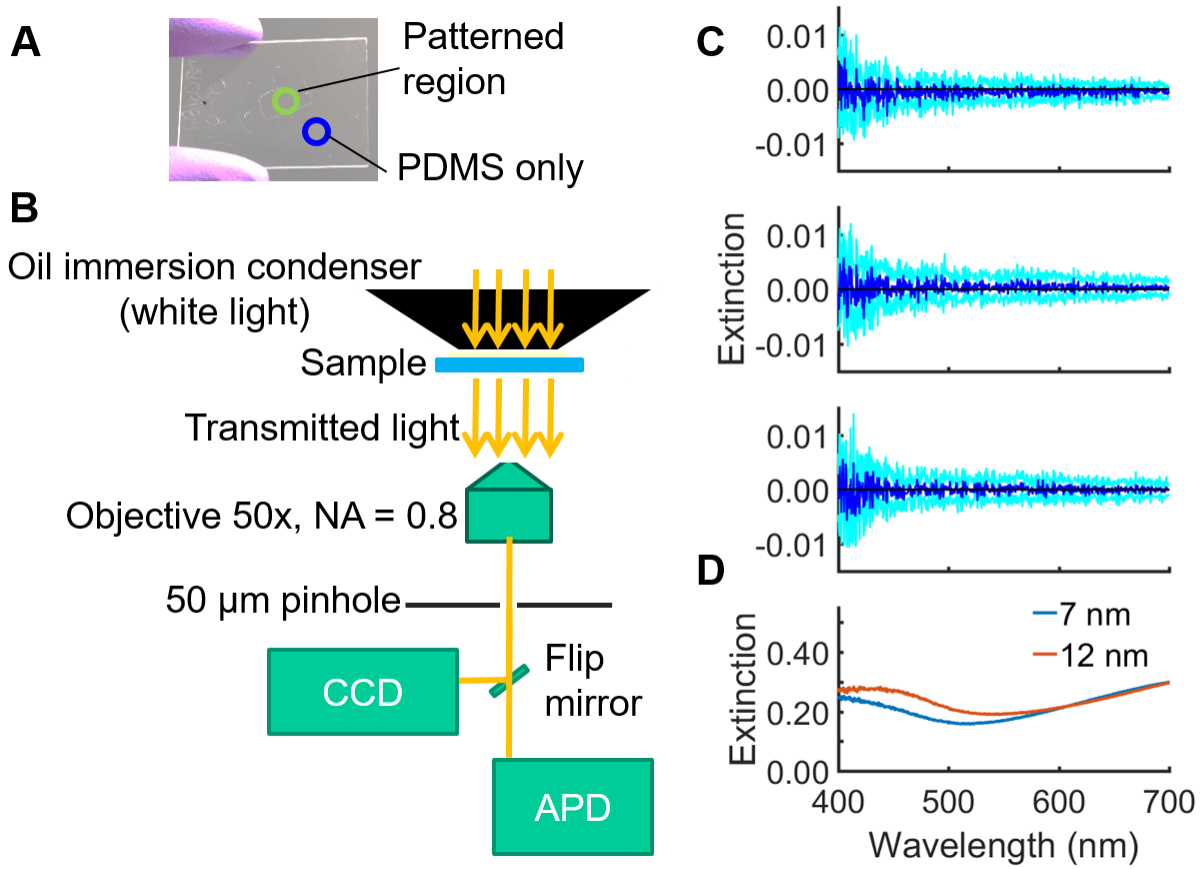

Figure III.S4: Optical extinction spectroscopy of lifted-off monolayers. (A) Photograph of PDMS indicating a region containing a lifted-off monolayer. **(B)** Schematic showing the configuration for measuring optical extinction with sub-micron resolution. The locations to collect spectra were selected after acquiring initial images on an avalanche photodiode (APD). The transmitted light was then redirected to a charge-coupled device (CCD) spectrometer. Signals were collected from regions with ($I_{gold\ +\ substrate}$) and without ($I_{substrate}$) lifted-off monolayers and extinctions were calculated using the following equation:

$$Extinction_{gold} = -log\left(\frac{I_{gold+substrate}}{I_{substrate}}\right)$$

(C) Representative spectra from three individual ~1-um areas containing lifted-off Au monolayers. The dark lines are averages of three spectra, while the light lines indicate standard deviation envelopes. **(D)** Extinction spectra of nanothin Au films. Note the range of the y-axis in **(D)** compared with ranges in **(C)**. The thicknesses of the Au films measured in D were confirmed by atomic force microscopy.

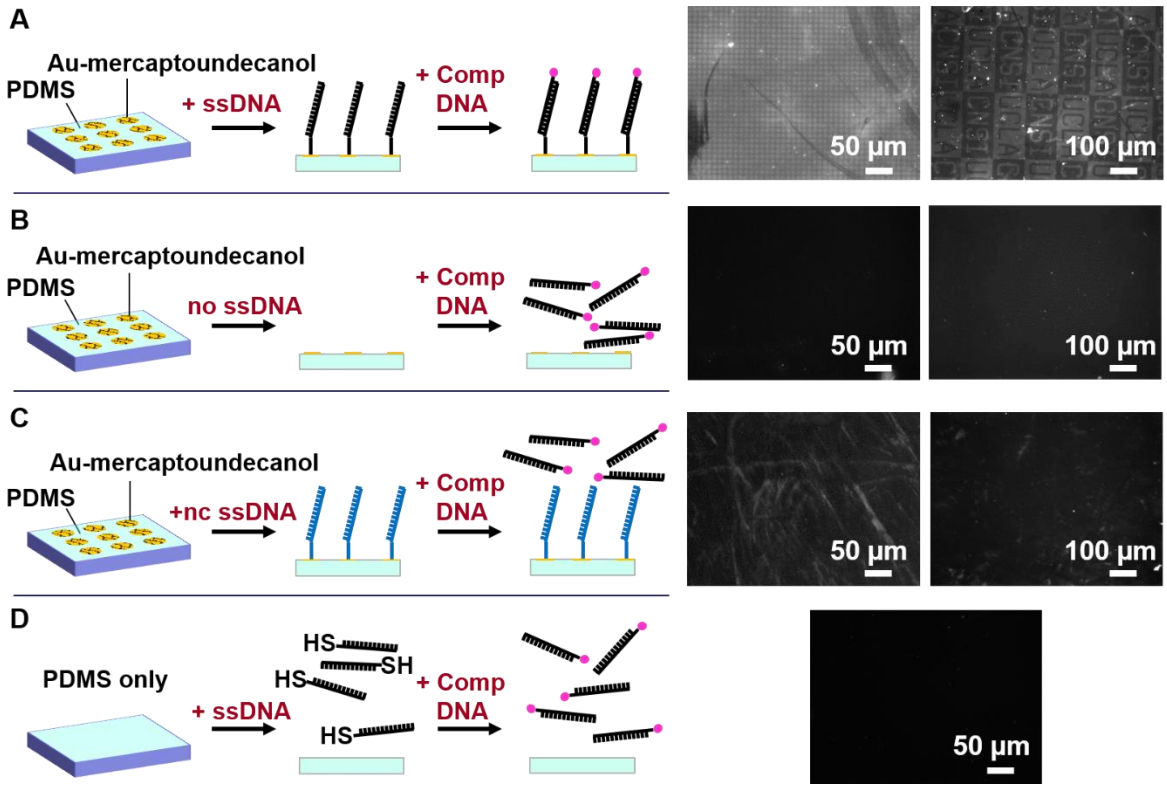

Figure III.S5: Experiments to test the specificity of DNA hybridization on Au-mercaptoundecanol monolayers. (A) Typical substrates with Au-mercaptoundecanol monolayers patterned in circles (left) or CNSI letters/UCLA relief (right) with self-assembled thiolated single-stranded DNA hybridized with fluorescent-dye-labeled complementary sequences. **(B)** Thiolated DNA was omitted. **(C)** Noncomplementary thiolated single-stranded DNA was self-assembled prior to hybridization. **(D)** Unpatterned substrate having no Au-mercaptoundecanol monolayers. The same thiolated DNA and fluorescently-labeled complementary sequences in **Figure III.2** were used here.

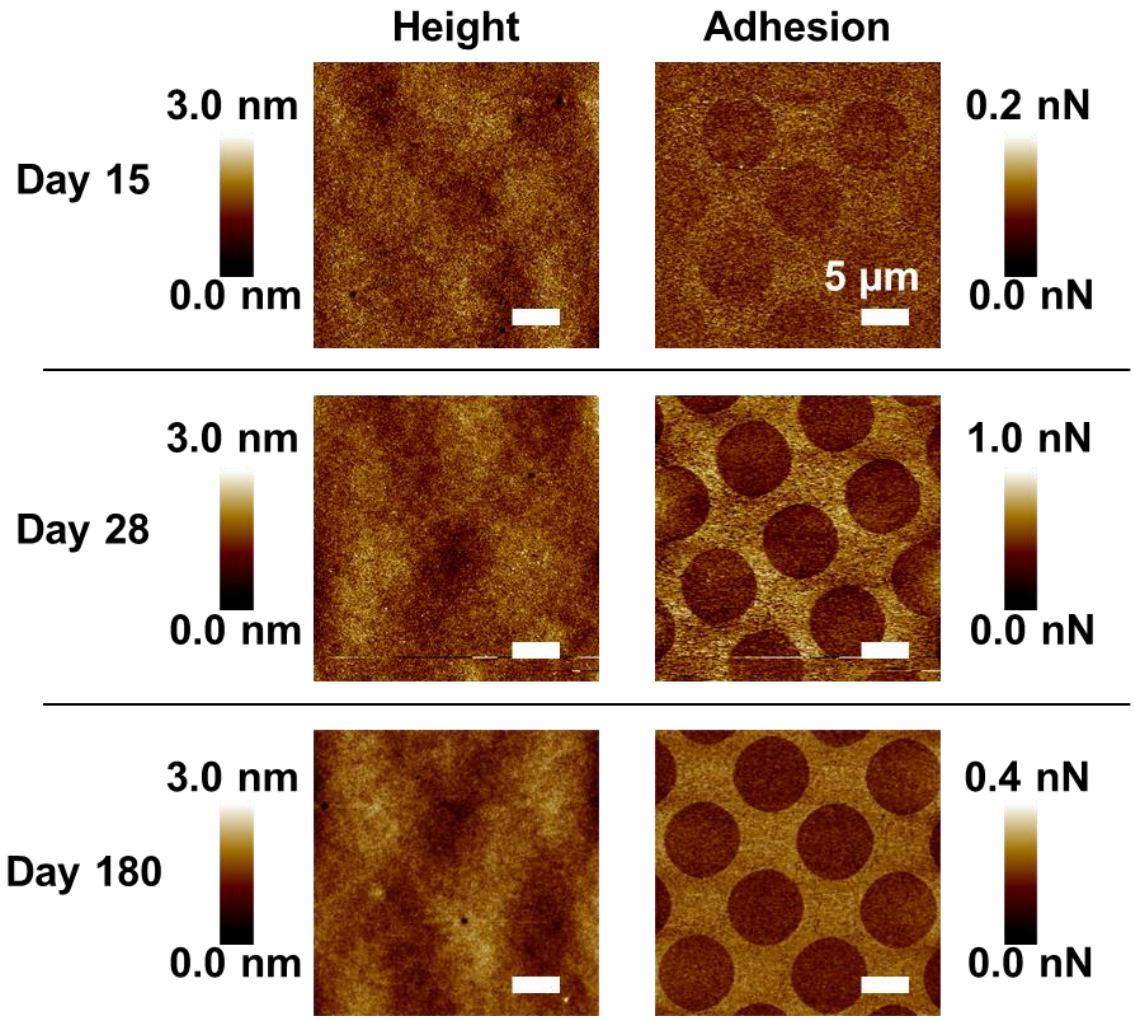

Figure III.S6: Atomic force micrographs of a Au-alkanethiol monolayer pattern on flat polydimethylsiloxane at 15, 28, and 180 days after sample preparation. The sample was rinsed with ethanol and dried with compressed nitrogen prior to recording each image.

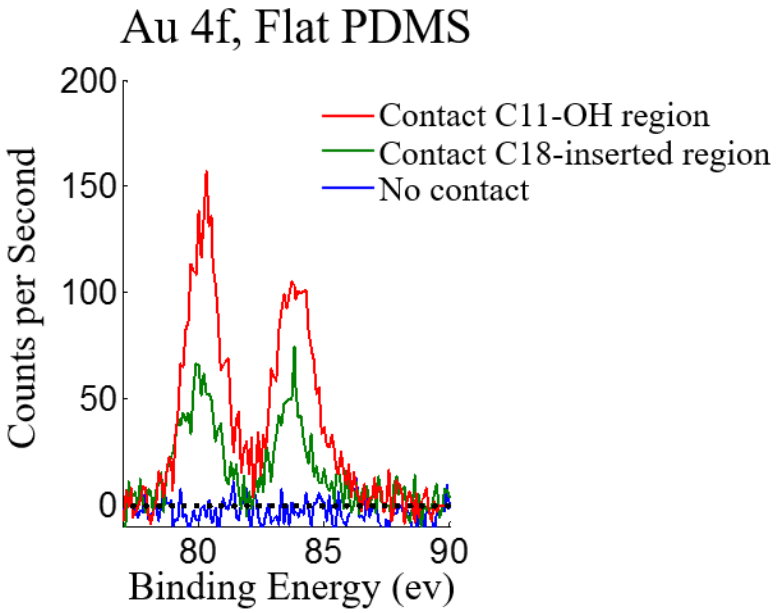

Figure III.S7: Representative X-ray photoelectron spectroscopy (XPS) spectra from different regions of flat polydimethylsiloxane (PDMS) contacted with self-assembled monolayer (SAM) molecules on a Au surface patterned by the procedure illustrated in **Figure SIII.1**. Here, chemical lift-off was performed by contacting an activated flat PDMS stamp with half of each Au substrate having a preformed SAM comprised of mercaptoundecanol (C11-OH). Each substrate was then immersed in a 1 mM ethanolic solution of octadecanethiol (C18) to insert C18 molecules into the contact regions. Then, entire substrates were contacted with new, activated flat PDMS stamps. Each region of the patterned PDMS was analyzed by XPS. Peak areas from the C18 contact regions (green trace) were 46 ± 12% of the peak areas from the C11-OH contact regions (red trace) (averaged across N=4 substrates). These measurements indicate that C11-OH molecules are not completely removed or displaced during lift-off and C18 insertion.

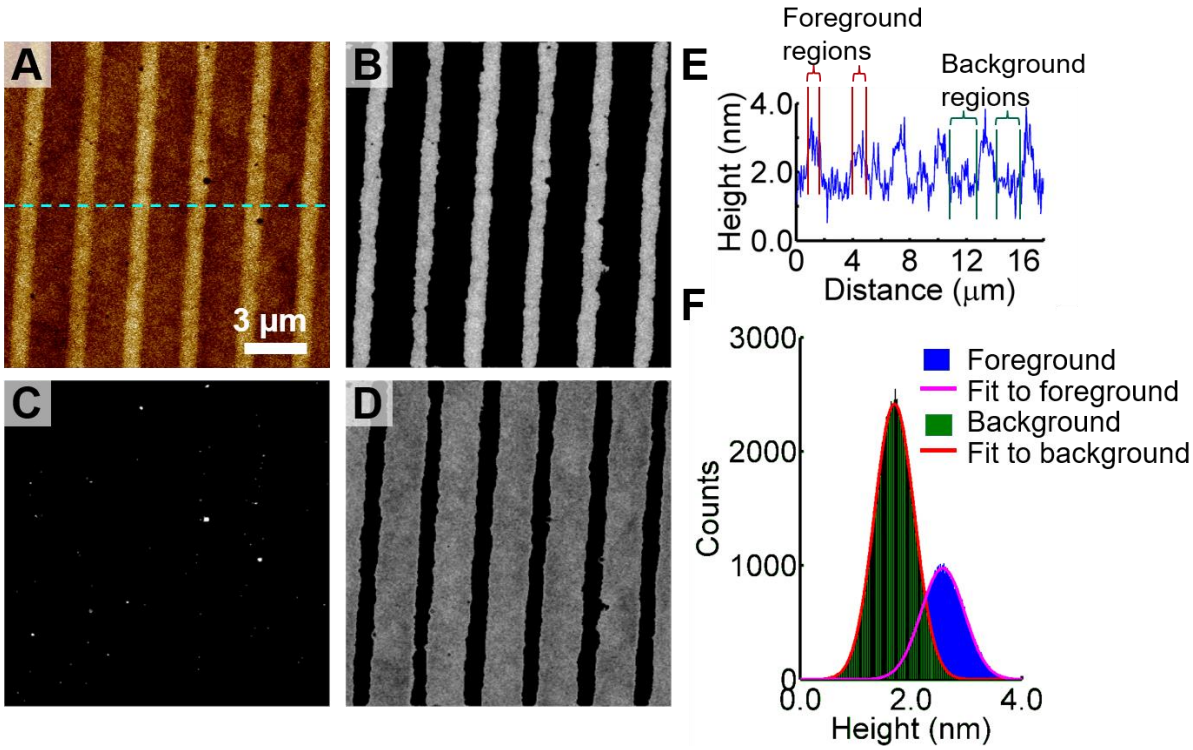

Figure III.S8: Demonstration of the Chan-Vese segmentation algorithm applied to a height map acquired by atomic force microscopy. (A) The recorded height map displayed with false color scale. **(B)** The foreground segment (light regions) identified by the algorithm, excluding the artifacts. **(C)** The artifacts identified by the algorithm. **(D)** The background segment (light regions), excluding artifacts. **(E)** Height profile along the line section drawn across the image in **(A)**. Red and green lines and brackets indicate examples of foreground regions and background regions, respectively, which are averaged to calculate the intensity difference in the 'line-by-line' approach. **(F)** Histograms of the heights determined from the pixel intensities in the foreground and background segments and Gaussian fits from the 'all-pixels' approach.

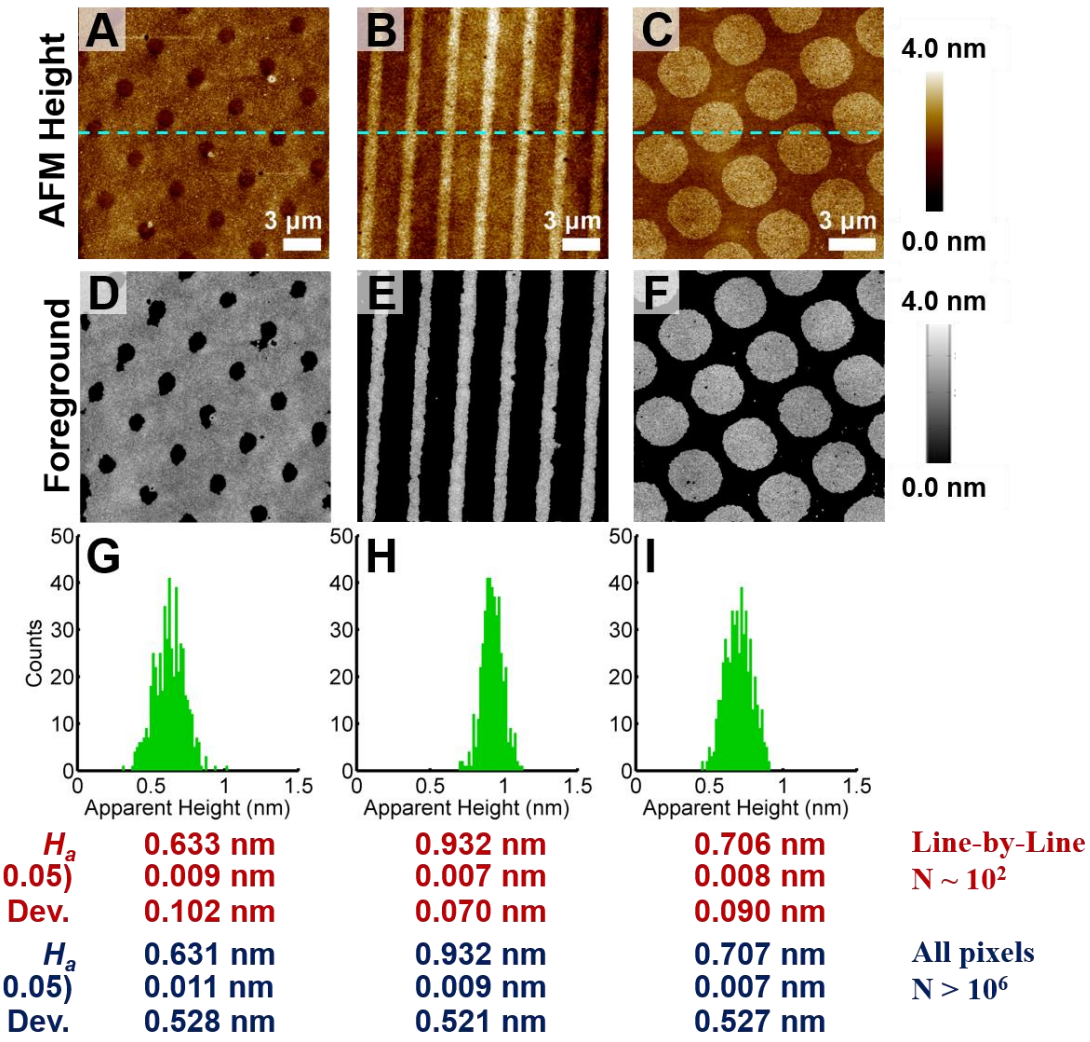

Figure III.S9: Analyses of apparent heights from atomic force micrographs. (A-C) The same height maps shown in **Figure III.1** of three different patterns of Au-alkanethiol monolayers on polydimethylsiloxane (PDMS) with representative line segments shown. **(D-F)** The 'foreground' segments (light regions) containing Au-alkanethiol complexes corresponding to the images in **(A-C)**. **(G-I)** Histograms of the average heights calculated from the differences of the 'foreground' and 'background' heights of each line. Using this approach, the calculated apparent height, H_a, for the foreground segment in each image is the average of the calculated heights from each line. The values for H_a, 95% confidence intervals (95% CI), and standard deviations are indicated below each graph. Values are reported for the line-by-line approach *vs.* the all-pixel approach.

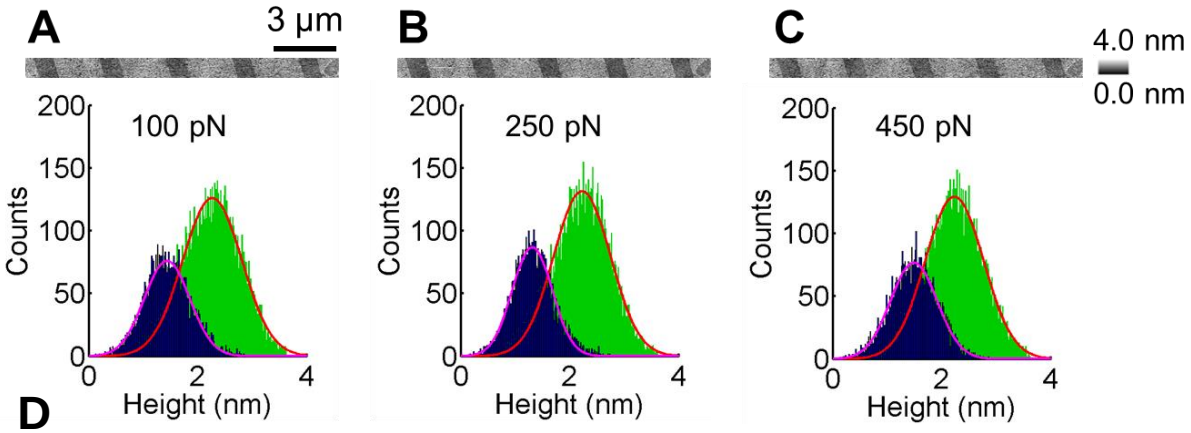

D

Force (pN)	Apparent height (nm)	95% Confidence interval (nm)	HWHM (nm)
100	0.80	0.03	0.49
150	0.88	0.03	0.47
200	0.87	0.03	0.44
250	0.85	0.03	0.44
300	0.80	0.03	0.46
350	0.75	0.03	0.46
400	0.72	0.03	0.46
450	0.74	0.03	0.48

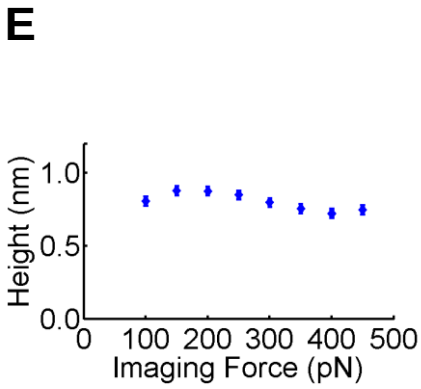

Figure III.S10: Influence of imaging force on apparent height. (A-C) Height maps of the same 15 μm × 0.93 μm area acquired by atomic force microscopy using the forces indicated on the graphs below. Each graph displays histograms of the heights of the Au-alkanethiol monolayer-containing regions (blue) and the polydimethylsiloxane (PDMS)-only regions (green), as detected by the segmentation algorithm. **(D)** Apparent heights, confidence intervals, and half-widths at half-maxima calculated for each image under different force setpoints. **(E)** Plot of apparent height *vs*. imaging force. Each data point is the apparent height (calculated by Chan-Vese segmentation) ± the confidence interval.

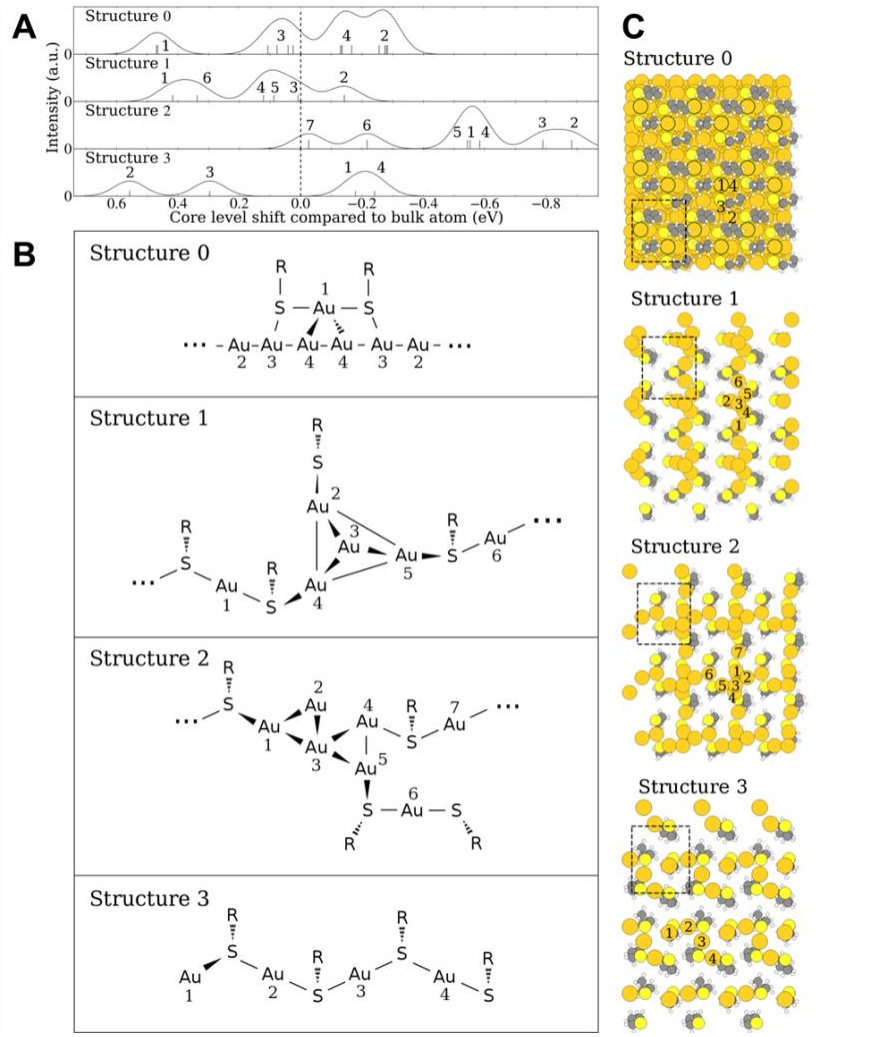

Figure III.S11: Core-level shift spectra of RS-Au-SR units on Au{111} and three computationally lifted-off Au-alkanethiol complexes and their structures. (A) The calculated core-level shift spectra with 0.05 eV Gaussian widening of the peaks. The x-axis represents the energy difference between the shift of an atom in the Au-alkanethiol complex and a bulk atom; a bulk atom is at 0 eV (marked with dashed vertical line). The peaks in the spectra are labeled with numbers corresponding to the Au atoms labeled in the structures of panels **(B)** and **(C)**. **(B)** Skeletal formulae and indices for Au atoms. The label R refers to butyl chains. The three dots in structures 0, 1, and 2 refer to the periodic complexes. Structure 0 has close-packed RS-Au-SR units on top of an ideal fcc Au{111} surface. Structures 1 and 2 correspond to the removed complexes in the simulations of **Figure III.5A,B**, respectively. Structure 3 originates from another lift-off simulation with similar initial conditions as **Figure III.5B**, however the wave functions were calculated using the double zeta-polarized linear combination of atomic orbitals basis in the grid-based projector augmented wave platform. **(C)** Space-filling structures corresponding to the same structures in B. Structure 0 is shown from above the SAM, while the other structures are shown from below the lifted-off complexes. The dashed rectangles represent the computational unit cell. The circled Au atoms in Structure 0 are adatoms bound between the sulfur atoms.

III.F. References

(1) Liao, W.-S.; Cheunkar, S.; Cao, H. H.; Bednar, H. R.; Weiss, P. S.; Andrews, A. M. Subtractive Patterning via Chemical Lift-Off Lithography. *Science* **2012,** *337*, 1517–1521.

(2) Andrews, A. M.; Liao, W.-S.; Weiss, P. S. Double-Sided Opportunities Using Chemical Lift-Off Lithography. *Acc. Chem. Res.* **2016,** *49*, 1449–1457.

(3) Xia, Y.; Whitesides, G. M. In *Encyclopedia of Materials: Science and Technology*; Elsevier Science Ltd., 2001.

(4) Smith, R. K.; Lewis, P. A.; Weiss, P. S. Patterning Self-Assembled Monolayers. *Prog. Surf. Sci.* **2004,** *75*, 1–68.

(5) Srinivasan, C.; Mullen, T. J.; Hohman, J. N.; Anderson, M. E.; Dameron, A. A.; Andrews, A. M.; Dickey, E. C.; Horn, M. W.; Weiss, P. S. Scanning Electron Microscopy of Nanoscale Chemical Patterns. *ACS Nano* **2007,** *1*, 191–201.

(6) Carlson, A.; Bowen, A. M.; Huang, Y.; Nuzzo, R. G.; Rogers, J. A. Transfer Printing Techniques for Materials Assembly and Micro/Nanodevice Fabrication. *Adv. Mater.* **2012,** *24*, 5284–5318.

(7) Xu, X.; Yang, Q.; Cheung, K. M.; Zhao, C.; Wattanatorn, N.; Belling, J. N.; Abendroth, J. M.; Slaughter, L. S.; Mirkin, C. A.; Andrews, A. M.; Weiss, P. S. Polymer-Pen Chemical Lift-Off Lithography. *Nano Lett.* **2017,** *17*, 3302–3311.

(8) Claridge, S. A.; Liao, W.-S.; Thomas, J. C.; Zhao, Y.; Cao, H. H.; Cheunkar, S.; Serino, A. C.; Andrews, A. M.; Weiss, P. S. From the Bottom Up: Dimensional Control and Characterization in Molecular Monolayers. *Chem. Soc. Rev.* **2013,** *42*, 2725–2745.

(9) Kim, J.; Rim, Y. S.; Chen, H.; Cao, H. H.; Nakatsuka, N.; Hinton, H. L.; Zhao, C.; Andrews, A. M.; Yang, Y.; Weiss, P. S. Fabrication of High-Performance Ultrathin In2O3 Film Field-Effect Transistors and Biosensors Using Chemical Lift-Off Lithography. *ACS Nano* **2015,** *9*, 4572–4582.

(10) Cao, H. H.; Nakatsuka, N.; Serino, A. C.; Liao, W.-S.; Cheunkar, S.; Yang, H.; Weiss, P. S.; Andrews, A. M. Controlled DNA Patterning by Chemical Lift-Off Lithography: Matrix Matters. *ACS Nano* **2015,** *9*, 11439–11454.

(11) Cao, H. H.; Nakatsuka, N.; Liao, W.-S.; Serino, A. C.; Cheunkar, S.; Yang, H.; Weiss, P. S.; Andrews, A. M. Advancing Biocapture Substrates via Chemical Lift-Off Lithography. *Chem. Mater.* **2017,** *29*, 6829–6839.

(12) Abendroth, J. M.; Nakatsuka, N.; Ye, M.; Kim, D.; Fullerton, E. E.; Andrews, A. M.; Weiss, P. S. Analyzing Spin Selectivity in DNA-Mediated Charge Transfer via Fluorescence Microscopy. *ACS Nano* **2017,** *11*, 7516–7526.

(13) Zhao, C.; Xu, X.; Yang, Q.; Man, T.; Jonas, S. J.; Schwartz, J. J.; Andrews, A. M.; Weiss, P. S. Self-Collapse Lithography. *Nano Lett.* **2017,** *17*, 5035–5042.

(14) Butler, S. Z.; Hollen, S. M.; Cao, L.; Cui, Y.; Gupta, J. A.; Gutiérrez, H. R.; Heinz, T. F.; Hong, S. S.; Huang, J.; Ismach, A. F.; Johnston-Halperin, E.; Kuno, M.; Plashnitsa, V. V.; Robinson, R. D.; Ruoff, R. S.; Salahuddin, S.; Shan, J.; Shi, L.; Spencer, M. G.; Terrones, M.; Windl, W.; Goldberger, J. E. Progress, Challenges, and Opportunities in Two-Dimensional Materials Beyond Graphene. *ACS Nano* **2013,** *7*, 2898–2926.

(15) Bhimanapati, G. R.; Lin, Z.; Meunier, V.; Jung, Y.; Cha, J.; Das, S.; Xiao, D.; Son, Y.; Strano, M. S.; Cooper, V. R.; Liang, L.; Louie, S. G.; Ringe, E.; Zhou, W.; Kim, S. S.; Naik, R. R.; Sumpter, B. G.; Terrones, H.; Xia, F.; Wang, Y.; Zhu, J.; Akinwande, D.; Alem, N.; Schuller, J. A.; Schaak, R. E.; Terrones, M.; Robinson, J. A. Recent Advances in Two-Dimensional Materials beyond Graphene. *ACS Nano* **2015,** *9*, 11509–11539.

(16) Zhang, H. Ultrathin Two-Dimensional Nanomaterials. *ACS Nano* **2015,** *9*, 9451–9469.

(17) Tan, C.; Cao, X.; Wu, X.-J.; He, Q.; Yang, J.; Zhang, X.; Chen, J.; Zhao, W.; Han, S.; Nam, G.-H.; Sindoro, M.; Zhang, H. Recent Advances in Ultrathin Two-Dimensional Nanomaterials. *Chem. Rev.* **2017,** *117*, 6225–6331.

(18) Jacoby, M. 2-D Materials go Beyond Graphene. *Chem. Eng. News*, 2017, 36–40.

(19) Kung, L. A.; Kam, L.; Hovis, J. S.; Boxer, S. G. Patterning Hybrid Surfaces of Proteins and Supported Lipid Bilayers. *Langmuir* **2000,** *16*, 6773–6776.

(20) Meitl, M. A.; Zhu, Z.-T.; Kumar, V.; Lee, K. J.; Feng, X.; Huang, Y. Y.; Adesida, I.; Nuzzo, R. G.; Rogers, J. A. Transfer Printing by Kinetic Control of Adhesion to an Elastomeric Stamp. *Nat. Mater.* **2006,** *5*, 33–38.

(21) Hovis, J. S.; Boxer, S. G. Patterning and Composition Arrays of Supported Lipid Bilayers by Microcontact Printing. *Langmuir* **2001,** *17*, 3400–3405.

(22) Wisser, F. M.; Schumm, B.; Mondin, G.; Grothe, J.; Kaskel, S. Precursor Strategies for Metallic Nano- and Micropatterns using Soft Lithography. *J. Mater. Chem. C* **2015,** *3*, 2717–2731.

(23) Rogers, J. A. Nanometer-Scale Printing. *Science* **2012,** *337*, 1459–1460.

(24) Doron-Mor, I.; Barkay, Z.; Filip-Granit, N.; Vaskevich, A.; Rubinstein, I. Ultrathin Gold Island Films on Silanized Glass. Morphology and Optical Properties. *Chem. Mater.* **2004,** *16*, 3476–3483.

(25) Zheng, J.; Zhou, C.; Yu, M.; Liu, J. Different Sized Luminescent Gold Nanoparticles. *Nanoscale* **2012,** *4*, 4073–4083.

(26) Slaughter, L.; Chang, W.-S.; Link, S. Characterizing Plasmons in Nanoparticles and Their Assemblies with Single Particle Spectroscopy. *J. Phys. Chem. Lett.* **2011,** *2*, 2015–2023.

(27) Qin, D.; Xia, Y.; Whitesides, G. M. Soft Lithography for Micro- and Nanoscale Patterning. *Nat. Protoc.* **2010,** *5*, 491–502.

(28) Perdew, J. P.; Burke, K.; Ernzerhof, M. Generalized Gradient Approximation Made Simple. *Phys. Rev. Lett.* **1996,** *77*, 3865–3868.

(29) Enkovaara, J.; Rostgaard, C.; Mortensen, J. J.; Chen, J.; Dułak, M.; Ferrighi, L.; Gavnholt, J.; Glinsvad, C.; Haikola, V.; Hansen, H. A.; Kristoffersen, H. H.; Kuisma, M.; Larsen, A. H.; Lehtovaara, L.; Ljungberg, M.; Lopez-Acevedo, O.; Moses, P. G.; Ojanen, J.; Olsen, T.; Petzold, V.; Romero, N. A.; Stausholm-Møller, J.; Strange, M.; Tritsaris, G. A.; Vanin, M.; Walter, M.; Hammer, B.; Häkkinen, H.; Madsen, G. K. H.; Nieminen, R. M.; Nørskov, J. K.; Puska, M.; Rantala, T. T.; Schiøtz, J.; Thygesen, K. S.; Jacobsen, K. W. Electronic Structure Calculations with GPAW: a Real-Space Implementation of the Projector Augmented-Wave Method. *J. Phys.: Condens. Matter* **2010,** *22*, 253202.

(30) Mortensen, J. J.; Hansen, L. B.; Jacobsen, K. W. Real-Space Grid Implementation of the Projector-Augemented Wave Method. *Phys. Rev. B* **2005,** *71*, 035109.

(31) Bahn, S. R.; Jacobsen, K. W. An Object-Oriented Scripting Interface to a Legacy Electronic Structure Code. *Comput. Sci. Eng.* **2002,** *4*, 56–66.

(32) Guo, Q.; Li, F. Self-Assembled Alkanethiol Monolayers on Gold Surfaces: Resolving the Complex Structure at the Interface by STM. *Phys. Chem. Chem. Phys.* **2014,** *16*, 19074–19090.

(33) Gronbeck, H. The Bonding in Thiolate Protected Gold Nanoparticles from Au 4f Photoemission Core Level Shifts. *Nanoscale* **2012,** *4*, 4178–4182.

(34) Dokukin, M. E.; Sokolov, I. Quantitative Mapping of the Elastic Modulus of Soft Materials with HarmoniX and PeakForce QNM AFM Modes. *Langmuir* **2012,** *28*, 16060–16071.

(35) Lopez, G. P.; Biebuyck, H. A.; Whitesides, G. M. Scanning Electron Microscopy can Form Images of Patterns in Self-Assembled Monolayers. *Langmuir* **1993,** *9*, 1513–1516.

(36) Bittermann, A. G.; Jacobi, S.; Chi, L. F.; Fuchs, H.; Reichelt, R. Contrast Studies on Organic Monolayers of Different Molecular Packing in FESEM and Their Correlation with SFM Data. *Langmuir* **2001,** *17*, 1872–1877.

(37) Mack, N. H.; Dong, R.; Nuzzo, R. G. Quantitative Imaging of Protein Adsorption on Patterned Organic Thin-Film Arrays Using Secondary Electron Emission. *J. Am. Chem. Soc.* **2006,** *128*, 7871–7881.

(38) Kim, E.; Park, K.; Hwang, S. Electrochemical Investigation of Chemical Lift-off Lithography on Au and ITO. *Electrochim. Acta* **2017,** *246*, 165–172.

(39) Slaughter, L. S.; Wang, L.-Y.; Willingham, B. A.; Olson, J. M.; Swanglap, P.; Dominguez-Medina, S.; Link, S. Plasmonic Polymers Unraveled through Single Particle Spectroscopy. *Nanoscale* **2014,** *6*, 11451–11461.

(40) Seaborg, G. T.; Wahl, A. C. The Chemical Properties of Elements 94 and 93. *J. Am. Chem. Soc.* **1948,** *70*, 1128–1134.

(41) Seaborg, G. T. Transuranium Elements: Past, Present, and Future. *Acc. Chem. Res.* **1995,** *28*, 257–264.

(42) Claridge, S. A.; Castleman, A. W.; Khanna, S. N.; Murray, C. B.; Sen, A.; Weiss, P. S. Cluster-Assembled Materials. *ACS Nano* **2009,** *3*, 244–255.

(43) Schwartz, D. K. Mechanisms and Kinetics of Self-Assembled Monolayer Formation *Annu. Rev. Phys. Chem.* **2001,** *52*, 107–137.

(44) Schreiber, F. Structure and Growth of Self-Assembling Monolayers. *Prog. Surf. Sci.* **2000,** *65*, 151–257.

(45) Schoenherr, H.; Vancso, G. J. In *Scanning Force Microscopy of Polymers*; Springer: Heidelberg, Germany, 2010.

(46) Chan, T. F.; Vese, L. Active Contours without Edges. *IEEE Trans. Image Process.* **2001,** *10*, 266.

(47) Zosso, D.; An, J.; Stevick, J.; Takaki, N.; Weiss, M.; Slaughter, L. S.; Cao, H. H.; Weiss, P. S.; Bertozzi, A. L. Image Segmentation with Dynamic Artifacts Detection and Bias Correction. *Inverse Probl Imaging* **2017,** *11*, 577–600.

(48) Zosso, D.; Tran, G.; Osher, S. Non-Local Retinex---A Unifying Framework and Beyond. *SIAM J. Imaging Sci.* **2015,** *8*, 787–826.

(49) Love, J. C.; Estroff, L. A.; Kriebel, J. K.; Nuzzo, R. G.; Whitesides, G. M. Self-Assembled Monolayers of Thiolates on Metals as a Form of Nanotechnology. *Chem. Rev.* **2005,** *105*, 1103–1170.

(50) Zaccari, I.; Catchpole, B. G.; Laurenson, S. X.; Davies, A. G.; Wälti, C. Improving the Dielectric Properties of Ethylene-Glycol Alkanethiol Self-Assembled Monolayers. *Langmuir* **2014,** *30*, 1321–1326.

(51) Kim, D.-J.; Koo, K.-K. Influence of Alkyl Chain Length of Biotin Terminated n-Alkanethiolate SAMs on a Molecular Recognition between Streptavidin and Biotin. *Ind. Eng. Chem. Res.* **2004,** *10*, 920–926.

(52) Biscarini, F.; Bustamante, C.; Kenkre, V. M. Scanning Tunneling Microscopy. II. Calculation of Images of Atomic and Molecular Adsorbates. *Phys. Rev. B* **1995,** *51*, 11089–11102.

(53) Wastl, D. S. Ambient Atomic Resolution Atomic Force Microscopy with qPlus Sensors: Part 1. *Microsc. Res. Tech.* **2017,** *80*, 50–65.

(54) Shuster, M. J.; Vaish, A.; Gilbert, M. L.; Martinez-Rivera, M.; Nezarati, R. M.; Weiss, P. S.; Andrews, A. M. Comparison of Oligo(ethylene glycol)alkanethiols versus n-Alkanethiols: Self-Assembly, Insertion, and Functionalization. *J. Phys. Chem. C* **2011,** *115*, 24778–24787.

(55) Schwartz, J. J.; Hohman, J. N.; Morin, E. I.; Weiss, P. S. Molecular Flux Dependence of Chemical Patterning by Microcontact Printing. *ACS Appl. Mater. Interfaces* **2013,** *5*, 10310–10316.

(56) Stranick, S. J.; Parikh, A. N.; Allara, D. L.; Weiss, P. S. A New Mechanism for Surface Diffusion: Motion of a Substrate-Adsorbate Complex. *J. Phys. Chem.* **1994,** *98*, 11136–11142.

(57) Chaudhuri, A.; Lerotholi, T. J.; Jackson, D. C.; Woodruff, D. P.; Dhanak, V. Local Methylthiolate Adsorption Geometry on Au(111) from Photoemission Core-Level Shifts. *Phys. Rev. Lett.* **2009,** *102*, 126101.

(58) Xue, Y.; Li, X.; Li, H.; Zhang, W. Quantifying Thiol–Gold Interactions Towards the Efficient Strength Control. *Nat. Commun.* **2014,** *5*, 1–9.

(59) Huang, Z.; Chen, F.; Bennett, P. A.; Tao, N. Single Molecule Junctions Formed via Au−Thiol Contact: Stability and Breakdown Mechanism. *J. Am. Chem. Soc.* **2007,** *129*, 13225–13231.

(60) Frei, M.; Aradhya, S. V.; Hybertsen, M. S.; Venkataraman, L. Linker Dependent Bond Rupture Force Measurements in Single-Molecule Junctions. *J. Am. Chem. Soc.* **2012,** *134*, 4003–4006.

(61) Azubel, M.; Koivisto, J.; Malola, S.; Bushnell, D.; Hura, G. L.; Koh, A. L.; Tsunoyama, H.; Tsukuda, T.; Pettersson, M.; Häkkinen, H.; Kornberg, R. D. Electron Microscopy of Gold Nanoparticles at Atomic Resolution. *Science* **2014,** *345*, 909–912.

(62) Jadzinsky, P. D.; Calero, G.; Ackerson, C. J.; Bushnell, D. A.; Kornberg, R. D. Structure of a Thiol Monolayer-Protected Gold Nanoparticle at 1.1 Å Resolution. *Science* **2007,** *318*, 430–433.

(63) Maksymovych, P.; Sorescu, D. C.; Yates, J. T. Gold-Adatom-Mediated Bonding in Self-Assembled Short-Chain Alkanethiolate Species on the Au(111) Surface. *Phys. Rev. Lett.* **2006,** *97*, 146103.

(64) Wang, Y.; Chi, Q.; Hush, N. S.; Reimers, J. R.; Zhang, J.; Ulstrup, J. Scanning Tunneling Microscopic Observation of Adatom-Mediated Motifs on Gold–Thiol Self-Assembled Monolayers at High Coverage. *J. Phys. Chem. C* **2009,** *113*, 19601–19608.

(65) Vericat, C.; Vela, M. E.; Salvarezza, R. C. Self-Assembled Monolayers of Alkanethiols on Au(111): Surface Structures, Defects and Dynamics. *Phys. Chem. Chem. Phys.* **2005,** *7*, 3258–3268.

(66) Alaee, R.; Menzel, C.; Huebner, U.; Pshenay-Severin, E.; Bin Hasan, S.; Pertsch, T.; Rockstuhl, C.; Lederer, F. Deep-Subwavelength Plasmonic Nanoresonators Exploiting Extreme Coupling. *Nano Lett.* **2013,** *13*, 3482–3486.

(67) Hohman, J. N.; Zhang, P.; Morin, E. I.; Han, P.; Kim, M.; Kurland, A. R.; McClanahan, P. D.; Balema, V. P.; Weiss, P. S. Self-Assembly of Carboranethiol Isomers on Au{111}: Intermolecular Interactions Determined by Molecular Dipole Orientations. *ACS Nano* **2009,** *3*, 527–536.

(68) Stranick, S. J.; Parikh, A. N.; Tao, Y. T.; Allara, D. L.; Weiss, P. S. Phase Separation of Mixed-Composition Self-Assembled Monolayers into Nanometer Scale Molecular Domains. *J. Phys. Chem.* **1994,** *98*, 7636–7646.

(69) Smith, R. K.; Reed, S. M.; Lewis, P. A.; Monnell, J. D.; Clegg, R. S.; Kelly, K. F.; Bumm, L. A.; Hutchison, J. E.; Weiss, P. S. Phase Separation within a Binary Self-Assembled Monolayer on Au{111} Driven by an Amide-Containing Alkanethiol. *J. Phys. Chem. B* **2001,** *105*, 1119–1122.

(70) Hohman, J. N.; Thomas, J. C.; Zhao, Y.; Auluck, H.; Kim, M.; Vijselaar, W.; Kommeren, S.; Terfort, A.; Weiss, P. S. Exchange Reactions Between Alkanethiolates and Alkaneselenols on Au{111}. *J. Am. Chem. Soc.* **2014,** *136*, 8110–8121.

(71) Monnell, J. D.; Stapleton, J. J.; Jackiw, J. J.; Dunbar, T.; Reinerth, W. A.; Dirk, S. M.; Tour, J. M.; Allara, D. L.; Weiss, P. S. Ordered Local Domain Structures of Decaneselenolate and Dodecaneselenolate Monolayers on Au{111}. *J. Phys. Chem. B* **2004,** *108*, 9834–9841.

(72) Ribas-Arino, J.; Marx, D. Covalent Mechanochemistry: Theoretical Concepts and Computational Tools with Applications to Molecular Nanomechanics. *Chem. Rev.* **2012,** *112*, 5412–5487.

(73) Seema, P.; Behler, J.; Marx, D. Peeling by Nanomechanical Forces: A Route to Selective Creation of Surface Structures. *Phys. Rev. Lett.* **2015,** *115*, 036102.

(74) Chai, J.; Wong, L. S.; Giam, L.; Mirkin, C. A. Single-Molecule Protein Arrays Enabled by Scanning Probe Block Copolymer Lithography. *Proc. Natl. Acad. Sci. U.S.A.* **2011,** *108*, 19521–19525.

(75) Cerf, A.; Cipriany, B. R.; Benítez, J. J.; Craighead, H. G. Single DNA Molecule Patterning for High-Throughput Epigenetic Mapping. *Anal. Chem.* **2011,** *83*, 8073–8077.

(76) Levy-Sakin, M.; Grunwald, A.; Kim, S.; Gassman, N. R.; Gottfried, A.; Antelman, J.; Kim, Y.; Ho, S. O.; Samuel, R.; Michalet, X.; Lin, R. R.; Dertinger, T.; Kim, A. S.; Chung, S.; Colyer, R. A.; Weinhold, E.; Weiss, S.; Ebenstein, Y. Toward Single-Molecule Optical Mapping of the Epigenome. *ACS Nano* **2013,** *8*, 14–26.

(77) Kartalov, E. P.; Quake, S. R. Microfluidic Device Reads Up to Four Consecutive Base Pairs in DNA Sequencing-by-Synthesis. *Nucleic Acids Res.* **2004,** *32*, 2873–2879.

(78) Sun, Y.; Perch-Nielsen, I.; Dufva, M.; Sabourin, D.; Bang, D. D.; Høgberg, J.; Wolff, A. Direct Immobilization of DNA Probes on Non-Modified Plastics by UV Irradiation and Integration in Microfluidic Devices for Rapid Bioassay *Anal. Bioanal. Chem.* **2012,** *402*, 741–748.

(79) Trappmann, B.; Gautrot, J. E.; Connelly, J. T.; Strange, D. G. T.; Li, Y.; Oyen, M. L.; Cohen Stuart, M. A.; Boehm, H.; Li, B.; Vogel, V.; Spatz, J. P.; Watt, F. M.; Huck, W. T. S. Extracellular-Matrix Tethering Regulates Stem-Cell Fate. *Nat. Mater.* **2012,** *11*, 642–649.

(80) Bai, H.-J.; Shao, M.-L.; Gou, H.-L.; Xu, J.-J.; Chen, H.-Y. Patterned Au/Poly(dimethylsiloxane) Substrate Fabricated by Chemical Plating Coupled with Electrochemical Etching for Cell Patterning. *Langmuir* **2009,** *25*, 10402–10407.

(81) Tseng, P.; Di Carlo, D. Substrates with Patterned Extracellular Matrix and Subcellular Stiffness Gradients Reveal Local Biomechanical Responses. *Adv. Mater.* **2014,** *26*, 1242–1247.

(82) Tseng, P.; Pushkarsky, I.; Di Carlo, D. Metallization and Biopatterning on Ultra-Flexible Substrates via Dextran Sacrificial Layers. *PLoS One* **2014,** *9*, e106091.

(83) Heyries, K. A.; Marquette, C. A.; Blum, L. J. Straightforward Protein Immobilization on Sylgard 184 PDMS Microarray Surface. *Langmuir* **2007,** *23*, 4523–4527.

(84) Chen, C. S.; Mrksich, M.; Huang, S.; Whitesides, G. M.; Ingber, D. E. Geometric Control of Cell Life and Death. *Science* **1997,** *276*, 1425–1428.

(85) Chen, Y.; Kung, S.-C.; Taggart, D. K.; Halpern, A. R.; Penner, R. M.; Corn, R. M. Fabricating Nanoscale DNA Patterns with Gold Nanowires. *Anal. Chem.* **2010,** *82*, 3365–3370.

(86) Hou, X.; Zhang, Y. S.; Santiago, G. T.-d.; Alvarez, M. M.; Ribas, J.; Jonas, S. J.; Weiss, P. S.; Andrews, A. M.; Aizenberg, J.; Khademhosseini, A. Interplay Between Materials and Microfluidics. *Nat. Rev. Mater.* **2017,** *2*, 17016.

(87) Thomas, J. C.; Boldog, I.; Auluck, H. S.; Bereciartua, P. J.; Dušek, M.; Macháček, J.; Bastl, Z.; Weiss, P. S.; Baše, T. Self-Assembled p-Carborane Analogue of p-Mercaptobenzoic Acid on Au{111}. *Chem. Mater.* **2015,** *27*, 5425–5435.

(88) Thomas, J. C.; Schwartz, J. J.; Hohman, J. N.; Claridge, S. A.; Auluck, H. S.; Serino, A. C.; Spokoyny, A. M.; Tran, G.; Kelly, K. F.; Mirkin, C. A.; Gilles, J.; Osher, S. J.; Weiss, P. S. Defect-Tolerant Aligned Dipoles within Two-Dimensional Plastic Lattices. *ACS Nano* **2015,** *9*, 4734-4742.

(89) Kim, M.; Hohman, J. N.; Serino, A. C.; Weiss, P. S. Structural Manipulation of Hydrogen-Bonding Networks in Amide-Containing Alkanethiolate Monolayers via Electrochemical Processing. *J. Phys. Chem. C* **2010,** *114*, 19744–19751.

(90) Thomas, J. C.; Goronzy, D. P.; Dragomiretskiy, K.; Zosso, D.; Gilles, J.; Osher, S. J.; Bertozzi, A. L.; Weiss, P. S. Mapping Buried Hydrogen-Bonding Networks. *ACS Nano* **2016,** *10*, 5446–5451.

CHAPTER IV

Chemical Lift-Off Lithography of Metal and Semiconductor Surfaces

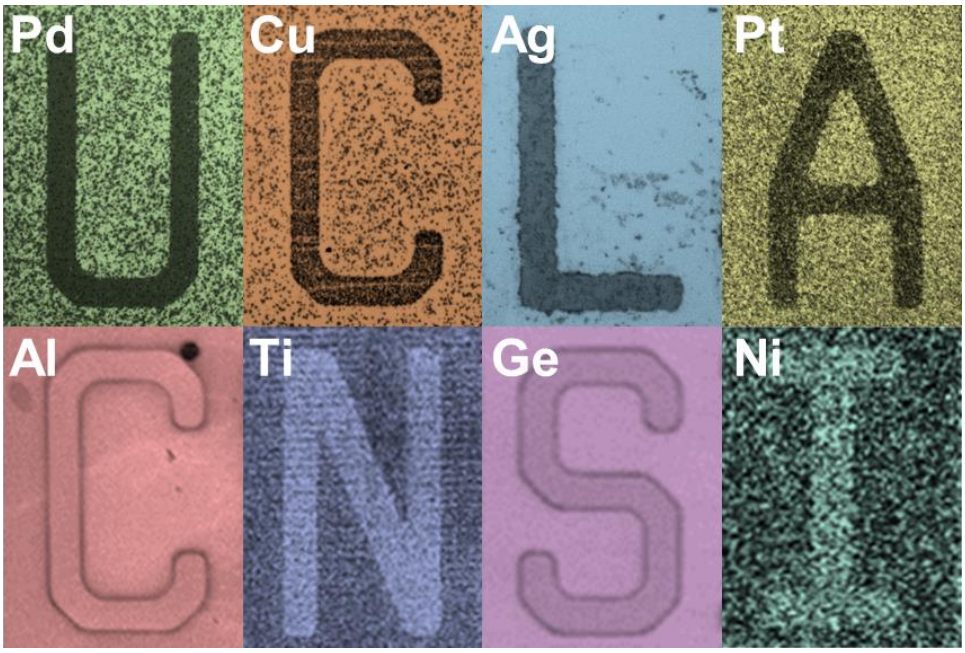

The information in this chapter was published in
ACS Materials Letters **2019**, *2*, 76–83
and has been reproduced here with permission.

Authors: **Cheung, K. M.**; Stemer, D. M.; Zhao, C.; Young T. D.; Belling, J. N.; Andrews, A. M.; Weiss, P. S.

IV.A. Introduction

Molecular self-assembled monolayers (SAMs) on surfaces are versatile systems for investigating and tailoring surface, interfacial, and environmental interactions.[1-5] There are a variety of SAM molecules with differing head and tail group functionalities that can be tuned to bind (covalently and noncovalently) and to interact with specific surfaces, with alkanethiol monolayers on Au surfaces representing a commonly used and well-studied system.[6-9] The patterning of alkanethiolate SAMs on metal surfaces imparts an additional level of control and dimension into these systems, which has led to a multitude of applications in surface science and nanotechnology.[1,2,4,6,10-12]

Molecular monolayers can be patterned *via* conventional lithographic techniques (*e.g.*, photolithography),[13,14] but are more commonly patterned using low-cost and high-throughput soft-lithographic methods.[2,3,15,16] Conventional soft lithography (*e.g.*, microcontact printing, μCP), involves the additive patterning of SAM molecules onto surfaces by transfer of molecular inks *via* contact of patterned polydimethylsiloxane (PDMS) stamps with the corresponding surfaces.[17-22] While μCP has significantly advanced the field of SAM patterning, it is inherently limited in the resolution of features produced due to lateral diffusion of ink molecules during and after the patterning is performed.[19,21-24] Advances in soft lithography have improved feature resolution[12-14,25,26] (*e.g.*, polymer pen lithography[27] and microdisplacement printing).[11]

In contrast to abundant additive patterning methods, chemical lift-off lithography (CLL) is a *subtractive* soft-lithographic strategy.[28,29] Here, alkanethiol molecules, with exposed functional tail groups (*e.g.*, -OH, -COOH, -NH_2), in preformed SAMs are removed from

Au surfaces only in areas contacted by patterned PDMS stamps.[28-30] Notably, as a result of the CLL process, Au atoms are transferred to the PDMS stamps.[28,29,31] Chemical lift-off lithography enables high-fidelity patterning of SAMs over a wide range of feature sizes (nanometer to millimeter).[28,29,32-34] This patterning process has inspired and enabled diverse applications including the patterning of bioactive molecules,[30,32,35-39] supported gold monolayers,[31] and the facile fabrication of field-effect transistor arrays.[40,41]

Nonetheless, CLL has been primarily used to pattern alkanethiol monolayers on Au surfaces, with the patterning of other coinage, transition, and reactive metal, semiconductor, and metal oxide surfaces representing potentially unexplored areas of interest.[28,42,43] The formation and patterning of alkanethiolate SAMs on other coinage metal surfaces (*e.g.*, Ag, Cu, Pd) have been previously demonstrated using μCP.[6,8,44-52] Alkanthiolate SAMs on transition and reactive metal surfaces are less studied as the reactivity of these surfaces typically leads to the formation of passivating metal oxide layers that hinders additive SAM patterning.[53-57] For subtractive patterning, such as CLL, the entire substrate surface is first functionalized with a SAM, and thus passivated preventing surface oxide formation prior to patterning.[28] Straightforward and direct self-assembly and patterning of molecules on reactive surfaces may be beneficial for a variety of systems including the investigation of spin-selectivity in molecular assemblies on ferromagnetic surfaces,[36,58] patterning of metal-oxide semiconductors for transistor and biosensor applications,[41,59,60] and growth of two-dimensional materials (*e.g.*, graphene nanoribbons).[61,62]

Herein, we extend CLL as a technique to pattern alkanethiolate SAMs on different coinage metals (Pt, Pd, Ag, Cu), transition and reactive metals (Ni, Ti, Al), and a

semiconductor (Ge). Using the patterned monolayers as molecular resists, we demonstrate pattern transfer to underlying metal substrates *via* wet etching. In all cases, we show that corresponding supported (mono)layers of substrate atoms are removed during the CLL process. Moreover, we can form atomic blends of mixed metal monolayers on PDMS stamp surfaces. These findings illustrate that CLL is a versatile technique for economical and high-throughput patterning of a multitude of different material surfaces using straightforward alkanethiol self-assembly.

IV.B. Experimental Methods

IV.B.1. Materials

Prime quality 4″ Si{100} wafers (P/B, 0.001-0.005 Ω-cm, thickness 500 μm) were purchased from Silicon Valley Microelectronics, Inc. (Santa Clara, CA, USA). Sylgard 184® silicone elastomer kits (lot #0008823745) were purchased from Ellsworth Adhesives (Germantown, WI, USA). 11-Mercapto-1-undecanol (MUO) was purchased from Sigma Aldrich.

IV.B.2. Chemical Lift-Off Lithography

Metal and semiconductor surfaces were prepared *via* electron-beam evaporation (Kurt J. Lesker Company, Jefferson Hills, PA or CHA Industries, SOLUTION, Fremont, CA) onto Si substrates. Self-assembled monolayers of MUO were formed on metal surfaces *via* immersion in 5 mM ethanolic solutions for 24 h. For reactive metal surfaces (*e.g.*, Cu, Ni, Ti, Al), substrates were immersed in degassed MUO solutions immediately after metal evaporation to minimize metal oxide formation. For Ge, SAMs were formed *via* immersion into a 1:1 (v/v) ethanol:water solution of MUO. Chemical lift-off lithography was performed as previously reported,[28,31] where surfaces were contacted with patterned or featureless

oxygen-plasma-activated PDMS stamps for 24 h, after which the stamps were removed. To form supported bimetallic monolayers, featureless PDMS stamps were brought into contact with functionalized Au surfaces for 1 h and then functionalized Ag surfaces for an additional 1 h immediately after lift-off from Au surfaces.

IV.B.3. Scanning Electron Microscopy

Scanning electron microscopy images were obtained using a Zeiss Supra 40VP scanning electron microscope with an Inlens secondary electron detector. Surfaces were imaged immediately after CLL. Accelerating voltages were adjusted for each metal surface to produce optimal contrast: 1 kV for Ni, Ti, and Al; 1.5 kV for Pt; 2 kV for Pd, Ag, and Cu; and 3 kV for Ge. Working distances were optimized for each image. Modulating accelerating voltages and working distances affects the contrast observed for patterned SAMs.[23] Images were processed *via* polynomial background subtraction using Gwyddion[63] and contrast limited adaptive histogram equalization in MATLAB.[64]

IV.B.4. Metal Etching

Patterned metal surfaces were etched with corresponding chemical wet etchants: Pt with concentrated *aqua regia* (3:1 v/v 12.1 M HCl:15.6 M HNO_3) for 20 min,[65] Pd with a solution of 0.2 M $K_2Cr_2O_7$ and 0.5 M HCl in 40% aqueous H_3PO_4 for 6 min,[66] Ag with an aqueous 25 mM $FeNO_3$ solution for 15 min,[51] and Cu with an aqueous 12 mM $FeCl_3$ solution for 30 s.[52]

IV.B.5. X-Ray Photoelectron Spectroscopy

X-ray photoelectron spectroscopy of PDMS surfaces post-CLL was carried out using an AXIS Ultra DLD photoelectron spectrometer (Kratos Analytical Inc., Chestnut Ridge, NY) and a monochromatic Al K_α X-ray source with a 200 μm circular spot size in ultrahigh vacuum (10^{-9} Torr). High-resolution spectra of Au 4f, Pt 4f, Pd 3d, Ag 3d, Cu 2p, Ni 2p, Ti 2p, Al 2p,

and Ge 3d regions were acquired at a pass energy of 20 eV using a 300 ms dwell time. For all scans, 15 kV was applied with an emission of 15 mA. An average of 30 scans were collected for each of the high-resolution spectra. Note, all spectra were collected under charge neutralization conditions (*i.e.*, electron flood gun)[58] to prevent charging of sample surfaces. Charge neutralization results in shifts of binding energy values.

IV.B.6. Atomic Force Microscopy

Patterned Ge surfaces after chemical lift-off lithography were imaged *via* atomic force microscopy using a Dimension Icon scanning probe microscope (Bruker, Billerica, MA). Surface topographies were measured using the PeakForce Quantitative Nanomechanical Property Mapping (PeakForce QNM) mode. ScanAsyst-Air cantilevers (Bruker, spring constant = 0.4 ± 0.1 N m^{-1}) were calibrated with a clean piece of silicon wafer before every measurement. A peak-force set-point of 400 pN and a scan rate of 1 Hz was maintained for all measurements.

IV.C. Results and Discussion

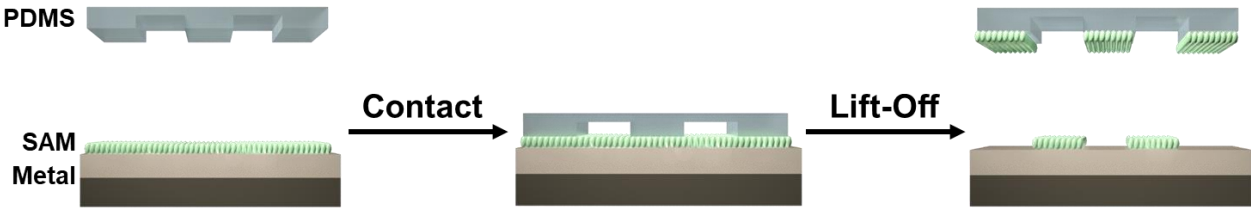

Figure IV.1. General scheme for chemical lift-off lithography. An oxygen-plasma-activated polydimethylsiloxane (PDMS) stamp is brought into contact with a metal or semiconductor surface functionalized with a self-assembled monolayer (SAM), in this case, 11-mercapto-1-undecanol. Lift-off of the PDMS stamp removes SAM molecules only in the contacted regions, patterning remaining SAMs on the substrate surfaces.

A schematic of the CLL process is shown in **Figure IV.1**. Patterned oxygen-plasma-activated PDMS stamps were brought into contact with SAMs of MUO on metal[28] or semiconductor surfaces. Stamp contact enabled removal of SAM molecules in the contacted substrate areas. We first investigated coinage metals besides Au used in our previous studies (*i.e.*, Pt, Pd, Ag, Cu). Self-assembled monolayers of alkanethiolates have been shown to form on other coinage metals;[44-46,49,67,68] thus, we predicted that CLL could be used to pattern these additional metal surfaces.

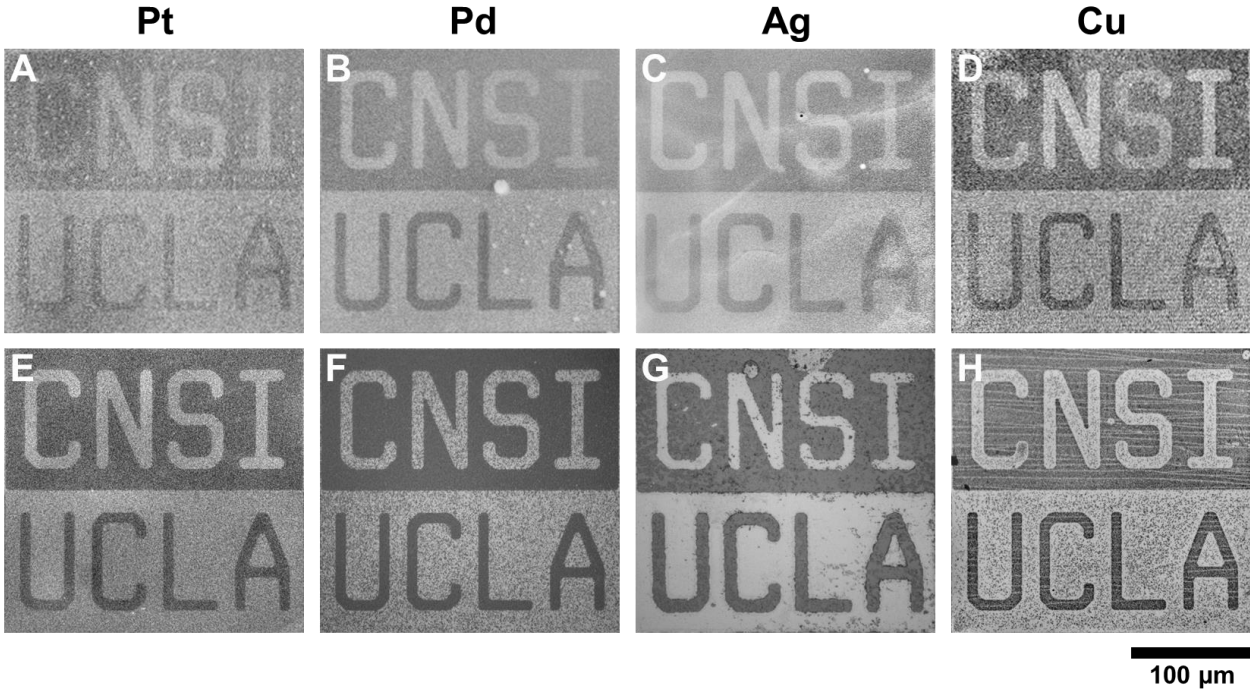

Figure IV.2. Chemical lift-off lithography (CLL) of coinage metal (Pt, Pd, Ag, Cu) surfaces. Metals are ordered in terms of increasing reactivity from left to right. **(A-D)** Representative scanning electron microscopy images of patterned self-assembled monolayers (SAMs) of 11-mercapto-1-undecanol (MUO) on metal surfaces after CLL. Monolayers were patterned such that MUO molecules remained in the "CNSI" letter regions and in the regions surrounding the "UCLA" letters. **(E-H)** Representative optical microscopy images of metal surfaces after chemical wet etching using the patterned SAMs as molecular resists.

Monolayers on metal surfaces were imaged using scanning electron microscopy (SEM) after patterning by CLL. Scanning electron micrographs of Pt, Pd, Ag, and Cu surfaces contacted by "CNSI/UCLA" patterned PDMS stamps showed evidence of negative features in MUO monolayers corresponding to the features of the stamp (**Figures IV.2A-D, IV.S1**). Features did not show evidence of broadening associated with lateral diffusion of MUO after patterning,[23] similar to the case of CLL on Au.[33]

Patterned monolayers on metal surfaces after CLL act as molecular resists to facilitate fabrication of metal nano/microstructures *via* chemical wet etching.[28,31,34,40,41] To demonstrate the functionality and resolution of the patterned SAMs, and to confirm that molecules were removed *via* CLL, we exposed patterned metal surfaces to chemical etchants selective for Pt, Pd, Ag, and Cu, respectively (see **Experimental Methods**).[47,48,51,52,65,69] In all cases, metal regions were selectively etched in regions corresponding to areas of SAM removal by CLL, transferring the pattern of the monolayer to the metal substrate (**Figure IV.2E-H**). We expect that not all SAM molecules are removed *via* CLL (*ca.* 70% for Au),[28] however sufficient numbers of molecules were removed from all coinage metal surfaces to facilitate selective etching of underlying metals in the lifted-off areas.

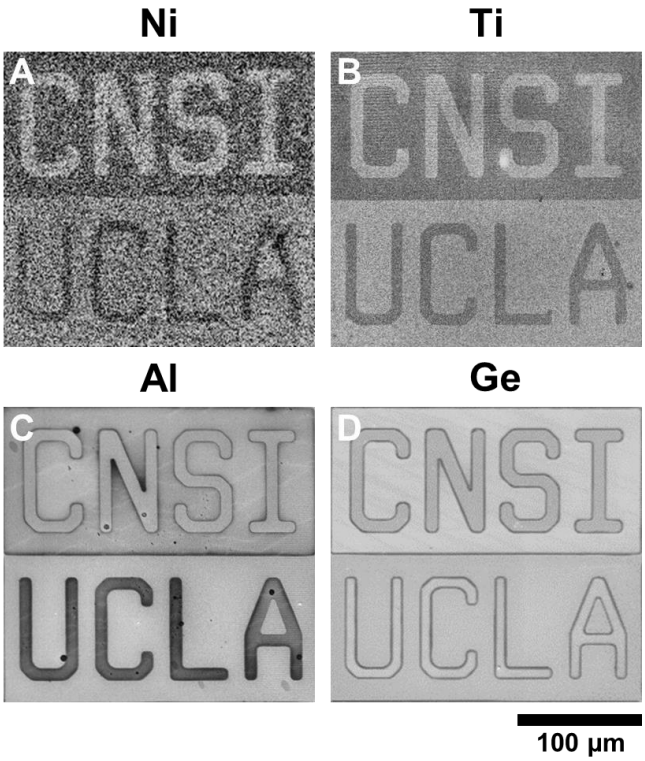

Figure IV.3. Chemical lift-off lithography (CLL) of transition or reactive metal and semiconductor surfaces. **(A-D)** Representative scanning electron microscopy images of patterned self-assembled monolayers of 11-mercapto-1-undecanol on the metal surfaces (Ni, Ti, Al) and a semiconductor surface (Ge) after CLL. Stamps with the same features as **Figure IV.2** were used.

Following the observations of coinage metal patterning, we explored extending CLL to transition and reactive metal surfaces (*i.e.*, Ni, Ti, Al), upon which alkanethiolate monolayers can be formed.[53-55] To prevent formation of surface oxides, substrates were immersed into degassed ethanolic MUO solutions to form SAMs immediately after metal evaporation. Since CLL removes regions of preformed SAMs, transition metal surfaces can be patterned straightforwardly without additional surface treatments (*i.e.*, metal oxide etching).[70] Oxide etching roughens metal surfaces,[71] whereas other methods for patterning transition metals, such as SAM displacement, limit the types of molecules that can be patterned (*i.e.*, molecules that are easily displaceable).[11] Transition metal surfaces

characterized using SEM indicated that SAMs on these surfaces were patterned using CLL (**Figures IV.3A-C, IV.S1**).

We performed CLL on Ge surfaces, a semiconductor that can be functionalized with alkanethiols *via* covalent Ge-S bonds,[71-74] to extend the lithographic capabilities of CLL beyond metals (**Figure IV.3D, IV.S1**). Direct patterning of molecules on semiconductor surfaces would foreseeably enable a myriad of applications for semiconductor device processing. For example, local work functions in patterned regions of semiconducting substrates might be tuned for band bending and alignment purposes.[75,76]

We noticed that the contrast observed *via* SEM for the patterned SAMs appears to differ for the different surfaces in **Figures IV.2 and IV.3**. The levels of contrast in SEM for patterned SAMs is related to a variety of factors, including SAM densities and order, as well as the accelerating voltage and working distance of the electron beam during image acquisition.[23,27,31] Given the rapidity of metal oxide formation, we expect that SAMs formed on reactive metal surfaces are not as highly ordered as on coinage metals; trace metal oxides on the former would affect SAM formation.[46,53-57] Differences in SAM formation (*i.e.*, order and density), and thus differences in CLL yield, could contribute to observed differences in contrast. Additionally, formation of oxides in regions of removed SAM molecules after CLL could alter SEM contrast due to differential charging effects.[77-79] Atomic force microscopy images of patterned SAMs on Ge surfaces showed the expected topographies of monolayers of MUO (**Figure IV.S2**),[28,31] suggesting that the contrast observed for Ge *via* SEM is mainly an effect of surface compositional differences arising from the patterned SAMs and potentially differential charging effects on the semiconducting surfaces.

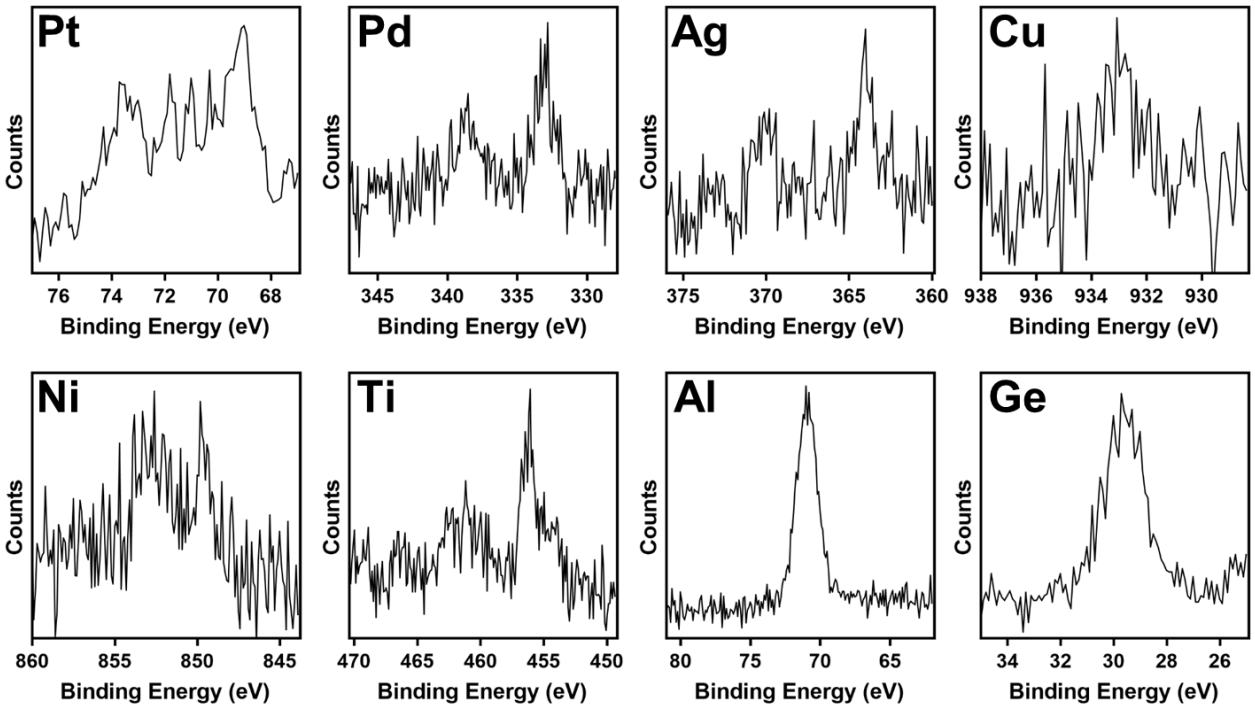

Figure IV.4. X-ray photoelectron spectroscopy (XPS) analysis of polydimethylsiloxane (PDMS) stamps after chemical lift-off lithography on Pt, Pd, Ag, Cu, Ni, Ti, Al, and Ge surfaces. Featureless PDMS stamps and XPS were used to investigate the presence of corresponding substrate atoms on the PDMS stamps, demonstrating that layers of substrate atoms are removed in the lift-off process, either nominal monolayers, or in some cases, potentially thicker layers.

To analyze whether substrate molecules were removed during CLL for the metal and semiconductor surfaces investigated herein, similar to previously studied Au substrates,[28,31] X-ray photoelectron spectroscopy (XPS) was performed on PDMS stamps post-CLL. In all cases, characteristic peaks corresponding to the metal or semiconductor substrate atoms were observed (**Figure IV.4**), demonstrating that layers of substrate atoms were removed by CLL from all surface types. In some cases, it appeared that layers greater than monolayer were removed (based on the differences in contrast observed in **Figure IV.3**, large signal-to-noise differences observed in the XPS spectra in **Figure IV.4**, and the relative elemental

sensitivities given in Table S1), similar to transfer printing techniques demonstrated by Rogers and others.[80-83]

We previously hypothesized that removal of Au atoms during CLL was partly due to the formation of covalent linkages between the PDMS stamp and SAM molecules, as well as formation of Au-alkanthiolate complexes that weaken the bond strengths between the outermost Au substrate atoms and the underlying Au substrate atoms.[28,31,84] For all elemental substrates tested in this report, the metal-sulfur bonds are stronger than the metal-metal bonds.[85] The energetics of these systems suggest that contributions from differences in bond enthalpies play roles in the removal of the outermost layer(s) of substrate atoms, in addition to adatom formation observed in some monolayer systems.[86] In sum, CLL can be used as a facile top-down method of fabricating and patterning supported metal[62] and semiconductor monolayer materials (*e.g.*, germanane)[87] on flexible and transparent polymer supports such as PDMS.

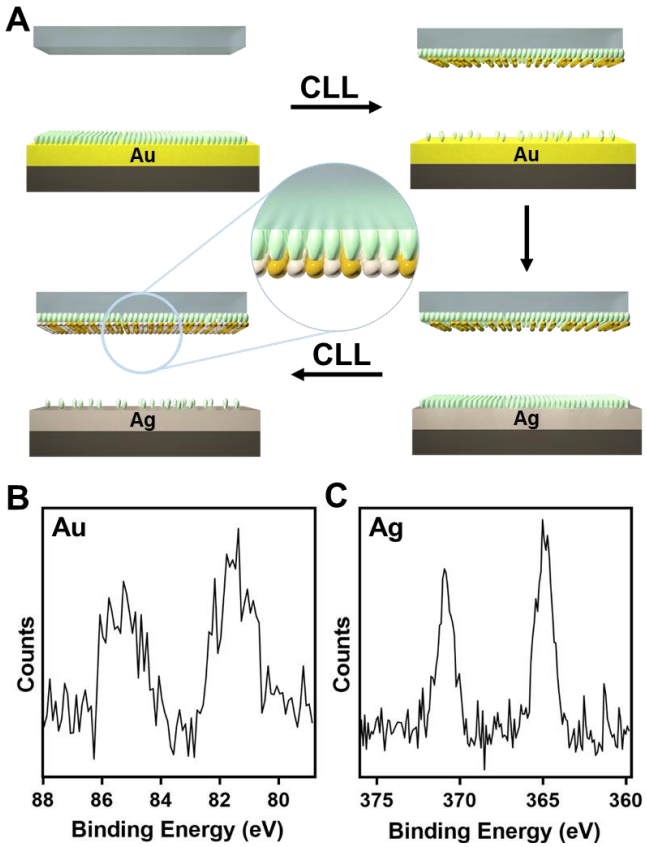

Figure IV.5. Sequential chemical lift-off lithography (CLL) of two different metals (Au, Ag) onto the same polydimethylsiloxane (PDMS) stamp. **(A)** Schematic illustration of the sequential CLL process. **(B,C)** X-ray photoelectron spectra of the PDMS stamp after the sequential CLL process showed characteristic peaks of both metals on the same stamp, demonstrating that both metals are "lifted-off" onto the PDMS stamp forming a supported mixed metal monolayer.

An advantage of soft lithography is the ability to perform multiple patterning steps to create straightforwardly complex multicomponent patterns.[12,28,39,88] To demonstrate patterning of multiple metals on the same PDMS support with CLL, we investigated the formation of bimetallic layers on PDMS stamps. Previous reports indicated that the PDMS is still activated after a single CLL step (and up to ~5 successive CLL steps using the same stamp on different surfaces.[28,31,42,89] We performed two successive CLL steps on two different metal surfaces (Au and Ag, respectively) using the *same* activated PDMS stamp (**Figure IV.5A**). X-ray photoelectron spectroscopy of the PDMS stamp after the sequential CLL process showed

peaks corresponding to both Au and Ag, demonstrating the formation of mixed-metal monolayers supported on PDMS (**Figure IV.5B-C**). Atomically blended bimetallic monolayers represent a new class of materials with unexplored properties and potential applications (*e.g.*, catalysis),[62,90] which can be fabricated straightforwardly using CLL.

IV.D. Conclusions and Prospects

In this study, SAMs of the same type of alkanthiolate molecule (MUO) were straightforwardly formed on different metal and semiconductor surfaces. Chemical lift-off lithography is not limited to the surfaces or SAM molecules studied herein;[29,31] presumably, any surface that can be functionalized with molecular monolayers (*e.g.*, metals,[70,91-93] semiconductors,[94] transition metal dichalcogenides)[95] could be patterned with CLL. Performing CLL with molecules containing additional functionalities within the alkyl backbone (*e.g.*, hydrogen-bonding interactions)[96] or functionalized cage molecules (*e.g.*, carboranethiolates),[97-99] which form relatively defect-free monolayers and can have a range of bond densities between the monolayer and substrate, may have significant effects on the overall efficiencies of CLL.

Monolayers formed on reactive metal surfaces are likely not well ordered due to trace metal oxide formation, yet they can be patterned with CLL. Changing the head group functionality of the SAM molecules to something that binds favorably to surface oxides (*e.g.*, phosphonic acids)[100] can enable the direct patterning of metal oxide surfaces.[42] However, CLL with these types of SAMs, in which the head group is not bound directly to the metal, would be hypothesized not to remove surface metal atoms in the lift-off process but instead, break the weakest bonds in the molecules constituting the SAM.[42]

We previously investigated the nanoscale structure and function of supported Au monolayers on PDMS fabricated with CLL and showed that these Au monolayers are ultrathin and optically transparent, yet they retain the chemical functionality of Au.[31] Accordingly, ultrathin monolayers fabricated from other metal and semiconductor surfaces may have chemical and physical properties that can be differentially exploited compared to bulk materials (*e.g.*, magnetism, Ni,[101] semiconductor, Ge).[87] Furthermore, functional metal monolayers could be used as supports for additional structural growth, enabling patterning of a diverse range of materials (*e.g.*, nanoparticles,[102,103] surface-tethered metal-organic frameworks and multilayers,[104-106] and metal-organic chalcogenolate assemblies)[107] on flexible and transparent substrates. Capabilities to create bimetallic and multi-metallic layers and monolayers with CLL adds an additional level of control to the generation and tailoring of supported metal monolayers with designed properties.

Collectively, we demonstrate CLL as a patterning technique that can be used to pattern SAMs on a variety of metal and semiconductor surfaces. Here, high-fidelity patterns of SAMs were generated on coinage, transition, and reactive metal, and semiconductor surfaces beyond Au. Patterned substrates were used as molecular resists for chemical wet etching to produce three-dimensional features. For all surfaces tested, XPS revealed the removal of corresponding substrate atoms during the CLL process. Moreover, reactive and reusable PDMS stamps enable the formation of bimetallic monolayers supported on PDMS by performing two sequential CLL steps on different substrates. Thus, we extend CLL to pattern a variety of surfaces straightforwardly with applications towards the fabrication and study of new materials and systems.

IV.E. Supplementary Materials

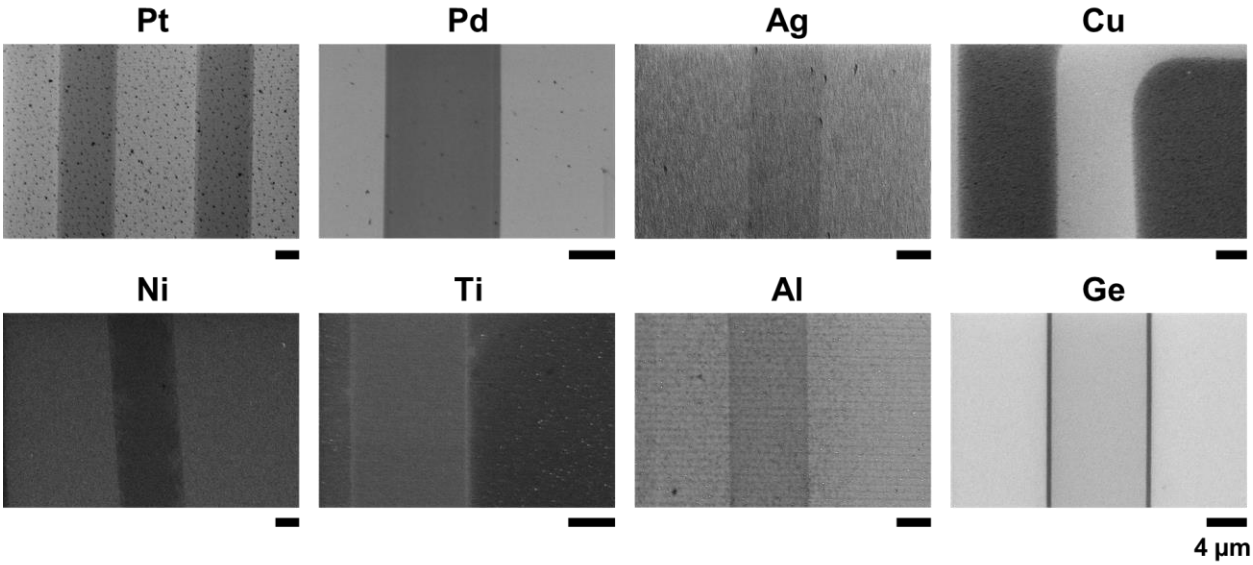

Figure IV.S1. Representative high magnification scanning electron microscope images of patterned self-assembled monolayers of 11-mercapto-1-undecanol (MUO) on metal and semiconductor surfaces after chemical lift-off lithography corresponding to main text **Figures IV.2**, **IV.3**. Regions where MUO was removed appear darker in contrast for Pt, Pd, Ag, Ni, Ti, and Al and brighter in contrast for Cu and Ge in these images. Scale bars are 4 µm for all images.

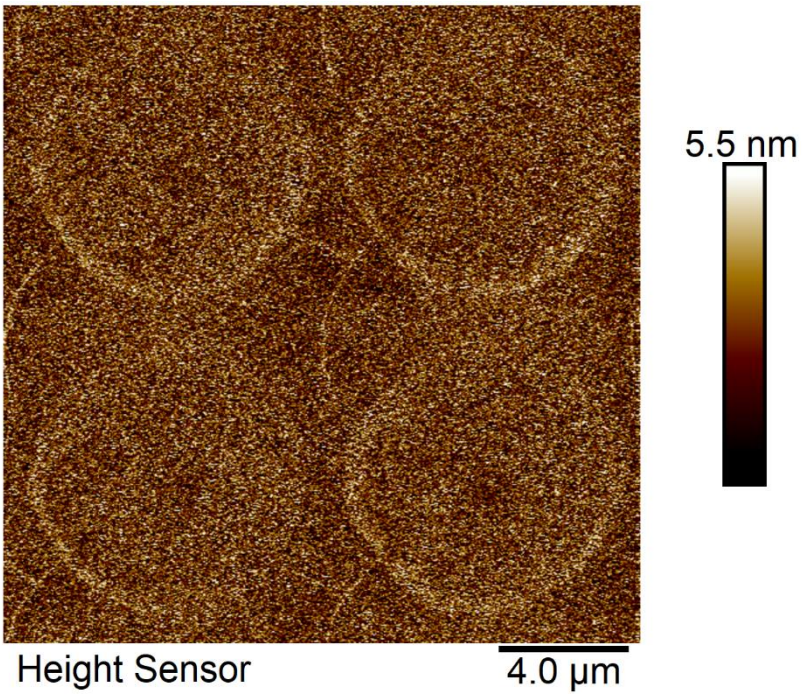

Figure IV.S2. Representative atomic force microscopy image of a patterned (7.5 µm circles) self-assembled monolayer of 11-mercapto-1-undecanol on Ge after chemical lift-off lithography.

XPS Peak	Relative Sensitivity Factor
Pt 4f	5.58
Pd 3d	5.36
Ag 3d	5.99
Cu 2p	5.32
Ni 2p	4.04
Ti 2p	2.00
Al 2p	0.193
Ge 3d	0.536

Table IV.S1. Relative sensitivity factors for metal and semiconductor peaks measured *via* X-ray photoelectron spectroscopy (XPS). Values are referenced from the CasaXPS software.

IV.F. References

(1) Wilbur, J. L.; Kumar, A.; Kim, E.; Whitesides, G. M. Microfabrication by Microcontact Printing of Self-Assembled Monolayers. *Adv. Mater.* **1994,** *6*, 600–604.

(2) Mrksich, M.; Whitesides, G. M. Patterning Self-Assembled Monolayers Using Microcontact Printing: A New Technology for Biosensors? *Trends Biotechnol.* **1995,** *13*, 228–235.

(3) Smith, R. K.; Lewis, P. A.; Weiss, P. S. Patterning Self-Assembled Monolayers. *Prog. Surf. Sci.* **2004,** *75*, 1–68.

(4) Gates, B. D.; Xu, Q.; Stewart, M.; Ryan, D.; Willson, C. G.; Whitesides, G. M. New Approaches to Nanofabrication: Molding, Printing, and Other Techniques. *Chem. Rev.* **2005,** *105*, 1171–1196.

(5) Braunschweig, A. B.; Huo, F.; Mirkin, C. A. Molecular Printing. *Nat. Chem.* **2009,** *1*, 353–358.

(6) Love, J. C.; Estroff, L. A.; Kriebel, J. K.; Nuzzo, R. G.; Whitesides, G. M. Self-Assembled Monolayers of Thiolates on Metals as a Form of Nanotechnology. *Chem. Rev.* **2005,** *105*, 1103–1170.

(7) Claridge, S. A.; Liao, W.-S.; Thomas, J. C.; Zhao, Y.; Cao, H. H.; Cheunkar, S.; Serino, A. C.; Andrews, A. M.; Weiss, P. S. From the Bottom Up: Dimensional Control and Characterization in Molecular Monolayers. *Chem. Soc. Rev.* **2013,** *42*, 2725–2745.

(8) Vericat, C.; Vela, M. E.; Corthey, G.; Pensa, E.; Cortés, E.; Fonticelli, M. H.; Ibañez, F.; Benitez, G. E.; Carro, P.; Salvarezza, R. C. Self-Assembled Monolayers of Thiolates on Metals: A Review Article on Sulfur-Metal Chemistry and Surface Structures. *RSC Adv.* **2014,** *4*, 27730–27754.

(9) Bent, S. F. Heads or Tails: Which Is More Important in Molecular Self-Assembly? *ACS Nano* **2007,** *1*, 10–12.

(10) Kumar, A.; Whitesides, G. M. Features of Gold Having Micrometer to Centimeter Dimensions Can Be Formed through a Combination of Stamping with an Elastomeric Stamp and an Alkanethiol ‘‘Ink’’ Followed by Chemical Etching. *Appl. Phys. Lett.* **1993,** *63*, 2002–2004.

(11) Dameron, A. A.; Hampton, J. R.; Smith, R. K.; Mullen, T. J.; Gillmor, S. D.; Weiss, P. S. Microdisplacement Printing. *Nano Lett.* **2005,** *5*, 1834–1837.

(12) Mullen, T. J.; Srinivasan, C.; Hohman, J. N.; Gillmor, S. D.; Shuster, M. J.; Horn, M. W.; Andrews, A. M.; Weiss, P. S. Microcontact Insertion Printing. *Appl. Phys. Lett.* **2007,** *90*, 063114.

(13) Anderson, M. E.; Srinivasan, C.; Hohman, J. N.; Carter, E. M.; Horn, M. W.; Weiss, P. S. Combining Conventional Lithography with Molecular Self-Assembly for Chemical Patterning. *Adv. Mater.* **2006,** *18*, 3258–3260.

(14) Srinivasan, C.; Anderson, M. E.; Carter, E. M.; Hohman, J. N.; Bharadwaja, S. S. N.; Trolier-McKinstry, S.; Weiss, P. S.; Horn, M. W. Extensions of Molecular Ruler Technology for Nanoscale Patterning. *J. Vac. Sci. Technol., B* **2006,** *24*, 3200–3204.

(15) Xia, Y.; Whitesides, G. M. Soft Lithography. *Angew. Chem. Int. Ed.* **1998,** *37*, 550–575.

(16) Rogers, J. A.; Nuzzo, R. G. Recent Progress in Soft Lithography. *Mater. Today* **2005,** *8*, 50–56.

(17) Jackman, R. J.; Wilbur, J. L.; Whitesides, G. M. Fabrication of Submicrometer Features on Curved Substrates by Microcontact Printing. *Science* **1995,** *269*, 664–666.

(18) Wilbur, J. L.; Kumar, A.; Biebuyck, H. A.; Kim, E.; Whitesides, G. M. Microcontact Printing of Self-Assembled Monolayers: Applications in Microfabrication. *Nanotechnology* **1996,** *7*, 452–457.

(19) Xia, Y.; Whitesides, G. M. Extending Microcontact Printing as a Microlithographic Technique. *Langmuir* **1997,** *13*, 2059–2067.

(20) Quist, A. P.; Pavlovic, E.; Oscarsson, S. Recent Advances in Microcontact Printing. *Anal. Bioanal. Chem.* **2005,** *381*, 591–600.

(21) Alom Ruiz, S.; Chen, C. S. Microcontact Printing: A Tool to Pattern. *Soft Matter* **2007,** *3*, 168–177.

(22) Perl, A.; Reinhoudt, D. N.; Huskens, J. Microcontact Printing: Limitations and Achievements. *Adv. Mater.* **2009,** *21*, 2257–2268.

(23) Srinivasan, C.; Mullen, T. J.; Hohman, J. N.; Anderson, M. E.; Dameron, A. A.; Andrews, A. M.; Dickey, E. C.; Horn, M. W.; Weiss, P. S. Scanning Electron Microscopy of Nanoscale Chemical Patterns. *ACS Nano* **2007,** *1*, 191–201.

(24) Schwartz, J. J.; Hohman, J. N.; Morin, E. I.; Weiss, P. S. Molecular Flux Dependence of Chemical Patterning by Microcontact Printing. *ACS Appl. Mater. Interfaces* **2013,** *5*, 10310–10316.

(25) Piner, R. D.; Zhu, J.; Xu, F.; Hong, S.; Mirkin, C. A. "Dip-Pen" Nanolithography. *Science* **1999,** *283*, 661–663.

(26) Huo, F.; Zheng, G.; Liao, X.; Giam, L. R.; Chai, J.; Chen, X.; Shim, W.; Mirkin, C. A. Beam Pen Lithography. *Nat. Nanotechnol.* **2010,** *5*, 637–640.

(27) Huo, F.; Zheng, Z.; Zheng, G.; Giam, L. R.; Zhang, H.; Mirkin, C. A. Polymer Pen Lithography. *Science* **2008,** *321*, 1658–1660.

(28) Liao, W.-S.; Cheunkar, S.; Cao, H. H.; Bednar, H. R.; Weiss, P. S.; Andrews, A. M. Subtractive Patterning *via* Chemical Lift-Off Lithography. *Science* **2012,** *337*, 1517–1521.

(29) Andrews, A. M.; Liao, W.-S.; Weiss, P. S. Double-Sided Opportunities Using Chemical Lift-Off Lithography. *Acc. Chem. Res.* **2016,** *49*, 1449–1457.

(30) Cao, H. H.; Nakatsuka, N.; Liao, W.-S.; Serino, A. C.; Cheunkar, S.; Yang, H.; Weiss, P. S.; Andrews, A. M. Advancing Biocapture Substrates *via* Chemical Lift-Off Lithography. *Chem. Mater.* **2017,** *29*, 6829–6839.

(31) Slaughter, L. S.; Cheung, K. M.; Kaappa, S.; Cao, H. H.; Yang, Q.; Young, T. D.; Serino, A. C.; Malola, S.; Olson, J. M.; Link, S.; Häkkinen, H.; Andrews, A. M.; Weiss, P. S. Patterning of Supported Gold Monolayers *via* Chemical Lift-Off Lithography. *Beilstein J. Nanotechnol.* **2017,** *8*, 2648–2661.

(32) Chen, C.-Y.; Wang, C.-M.; Li, H.-H.; Chan, H.-H.; Liao, W.-S. Wafer-Scale Bioactive Substrate Patterning by Chemical Lift-Off Lithography. *Beilstein J. Nanotechnol.* **2018,** *9*, 311–320.

(33) Xu, X.; Yang, Q.; Cheung, K. M.; Zhao, C.; Wattanatorn, N.; Belling, J. N.; Abendroth, J. M.; Slaughter, L. S.; Mirkin, C. A.; Andrews, A. M.; Weiss, P. S. Polymer-Pen Chemical Lift-Off Lithography. *Nano Lett.* **2017,** *17*, 3302–3311.

(34) Zhao, C.; Xu, X.; Yang, Q.; Man, T.; Jonas, S. J.; Schwartz, J. J.; Andrews, A. M.; Weiss, P. S. Self-Collapse Lithography. *Nano Lett.* **2017,** *17*, 5035–5042.

(35) Cao, H. H.; Nakatsuka, N.; Serino, A. C.; Liao, W.-S.; Cheunkar, S.; Yang, H.; Weiss, P. S.; Andrews, A. M. Controlled DNA Patterning by Chemical Lift-Off Lithography: Matrix Matters. *ACS Nano* **2015,** *9*, 11439–11454.

(36) Abendroth, J. M.; Nakatsuka, N.; Ye, M.; Kim, D.; Fullerton, E. E.; Andrews, A. M.; Weiss, P. S. Analyzing Spin Selectivity in DNA-Mediated Charge Transfer *via* Fluorescence Microscopy. *ACS Nano* **2017,** *11*, 7516–7526.

(37) Chen, C.-Y.; Wang, C.-M.; Chen, P.-S.; Liao, W.-S. Surface Functional DNA Density Control by Programmable Molecular Defects. *Chem. Commun.* **2018,** *54*, 4100–4103.

(38) Chen, C.-Y.; Wang, C.-M.; Chen, P.-S.; Liao, W.-S. Self-Standing Aptamers by an Artificial Defect-Rich Matrix. *Nanoscale* **2018,** *10*, 3191–3197.

(39) Cao, H. H.; Nakatsuka, N.; Deshayes, S.; Abendroth, J. M.; Yang, H.; Weiss, P. S.; Kasko, A. M.; Andrews, A. M. Small-Molecule Patterning via Prefunctionalized Alkanethiols. *Chem. Mater.* **2018,** *30*, 4017-4030.

(40) Kim, J.; Rim, Y. S.; Chen, H.; Cao, H. H.; Nakatsuka, N.; Hinton, H. L.; Zhao, C.; Andrews, A. M.; Yang, Y.; Weiss, P. S. Fabrication of High-Performance Ultrathin In_2O_3 Film Field-Effect Transistors and Biosensors Using Chemical Lift-Off Lithography. *ACS Nano* **2015,** *9*, 4572–4582.

(41) Zhao, C.; Xu, X.; Bae, S.-H.; Yang, Q.; Liu, W.; Belling, J. N.; Cheung, K. M.; Rim, Y. S.; Yang, Y.; Andrews, A. M.; Weiss, P. S. Large-Area, Ultrathin Metal-Oxide Semiconductor Nanoribbon Arrays Fabricated by Chemical Lift-Off Lithography. *Nano Lett.* **2018,** *18*, 5590–5595.

(42) Kim, E.; Park, K.; Hwang, S. Electrochemical Investigation of Chemical Lift-off Lithography on Au and ITO. *Electrochim. Acta* **2017,** *246*, 165–172.

(43) Nguyen, H. M.; Park, K.; Hwang, S. The Effect of an Antigalvanic Reduction of Silver on Gold for the Stability of a Self-Assembled Alkanethiol Monolayer and Chemical Lift-Off Lithography. *J. Phys. Chem. C* **2018,** *122*, 16070–16078.

(44) Laibinis, P. E.; Fox, M. A.; Folkers, J. P.; Whitesides, G. M. Comparisons of Self-Assembled Monolayers on Silver and Gold: Mixed Monolayers Derived from $HS(CH_2)_{21}X$ and $HS(CH_2)_{10}Y$ (X, Y = CH_3, CH_2OH) Have Similar Properties. *Langmuir* **1991,** *7*, 3167–3173.

(45) Laibinis, P. E.; Whitesides, G. M.; Allara, D. L.; Tao, Y. T.; Parikh, A. N.; Nuzzo, R. G. Comparison of the Structures and Wetting Properties of Self-Assembled Monolayers of *n*-Alkanethiols on the Coinage Metal Surfaces, Copper, Silver, and Gold. *J. Am. Chem. Soc.* **1991,** *113*, 7152–7167.

(46) Laibinis, P. E.; Whitesides, G. M. Self-Assembled Monolayers of *n*-Alkanethiolates on Copper Are Barrier Films That Protect the Metal against Oxidation by Air. *J. Am. Chem. Soc.* **1992,** *114*, 9022–9028.

(47) Xia, Y.; Zhao, X.-M.; Whitesides, G. M. Pattern Transfer: Self-Assembled Monolayers as Ultrathin Resists. *Microelectron. Eng.* **1996,** *32*, 255–268.

(48) Love, J. C.; Wolfe, D. B.; Chabinyc, M. L.; Paul, K. E.; Whitesides, G. M. Self-Assembled Monolayers of Alkanethiolates on Palladium Are Good Etch Resists. *J. Am. Chem. Soc.* **2002,** *124*, 1576–1577.

(49) Love, J. C.; Wolfe, D. B.; Haasch, R.; Chabinyc, M. L.; Paul, K. E.; Whitesides, G. M.; Nuzzo, R. G. Formation and Structure of Self-Assembled Monolayers of Alkanethiolates on Palladium. *J. Am. Chem. Soc.* **2003,** *125*, 2597–2609.

(50) Schneeweiss, M. A.; Rubinstein, I. In *Encyclopedia of Electrochemistry*; Bard, A. J., Ed., 2007; DOI:10.1002/9783527610426.bard100109.

(51) Xia, Y.; Kim, E.; Whitesides, G. M. Microcontact Printing of Alkanethiols on Silver and Its Application in Microfabrication. *J. Electrochem. Soc.* **1996,** *143*, 1070–1079.

(52) Xia, Y.; Kim, E.; Mrksich, M.; Whitesides, G. M. Microcontact Printing of Alkanethiols on Copper and Its Application in Microfabrication. *Chem. Mater.* **1996,** *8*, 601–603.

(53) Mekhalif, Z.; Riga, J.; Pireaux, J. J.; Delhalle, J. Self-Assembled Monolayers of *n*-Dodecanethiol on Electrochemically Modified Polycrystalline Nickel Surfaces. *Langmuir* **1997,** *13*, 2285–2290.

(54) Mekhalif, Z.; Delhalle, J.; Lang, P.; Garnier, F.; Pireaux, J. J. Comparative Study of the Electrodeposition of Polybithiophene Films on Titanium Electrodes: Bare and Modified with Aromatic and Aliphatic Thiols. *Synth. Met.* **1998,** *96*, 165–175.

(55) Mekhalif, Z.; Delhalle, J.; Lang, P.; Garnier, F.; Caudano, R. Electropolymerization of Bithiophene on Aluminum Surfaces Modified by $CH_3(CH_2)_9$–SH and ϕ–$(CH_2)_m$–SH, m = 0 to 3. *J. Electrochem. Soc.* **1999,** *146*, 2913–2918.

(56) Lee, N.; Choi, S.; Kang, S. Self-Assembled Monolayer as an Antiadhesion Layer on a Nickel Nanostamper in the Nanoreplication Process for Optoelectronic Applications. *Appl. Phys. Lett.* **2006,** *88*, 073101.

(57) Rajalingam, S.; Devillers, S.; Dilimon, V. S.; Delhalle, J.; Mekhalif, Z. Self-Assembled Monolayers of *n*-Dodecanethiol on Nickel Surfaces Using 2-Hydroxyethylammonium Formate as Reducing Medium. *J. Electrochem. Soc.* **2017,** *164*, E36–E41.

(58) Abendroth, J. M.; Cheung, K. M.; Stemer, D. M.; El Hadri, M. S.; Zhao, C.; Fullerton, E. E.; Weiss, P. S. Spin-Dependent Ionization of Chiral Molecular Films. *J. Am. Chem. Soc.* **2019,** *141*, 3863–3874.

(59) Nakatsuka, N.; Yang, K.-A.; Abendroth, J. M.; Cheung, K. M.; Xu, X.; Yang, H.; Zhao, C.; Zhu, B.; Rim, Y. S.; Yang, Y.; Weiss, P. S.; Stojanović, M. N.; Andrews, A. M. Aptamer–Field-Effect Transistors Overcome Debye Length Limitations for Small-Molecule Sensing. *Science* **2018,** *362*, 319–324.

(60) Cheung, K. M.; Yang, K.-A.; Nakatsuka, N.; Zhao, C.; Ye, M.; Jung, M. E.; Yang, H.; Weiss, P. S.; Stojanović, M. N.; Andrews, A. M. Phenylalanine Monitoring via Aptamer-Field-Effect Transistor Sensors. *ACS Sensors* **2019**, DOI:10.1021/acssensors.9b01963.

(61) Han, P.; Akagi, K.; Federici Canova, F.; Shimizu, R.; Oguchi, H.; Shiraki, S.; Weiss, P. S.; Asao, N.; Hitosugi, T. Self-Assembly Strategy for Fabricating Connected Graphene Nanoribbons. *ACS Nano* **2015,** *9*, 12035–12044.

(62) Zhang, H. Ultrathin Two-Dimensional Nanomaterials. *ACS Nano* **2015,** *9*, 9451–9469.

(63) Nečas, D.; Klapetek, P. Gwyddion: An Open-Source Software for SPM Data Analysis. *Cent. Eur. J. Phys.* **2012,** *10*, 181–188.

(64) Goldstein, J. I.; Newbury, D. E.; Michael, J. R.; Ritchie, N. W. M.; Scott, J. H. J.; Joy, D. C. In *Scanning Electron Microscopy and X-Ray Microanalysis*; Goldstein, J. I.; Newbury, D. E.; Michael, J. R.; Ritchie, N. W. M.; Scott, J. H. J.; Joy, D. C., Eds.; Springer New York: New York, NY, 2018; pp 123–131..

(65) Köllensperger, P. A.; Karl, W. J.; Ahmad, M. M.; Pike, W. T.; Green, M. Patterning of Platinum (Pt) Thin Films by Chemical Wet Etching in Aqua Regia. *J. Micromech. Microeng.* **2012,** *22*, 067001.

(66) Shankoff, T. Chemical Etchant for Palladium. US3839110A, October 1, 1974.

(67) Li, Z.; Chang, S.-C.; Williams, R. S. Self-Assembly of Alkanethiol Molecules onto Platinum and Platinum Oxide Surfaces. *Langmuir* **2003,** *19*, 6744–6749.

(68) Petrovykh, D. Y.; Kimura-Suda, H.; Opdahl, A.; Richter, L. J.; Tarlov, M. J.; Whitman, L. J. Alkanethiols on Platinum: Multicomponent Self-Assembled Monolayers. *Langmuir* **2006,** *22*, 2578–2587.

(69) Gorman, C. B.; Biebuyck, H. A.; Whitesides, G. M. Use of a Patterned Self-Assembled Monolayer To Control the Formation of a Liquid Resist Pattern on a Gold Surface. *Chem. Mater.* **1995,** *7*, 252–254.

(70) Shaheen, A.; Sturm, J. M.; Ricciardi, R.; Huskens, J.; Lee, C. J.; Bijkerk, F. Characterization of Self-Assembled Monolayers on a Ruthenium Surface. *Langmuir* **2017,** *33*, 6419-6426.

(71) Hohman, J. N.; Kim, M.; Bednar, H. R.; Lawrence, J. A.; McClanahan, P. D.; Weiss, P. S. Simple, Robust Molecular Self-Assembly on Germanium. *Chem. Sci.* **2011,** *2*, 1334–1343.

(72) Han, S. M.; Ashurst, W. R.; Carraro, C.; Maboudian, R. Formation of Alkanethiol Monolayer on Ge(111). *J. Am. Chem. Soc.* **2001,** *123*, 2422–2425.

(73) Ardalan, P.; Musgrave, C. B.; Bent, S. F. Formation of Alkanethiolate Self-Assembled Monolayers at Halide-Terminated Ge Surfaces. *Langmuir* **2009,** *25*, 2013–2025.

(74) Nathan Hohman, J.; Kim, M.; Lawrence, J. A.; McClanahan, P. D.; Weiss, P. S. High-Fidelity Chemical Patterning on Oxide-Free Germanium. *J. Phys.: Condens. Matter* **2012,** *24*, 164214.

(75) Kim, J.; Rim, Y. S.; Liu, Y.; Serino, A. C.; Thomas, J. C.; Chen, H.; Yang, Y.; Weiss, P. S. Interface Control in Organic Electronics Using Mixed Monolayers of Carboranethiol Isomers. *Nano Lett.* **2014,** *14*, 2946–2951.

(76) Serino, A. C.; Anderson, M. E.; Saleh, L. M. A.; Dziedzic, R. M.; Mills, H.; Heidenreich, L. K.; Spokoyny, A. M.; Weiss, P. S. Work Function Control of Germanium through Carborane-Carboxylic Acid Surface Passivation. *ACS Appl. Mater. Interfaces* **2017,** *9*, 34592–34596.

(77) Borchert, A. M.; Vecchio, K. S.; Stein, R. D. The Use of Charging Effects in Al/Al_2O_3 Metal-Matrix Composites as a Contrast Mechanism in the SEM. *Scanning* **1991,** *13*, 344–349.

(78) Abe, H.; Babin, S.; Borisov, S.; Hamaguchi, A.; Kadowaki, M.; Miyano, Y.; Yamazaki, Y. Contrast Reversal Effect in Scanning Electron Microscopy Due to Charging. *J. Vac. Sci. Technol., B* **2009,** *27*, 1039–1042.

(79) Kim, K. H.; Akase, Z.; Suzuki, T.; Shindo, D. Charging Effects on SEM/SIM Contrast of Metal/Insulator System in Various Metallic Coating Conditions. *Mater. Trans.* **2010,** *51*, 1080–1083.

(80) Hovis, J. S.; Boxer, S. G. Patterning Barriers to Lateral Diffusion in Supported Lipid Bilayer Membranes by Blotting and Stamping. *Langmuir* **2000,** *16*, 894–897.

(81) Rogers, J. A. Nanometer-Scale Printing. *Science* **2012,** *337*, 1459–1460.

(82) Carlson, A.; Bowen, A. M.; Huang, Y.; Nuzzo, R. G.; Rogers, J. A. Transfer Printing Techniques for Materials Assembly and Micro/Nanodevice Fabrication. *Adv. Mater.* **2012,** *24*, 5284–5318.

(83) Meitl, M. A.; Zhu, Z.-T.; Kumar, V.; Lee, K. J.; Feng, X.; Huang, Y. Y.; Adesida, I.; Nuzzo, R. G.; Rogers, J. A. Transfer Printing by Kinetic Control of Adhesion to an Elastomeric Stamp. *Nature Materials* **2006,** *5*, 33–38.

(84) Stranick, S. J.; Parikh, A. N.; Allara, D. L.; Weiss, P. S. A New Mechanism for Surface Diffusion: Motion of a Substrate-Adsorbate Complex. *J. Phys. Chem.* **1994,** *98*, 11136–11142.

(85) Dean, J. A. *Lange's Handbook of Chemistry, 15th ed.*; McGraw-Hill: New York, 1998.

(86) Skulason, H.; Frisbie, C. D. Detection of Discrete Interactions upon Rupture of Au Microcontacts to Self-Assembled Monolayers Terminated with $-S(CO)CH_3$ or $-SH$. *J. Am. Chem. Soc.* **2000,** *122*, 9750-9760.

(87) Bianco, E.; Butler, S.; Jiang, S.; Restrepo, O. D.; Windl, W.; Goldberger, J. E. Stability and Exfoliation of Germanane: A Germanium Graphane Analogue. *ACS Nano* **2013,** *7*, 4414–4421.

(88) Dameron, A. A.; Hampton, J. R.; Gillmor, S. D.; Hohman, J. N.; Weiss, P. S. Enhanced Molecular Patterning via Microdisplacement Printing. *J. Vac. Sci. Technol., B* **2005,** *23*, 2929-2932.

(89) Yang, Q. Ph.D. Dissertation, University of California, Los Angeles, Los Angeles, California, 2018.

(90) Chen, J. G.; Menning, C. A.; Zellner, M. B. Monolayer Bimetallic Surfaces: Experimental and Theoretical Studies of Trends in Electronic and Chemical Properties. *Surf. Sci. Rep.* **2008,** *63*, 201–254.

(91) Kataby, G.; Prozorov, T.; Koltypin, Y.; Cohen, H.; Sukenik, C. N.; Ulman, A.; Gedanken, A. Self-Assembled Monolayer Coatings on Amorphous Iron and Iron Oxide Nanoparticles: Thermal Stability and Chemical Reactivity Studies. *Langmuir* **1997,** *13*, 6151–6158.

(92) Nogues, C.; Lang, P. Self-Assembled Alkanethiol Monolayers on a Zn Substrate: Structure and Organization. *Langmuir* **2007,** *23*, 8385–8391.

(93) Devillers, S.; Hennart, A.; Delhalle, J.; Mekhalif, Z. 1-Dodecanethiol Self-Assembled Monolayers on Cobalt. *Langmuir* **2011,** *27*, 14849–14860.

(94) Baum, T.; Ye, S.; Uosaki, K. Formation of Self-Assembled Monolayers of Alkanethiols on GaAs Surface with in Situ Surface Activation by Ammonium Hydroxide. *Langmuir* **1999,** *15*, 8577–8579.

(95) Presolski, S.; Pumera, M. Covalent Functionalization of MoS_2. *Mater. Today* **2016,** *19*, 140–145.

(96) Thomas, J. C.; Goronzy, D. P.; Dragomiretskiy, K.; Zosso, D.; Gilles, J.; Osher, S. J.; Bertozzi, A. L.; Weiss, P. S. Mapping Buried Hydrogen-Bonding Networks. *ACS Nano* **2016,** *10*, 5446-5451.

(97) Thomas, J. C.; Schwartz, J. J.; Hohman, J. N.; Claridge, S. A.; Auluck, H. S.; Serino, A. C.; Spokoyny, A. M.; Tran, G.; Kelly, K. F.; Mirkin, C. A.; Gilles, J.; Osher, S. J.; Weiss, P. S. Defect-Tolerant Aligned Dipoles within Two-Dimensional Plastic Lattices. *ACS Nano* **2015,** *9*, 4734-4742.

(98) Thomas, J. C.; Boldog, I.; Auluck, H. S.; Bereciartua, P. J.; Dušek, M.; Macháček, J.; Bastl, Z.; Weiss, P. S.; Baše, T. Self-Assembled *p*-Carborane Analogue of *p*-Mercaptobenzoic Acid on Au{111}. *Chem. Mater.* **2015,** *27*, 5425-5435.

(99) Thomas, J. C.; Goronzy, D. P.; Serino, A. C.; Auluck, H. S.; Irving, O. R.; Jimenez-Izal, E.; Deirmenjian, J. M.; Macháček, J.; Sautet, P.; Alexandrova, A. N.; Baše, T.; Weiss, P. S. Acid–Base Control of Valency within Carboranedithiol Self-Assembled Monolayers: Molecules Do the Can-Can. *ACS Nano* **2018,** *12*, 2211-2221.

(100) Gao, W.; Dickinson, L.; Grozinger, C.; Morin, F. G.; Reven, L. Self-Assembled Monolayers of Alkylphosphonic Acids on Metal Oxides. *Langmuir* **1996,** *12*, 6429–6435.

(101) Mandziak, A.; de la Figuera, J.; Ruiz-Gómez, S.; Soria, G. D.; Pérez, L.; Prieto, P.; Quesada, A.; Foerster, M.; Aballe, L. Structure and Magnetism of Ultrathin Nickel-Iron Oxides Grown on Ru(0001) by High-Temperature Oxygen-Assisted Molecular Beam Epitaxy. *Sci. Rep.* **2018,** *8*, 17980.

(102) Chen, C.-Y.; Chang, C.-H.; Wang, C.-M.; Li, Y.-J.; Chu, H.-Y.; Chan, H.-H.; Huang, Y.-W.; Liao, W.-S. Large Area Nanoparticle Alignment by Chemical Lift-Off Lithography. *Nanomaterials* **2018,** *8*, 71.

(103) Ashley, M. J.; Bourgeois, M. R.; Murthy, R. R.; Laramy, C. R.; Ross, M. B.; Naik, R. R.; Schatz, G. C.; Mirkin, C. A. Shape and Size Control of Substrate-Grown Gold Nanoparticles for Surface-Enhanced Raman Spectroscopy Detection of Chemical Analytes. *J. Phys. Chem. C* **2018,** *122*, 2307–2314.

(104) Ohnsorg, M. L.; Beaudoin, C. K.; Anderson, M. E. Fundamentals of MOF Thin Film Growth *via* Liquid-Phase Epitaxy: Investigating the Initiation of Deposition and the Influence of Temperature. *Langmuir* **2015,** *31*, 6114–6121.

(105) Hatzor, A.; Weiss, P. S. Molecular Rulers for Scaling Down Nanostructures. *Science* **2001,** *291*, 1019–1020.

(106) Lau, J.; Trojniak, A. E.; Maraugha, M. J.; VanZanten, A. J.; Osterbaan, A. J.; Serino, A. C.; Ohnsorg, M. L.; Cheung, K. M.; Ashby, D. S.; Weiss, P. S.; Dunn, B. S.; Anderson, M. E. Conformal Ultrathin Film MOF Analogs: Characterization of Growth, Porosity, and Electronic Transport. *Chem. Mater.* **2019**, DOI:10.1021/acs.chemmater.9b03141.

(107) Trang, B.; Yeung, M.; Popple, D. C.; Schriber, E. A.; Brady, M. A.; Kuykendall, T. R.; Hohman, J. N. Tarnishing Silver Metal into Mithrene. *J. Am. Chem. Soc.* **2018,** *140*, 13892–13903.

CHAPTER V

Large-Area, Ultrathin Metal-Oxide Semiconductor Nanoribbon Arrays Fabricated by Chemical Lift-Off Lithography

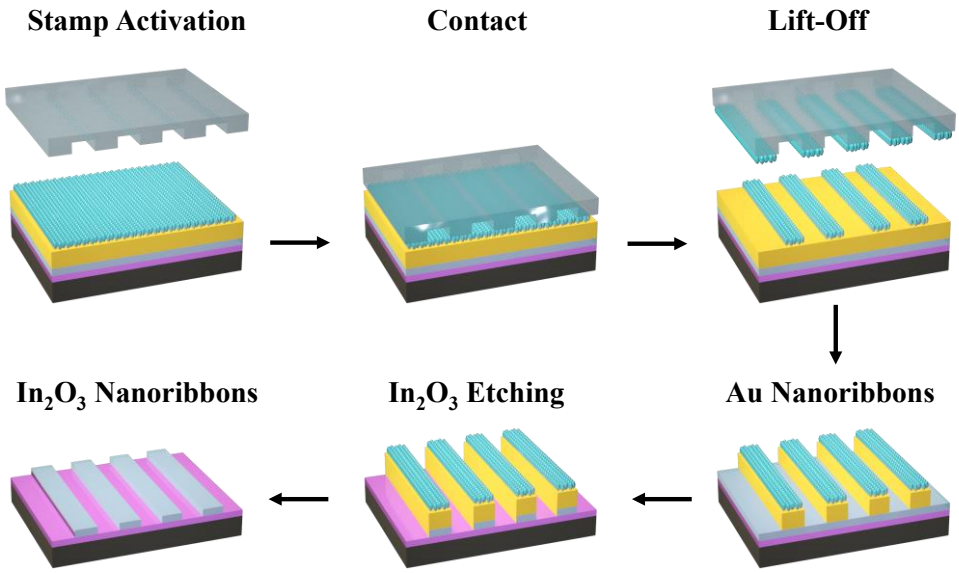

The information in this chapter was published in
Nano Lett. **2018**, *18*, 5590–5595
and has been reproduced here with permission.

Authors: Zhao C.; Xu X.; Bae, S- H.; Yang, Q.; Liu W.; Belling J. N.; **Cheung, K. M.**; Rim Y. S.; Yang, Y.; Andrews, A. M.; Weiss, P. S.

V.A. Introduction

One-dimensional (1D) nanomaterials, such as nanowires, nanotubes, and nanoribbons, possess large surface-to-volume ratios and tunable physical properties. These characteristics can be leveraged to achieve superior performance over bulk materials in a variety of applications, including electronics,[1-5] optics and photonics,[6-10] energy-storage and conversion devices,[11,12] biological and chemical sensors,[13-19] intracellular delivery of bioactive molecules,[20] and medical devices.[21,22] For example, Si nanowires (SiNWs) and carbon nanotubes (CNTs) have been employed as channel components in field-effect transistors (FETs) for highly effective sensing of proteins,[23,24] DNA,[25,26] viruses,[27] and neurotransmitters.[28] However, significant problems remain to be solved before 1D nanomaterials find widespread use.

Bottom-up techniques, such as chemical vapor deposition (CVD) and solution processes,[29-33] dominate 1D-nanomaterial fabrication. However, these strategies have poor control over the orientations of as-grown nanostructures, often on substrates other than the final devices. Bottom-up methods require additional steps to transfer nanostructures and then to control their positions and orientations in devices.[34,35] For example, SiNWs and CNTs, typically synthesized by CVD, require precise control over specific growth parameters to produce high-quality 1D nanomaterials suitable for electronic devices.[29,36] Moreover, nanowires synthesized by CVD are randomly orientated greatly increasing the complexity of device fabrication.[37] Performance is limited by poor control over the numbers of functional nanowires present in devices.[38,39]

Top-down approaches, including photolithography and electron-beam lithography (EBL), are widely used in the semiconductor industry to fabricate 1D nanomaterials. Top-

down methods enable precise control over final shapes, sizes, positions, and orientations of the as-fabricated structures,[40,41] providing ready integration with devices and high reproducibility.[42,43] Nonetheless, top-down techniques suffer from substantial equipment and usage costs. Patterns produced *via* photolithography are limited by the costs of masks and photon sources. By contrast, EBL achieves nanometer-resolution patterning but at the expense of time-consuming serial writing processes. These drawbacks represent significant barriers for many users, hence the need for alternative high-throughput, economical nanoscale patterning strategies.

Recently, we reported a straightforward, high-fidelity nanopatterning technique called chemical lift-off lithography (CLL),[44-49] wherein oxygen plasma-activated polydimethylsiloxane (PDMS) stamps selectively remove portions of a self-assembled monolayer (SAM) in contacted areas without observable lateral diffusion at feature edges. The remaining SAM molecules in the non-contacted regions act as molecular resists during subsequent etching of the freshly exposed underlying substrate. We previously demonstrated that CLL can be used to simplify device fabrication, as well as to enable biomolecule patterning to investigate DNA hybridization and spin-selective electron transport.[50-54] High-fidelity chemical patterns with line widths as narrow as 40 ± 2 nm were achieved using CLL, with the possibility of features as narrow as 5 nm (corresponding to ~10 molecules).[46] As with other top-down patterning approaches, however, CLL relies on expensive nanofabricated masters to create PDMS stamps to produce nanoscale structures. Masters for CLL have been produced using low-throughput EBL methods, limiting impact.[47,48]

Many top-down nanofabrication processes, including CLL, have focused on patterning metals and group IV and III-V semiconductors (*e.g.*, Au and Si).[55] Metal oxides represent an increasingly important material class in numerous applications due to their electronic, mechanical, and optical properties.[45,56-58] To date, top-down approaches for fabricating metal-oxide nanomaterials are underdeveloped compared to patterning methods for other types of materials, yet patterned semiconductors are of interest for applications including electronics, displays and lighting, ultrasensitive biosensors, and wearable, flexible sensors.[59-61]

We report on the fabrication of large-area In_2O_3 nanoribbon arrays using CLL, but *without* using masters generated *via* EBL. We utilize metal oxide nanoribbons as semiconducting channels in FET architectures. Through this demonstration, we extend the range and applicability of CLL patterning to nanoscale features on semiconducting metal oxides for functional electronic devices, achieving current on/off ratios of $\sim 10^7$ and a peak mobility of 13.7 $cm^2\ V^{-1}\ s^{-1}$, economically and at high throughput.

V.B. Experimental Methods

V.B.1. Materials

Prime quality 4″ Si{100} wafers (P/B, 0.001-0.005 Ω-cm, thickness 500 μm) were purchased from Silicon Valley Microelectronics, Inc. (Santa Clara, CA, USA). Sylgard 184® silicone elastomer kits (lot #0008823745) were purchased from Ellsworth Adhesives (Germantown, WI, USA). (7–8% Vinylmethylsiloxane)–(dimethylsiloxane) copolymer, platinum divinyltetramethyl-disiloxane complex in xylene, and (25–30% methylhydrosiloxane)–(dimethylsiloxane) copolymer were all purchased from Gelest Inc. (Morrisville, PA, USA) and

used as received. 2,4,6,8-Tetramethyl-2,4,6,8-tetravinylcyclotetrasiloxane, indium(III) nitrate hydrate (99.999%), iron nitrate, thiourea, ammonium hydroxide, hydrogen peroxide, ethylenediaminetetraacetic acid disodium salt dihydrate (EDTA), and acetic acid were purchased from Sigma-Aldrich (St. Louis, MO, USA) and used as received. Commercially available HD-DVD-R recordable 1× speed 15 GB blank discs and DVD-R recordable 16× speed 4.7 GB blank discs (Memorex) were purchased and used as received. The SPR 700-1.2 photoresist and MF-26A developer were obtained from the Integrated Systems Nanofabrication Cleanroom (ISNC) at UCLA. Water was deionized before use (18.2 MΩ cm) using a Milli-Q system (Millipore, Billerica, MA).

V.B.2. Substrate Fabrication

A 100-nm-thick SiO_2 film was thermally grown on Si{100} wafers. If needed, SiO_2/Si wafers are also available for purchase at Silicon Valley Microelectronics, Inc. (Santa Clara, CA, USA). Next, 10-nm Ti and 30-nm Au films were deposited onto In_2O_3 films using a CHA solution electron-beam evaporator at high vacuum (10^{-8} Torr) with an evaporation rate of 0.1 nm/s. The Au/Ti/In_2O_3/Si substrates were then annealed in a hydrogen flame for ~10 s to remove adsorbed organic contaminants on the Au surfaces. Substrates were then immersed into an ethanolic 1 mM 11-mercapto-1-undecanol solution overnight for self-assembled monolayer formation on Au surfaces.

V.B.3. Preparation of HD-DVD and DVD Masters

Commercially available HD-DVD-R recordable 1× speed 15 GB blank discs and DVD-R recordable 16× speed 4.7 GB blank discs were used to produce masters for patterning. Both HD-DVD and DVD discs have similar structures and therefore the preparation processes are the same. The HD-DVD discs were cut into wedge-shaped pieces. A razor blade was used to

separate the discs at the edges between Layer II and Layer III in **Figure V.1a**, and jagged edges were removed. The transparent part of the discs with the dye (Layer III in **Figure V.1a**) were then rinsed with ethanol to remove the dye from the surfaces. The slices were then put into a beaker of ethanol for 1-2 min. After that, they were blow dried under a N_2 flow.

V.B.4. Hard PDMS (*h*-PDMS) Stamps

For soft PDMS, which should be prepared before starting the *h*-PDMS preparation process, a mixture of Sylgard® 184 elastomer base and curing agent (10:1) was thoroughly mixed and degassed in a vacuum desiccator. For *h*-PDMS, 3.4 g (7–8% vinylmethylsiloxane)–(dimethylsiloxane) copolymer, 18 μL of platinum divinyltetramethyl-disiloxane complex in xylene, and 50 μL of 2,4,6,8-tetramethyl-2,4,6,8-tetravinylcyclotetrasiloxane were mixed and degassed for <5 min. Then 1 g of (25–30% methylhydrosiloxane)–(dimethylsiloxane) copolymer was added and mixed gently. The mixture was poured onto HD-DVD masters and spin-coated at 1000 rpm for 40 s. Stamps were annealed at 65 °C for 15 min. Soft PDMS was then poured onto the backsides of the *h*-PDMS stamps and annealed at 65 °C overnight.

After the final curing step, stamps were slowly peeled away from masters and stored in clean petri dishes. Stamps were rinsed with ethanol and dried under N_2 flow before use. Clean PDMS stamps were treated in oxygen plasma (Harrick Plasma, Ithaca, NY, USA) for 40 s at a power of 18 W and a pressure of 10 psi to generate activated surfaces. A pair of tweezers was used to place PDMS stamps onto substrates without applying a vertical compression force. In the stamp removal process, one pair of tweezers was used to hold the substrates and another pair was used to lift off the stamps.

V.B.5. Wet Etching

After PDMS stamp removal from SAM-functionalized substrates, each substrate was immersed into an aqueous solution of 20 mM iron nitrate and 30 mM thiourea to etch the Au films selectively. The etching rate was ~1 nm/min and the samples were put into the etching solution for 30 min. Substrates were then rinsed with deionized (DI) water and dried under N_2. Substrates were immersed into a solution containing 0.42 g EDTA, 1 mL hydrogen peroxide, and 0.42 mL ammonia hydrate in 10 mL deionized water for ~3 min to etch through the 10 nm Ti layer. The In_2O_3 was then removed from the exposed areas by immersion in acetic acid for 10 min. Samples were annealed at 100 °C for 1 h after the wet etching process.

V.B.6. Field-Effect Transistor Device Fabrication

Interdigitated Au source and drain electrodes (45 μm length, 1300 μm width) were patterned on top of the In_2O_3 nanoribbons to obtain uniform current distributions. Electrodes were patterned by standard photolithography. The 10 nm Ti and 30 nm Au films were deposited *via* a CHA solution e-beam evaporator at high vacuum (10^{-8} Torr) at an evaporation rate of 0.1 nm/s.

V.B.7. Substrate characterization

Scanning electron microscope (SEM) images were obtained using a Zeiss Supra 40VP scanning electron microscope with an Inlens SE Detector (Inlens secondary electron detector). Atomic force microscope (AFM) imaging was performed on a Bruker FastScan system (Bruker, Billerica, MA) under PeakForce tapping mode with a ScanAsyst-Air cantilevers (Bruker, spring constant = 0.4 ± 0.1 N/m). Electronic performance measurements were carried out on a manual analytical probe station (Signatone, Gilroy, CA)

equipped with a Keithley 4200A (Tektronix, Beaverton, OR) semiconductor parameter analyzer. Optical images were taken with a digital camera attached to a Zeiss Axiotech optical microscope.

V.C. Results and Discussion

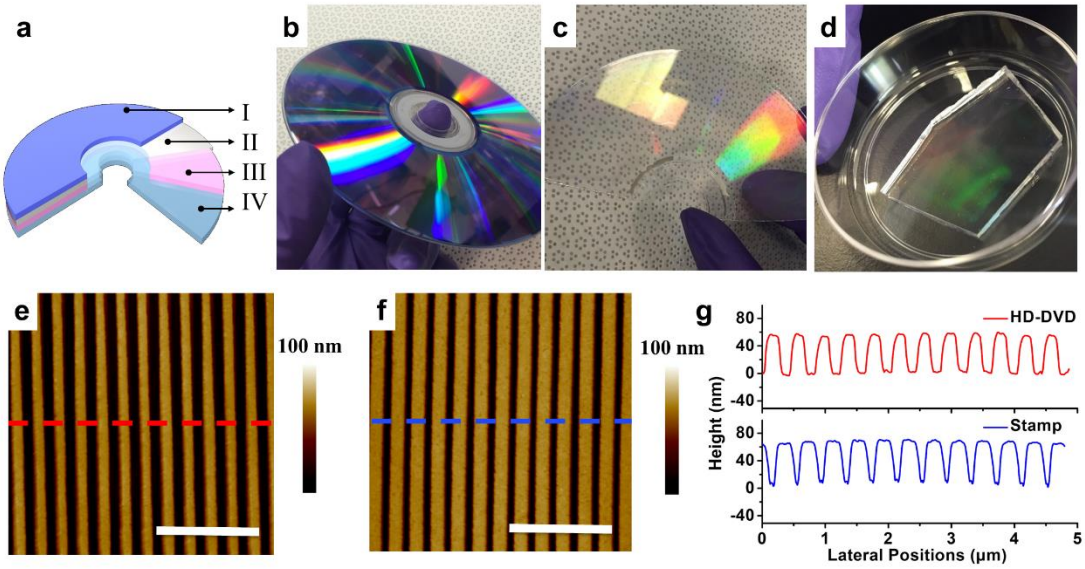

Figure V.1. (a) Schematic architecture of a high-definition digital-versatile disc (HD-DVD): layer I, polycarbonate protective layer; layer II, mirror-like metal film; layer III, data recording film; layer IV, polycarbonate layer containing concentric rings with typical widths of 250 nm and periodicities of 400 nm. **(b-d)** Photographs of an HD-DVD, an HD-DVD master (layer IV), and a patterned polydimethylsiloxane (PDMS) stamp, respectively. Atomic force micrographs of **(e)** a representative HD-DVD master and **(f)** a patterned PDMS stamp. Scale bars are 2 μm. **(g)** Topographic profiles across the corrugated features in **(e)** and **(f)**.

Most commonly used thin-film metal oxide deposition strategies rely on physical/chemical vapor deposition methods, such as pulsed-laser deposition,[62] sputtering,[63] and atomic-layer deposition,[64] requiring complex processes, extreme conditions (*e.g.*, high temperature, vacuum), and costly equipment. Recently, simple, scalable sol-gel-based processes have emerged as alternatives for preparing high quality semiconducting metal-oxide films.[65-68]

Here, thin films of In_2O_3 were prepared *via* a sol-gel process. Aqueous solutions (0.1 M) of $In(NO_3)_3$ were spin-coated onto SiO_2/Si substrates (100 nm, thermally grown SiO_2 dielectric on heavily doped, *p*-type Si substrates with resistivities of 1–5 mΩ·cm). Following deposition, substrates were heated to 100 °C for 5 min and annealed at 350 °C for 3 h. The thicknesses of the resulting In_2O_3 films were ~3 nm with typical average surface roughnesses of ~0.06 nm determined *via* atomic force microscopy (AFM) (**Figure V.S1**). Note that the In_2O_3 films fabricated via the sol-gel process are amorphous.[45]

Commercially available optical storage media, such as compact discs (CDs) and DVDs are patterned with sub-micron periodic gratings that can be used directly as economical templates for soft lithography. We employed HD-DVDs as masters for CLL PDMS stamps. The HD-DVDs have quasi-1D feature widths of ~200 nm, spaced at a pitch of 400 nm. As shown in **Figure V.1a**, each HD-DVD is composed of a protection layer (I), a reflective layer (II), a recording layer (III), and a polycarbonate layer (IV) composed of embossed concentric rings that form the basis of the patterns used herein. Layer IV was exposed simply by removing layers I and II with a razor blade and dissolving layer III with ethanol (**Figure V.1c**). Atomic force microscopy confirmed the expected, grooved pattern on the surface of layer IV, as seen in **Figure V.1e**. To replicate layer IV features precisely, hard PDMS (*h*-PDMS) was used as the stamp material due to its stiffness compared to regular (soft) Sylgard 184 PDMS.[69] Unpolymerized *h*-PDMS was spin-coated onto masters (2 cm × 2 cm, 40 s at 1000 rpm) and cured at 65 °C for 10 min to form thin and robust films. A layer of soft PDMS (~5 mm) was then applied and cured at 65 °C overnight to form a support for the pattern-containing *h*-PDMS film and to prevent cracking, prior to demolding stamps from masters. These stamps (**Figure V.1d**) are reusable and can be employed for repeated, wafer-scale CLL patterning.

Atomic-force micrographs of patterned PDMS surfaces (**Figure V.1f**) confirmed precise replication of HD-DVD features with depths of ~60 nm.

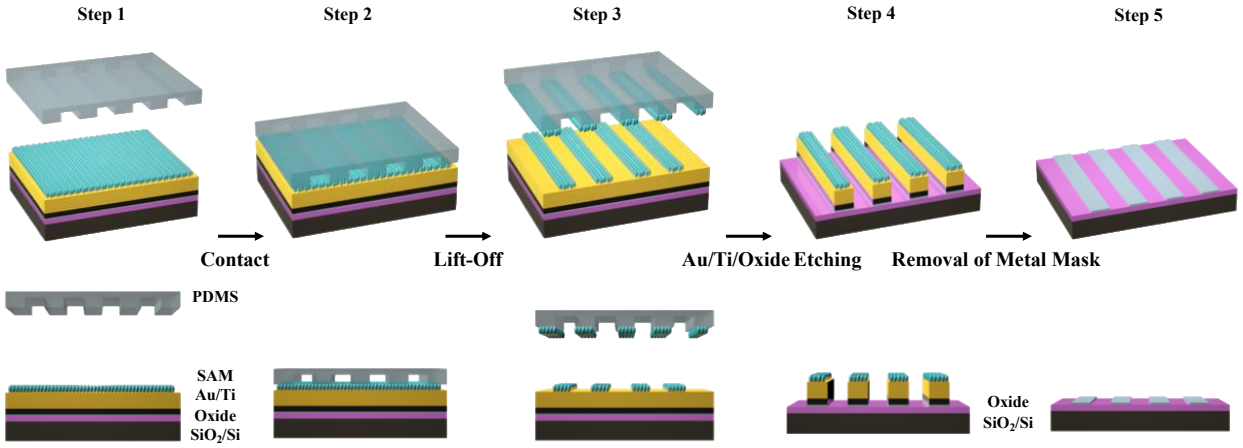

Figure V.2. Fabrication scheme of In_2O_3 nanoribbons. Step 1: a thin film of 3-nm In_2O_3 is deposited on a SiO_2/Si substrate *via* a sol-gel process followed by Au (30 nm)/Ti (10 nm) deposition and functionalization with a self-assembled monolayer (SAM). Step 2: a polydimethylsiloxane (PDMS) stamp, activated by an oxygen plasma, is brought into conformal contact with the substrate. Step 3: Upon lifting the stamp from the surface, SAM molecules in the contacted areas are removed, transferring the pattern (periodic lines and spaces) into the SAM. Step 4: Successive selective etch processes remove Au/Ti and In_2O_3 layers from unprotected regions on the surface. Step 5: Remaining SAM, Au, and Ti are removed to produce In_2O_3 nanoribbon arrays.

The scheme used to fabricate In_2O_3 nanoribbons is illustrated in **Figure V.2**. *Step 1:* layers of Ti (10 nm) and Au (30 nm) were deposited on previously prepared In_2O_3 films. The Au/Ti/In_2O_3/SiO_2/Si stacks were then incubated in 1 mM ethanolic solutions of 11-mercapto-1-undecanol ($HSCH_2(CH_2)_9CH_2OH$) to form SAMs terminated with hydroxyl moieties, enabling CLL patterning. *Step 2:* oxygen plasma was used to "activate" PDMS stamp surfaces, generating siloxyl groups (SiOH). Stamps were then brought into conformal contact with SAMs. Condensation reactions occur between the hydroxyl-terminated SAMs and the SiOH groups of the activated *h*-PDMS, forming covalent linkages (Si–O–SAM). *Step 3:* Upon removal of the stamps, molecules within the contracted regions of the SAMs were selectively

removed transferring the stamp pattern to the monolayer. Notably, in the lift-off process, monolayers of Au atoms are also removed as Au–S bonds (between SAM molecules and the underlying Au substrate atoms) are stronger than Au–Au bonds in the substrates.

Scanning electron microscopy of CLL-patterned SAMs (**Figure V.3a)** confirmed the presence of 1D features (200 nm linewidths) over large areas, matching those on the stamps (**Figure V.1f**). *Step 4:* Intact monolayers in the non-contacted regions acted as resists for successive etching by solutions of $Fe(NO_3)_3$ and thiourea (removing exposed Au) and EDTA disodium salt, NH_4OH, and H_2O_2 (removing Ti), thereby transferring the SAM patterns through the metal layers. The metal layers acted as etch masks, protecting the underlying In_2O_3 films from removal by glacial acetic acid. The resulting Au/Ti/In_2O_3 nanoribbons were investigated by AFM (**Figure V.3b**) and found to have heights of ~45 nm, corresponding to the sum of the expected heights of the constituent layers above the surrounding Si/SiO_2 surfaces exposed by previous etch processes. *Step 5*: metal layers were completely removed to expose arrays of In_2O_3 nanoribbons extending over centimeter length scales (**Figure V.3c)**. The widths (~200 nm) and heights (~3 nm) of the metal oxide nanoribbons are the smallest, to our knowledge, fabricated *via* top-down approaches.

To demonstrate the versatility of CLL patterning for additional feature sizes, In_2O_3 nanoribbons of different linewidths (350 nm and 1500 nm) were fabricated using alternate master patterns (**Figure V.3d and V.3e**, respectively). The Au nanoribbons produced as an intermediate product of this process (*Step 4*) can also be used for a variety of applications, such as surface plasmon resonance biosensors. Note that In_2O_3 nanoribbon edges are rougher than those of similarly produced Au nanoribbons and the feature sizes are reduced;

this is a common phenomenon associated with isotropic etch processes, which can undercut regions below the protective masks.

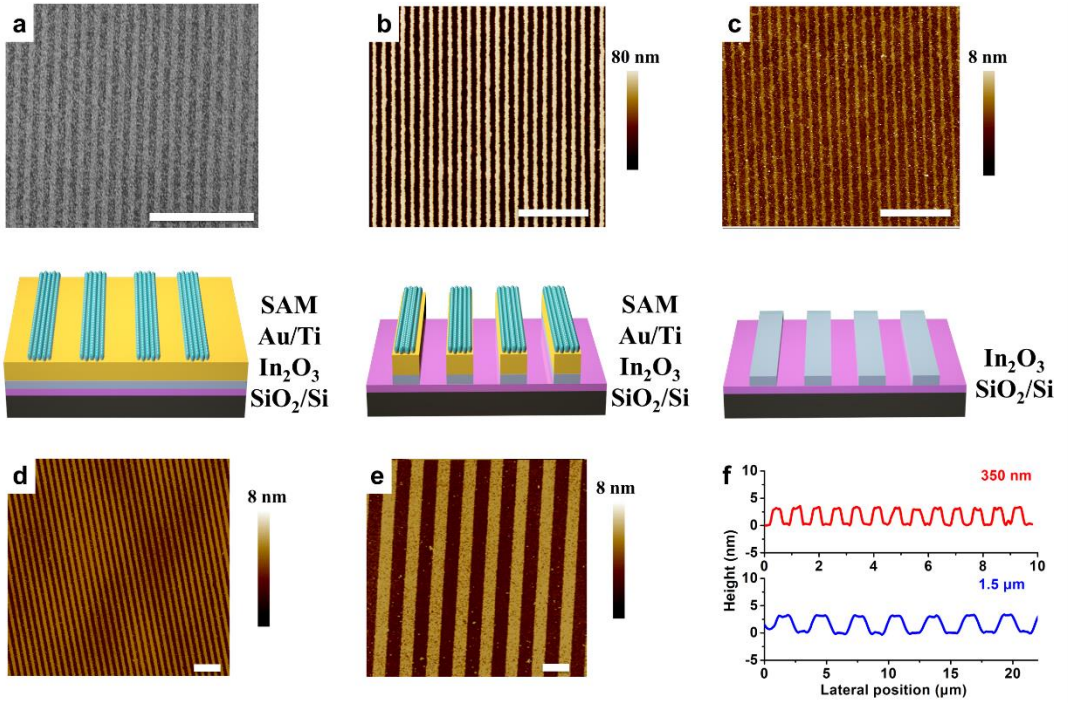

Figure V.3. (a) (top) Scanning electron microscope image and (bottom) schematic of a self-assembled monolayer (SAM) patterned *via* chemical lift-off lithography. **(b,c)** (top) Topographic images measured using atomic force microscopy (AFM) and (bottom) schematic illustrations of SAM/Au/Ti/In_2O_3 and bare In_2O_3 nanoribbons, respectively, with line widths of ~200 nm. Atomic force topographs of In_2O_3 nanoribbons with line widths of **(d)** 350 nm and **(e)** 1.5 μm. Thicknesses of each set of In_2O_3 nanoribbons **(c-e)** were measured to be ~3 nm by AFM. **(f)** Height profiles of (top) 500-nm-wide In_2O_3 nanoribbons and (bottom) 1.5-μm-wide nanoribbons. Scale bars in all images are 3 μm.

Field-effect transistors have key advantages over optical or electrochemical platforms for biosensing applications, including low detection limits, real-time and label-free measurements, and simple integration with standard semiconductor-device processing.[45] To evaluate the performance of In_2O_3 nanoribbons in devices, we constructed FETs in a bottom-gate, top-contact configuration as shown in **Figure V.4**. Gold electrodes were deposited atop arrays of as-prepared In_2O_3 nanoribbons *via* electron-beam evaporation

through conventional photolithography. The device measurement setup is shown in **Figure V.S2**. As shown in **Figure V.S3**, interdigitated electrodes with widths of 1300 μm and lengths of 45 μm were used.

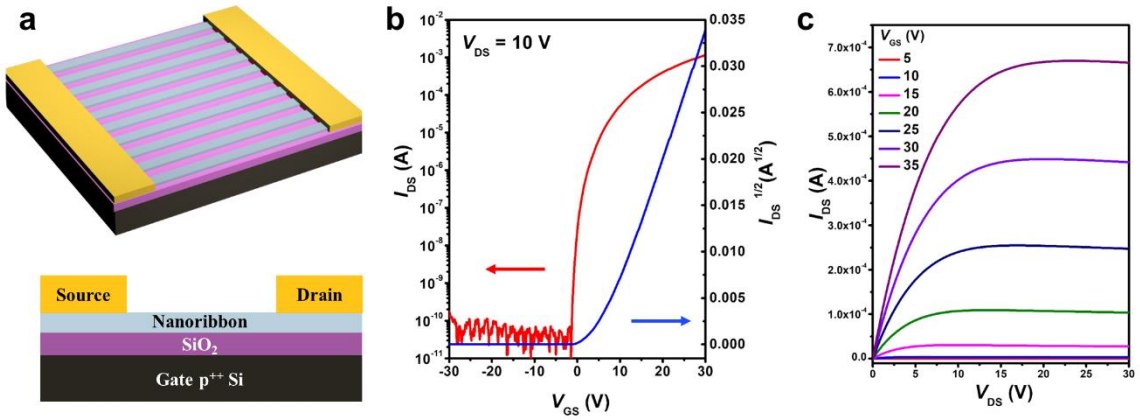

Figure V.4. (a) Schematic illustrations of an In_2O_3 field-effect transistor (FET) in a bottom-gate-top-contact configuration. Gate: Si (p^{++}); Source/Drain: Au; semiconducting channel: In_2O_3 nanoribbons. The widths and lengths of the inter-digital electrodes are 1300 and 45 μm, respectively. The widths and pitches of the nanoribbons are 200 and 400 nm, respectively. **(b)** Transfer and **(c)** output characteristics of an ultrathin In_2O_3 nanoribbon FET, showing the measured current between the drain and source (I_{DS}) in response to varying gate to source voltages (V_{GS}) and source to drain (V_{DS}) potentials, relative to the source. Devices displayed *n*-type pinch-off behavior with carrier motilities of 10.0 ± 2.6 $cm^2\ V^{-1}\ s^{-1}$, averaged over 10 devices with a peak value of 13.7 $cm^2\ V^{-1}\ s^{-1}$, and a current on/off ratio $>10^7$.

The spatially ordered arrangement of In_2O_3 nanoribbons on surfaces facilitated straightforward fabrication of FETs with consistent numbers of channels per device, controlled by the widths of the contact electrodes. Here, ~3000 200-nm-wide In_2O_3 nanoribbons were incorporated into each FET device. These FETs had high field-effect mobilities (μ_{sat}=10.0 ± 2.6 $cm^2\ V^{-1}\ s^{-1}$), averaged over 10 devices with a peak value of 13.7 $cm^2\ V^{-1}\ s^{-1}$ and a current on/off ratio $>10^7$. We attribute the variations in mobilities to imperfections of the sol-gel-processed thin-film material itself (such as defects), as we have observed similar variations in analogous thin film FETs.[45] These nanoribbon FETs have

similar electronic properties to In_2O_3 thin-film transistors,[45] but have higher surface-to-volume ratios. The performance of these devices, such as current on/off ratio, exceeded those previously reported for 1D nanowire-based devices fabricated *via* bottom-up approaches.[15,16] High-performance In_2O_3 nanoribbon FETs can be used in a variety of applications, such as electronic devices and ultrasensitive FET-based pH, gas, chemical, and biological sensors, where the surface of In_2O_3 can be functionalized with a variety of molecules including antibodies and aptamers using linkers such as (3-aminopropyl)trimethoxysilane.[45,57,59,65]

V.D. Conclusions and Prospects

In summary, we report a high-throughput, large-scale strategy enabling fabrication of ultrathin, metal oxide nanoribbons that are readily integrated into devices. We leverage and extend the capabilities of CLL, in combination with selective etching processes, to pattern, successively, SAMs, metal films, and ultrathin layers of In_2O_3 to create arrays of periodic, 1D nanostructures. Nanoribbons fabricated by this approach are uniform and continuous over centimeter scales. We demonstrate high-performance FETs fabricated using In_2O_3 nanoribbons having carrier mobilities up to 13.7 $cm^2 V^{-1} s^{-1}$ and on/off current ratios $>10^7$. By employing widely available low-cost HD-DVDs as nanostructured master patterns, in conjunction with CLL, a scalable and high-fidelity chemical patterning technique that does not require sophisticated equipment and facilities, we lower barriers to nanostructure and device fabrication. The advances demonstrated here serve to extend large-area nanofabrication and to broaden application and user bases by providing alternative patterning strategies to photo- and electron-beam lithographies. This work provides a

general approach for the facile and large-scale patterning of semiconductor 1D nanostructure arrays with high-surface-to-volume ratios, which have a broad range of applications in electronic devices, optical devices, displays, and biochemical sensors.

V.E. Supplementary Materials

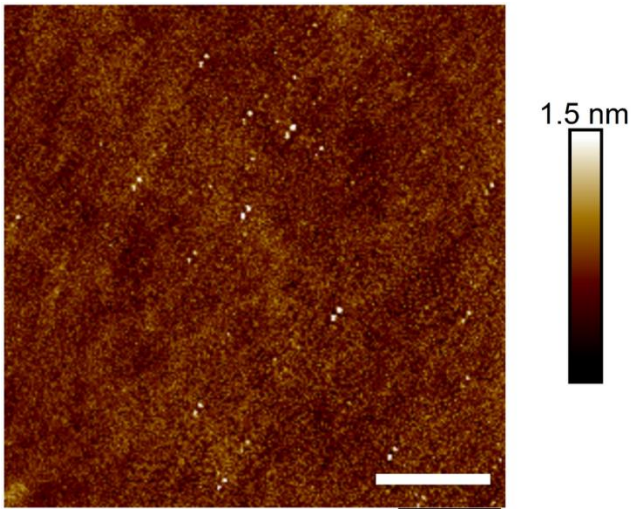

Figure V.S1. Atomic force microscope image of In_2O_3 films. The average roughness (Ra) is ~0.06 nm. The scale bar is 1 μm.

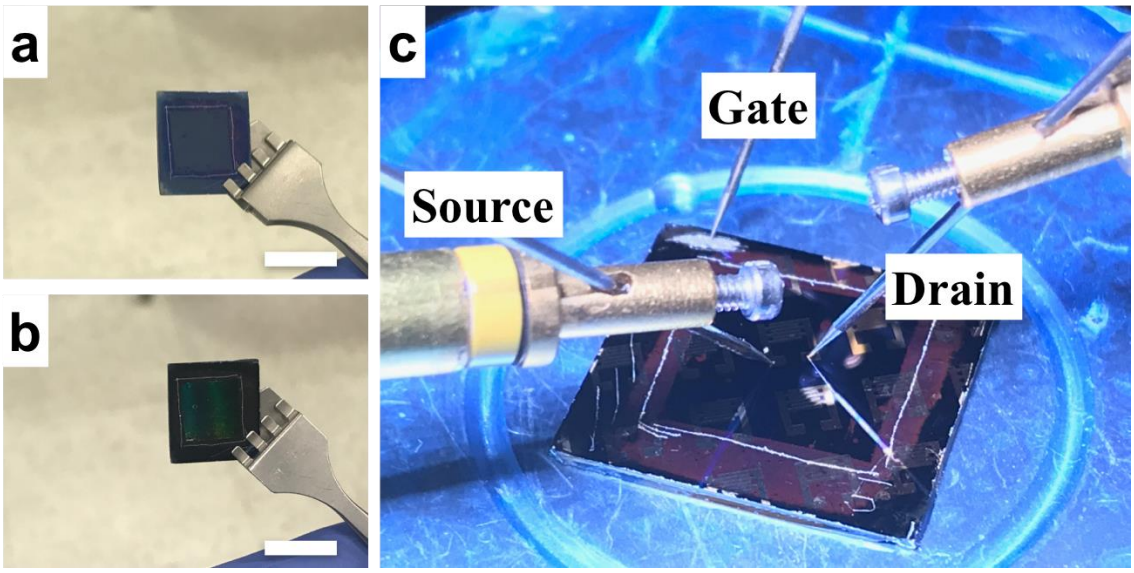

Figure V.S2. Images of the fabricated devices and test configuration. **(a,b)** In_2O_3 nanoribbons on a 1.5 cm × 1.5 cm Si wafer. The 1 cm × 1 cm square region in the center contains the nanoribbons. The rainbow colors in the central region of the bottom image **(b)** indicate light interference from the periodic nanoribbon pattern. **(c)** Device test configuration using a probe station with bottom gate and top source/drain electrodes.

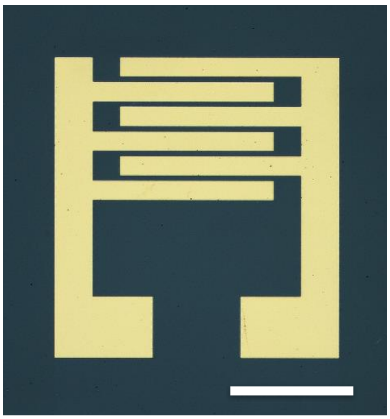

Figure V.S3. Photograph of a representative device with the interdigitated electrode configuration. The widths and lengths of the inter-digital electrodes are 1300 and 45 μm, respectively. The scale bar is 1000 μm.

V.F. References

(1) Cui, Y.; Lieber, C. M. Functional Nanoscale Electronic Devices Assembled Using Silicon Nanowire Building Blocks. *Science* **2001,** *291*, 851–853.

(2) Xu, X.; Liu, C.; Kim, K.; Fan, D. L. Electric-Driven Rotation of Silicon Nanowires and Silicon Nanowire Motors. *Adv. Funct. Mater.* **2014,** *24*, 4843–4850.

(3) Memisevic, E.; Hellenbrand, M.; Lind, E.; Persson, A. R.; Sant, S.; Schenk, A.; Svensson, J.; Wallenberg, R.; Wernersson, L. E. Individual Defects in InAs/InGaAsSb/GaSb Nanowire Tunnel Field-Effect Transistors Operating below 60 mV/decade. *Nano Lett.* **2017,** *17*, 4373–4380.

(4) Lee, H.; Manorotkul, W.; Lee, J.; Kwon, J.; Suh, Y. D.; Paeng, D.; Grigoropoulos, C. P.; Han, S.; Hong, S.; Yeo, J.; Ko, S. H. Nanowire-on-Nanowire: All-Nanowire Electronics by On-Demand Selective Integration of Hierarchical Heterogeneous Nanowires. *ACS Nano* **2017,** *11*, 12311–12317.

(5) Qiu, C.; Zhang, Z.; Xiao, M.; Yang, Y.; Zhong, D.; Peng, L. M. Scaling Carbon Nanotube Complementary Transistors to 5-nm Gate Lengths. *Science* **2017,** *355*, 271–276.

(6) Huang, M. H.; Mao, S.; Feick, H.; Yan, H.; Wu, Y.; Kind, H.; Weber, E.; Russo, R.; Yang, P. Room-Temperature Ultraviolet Nanowire Nanolasers. *Science* **2001,** *292*, 1897–1899.

(7) Law, M.; Sirbuly, D. J.; Johnson, J. C.; Goldberger, J.; Saykally, R. J.; Yang, P. Nanoribbon Waveguides for Subwavelength Photonics Integration. *Science* **2004,** *305*, 1269–1273.

(8) Xu, X.; Kim, K.; Fan, D. Tunable Release of Multiplex Biochemicals by Plasmonically Active Rotary Nanomotors. *Angew. Chem. Int. Ed.* **2015,** *54*, 2525–2529.

(9) Liu, P.; He, X.; Ren, J.; Liao, Q.; Yao, J.; Fu, H. Organic-Inorganic Hybrid Perovskite Nanowire Laser Arrays. *ACS Nano* **2017,** *11*, 5766–5773.

(10) Xu, X.; Yang, Q.; Wattanatorn, N.; Zhao, C.; Chiang, N.; Jonas, S. J.; Weiss, P. S. Multiple-Patterning Nanosphere Lithography for Fabricating Periodic Three-Dimensional Hierarchical Nanostructures. *ACS Nano* **2017,** *11*, 10384–10391.

(11) Law, M.; Greene, L. E.; Johnson, J. C.; Saykally, R.; Yang, P. Nanowire Dye-Sensitized Solar Cells. *Nat. Mater.* **2005,** *4*, 455–459.

(12) Zhang, L.; Jia, Y.; Wang, S.; Li, Z.; Ji, C.; Wei, J.; Zhu, H.; Wang, K.; Wu, D.; Shi, E.; Fang, Y.; Cao, A. Carbon Nanotube and CdSe Nanobelt Schottky Junction Solar Cells. *Nano Lett.* **2010,** *10*, 3583–3589.

(13) Kong, J. Nanotube Molecular Wires as Chemical Sensors. *Science* **2000,** *287*, 622–625.

(14) Cui, Y.; Wei, Q.; Park, H.; Lieber, C. M. Nanowire Nanosensors for Highly Sensitive and Selective Detection of Biological and Chemical Species. *Science* **2001,** *293*, 1289–1292.

(15) Li, C.; Zhang, D.; Liu, X.; Han, S.; Tang, T.; Han, J.; Zhou, C. In_2O_3 Nanowires as Chemical Sensors. *Appl. Phys. Lett.* **2003,** *82*, 1613–1615.

(16) Zhang, D.; Liu, Z.; Li, C.; Tang, T.; Liu, X.; Han, S.; Lei, B.; Zhou, C. Detection of NO_2 down to ppb Levels Using Individual and Multiple In_2O_3 Nanowire Devices. *Nano Lett.* **2004,** *4*, 1919–1924.

(17) Cheng, Y.; Xiong, P.; Yun, C. S.; Strouse, G. F.; Zheng, J. P.; Yang, R. S.; Wang, Z. L. Mechanism and Optimization of pH Sensing Using SnO_2 Nanobelt Field Effect Transistors. *Nano Lett.* **2008,** *8*, 4179–4184.

(18) Xu, X.; Li, H.; Hasan, D.; Ruoff, R. S.; Wang, A. X.; Fan, D. L. Near-Field Enhanced Plasmonic-Magnetic Bifunctional Nanotubes for Single Cell Bioanalysis. *Adv. Funct. Mater.* **2013,** *23*, 4332–4338.

(19) Kim, K.; Xu, X.; Guo, J.; Fan, D. L. Ultrahigh-Speed Rotating Nanoelectromechanical System Devices Assembled from Nanoscale Building Blocks. *Nat. Commun.* **2014,** *5*, 3632.

(20) Xu, X.; Hou, S.; Wattanatorn, N.; Wang, F.; Yang, Q.; Zhao, C.; Yu, X.; Tseng, H.-R.; Jonas, S. J.; Weiss, P. S. Precision-Guided Nanospears for Targeted and High-Throughput Intracellular Gene Delivery. *ACS Nano* **2018,** *12*, 4503–4511.

(21) Kim, J.; Lee, M.; Shim, H. J.; Ghaffari, R.; Cho, H. R.; Son, D.; Jung, Y. H.; Soh, M.; Choi, C.; Jung, S.; Chu, K.; Jeon, D.; Lee, S. T.; Kim, J. H.; Choi, S. H.; Hyeon, T.; Kim, D. H. Stretchable Silicon Nanoribbon Electronics for Skin Prosthesis. *Nat. Commun.* **2014,** *5*, 5747.

(22) Liu, R.; Chen, R.; Elthakeb, A. T.; Lee, S. H.; Hinckley, S.; Khraiche, M. L.; Scott, J.; Pre, D.; Hwang, Y.; Tanaka, A.; Ro, Y. G.; Matsushita, A. K.; Dai, X.; Soci, C.; Biesmans, S.; James, A.; Nogan, J.; Jungjohann, K. L.; Pete, D. V.; Webb, D. B.; Zou, Y.; Bang, A. G.; Dayeh, S. A. High Density Individually Addressable Nanowire Arrays Record Intracellular Activity from Primary Rodent and Human Stem Cell Derived Neurons. *Nano Lett.* **2017,** *17*, 2757–2764.

(23) So, H. M.; Won, K.; Kim, Y. H.; Kim, B. K.; Ryu, B. H.; Na, P. S.; Kim, H.; Lee, J. O. Single-Walled Carbon Nanotube Biosensors using Aptamers as Molecular Recognition Elements. *J. Am. Chem. Soc.* **2005,** *127*, 11906–11907.

(24) Stern, E.; Vacic, A.; Rajan, N. K.; Criscione, J. M.; Park, J.; Ilic, B. R.; Mooney, D. J.; Reed, M. A.; Fahmy, T. M. Label-Free Biomarker Detection from Whole Blood. *Nat. Nanotechnol.* **2010,** *5*, 138–142.

(25) Hahm, J.-i.; Lieber, C. M. Direct Ultrasensitive Electrical Detection of DNA and DNA Sequence Variations Using Nanowire Nanosensors. *Nano Lett.* **2004,** *4*, 51–54.

(26) Sorgenfrei, S.; Chiu, C. Y.; Gonzalez, R. L., Jr.; Yu, Y. J.; Kim, P.; Nuckolls, C.; Shepard, K. L. Label-Free Single-Molecule Detection of DNA-Hybridization Kinetics with a Carbon Nanotube Field-Effect Transistor. *Nat. Nanotechnol.* **2011,** *6*, 126–132.

(27) Patolsky, F.; Zheng, G.; Hayden, O.; Lakadamyali, M.; Zhuang, X.; Lieber, C. M. Electrical Detection of Single Viruses. *Proc. Natl. Acad. Sci. U. S. A.* **2004,** *101*, 14017–14022.

(28) Li, B. R.; Hsieh, Y. J.; Chen, Y. X.; Chung, Y. T.; Pan, C. Y.; Chen, Y. T. An Ultrasensitive Nanowire-Transistor Biosensor for Detecting Dopamine Release from Living PC12 Cells under Hypoxic Stimulation. *J. Am. Chem. Soc.* **2013,** *135*, 16034–16037.

(29) Patolsky, F.; Zheng, G.; Lieber, C. M. Fabrication of Silicon Nanowire Devices for Ultrasensitive, Label-Free, Real-Time Detection of Biological and Chemical Species. *Nat. Protoc.* **2006,** *1*, 1711–1724.

(30) Wang, Z. L. Piezoelectric Nanogenerators Based on Zinc Oxide Nanowire Arrays. *Science* **2006,** *312*, 242–246.

(31) Liu, C.; Xu, X.; Rettie, A. J. E.; Mullins, C. B.; Fan, D. L. One-Step Waferscale Synthesis of 3-D ZnO Nanosuperstructures by Sesigned Catalysts for Substantial Improvement of Solar Water Oxidation Efficiency. *J. Mater. Chem. A* **2013,** *1*, 8111.

(32) Gao, N.; Zhou, W.; Jiang, X.; Hong, G.; Fu, T. M.; Lieber, C. M. General Strategy for Biodetection in High Ionic Strength Solutions using Transistor-Based Nanoelectronic Sensors. *Nano Lett.* **2015,** *15*, 2143–2148.

(33) Constantinou, M.; Rigas, G. P.; Castro, F. A.; Stolojan, V.; Hoettges, K. F.; Hughes, M. P.; Adkins, E.; Korgel, B. A.; Shkunov, M. Simultaneous Tunable Selection and Self-Assembly of Si Nanowires from Heterogeneous Feedstock. *ACS Nano* **2016,** *10*, 4384–4394.

(34) Xu, F.; Durham, J. W.; Wiley, B. J.; Zhu, Y. Strain-Release Assembly of Nanowires on Stretchable Substrates. *ACS Nano* **2011,** *5*, 1556–1563.

(35) Yao, J.; Yan, H.; Lieber, C. M. A Nanoscale Combing Technique for the Large-Scale Assembly of Highly Aligned Nanowires. *Nat. Nanotechnol.* **2013,** *8*, 329–335.

(36) Alam, S. B.; Panciera, F.; Hansen, O.; Molhave, K.; Ross, F. M. Creating New VLS Silicon Nanowire Contact Geometries by Controlling Catalyst Migration. *Nano Lett.* **2015,** *15*, 6535–6541.

(37) Ishikawa, F. N.; Curreli, M.; Chang, H. K.; Chen, P. C.; Zhang, R.; Cote, R. J.; Thompson, M. E.; Zhou, C. A Calibration Method for Nanowire Biosensors to Suppress Device-To-Device Variation. *ACS Nano* **2009,** *3*, 3969–3976.

(38) Li, J.; Zhang, Y.; To, S.; You, L.; Sun, Y. Effect of Nanowire Number, Diameter, and Doping Density on Nano-FET Biosensor Sensitivity. *ACS Nano* **2011,** *5*, 6661–6668.

(39) Lee, B. Y.; Sung, M. G.; Lee, J.; Baik, K. Y.; Kwon, Y. K.; Lee, M. S.; Hong, S. Universal Parameters for Carbon Nanotube Network-Based Sensors: Can Nanotube Sensors be Reproducible? *ACS Nano* **2011,** *5*, 4373–4379.

(40) Stern, E.; Klemic, J. F.; Routenberg, D. A.; Wyrembak, P. N.; Turner-Evans, D. B.; Hamilton, A. D.; LaVan, D. A.; Fahmy, T. M.; Reed, M. A. Label-Free Immunodetection with CMOS-Compatible Semiconducting Nanowires. *Nature* **2007,** *445*, 519–522.

(41) Knopfmacher, O.; Tarasov, A.; Fu, W.; Wipf, M.; Niesen, B.; Calame, M.; Schonenberger, C. Nernst Limit in Dual-Gated Si-Nanowire FET Sensors. *Nano Lett.* **2010,** *10*, 2268–2274.

(42) Tong, H. D.; Chen, S.; van der Wiel, W. G.; Carlen, E. T.; van den Berg, A. Novel Top-Down Wafer-Scale Fabrication of Single Crystal Silicon Nanowires. *Nano Lett.* **2009,** *9*, 1015–1022.

(43) Hwang, S. W.; Lee, C. H.; Cheng, H.; Jeong, J. W.; Kang, S. K.; Kim, J. H.; Shin, J.; Yang, J.; Liu, Z.; Ameer, G. A.; Huang, Y.; Rogers, J. A. Biodegradable Elastomers and Silicon Nanomembranes/Nanoribbons for Stretchable, Transient Electronics, and Biosensors. *Nano Lett.* **2015,** *15*, 2801–2808.

(44) Liao, W. S.; Cheunkar, S.; Cao, H. H.; Bednar, H. R.; Weiss, P. S.; Andrews, A. M. Subtractive Patterning via Chemical Lift-Off Lithography. *Science* **2012,** *337*, 1517–1521.

(45) Kim, J.; Rim, Y. S.; Chen, H.; Cao, H. H.; Nakatsuka, N.; Hinton, H. L.; Zhao, C.; Andrews, A. M.; Yang, Y.; Weiss, P. S. Fabrication of High-Performance Ultrathin In_2O_3 Film Field-Effect Transistors and Biosensors Using Chemical Lift-Off Lithography. *ACS Nano* **2015,** *9*, 4572–4582.

(46) Andrews, A. M.; Liao, W. S.; Weiss, P. S. Double-Sided Opportunities Using Chemical Lift-Off Lithography. *Acc. Chem. Res.* **2016,** *49*, 1449–1457.

(47) Xu, X.; Yang, Q.; Cheung, K. M.; Zhao, C.; Wattanatorn, N.; Belling, J. N.; Abendroth, J. M.; Slaughter, L. S.; Mirkin, C. A.; Andrews, A. M.; Weiss, P. S. Polymer-Pen Chemical Lift-Off Lithography. *Nano Lett.* **2017,** *17*, 3302–3311.

(48) Zhao, C.; Xu, X.; Yang, Q.; Man, T.; Jonas, S. J.; Schwartz, J. J.; Andrews, A. M.; Weiss, P. S. Self-Collapse Lithography. *Nano Lett.* **2017,** *17*, 5035–5042.

(49) Slaughter, L. S.; Cheung, K. M.; Kaappa, S.; Cao, H. H.; Yang, Q.; Young, T. D.; Serino, A. C.; Malola, S.; Olson, J. M.; Link, S.; Hakkinen, H.; Andrews, A. M.; Weiss, P. S. Patterning of Supported Gold Monolayers via Chemical Lift-Off Lithography. *Beilstein J. Nanotechnol.* **2017,** *8*, 2648–2661.

(50) Cao, H. H.; Nakatsuka, N.; Serino, A. C.; Liao, W. S.; Cheunkar, S.; Yang, H.; Weiss, P. S.; Andrews, A. M. Controlled DNA Patterning by Chemical Lift-Off Lithography: Matrix Matters. *ACS Nano* **2015,** *9*, 11439–11454.

(51) Abendroth, J. M.; Nakatsuka, N.; Ye, M.; Kim, D.; Fullerton, E. E.; Andrews, A. M.; Weiss, P. S. Analyzing Spin Selectivity in DNA-Mediated Charge Transfer via Fluorescence Microscopy. *ACS Nano* **2017,** *11*, 7516–7526.

(52) Cao, H. H.; Nakatsuka, N.; Liao, W.-S.; Serino, A. C.; Cheunkar, S.; Yang, H.; Weiss, P. S.; Andrews, A. M. Advancing Biocapture Substrates via Chemical Lift-Off Lithography. *Chem. Mater.* **2017,** *29*, 6829–6839.

(53) Chen, C. Y.; Wang, C. M.; Chen, P. S.; Liao, W. S. Surface Functional DNA Density Control by Programmable Molecular Defects. *Chem. Commun.* **2018,** *54*, 4100–4103.

(54) Chen, C. Y.; Wang, C. M.; Chen, P. S.; Liao, W. S. Self-Standing Aptamers by an Artificial Defect-Rich Matrix. *Nanoscale* **2018,** *10*, 3191–3197.

(55) Ko, H.; Takei, K.; Kapadia, R.; Chuang, S.; Fang, H.; Leu, P. W.; Ganapathi, K.; Plis, E.; Kim, H. S.; Chen, S. Y.; Madsen, M.; Ford, A. C.; Chueh, Y. L.; Krishna, S.; Salahuddin, S.; Javey, A. Ultrathin Compound Semiconductor on Insulator Layers for High-Performance Nanoscale Transistors. *Nature* **2010,** *468*, 286–289.

(56) Rim, Y. S.; Bae, S. H.; Chen, H.; Yang, J. L.; Kim, J.; Andrews, A. M.; Weiss, P. S.; Yang, Y.; Tseng, H. R. Printable Ultrathin Metal Oxide Semiconductor-Based Conformal Biosensors. *ACS Nano* **2015,** *9*, 12174–12181.

(57) Chen, H.; Rim, Y. S.; Wang, I. C.; Li, C.; Zhu, B.; Sun, M.; Goorsky, M. S.; He, X.; Yang, Y. Quasi-Two-Dimensional Metal Oxide Semiconductors Based Ultrasensitive Potentiometric Biosensors. *ACS Nano* **2017,** *11*, 4710–4718.

(58) Rim, Y. S.; Chen, H.; Zhu, B.; Bae, S.-H.; Zhu, S.; Li, P. J.; Wang, I. C.; Yang, Y. Interface Engineering of Metal Oxide Semiconductors for Biosensing Applications. *Adv. Mater. Inter.* **2017,** *4*, 1700020.

(59) Aroonyadet, N.; Wang, X.; Song, Y.; Chen, H.; Cote, R. J.; Thompson, M. E.; Datar, R. H.; Zhou, C. Highly Scalable, Uniform, and Sensitive Biosensors Based on Top-Down Indium Oxide Nanoribbons and Electronic Enzyme-Linked Immunosorbent Assay. *Nano Lett.* **2015,** *15*, 1943–1951.

(60) Liu, Q.; Aroonyadet, N.; Song, Y.; Wang, X.; Cao, X.; Liu, Y.; Cong, S.; Wu, F.; Thompson, M. E.; Zhou, C. Highly Sensitive and Quick Detection of Acute Myocardial Infarction Biomarkers Using In_2O_3 Nanoribbon Biosensors Fabricated Using Shadow Masks. *ACS Nano* **2016,** *10*, 10117–10125.

(61) Liu, Q.; Liu, Y.; Wu, F.; Cao, X.; Li, Z.; Alharbi, M.; Abbas, A. N.; Amer, M. R.; Zhou, C. Highly Sensitive and Wearable In_2O_3 Nanoribbon Transistor Biosensors with

Integrated On-Chip Gate for Glucose Monitoring in Body Fluids. *ACS Nano* **2018,** *12*, 1170–1178.

(62) Nomura, K.; Ohta, H.; Takagi, A.; Kamiya, T.; Hirano, M.; Hosono, H. Room-Temperature Fabrication of Transparent Flexible Thin-Film Transistors using Amorphous Oxide Semiconductors. *Nature* **2004,** *432*, 488–492.

(63) Martins, R. F. P.; Ahnood, A.; Correia, N.; Pereira, L. M. N. P.; Barros, R.; Barquinha, P. M. C. B.; Costa, R.; Ferreira, I. M. M.; Nathan, A.; Fortunato, E. E. M. C. Recyclable, Flexible, Low-Power Oxide Electronics. *Adv. Funct. Mater.* **2013,** *23*, 2153–2161.

(64) Lin, Y. Y.; Hsu, C. C.; Tseng, M. H.; Shyue, J. J.; Tsai, F. Y. Stable and High-Performance Flexible ZnO Thin-Film Transistors by Atomic Layer Deposition. *ACS Appl. Mater. Inter.* **2015,** *7*, 22610–22617.

(65) Kim, H. S.; Byrne, P. D.; Facchetti, A.; Marks, T. J. High Performance Solution-Processed Indium Oxide Thin-Film Transistors. *J. Am. Chem. Soc.* **2008,** *130*, 12580–12581.

(66) Banger, K. K.; Yamashita, Y.; Mori, K.; Peterson, R. L.; Leedham, T.; Rickard, J.; Sirringhaus, H. Low-Temperature, High-Performance Solution-Processed Metal Oxide Thin-Film Transistors Formed by a 'Sol-Gel on Chip' Process. *Nat. Mater.* **2011,** *10*, 45–50.

(67) Hwan Hwang, Y.; Seo, J.-S.; Moon Yun, J.; Park, H.; Yang, S.; Ko Park, S.-H.; Bae, B.-S. An 'Aqueous Route' for the Fabrication of Low-Temperature-Processable Oxide Flexible Transparent Thin-Film Transistors on Plastic Substrates. *NPG Asia Materials* **2013,** *5*, e45.

(68) Rim, Y. S.; Chen, H.; Song, T.-B.; Bae, S.-H.; Yang, Y. Hexaaqua Metal Complexes for Low-Temperature Formation of Fully Metal Oxide Thin-Film Transistors. *Chem. Mater.* **2015,** *27*, 5808–5812.

(69) Qin, D.; Xia, Y.; Whitesides, G. M. Soft Lithography for Micro- and Nanoscale Patterning. *Nat. Protoc.* **2010,** *5*, 491–502.

CHAPTER VI

Phenylalanine Monitoring *via*

Aptamer-Field-Effect Transistor Sensors

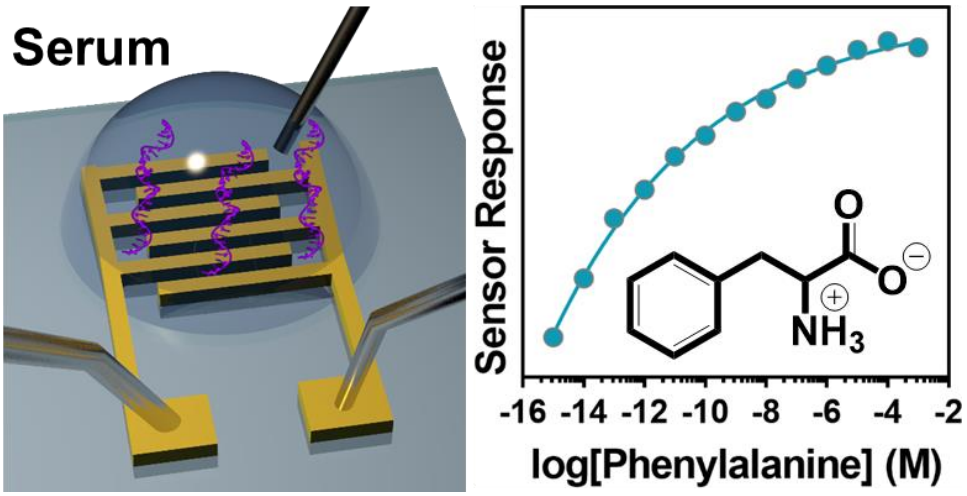

The information in this chapter was published in
ACS Sensors **2019**, ASAP DOI: 10.1021/acssensors.9b01963
and has been reproduced here with permission.

Authors: **Cheung, K. M.**; Yang, K-. A.; Nakatsuka, N.; Zhao C.; Ye, M.; Jung, M. E.; Yang, H.; Weiss, P. S.; Stojanović, M. N.; Andrews, A. M.

VI.A. Introduction

Phenylketonuria (PKU) is an autosomal recessive genetic disorder involving mutations in the gene that encodes phenylalanine hydroxylase (PAH), a liver enzyme that converts the essential amino acid phenylalanine to tyrosine (**Figure VI.1A**).[1-7] In the United States, PKU occurs in ~1/10,000-15,000 babies yearly. Diagnosis at birth is critical.[1,3,4,7,8] This 'inborn error of metabolism' leads to hyperphenylalaninemia in the blood and brain.[1-5,7,9] Elevated phenylalanine causes abnormalities in brain development associated with permanent intellectual impairment. Screening newborns for PKU involves laboratory testing by a bacterial inhibition assay, *i.e.*, the Guthrie test,[10] or more recently, tandem mass spectrometry.[11] Although sufficient for diagnosis, these methods involve turnaround times of *days* to inform treatment providers and families.[12]

Phenylketonuria is primarily managed through strict avoidance of phenylalanine-containing foods.[1,3,4,7,13,14] Early-life dietary management largely prevents the damaging effects of PKU on brain development.[15-17] However, even modestly uncontrolled blood phenylalanine levels in children and adults have been correlated with cognitive and psychiatric sequelae.[1,7,18-21] Nevertheless, studies on this topic are sparse, partly because technologies for straightforward monitoring of blood phenylalanine levels in clinical studies are not readily available.[1,18]

Phenylalanine serum concentrations in healthy individuals are 60±30 μM.[17] Current treatment guidelines for individuals with PKU are to maintain blood phenylalanine levels between 120 and 360 μM. Moderate hyperphenylalaninemia is associated with blood levels ranging from 360 to 600 μM, while untreated PKU is characterized by phenylalanine levels >1000 μM (with concentrations >3000 μM having been reported).[1,3,7,22]

Emerging treatments for PKU are based on enzyme replacement with PEGylated versions of bacterial phenylalanine ammonia lyase.[23] Enzyme substitution decreases phenylalanine levels in patients with PKU and reduces the need for dietary restrictions, which can be exceedingly difficult to maintain over a lifetime.[23] In 2017, the U.S. Food and Drug Administration approved the first enzyme substitution therapy, pegvaliase (Palynziq™).[23] However, pegvaliase and related treatment strategies can result in hypophenylalaninemia, which negatively affects protein synthesis, and thus, growth in children, and neurotransmitter synthesis in children and adults.[17,23] In light of the present clinical picture, improvements in phenylalanine monitoring are indicated to provide insights into the pharmacokinetics[24] and efficacy of current and future PKU treatment strategies and their combinations.[25] Enabling patients to determine their own blood phenylalanine levels will be empowering. Regardless, there are no at-home or point-of-care options for measuring phenylalanine.[26-28]

Field-effect transistors (FETs) modified with protein receptors have been developed for rapid electronic, reagentless detection of biological targets.[29-37] Receptor recognition of charged targets and/or target-induced receptor reorientation gate the semiconductor channels of FETs to modulate transconductance. However, bioFETs based on protein receptors or antibodies are not feasible for direct sensing in biological fluids because large receptors (~10 nm) are too far away from semiconductor channels relative to the Debye screening length. At physiological ion concentrations, the Debye length is on the order of 1 nm.[30,38]

Recently, we developed thin-film metal oxide FETs functionalized with oligonucleotide stem-loop receptors (aptamers).[39-42] We discovered that target-mediated

reorganization of a portion of the highly negatively charged backbones of small oligonucleotides (and rearrangement of associated counter ions) occurs near enough to the semiconductor surfaces to circumvent Debye-length limitations under biological conditions.[43-46] Aptamer-FETs have enabled sensitive and selective detection of small molecules, including neutral targets, in physiological buffers and fluids, and complex biological matrices.[30]

Here, previously unreported aptamers for direct phenylalanine detection were coupled with nanometer-thin In_2O_3 FETs. Phenylalanine was detected over many orders of magnitude in physiological solutions. Selectivity for phenylalanine over closely structured endogenous and exogenous aromatic amino acid analogs (**Figure VI.1B**) and metabolites was excellent, particularly for one of the phenylalanine aptamers. Phenylalanine sensing was carried out in serum from mice with induced hyperphenylalaninemia, demonstrating the ability of aptamer-FETs to detect biologically important differences in phenylalanine concentrations. Aptamer sequences were rationally modified to shift device sensitivities towards physiologically relevant concentrations. These findings portend the use of aptamer-functionalized FETs for phenylalanine monitoring in PKU patients and other relevant populations.

VI.B. Experimental Methods

VI.B.1. Materials

All materials were purchased from Sigma-Aldrich Co. (St. Louis, MO), unless otherwise noted. The amino acids used throughout were the L-forms, *i.e.*, L-phenylalanine (Sigma P5482 and P2126), L-tyrosine (Sigma T3754), and L-tryptophan (Sigma 93659 and T0254).

Oligonucleotides were obtained from Integrated DNA Technologies (Coralville, IA). The SYLGARD 184 used to make polydimethylsiloxane (PDMS) wells was from Dow Corning Corporation (Midland, MI). Water was deionized before use (18.2 MΩ) with a Milli-Q system (Millipore, Billerica, MA).

para-Ethynylphenylalanine (PEPA) was synthesized by a previously reported route[47] with minor modifications. Trimethylsilyl acetylene was coupled under palladium catalysis to to *N*-acetyl-4-iodophenylalanine methyl ester,[48] followed by deprotection and purification. The nuclear magnetic resonance spectroscopy (NMR) data matched spectra reported in the literature (**Figure VI.S1**).

VI.B.2. Phenylalanine Aptamer Selection

Phenylalanine aptamer selection was carried out as per a previously reported strategy.[41] Initial selection resulted in isolation of an aptamer for phenylalanine complexed with pentamethylcyclopentadienyl rhodium(III) (Cp*Rh). This previously reported aptamer, which we designate Phe-Cp*Rh 1, showed cross-reactivity with the analogous tryptophan-Cp*Rh complex (Trp-Cp*Rh), limiting its use in practical applications. To reduce cross-reactivity, additional selections for Phe-Cp*Rh were performed with Trp-Cp*Rh counter-selection,[41,42] which resulted in the isolation of two new Phe-Cp*Rh aptamers, which we designate Phe-Cp*Rh 2 and Phe-Cp*Rh 3 (**Table VI.S1**). These previously unreported Phe-Cp*Rh aptamers were not cross-reactive with Trp-Cp*Rh (**Figures VI.S2C**, **VI.S3**). However, Phe-Cp*Rh 2 showed cross reactivity with Tyr-Cp*Rh (**Figure VI.S2C**).

Unexpectedly, as byproducts of the selections for additional Phe-Cp*Rh aptamers, we identified three aptamers that directly recognize phenylalanine, rather than the Phe-Cp*Rh complex. These previously unreported, direct-binding aptamers are designated Phe 1, Phe 2,

and Phe 3 (**Table VI.S1**). An excess of phenylalanine (1 mM) was used in the selection procedures to produce the Phe-Cp*Rh complex such that Cp*Rh was the limiting reagent. Under these conditions, a large excess of free phenylalanine, which also interacted with the oligonucleotide sequences, was present along with the Phe-Cp*Rh complex in the target solutions. We compared the responses of Phe 1 to phenylalanine with and without Cp*Rh (**Figure VI.S4**). In the presence of Cp*Rh, phenylalanine prefers to complex with Cp*Rh, however the remaining free phenylalanine in solution was detected by Phe 1.

Fluorescence assays were carried out in 20 mM HEPES, 1 M NaCl, 10 mM $MgCl_2$, and 5 mM KCl (pH 7.5) using a Victor II microplate reader (PerkinElmer). Each aptamer sequence was modified with fluorescein at the 5' end. Complementary strands were 3'-modified with dabcyl for solution quenching determination of dissociation constants (K_d) (**Table VI.S1**) and for selectivity testing. Concentrations of aptamers and complementary strands were empirically determined and aptamer K_d values were calculated as per previously published methods.[30,40,41] Putative aptamer secondary structures shown were predicted using *Mfold* (http://unafold.rna.albany.edu/?q=mfold).

VI.B.3. Field-Effect Transistor Measurements

Polydimethylsiloxane wells were sealed on individual FETs to hold sensing solutions. Substrates had inter-FET distances (~2 mm) that were large enough to enable isolation of single FET devices within the PDMS wells (**Figure VI.S6**). Ringer's solution (147 mM NaCl, 4 mM KCl, 2.25 mM $CaCl_2$, pH 7.4) was used as the electrolyte solution. The Ag/AgCl reference electrodes (World Precision Instruments, Inc., Sarasota, FL) were placed in sensing solutions in a top-gate (solution-gate) device configuration. Measurements were performed

using a manual analytical probe station (Signatone, Gilroy, CA) equipped with a Keithley 4200A-SCS (Tektronix, Beaverton, OR) semiconductor parameter analyzer.

Source-drain current (I_{DS}) transfer curves were obtained wherein gate voltages (V_{GS}) were varied from 0 to 400 mV with a step voltage of 5 mV. The drain voltage (V_D) was held at 10 mV throughout. Five sweeps were averaged for each transfer curve. Calibrated responses were calculated by dividing the absolute sensor response (ΔI), which takes into account baseline subtraction, by the change in source-drain current with voltage sweep ($\Delta I_{DS}/\Delta V_G$).[49] Aptamer-FET responses at V_G=375 mV were used to calculate mean calibrated responses.

VI.B.4. Mouse Serum

Mice were generated at the University of California, Los Angeles (UCLA) from a core colony of a serotonin transporter (SERT)-deficient lineage maintained on a mixed CD1 × 129S6/SvEv background *via* heterozygous SERT-deficient (SERT+/-) pairings. For this study, three pairs of SERT wildtype (SERT+/+) mice from the core colony were bred to produce 18 wildtype pups. All mice were maintained on a 12-h light/dark cycle (lights on at 0600 h (Zeitgeber time, *ZT* 0)) with *ad libitum* food and water. The Association for Assessment and Accreditation of Laboratory Animal Care International has fully accredited UCLA. All animal care and use met the requirements of the NIH Guide for the Care and Use of Laboratory Animals, revised 2011. The UCLA Chancellor's Animal Research Committee (Institutional Animal Care and Use Committee) preapproved all procedures.

For postnatal treatment, pups from each litter were randomly assigned to one of three groups: (1) Saline (vehicle control); (2) 100 mg/kg *para*-chlorophenylalanine (Sigma #C3635);[50] or (3) 10 mg/kg *para*-ethynylphenylalanine.[51] Doses were calculated based on

the free base form of each compound. The pH values of PEPA and PCPA saline were adjusted to pH 7.4 prior to injection. Dosing solutions were filtered *via* 0.22 μm filters for sterilization.

Each litter contained all treatment groups. Each pup received a subcutaneous injection of the assigned treatment daily during ZT 6-8 on postnatal days (P)4-21. The injection volume was 10 mL/kg during P4-11, and 5 mL/kg during P12-21. A total of three of the 18 pups were excluded from this study: 1/6 saline-treated and 1/6 PCPA-treated subjects died during the postnatal period. In addition, 1/6 PEPA-treated subjects stopped receiving injections at P17 due to body weight loss for two continuous days. The data from the remaining *N*=5 mice per treatment group are reported.

Pups were weaned after the last injection on P21 and housed with their same-sex siblings. Two hours after the last injection, subjects were euthanized by decapitation under deep anesthesia with isoflurane. Whole blood samples were collected *via* cardiac puncture and placed in microcentrifuge tubes pre-chilled on ice for 30-60 min. Following coagulation, blood samples were centrifuged at 16,000 g for 15 min at 4 °C twice. After each centrifugation, supernatants were removed and transferred to clean microcentrifuge tubes on ice.

Serum samples were aliquoted and stored at -80 °C until analysis. Aptamer-FET and high performance liquid chromatography (HPLC) measurements were carried out by investigators blind to the treatment group identification of each sample. All serum samples for aptamer-FET measurements were diluted to ~10 pM phenylalanine in 1× Ringer's buffer, using the same serial dilution strategy, *i.e.*, first 1:10, then 1:100, and finally 1:1.5, which was based on the average phenylalanine concentration determined in mouse serum by HPLC.

VI.B.5. Circular Dichroism Spectroscopy

Intensities and positions of positive and negative peaks for oligonucleotides in circular dichroism (CD) spectra correspond to exciton interactions induced by stacking of hydrophobic bases in asymmetric helices.[45,46,52] Aptamer and target concentrations were 2 μM in 1× Ringer's buffer. Thiolated aptamers were heated at 95 °C for 5 min and cooled to room temperature slowly to relax DNA molecules into extended conformations. Spectra were collected using a JASCO J-715 circular dichroism spectrophotometer (Oklahoma City, OK). Four scans with 0.5-nm resolution, 1.0-nm bandwidth, a 4-s response time, and a 20 nm/min scan rate were acquired per sample. Scans of 1× Ringer's solution were subtracted as background.

VI.B.6. High-Performance Liquid Chromatography

A modified *o*-phthalaldehyde-sulfite (OPA-S) method was used to analyze phenylalanine in serum samples.[53] On the day of analysis, 0.1 M perchloric acid (Acros Organic #AC42403) was freshly prepared, protected from light, and stored on ice. A series of 11 phenylalanine standards (0-50 μM) were prepared in 0.1 M perchloric acid to establish standard curves. Solutions for phenylalanine analysis *via* the OPA-S method included neutralization solution (0.4 M boric acid (Sigma #31144), pH 10.4-10.5) and derivatization solution (14.9 mM phthaldialdehyde (OPA, Sigma #P0657), 47.6 mM sodium sulfite (Sigma #71989), and 5% methanol (EMD #MMX04751) in 0.36 M boric acid, pH 10.4-10.5), which were prepared the day of analysis ~1 h before use and protected from light.

Serum samples were removed from a -80 °C freezer and thawed on wet ice. Then, 168 μL of ice-cold 0.1 M perchloric acid solution was added to 7 μL of each serum sample. Samples were briefly vortexed and centrifuged at 16,000 g at 4 °C for 15 min two times. After

each centrifugation, supernatants were immediately removed and transferred to clean microcentrifuge tubes on ice.

For derivatization, 50 µL each of the phenylalanine standard solutions and serum samples were neutralized with 50 µL of neutralization solution at room temperature in black microcentrifuge tubes, followed by addition of 50 µL of derivatization solution. The derivatization reaction was allowed to proceed for 10 min in the dark. Derivatization was stopped by adding 500 µL of the mobile phase (0.2 M phosphate buffer, pH 4.8, with 0.13 mM EDTA in 25% MeOH in deionized water) to each sample. Derivatized samples and standards were immediately analyzed by HPLC with electrochemical detection. The instrument was an Eicom integrated HPLC system (HTEC-500) that included an Insight Autosampler (Eicom Corporation, San Diego, CA). Electrochemical detection occurred at a pure graphite working electrode (WE-PG; Eicom Corporation, San Diego, CA) at an optimized applied potential of +650 mV *vs.* Ag/AgCl. The stationary phase was a Phenomenex Kinetex column (2.6 µm particle size, 3.0 mm ID × 10 mm, Phenomenex # 00D-4462-Y0, Phenomenex, Torrance, CA). Separation occurred at a flow rate of 350 µL/min. The column temperature was maintained at 30 °C. The retention time of phenylalanine was ~22 min.

VI.B.7. Statistics

Data for fluorescence assays and FET calibrated responses are reported as means ± standard errors of the means and were analyzed using GraphPad Prism v7.04 (GraphPad Software Inc., San Diego, CA) *via* one-way analysis of variance followed by Tukey's multiple comparisons *post hoc* tests. Cross-validation data for phenylalanine levels were analyzed by linear regression analysis. In all cases, $P<0.05$ was considered statistically significant.

VI.C. Results and Discussion

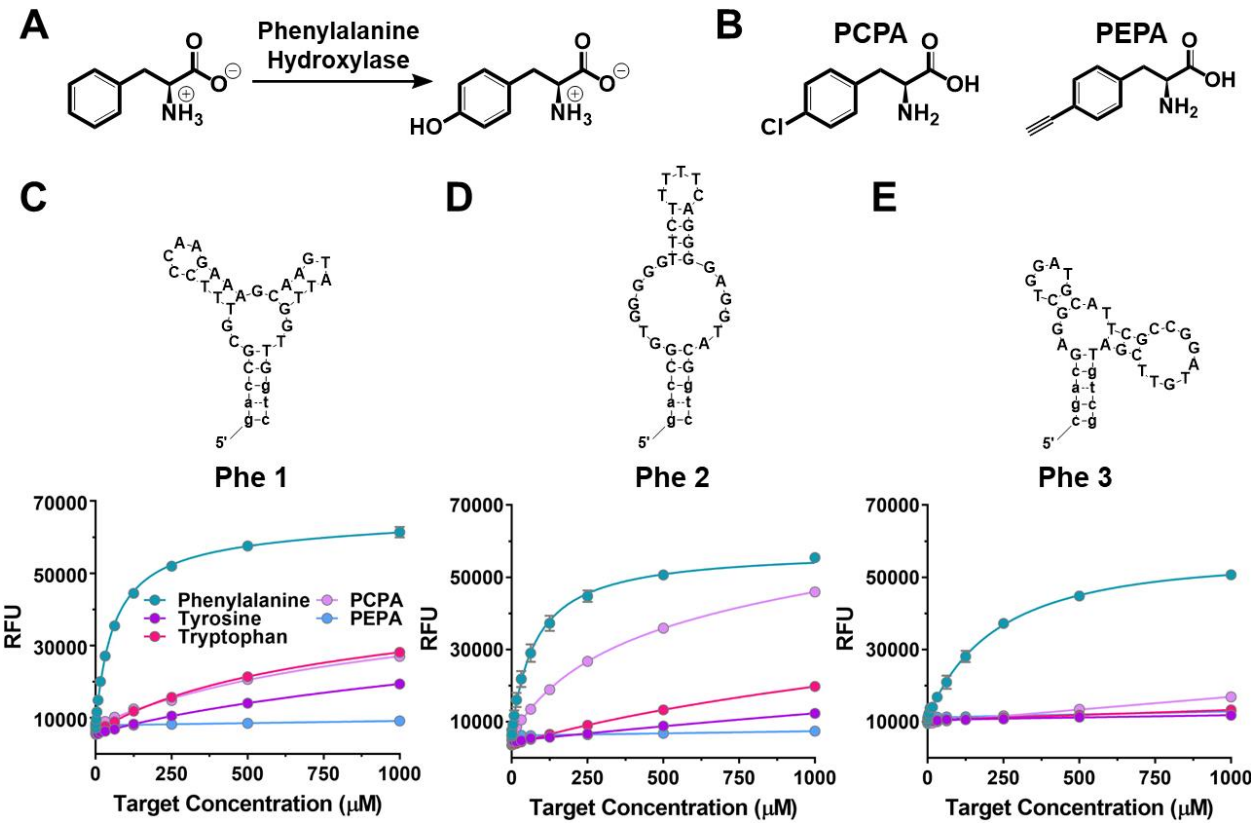

Figure VI.1. Aptamers for phenylalanine. (A) In humans and mice, phenylalanine is *para*-hydroxylated to form tyrosine by the liver enzyme phenylalanine hydroxylase (PAH). The genetic disorder phenylketonuria is caused by mutations in the PAH gene, which result in high blood and brain levels of phenylalanine. **(B)** Phenylalanine analogs *para*-chlorophenylalanine (PCPA) and *para*-ethynylphenylalanine (PEPA). **(C-E)** Three phenylalanine-specific aptamer sequences (Phe 1, Phe 2, and Phe 3) were isolated for sensor development. All three aptamers showed concentration-dependent responses towards phenylalanine determined *via* competitive fluorescence assays. Responses were measured for other aromatic amino acids (tyrosine and tryptophan) and the phenylalanine analogs (PCPA and PEPA). Fluorescence concentration curves enabled determination of solution dissociation constants (K_d) for Phe 1 (10 μM), Phe 2 (7 μM), and Phe 3 (16 μM). Here, N=6 for each phenylalanine concentration; N=3 for each nonspecific molecule concentration. Standard errors of the means for each datum were too small to be displayed in some cases; RFU is relative fluorescence units.

Three previously unreported DNA aptamer sequences that directly recognize the amino acid phenylalanine were identified *via* solution-phase, *in vitro* systematic evolution of ligands by exponential enrichment (SELEX) (**Figure VI.1C-E**).[39,41,42] Dissociation constants were

determined using competitive fluorescence assays.[30,40,41] Quencher-labeled complementary sequences (**Table VI.S1** and **Figure VI.S7**) were displaced from fluorescently labeled aptamer sequences upon phenylalanine binding resulting in increases in fluorescence intensities, as shown in **Figure VI.1C-E**.[30,40,41] Solution dissociation constants (K_d) were 10 μM, 7 μM, and 16 μM for Phe 1, Phe 2, and Phe 3, respectively. Dissociation constants measured for Phe 1 and 2 *via* dye displacement assays were consistent with those measured *via* competitive binding assays (**Figure VI.S8**). Dye displacement did not work for the Phe 3 aptamer. This result is sometimes the case for dye displacement, which is why we do not use this method as a primary means of determining dissociation constants.

Selections initially had been carried out using a strategy to try to increase aptamer selectivity towards low epitope targets by associating targets with metal complexes.[41] In addition to a previously reported aptamer sequence recognizing phenylalanine complexed with pentamethylcyclopentadienyl rhodium(III) (Cp*Rh) (sequence herein referred to as Phe-Cp*Rh 1),[41] two previously unreported sequences, Phe-Cp*Rh 2 and Phe-Cp*Rh 3 were characterized (**Figures VI.S2,S3**).

Selectivity testing for the three direct-detection phenylalanine aptamers using competitive florescence assays showed reduced (Phe 1 and Phe 2) or negligible (Phe 3) responses towards the endogenous aromatic amino acids tyrosine and tryptophan (**Figure VI.1C-E**). We also investigated selectivity of the direct-detection phenylalanine aptamers for two phenylalanine analogs, *para*-chlorophenylalanine (PCPA) and *para*-ethynylphenylalanine (PEPA) (**Figure VI.1B**), which potentially induce hyperphenylalaninemia in animal models (*vide infra*).[54-58] The Phe 3 aptamer showed minimal responses to PCPA or PEPA *via* competitive fluorescence assays (**Figure VI.1E**), in

contrast to Phe 1 and Phe 2 (**Figure VI.1C-D**), and the Phe-Cp*Rh aptamers (**Figure VI.S9**), all of which had appreciable responses to PCPA.

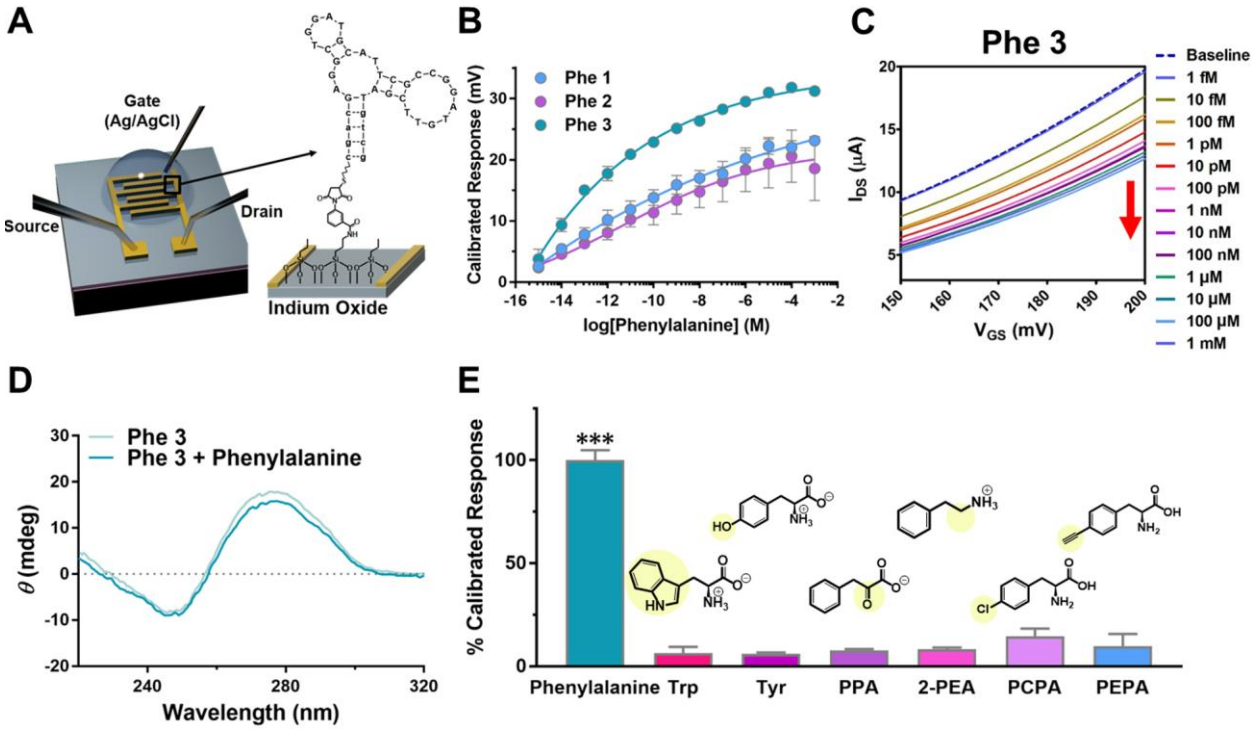

Figure VI.2. Detection of phenylalanine *via* aptamer-field-effect transistor sensors. (A) Schematic of the FET platform and surface chemistry. Here, FETs were composed of 4-nm thin-film In_2O_3 as the channel material, with a 10-nm Ti adhesion layer and a 30-nm top Au layer patterned as interdigitated electrodes over the semiconductor layer. Sensing was performed by applying a source-drain bias voltage, sweeping the gate voltage with respect to a Ag/AgCl reference electrode in a solution-gated configuration, and measuring changes in source-drain currents. Thiolated aptamers were tethered to semiconductor surfaces using *m*-maleimidobenzoyl-*N*-hydroxysuccinimide ester to crosslink thiol groups to amine-terminated silanes, co-self-assembled with methyl-terminated silanes, which served as spacer molecules to optimize aptamer surface densities for target recognition. **(B)** Each of three phenylalanine aptamers attached to FETs (Phe 1, Phe 2, Phe 3) produced concentration-dependent responses in 1× Ringer's solution. **(C)** Representative transfer (I_{DS}-V_{GS}) curves for Phe 3 aptamer-FETs upon increasing phenylalanine concentrations. **(D)** Circular dichroism spectra of Phe 3 in 1× Ringer's solution before and after introduction of phenylalanine (2 µM). Spectra shown are averages of N=3 spectra each. **(E)** The Phe 3 aptamer, when incorporated into FETs, had negligible responses to nonspecific targets, including tryptophan (Trp), tyrosine (Tyr), phenylypyruvic acid (PPA), 2-phenylethylamine (2-PEA), *para*-chlorophenylalanine (PCPA), or *para*-ethynylphenylalanine (PEPA) compared to phenylalanine (all targets at 100 µM) [$F(6, 10)=76$; $P<0.001$]. Error bars, are standard errors of the means with N=3 for **B**, and N=3 for phenylalanine, PCPA, and PEPA and N=2 for Trp, Tyr, PPA, and 2-PEA in **E**. ***$P<0.001$ *vs.* all nonspecific targets.

Next, each of the phenylalanine-specific aptamers was attached to the semiconducting channels of FETs for electronic detection of phenylalanine (**Figure VI.2A**).[29,30] As in our prior aptamer-FET studies, shortened,[59,60] thiolated aptamers were attached to In_2O_3 surfaces *via* covalent modification to self-assembled silanes using *m*-maleimidobenzoyl-*N*-hydroxysuccinimide as a crosslinker.[29,30] Field-effect transistors were operated in a top-gate setup. The source-drain current (I_{DS}) was measured while sweeping the gate voltage (V_{GS}) during target exposure (**Figure VI.2A**).[29,30] Reorganization of surface-tethered negatively charged oligonucleotides occurred in close proximity to metal-oxide semiconducting surfaces upon target capture to gate FET transconductances resulting in target-concentration-dependent current changes under physiological ionic conditions (**Figure VI.2B**).[30]

Phenylalanine-aptamer-FETs showed a wide range of concentration-dependent responses to phenylalanine (fM detection limit) in 1× Ringer's solution, which mimics the ionic composition of the plasma fraction of human blood (**Figure VI.2B**). Sensing in physiological buffers that have similar ion concentrations to the target biological matrix is important for evaluating oligonucleotide receptors because interactions with different types and concentrations of solution ions may result in alternate aptamer secondary structures and thus, differences in sensor sensitivities and selectivities.[61,62]

We also tested one of the aptamers recognizing phenylalanine complexed with Cp*Rh when attached to FETs, as an example of the use of this type of aptamer. The Phe-Cp*Rh 2 aptamer showed similar concentration-dependent responses (**Figure VI.S2D**) to those of the direct detection sequences (**Figure VI.2B**), suggesting that metal complexation to increase sensitivity, which would complicate point-of-care or at-home monitoring

approaches, is unnecessary[41] and direct phenylalanine detection is sufficient in the context of FET sensors.

Target-concentration-dependent decreases in current were observed for FET transfer curves (I_{DS}-V_{GS} sweeps) for each of the three direct sensing aptamers (**Figures VI.2C**, **VI.S10**). We attribute decreases in FET transfer characteristics on *n*-type semiconductors to a dominant effect of negatively charged DNA aptamer backbones moving closer to semiconductor channel surfaces to increase electrostatic repulsion of charge carriers (band bending) and to gate transconductance upon target binding.[30] We previously determined that aptamer-FET small-molecule sensing is due to gating associated with the reorganization of charged DNA aptamer backbones and not to target charge. Target-aptamer interaction can reorient aptamer charge toward or away from semiconductor channels, based on specific aptamers.[30]

We performed circular dichroism (CD) spectroscopy to investigate target-induced changes in aptamer secondary structures for the three phenylalanine direct-sensing aptamers, as we have been able to associate CD spectral changes with individual aptamer-FET responses.[30] The spectra for Phe 3 showed a small but reproducible decrease in peak intensity at 280 nm after target capture, potentially corresponding to target-induced formation of hairpin motifs (**Figure VI.2D**).[52] Spectra showed negligible changes in peak positions or intensities for Phe 1 or Phe 2 upon association with phenylalanine (**Figure VI.S11**). These findings suggest that the latter two aptamers do not form new secondary structural motifs upon target recognition and that all three aptamers primarily undergo adaptive target binding largely involving pre-formed secondary structures.[30]

Of the three direct-detection phenylalanine aptamers, Phe 3 showed the largest target-related responses and the smallest replication variability when integrated with FETs (**Figure VI.2B**). The Phe 3 aptamer also showed the highest selectivity towards nonspecific molecules compared to Phe 1 and Phe 2 in competitive fluorescence assays (**Figure VI.1C-E**); thus, we focused on investigating this sequence further. To test selectivity on FETs, we measured the responses of Phe 3-aptamer-FETs to the aromatic amino acid tryptophan, the phenylalanine metabolites tyrosine, phenylpyruvic acid, and 2-phenylethylamine, and the two phenylalanine analogs (**Figure VI.2E**). Sensor responses upon exposure to 100 μM solutions of five of the nonspecific molecules were <10% of the average response to an equivalent concentration of phenylalanine; responses to PCPA were 15% of the average phenylalanine response. Concentrations of nonspecific molecules were selected based on their physiologically relevant concentrations.[63-65] As a further indication of selectivity, responses of FETs functionalized with a scrambled version of the Phe 3 sequence having the same numbers and types of nucleotides as the correct Phe 3 aptamer sequence but with a different predicted secondary structure were negligible (**Figure VI.S5**).

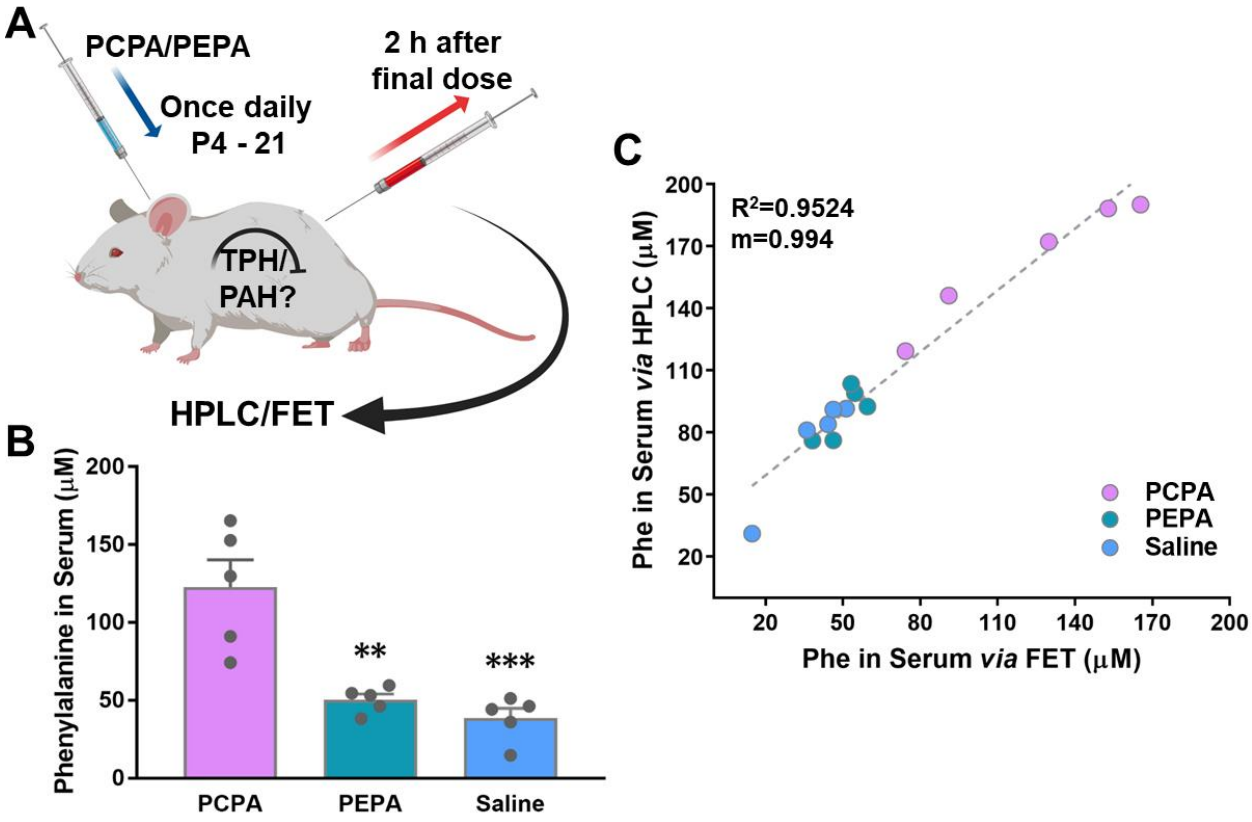

Figure VI.3. Aptamer-field-effect transistors (FETs) differentiate serum phenylalanine levels. (A) Schematic illustration of the *in vivo* experimental design. Mice were treated once per day with *para*-chlorophenylalanine (PCPA) or *para*-ethynylphenylalanine (PEPA) during postnatal days (P)4-21. These phenylalanine analogs inhibit tryptophan hydroxylase (TPH). Some studies suggest that PCPA may *also* inhibit phenylalanine hydroxylase (PAH). Serum samples were collected 2 h after the final injection of each analog on P21. Phenylalanine concentrations were measured by Phe 3-aptamer-FETs and cross-correlated with high-performance liquid chromatography (HPLC) as a reference method (**Figure VI.S12**). **(B)** Mice treated with PCPA had modestly elevated serum phenylalanine concentrations compared to mice treated with PEPA or saline [$F(2,12)=17.3$; $P<0.01$]. Data points depict levels from individual animals. Error bars are standard errors of the means with $N=5$ for each treatment group. $^{**}P<0.01$ *vs.* PCPA; $^{***}P<0.001$ *vs.* PCPA. **(C)** Correlation of phenylalanine concentrations measured in individual mouse serum samples *via* aptamer-FETs *vs.* HPLC with the corresponding linearity index (R^2) and regression slope (m). $P=0.762$ (Run's test), deviation from linearity is not significant.

To investigate Phe 3-aptamer-FET detection of clinically relevant phenylalanine levels, we measured phenylalanine in serum (diluted with 1× Ringer's solution) from mice injected daily with PCPA, PEPA, or saline during postnatal days 4-21 (**Figure VI.3A**). This

postnatal period in mice is the human developmental equivalent of the last trimester of pregnancy and the first postnatal year.[66,67] We selected this treatment period because it is important for determining the impact of elevated phenylalanine levels on cortical axon development.[68] Both *para*-substituted phenylalanine analogs inhibit tryptophan hydroxylase (TPH), which converts dietary tryptophan to 5-hydroxytryptophan. The latter is decarboxylated to produce the neurotransmitter serotonin (5-hydroxytryptamine).[51,69-71] However, whereas PCPA has been reported to inhibit PAH activity, in addition to TPH,[54-58] PEPA has been suggested to lack inhibitory effects on PAH.[51]

Mice receiving PCPA showed a doubling of the concentration of serum phenylalanine levels (individual levels ranging from ~90 to 160 μM) compared to mice exposed to PEPA or saline (**Figure VI.3B**). Phenylalanine concentrations in mouse serum samples were cross-validated *via* HPLC with electrochemical detection (**Figure VI.S12**). Individual phenylalanine serum sample levels determined using aptamer-FETs were highly correlated when compared to those measured by HPLC (R^2=0.95; **Figure VI.3C**). The slope of the regression line correlating phenylalanine levels determined by both methods was ~1 indicating that Phe 3-aptamer-FETs accurately reported phenylalanine levels.

Phenylalanine levels detected by aptamer-FETs in PCPA-treated mice (~120 μM) were at the low end of the range of serum levels in humans with modestly elevated phenylalanine, *i.e.*, PKU patients adhering to dietary restrictions, and possibly, phenylalanine levels in some PKU carriers, *i.e.*, individuals with one mutant PAH allele (*ca.* one in 50 Caucasians).[72,73] Thus, aptamer-FETs can be used to differentiate modest yet physiologically relevant changes in phenylalanine levels.

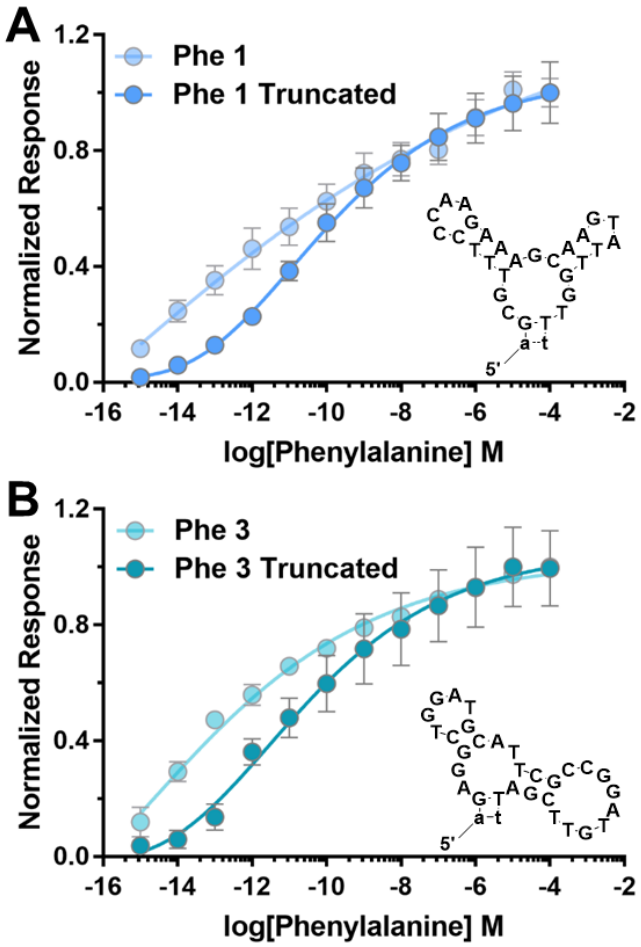

Figure VI.4. Tuning aptamer-field-effect transistor (FET) responses *via* aptamer stem truncation. (A-B) Aptamer-FET sensing of phenylalanine with truncated versions of Phe 1 and Phe 3 aptamers, respectively (truncated sequences are shown in the corresponding insets). Normalized response data for phenylalanine sensing on FETs using unmodified Phe 1 and Phe 3 sequences are presented for comparison and are reproduced from **Figure VI.2B**. Error bars are standard errors of the means with *N*=3 for all data.

The Phe 3 aptamer-FETs were sufficient to detect biologically relevant differences in phenylalanine levels in diluted serum (**Figure VI.3**). Removing base pairs from aptamer stem regions destabilizes aptamer secondary structures, particularly in stem-loop aptamers isolated by solution SELEX where stem closure plays an important role in identifying target-specific sequences.[59,74-76] We reasoned that stem truncation could be used to shift aptamer-

FET sensitivity ranges closer to the therapeutic range of PKU patients, thereby reducing the need for serum dilution.

Strategically deleting complementary C-G base pairs (C-G base pairs form three hydrogen bonds *vs.* A-T base pairs, which are weaker in forming only two hydrogen bonds) in the stem regions of Phe 1 and Phe 3 (**Table VI.S2**) shifted the corresponding aptamer-FET concentration curves to the right, *i.e.*, towards higher phenylalanine concentrations (**Figure VI.4**). These modifications also increased the steepness of the concentration curves such that small differences in phenylalanine levels in the steepest regions of these curves would be more highly differentiable.

Notably, the serum phenylalanine concentration range in PKU patients is ~10-1000 μM.[1] Thus, narrowing the sensitivity range of aptamer-FET sensors, in addition to reducing the binding affinity, *i.e.*, shifting to higher K_d, advances this strategy toward an at-home monitoring scenario wherein phenylalanine might be determined in whole blood from finger or heel sticks without the need for dilution. Stem destabilization, in addition to decreasing aptamer densities,[30] and/or tuning FET characteristics[77] and measurement parameters can eventually be combined to achieve phenylalanine detection in undiluted blood.

There are numerous benefits and opportunities for at-home phenylalanine monitoring. In a National Institutes of Health (NIH) consensus panel on "PKU: screening and management", the NIH recommended the development of reliable home testing methods for measuring phenylalanine to increase adherence to dietary treatments.[78] There is consensus from PKU patients that at-home measurement of phenylalanine will make disease management, *i.e.*, following a PKU diet and/or enzyme substitution dosing, easier to achieve

and to maintain throughout life.[26] National Institutes of Health guidelines for monitoring frequency in PKU patients are once weekly during the first year of life, twice per month for individuals 1-12 years of age, and at least monthly thereafter. In women with PKU prior to and during pregnancy and lactation, frequency should increase to at least weekly.

Phenylalanine has been determined using chromatographic,[79,80] plasmonic,[81] and fluorimetric techniques.[79,82-84] These methods involve specialized laboratory instrumentation and sometimes, complex extractions. As such, these methods are largely incompatible with point-of-care or at-home monitoring. Colorimetric, paper-based detection platforms show promise for PKU diagnosis and monitoring in low-resource settings,[85,86] but use enzyme-based recognition elements, which can lose activity over time due to denaturation.[87] Electrochemical signal transduction has been used for phenylalanine sensing[88,89] or a conductive electrode design involving graphene oxide, which is intrinsically defect prone and synthetically heterogeneous.[90] Hasanzadeh and coworkers[91,92] reported an electrochemical strategy involving phenylalanine capture *via* a previously reported RNA phenylalanine aptamer (K_d~120 μM)[93] followed by phenylalanine oxidation at gold electrodes. Compared to RNA, aptamers comprised of DNA are advantageous in terms of higher stability when exposed to biological matrices, such as serum.[94]

VI.D. Conclusions and Prospects

We have identified three new DNA-based receptors that recognize the biochemically and medically important target phenylalanine. We also report two new aptamers that recognize a phenylalanine-organometallic complex (Phe-Cp*Rh). The direct-binding phenylalanine aptamers (and one of the Phe-Cp*Rh aptamers) were integrated with thin-film metal-oxide

field-effect transistors (FETs). Phenylalanine-FET sensors detected phenylalanine under physiological ionic conditions over six orders of magnitude with fM detection limits. Sensors incorporating the Phe 3 direct-detection aptamer showed exceptional selectivity for phenylalanine *vs.* similarly structured aromatic amino acids and metabolites. The accuracy and precision of Phe 3 aptamer-FET sensors were excellent compared to a gold-standard laboratory method.[62]

The ability to differentiate clinically relevant differences in serum phenylalanine levels with a minimal dilution step demonstrates the capability of aptamer-FETs for future use in electronic point-of-care devices for PKU diagnosis and management. In principle, aptamer-FET sensors can also be used for *in vivo* monitoring to investigate transiently induced or permanently maintained (through continuous administration of PCPA or *via* mice with constitutive reductions in PAH)[95] elevations in phenylalanine. Rapid monitoring in PKU animal models will enable investigating how changes in PAH activity or diet impact temporally resolved phenylalanine levels.

In sum, DNA aptamers are readily synthesized[96] and the FET fabrication methods used here are straightforward and easily scaled up. We have miniaturized[29] and nanostructured[77] In_2O_3 thin-film FETs using low-cost soft-lithographic methods.[97-99] We have also fabricated In_2O_3 FETs on flexible substrates[100] demonstrating capabilities to tailor device performance and architectures for specific biomedical applications.

Aptamer-FET sensors can be rapidly deployed, with minor adjustments, at the point-of-care level, *e.g.*, in clinical laboratories. While not the focus of this work, we have developed prototype instrumentation and analysis software that is low-cost, has a relatively small footprint, and can perform multiplexed FET sensing. Translation for at-home monitoring will

require additional development of FET-measurement technology to reduce size for portability, *i.e.*, hand-held devices, and validation in clinical samples.[101] We anticipate that phenylalanine sensing *via* aptamer-FETs will improve phenylketonuria disease management and monitoring in other at-risk populations.

VI.E. Supplementary Materials

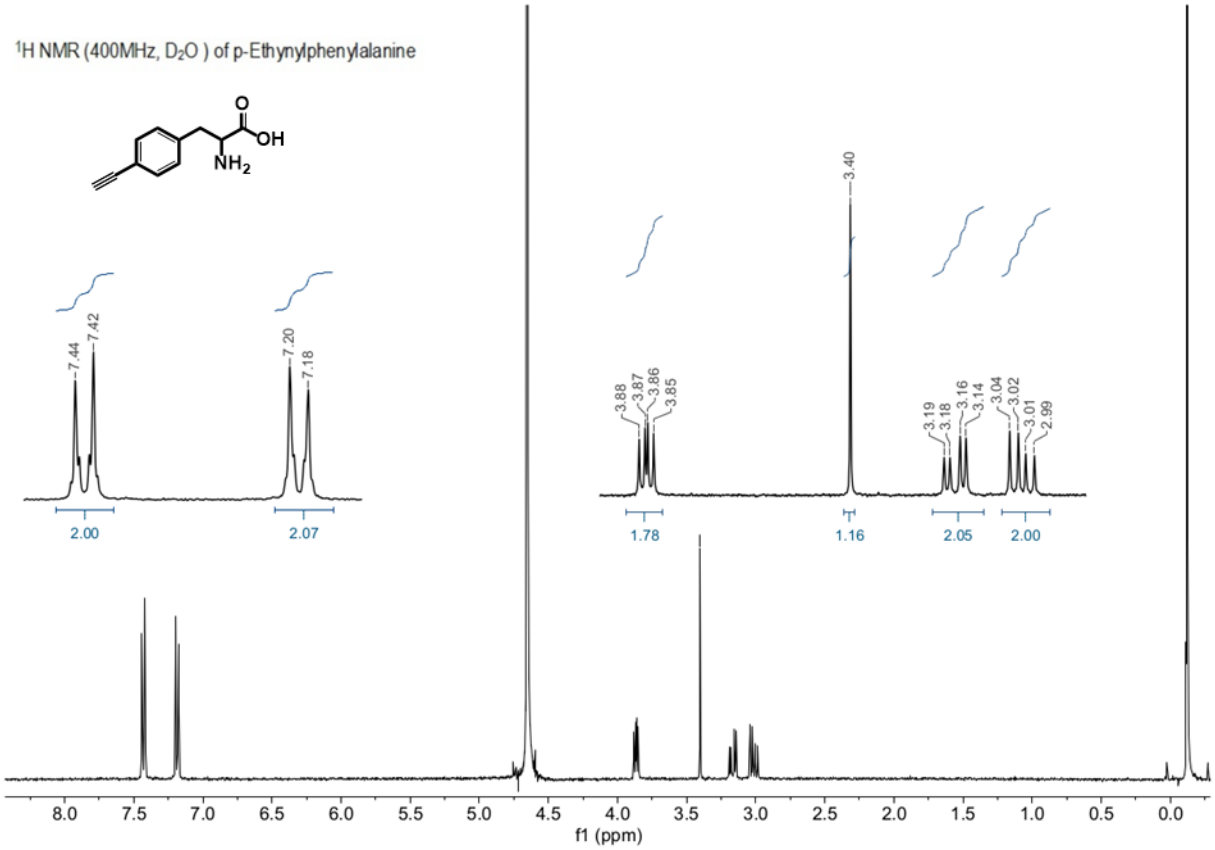

Figure VI.S1. ^{1}H Nuclear magnetic resonance spectrum of *para*-ethynylphenylalanine.

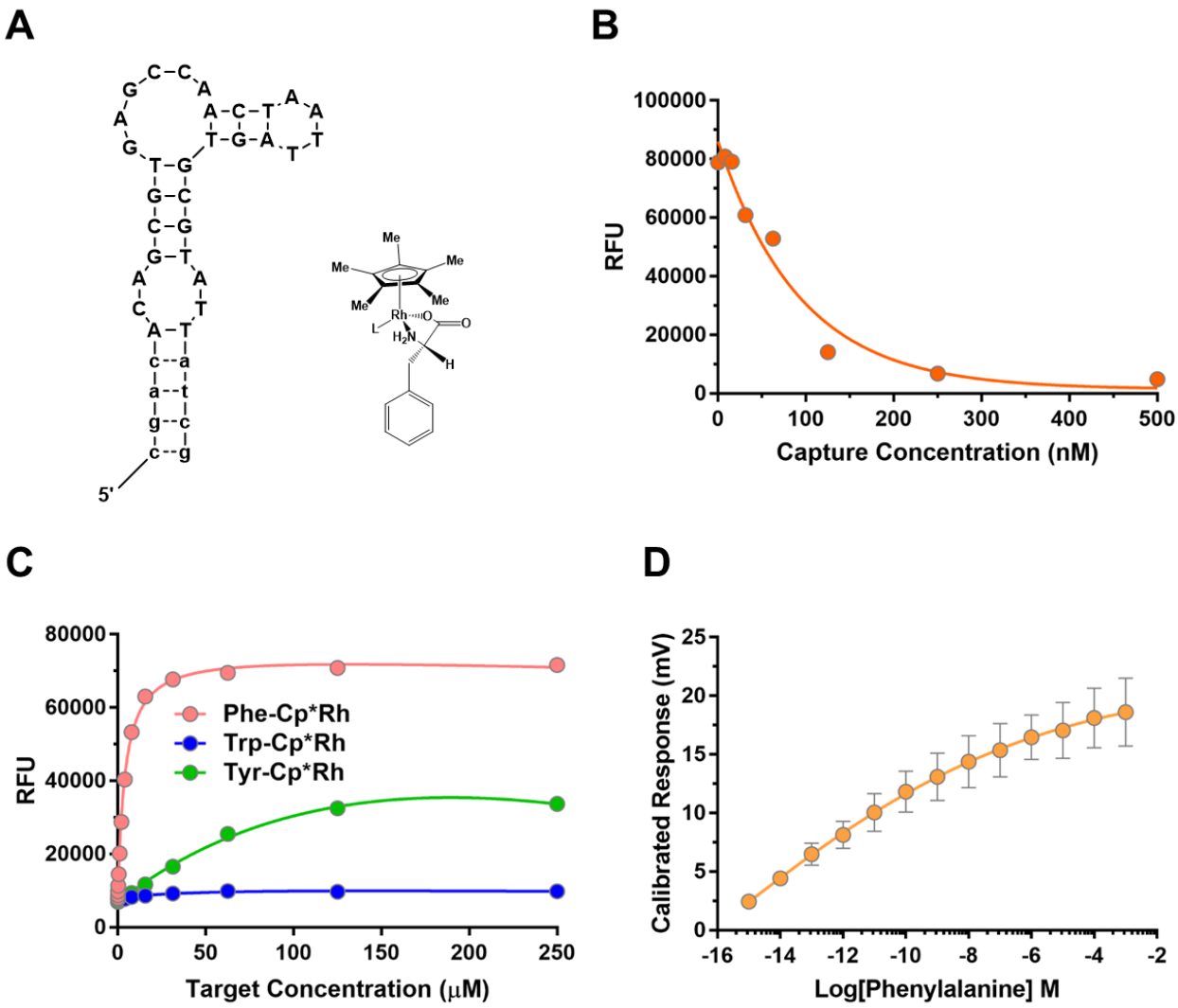

Figure VI.S2. Characterization of a phenylalanine-pentamethylcyclopentadienyl rhodium complex (Phe-Cp*Rh 2)-specific aptamer. **(A)** Aptamer sequence (left) isolated for specificity for Phe-Cp*Rh (right). **(B)** Quenching curve for Phe-Cp*Rh 2. **(C)** Competitive fluorescence assay to investigate selectivity of Phe-Cp*Rh 2. A solution K_d of ~0.8 μM was determined from the fluorescence concentration curve. **(D)** Field-effect transistor sensing using Phe-Cp*Rh 2 demonstrated responses over a wide range of concentrations (fM-mM). For B, C, and D, *N*=3 with error bars representing standard errors of the means, which are smaller than the data points shown in B and C; RFU is relative fluorescence units.

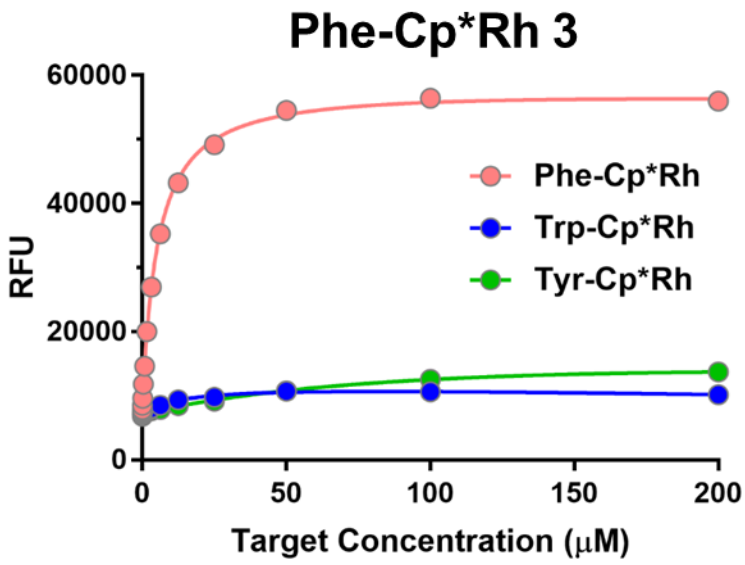

Figure VI.S3. Competitive fluorescence assay of Phe-Cp*Rh 3 to investigate selectivity for rhodium complexes (Cp*Rh) with tryptophan (Trp) or tyrosine (Tyr) *vs* phenylalanine. A solution K_d of ~70 nM was determined from the phenylalanine fluorescence concentration curve.

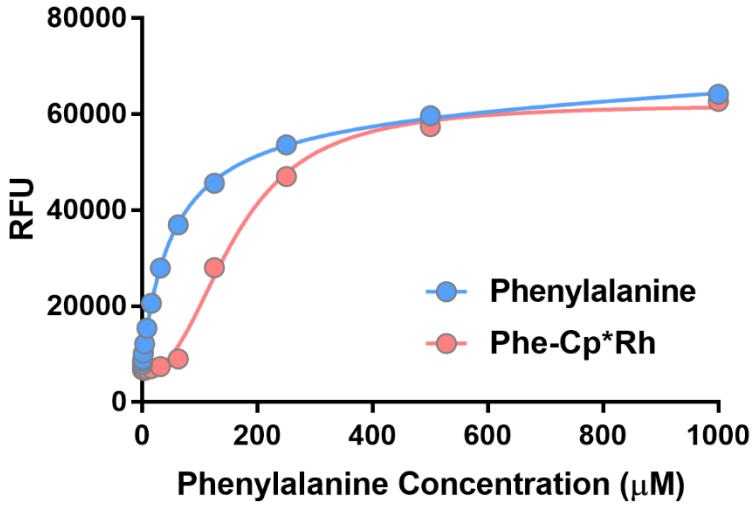

Figure VI.S4. Competitive fluorescence assay of Phe 1 upon exposure to free phenylalanine *vs.* coincubation with an excess of phenylalanine in combination with the organometallic complex (Cp*Rh) to form Phe-Cp*Rh+free phenylalanine. *N*=3 with error bars representing standard errors of the means, which are smaller than the data points shown; RFU is relative fluorescence units.

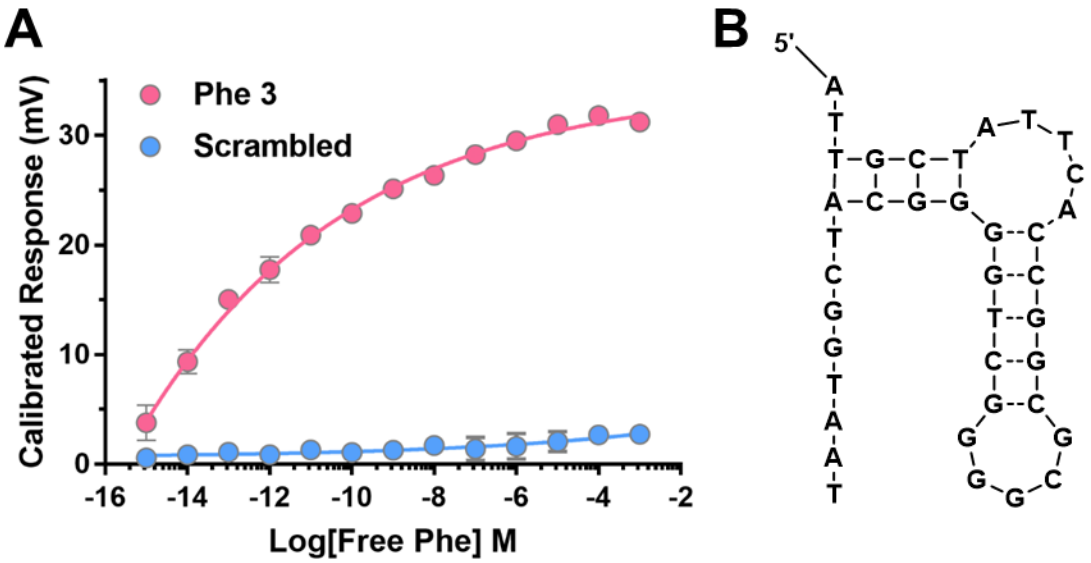

Figure VI.S5. (A) Field-effect transistor sensing of phenylalalnine using a **(B)** scrambled sequence, *i.e.*, the same numbers and types of nucleotides as Phe 3, but with a different predicted secondary structure. Negligible responses were observed over all concentrations tested for the scrambled sequence. Data for the correct Phe 3 sequence are presented for reference and are the same data depicted in main text **Figure VI.2B**. Error bars are standard errors of the means with *N*=3 for Phe 3 and *N*=2 for the scrambled sequence.

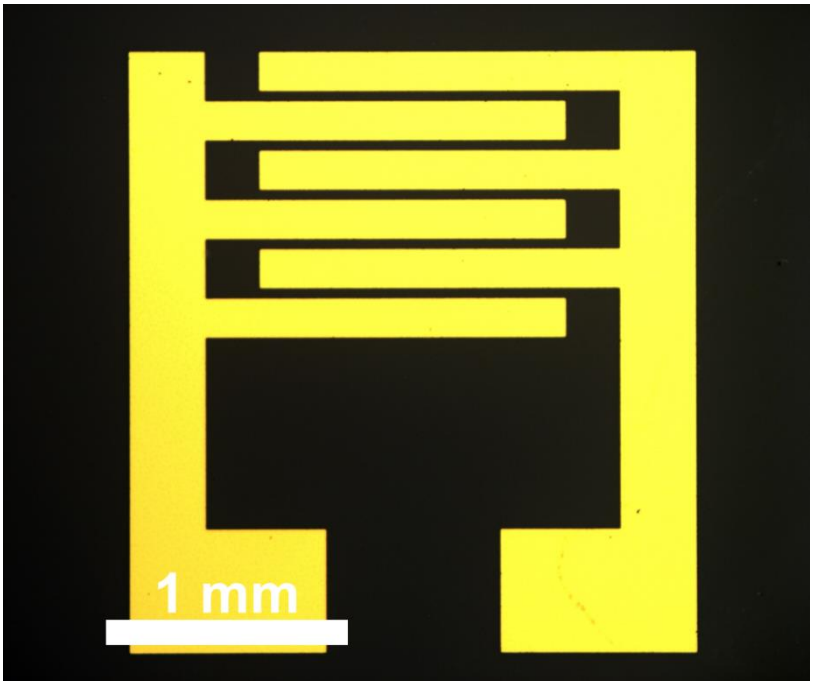

Figure VI.S6. Optical microscopy image of an individual field-effect transistor (FET) representative of FETs used throughout all experiments.

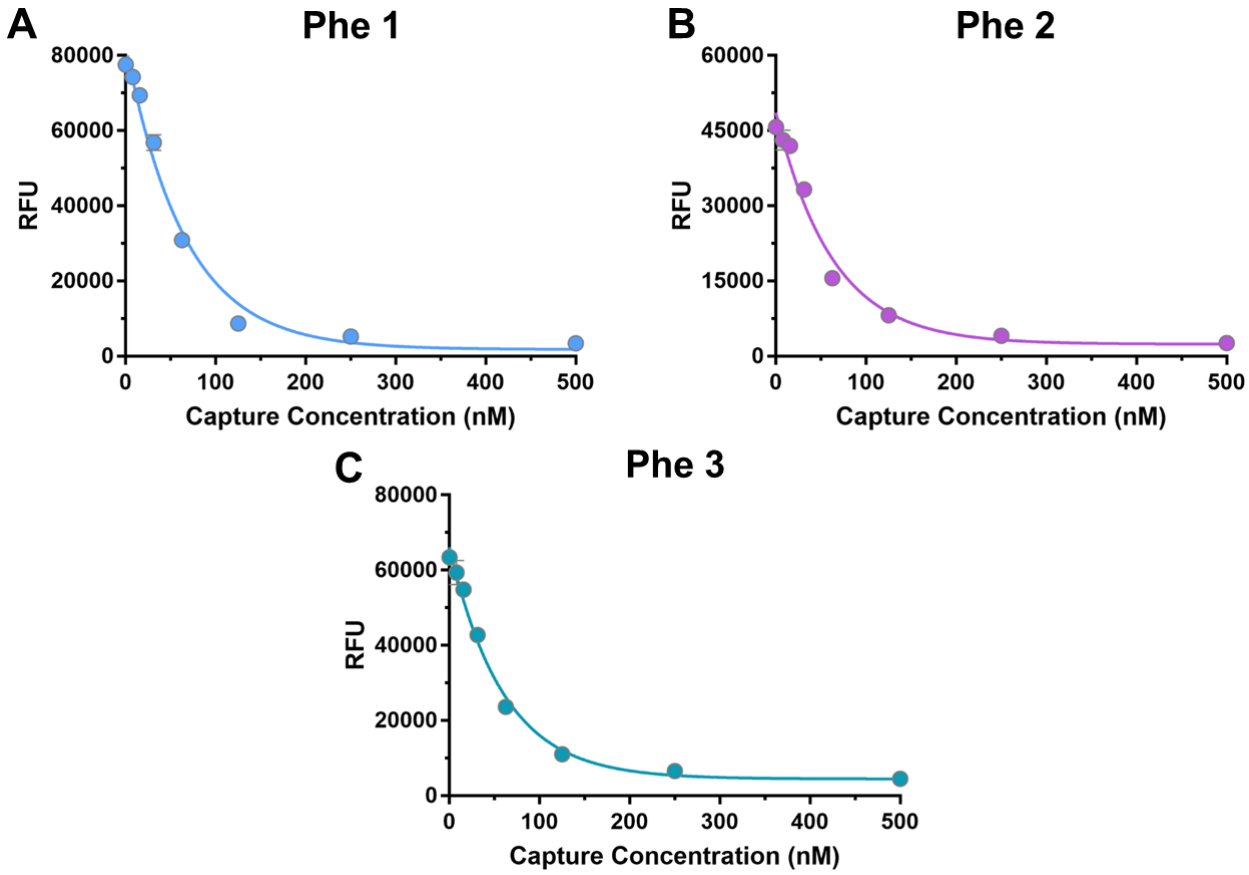

Figure VI.S7. **(A-C)** Fluorescence quenching curves for Phe 1, Phe 2, and Phe 3, respectively. For A-C, *N*=3 with error bars representing standard errors of the means, which are smaller than the data points shown; RFU is relative fluorescence units.

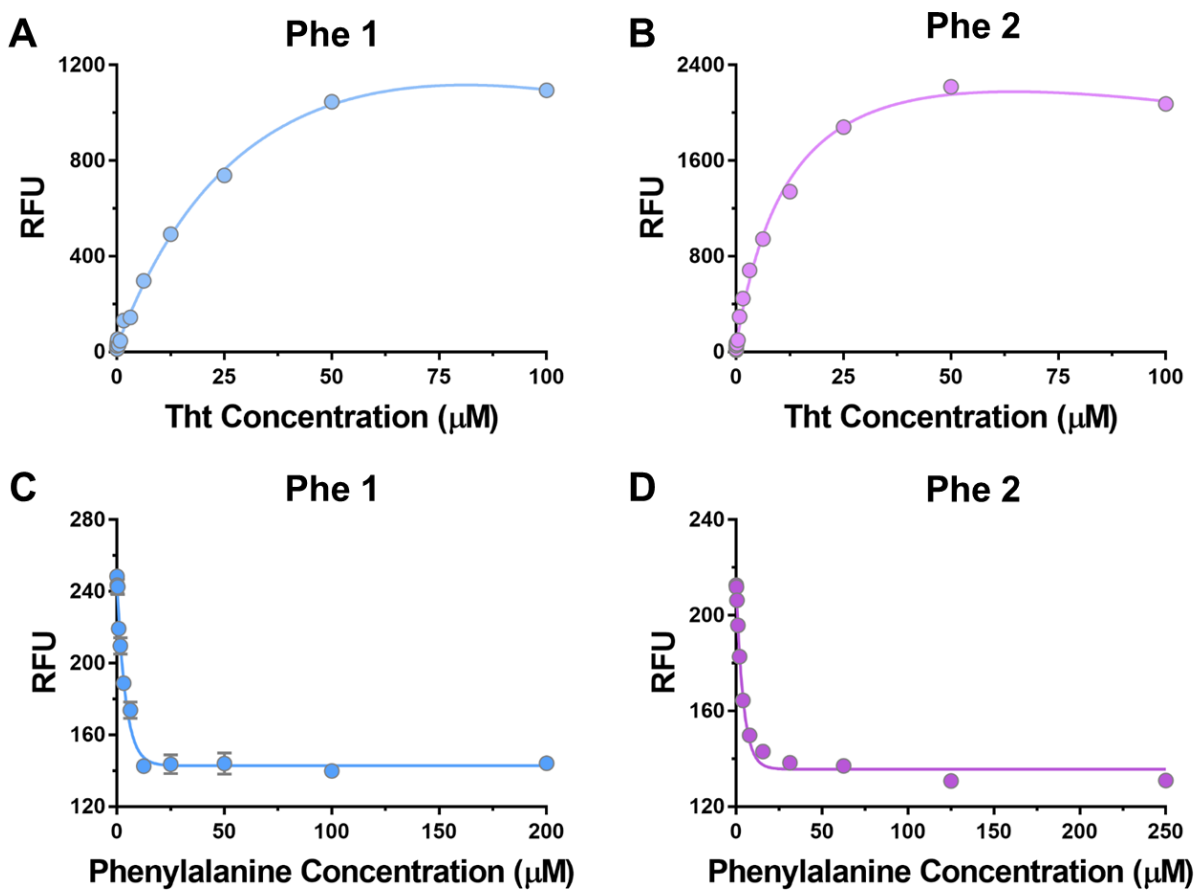

Figure VI.S8. Thioflavin T (Tht) dye displacement assays. **(A-B)** Thioflavin T binding and **(C-D)** displacement curves for Phe 1 and 2, respectively. Solution dissociation constants (K_d) calculated for Phe 1 (10 μM) and Phe 2 (6 μM) were consistent with those measured *via* competitive binding assays (**Figure VI.1**). Note, Tht binding/displacement does not occur universally for all aptamers, *e.g.*, Phe 3, and is contingent on DNA secondary structural motifs. For A-D, *N*=3 with error bars representing standard errors of the means, which are smaller than the data points shown in some cases; RFU is relative fluorescence units.[102,103]

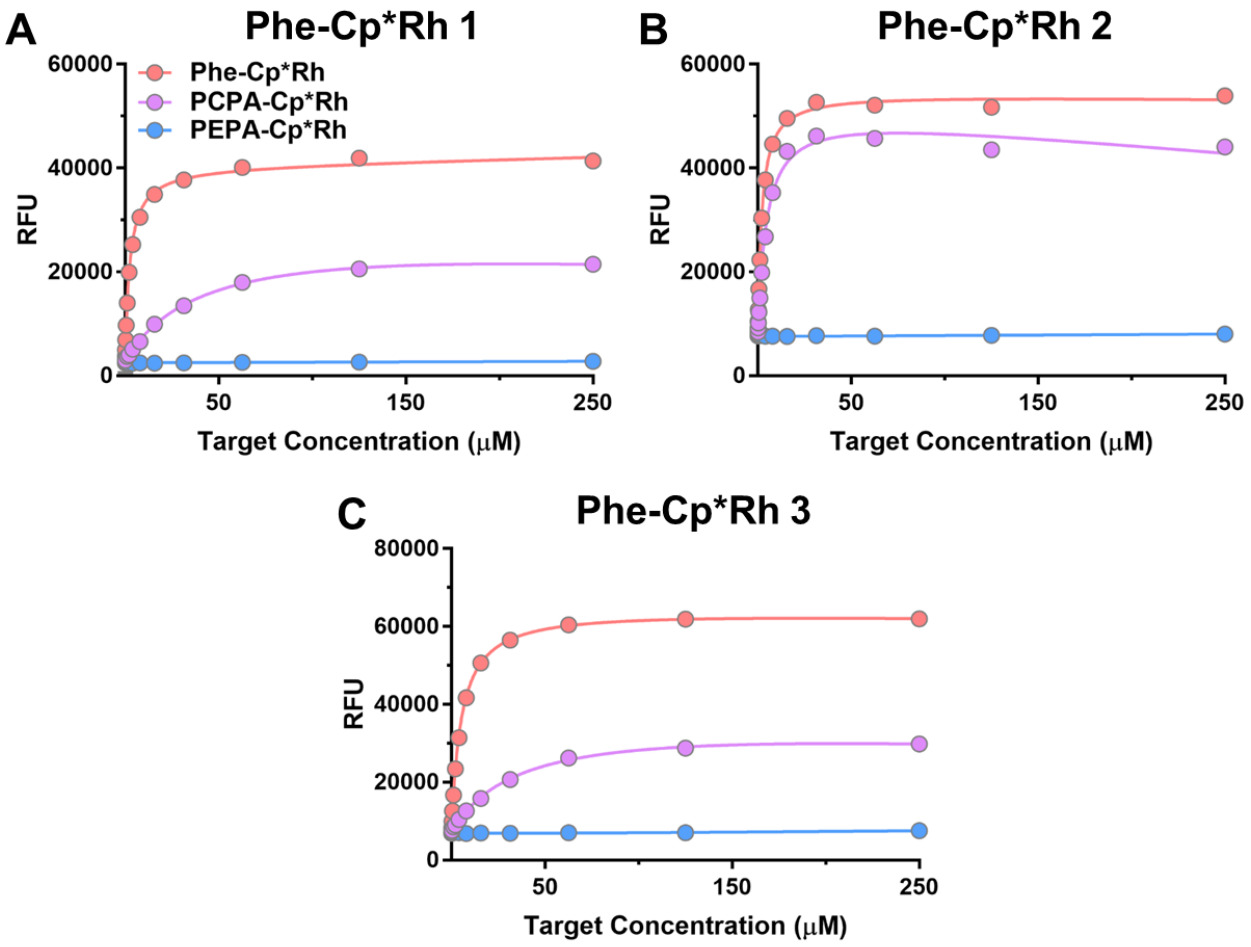

Figure VI.S9. Selectivity data for **(A)** the previously reported[41] (Phe-Cp*Rh 1) and **(B-C)** newly isolated (Phe-Cp*Rh 2, Phe-Cp*Rh 3) Phe-Cp*Rh aptamers *via* competitive fluorescence assays towards *para*-chlorophenylalanine (PCPA) or *para*-ethynylphenylalanine (PEPA). All three aptamers showed varying degrees of cross-reactivity with PCPA and minimal responses to PEPA. For A-C, *N*=3 with error bars representing standard errors of the means, which are smaller than the data points shown; RFU is relative fluorescence units.

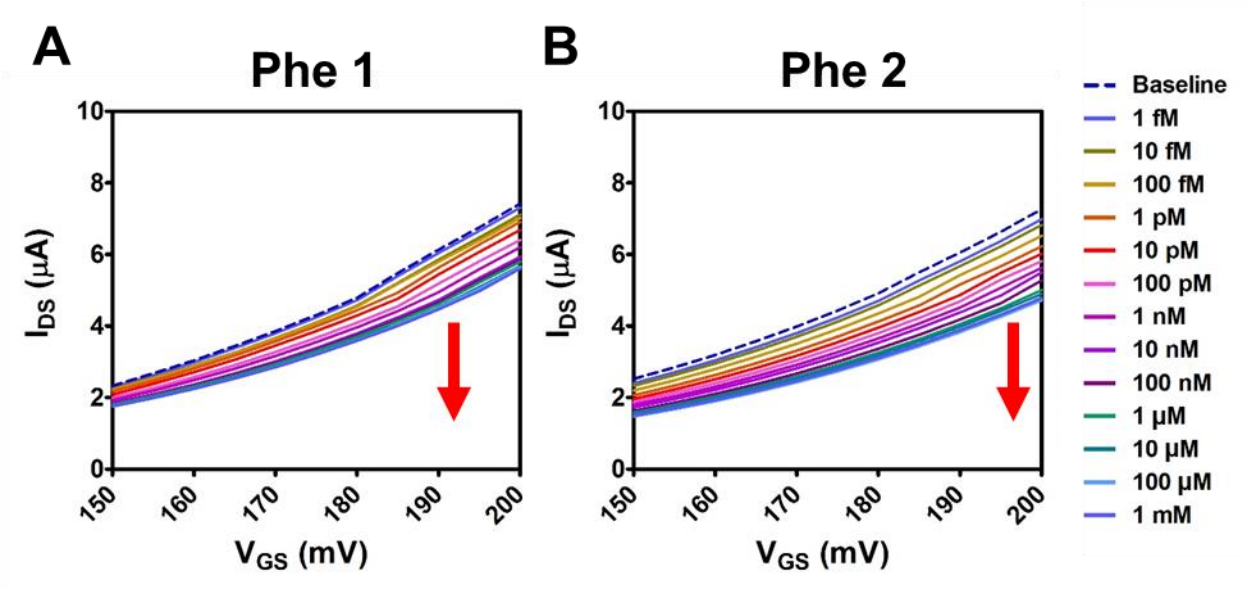

Figure VI.S10. (A-B) Transfer characteristics (I-V curves) of field-effect transistors functionalized with the phenylalanine-specific aptamers Phe 1 and Phe 2 upon exposure to increasing concentrations of phenylalanine in 1× Ringer's solution.

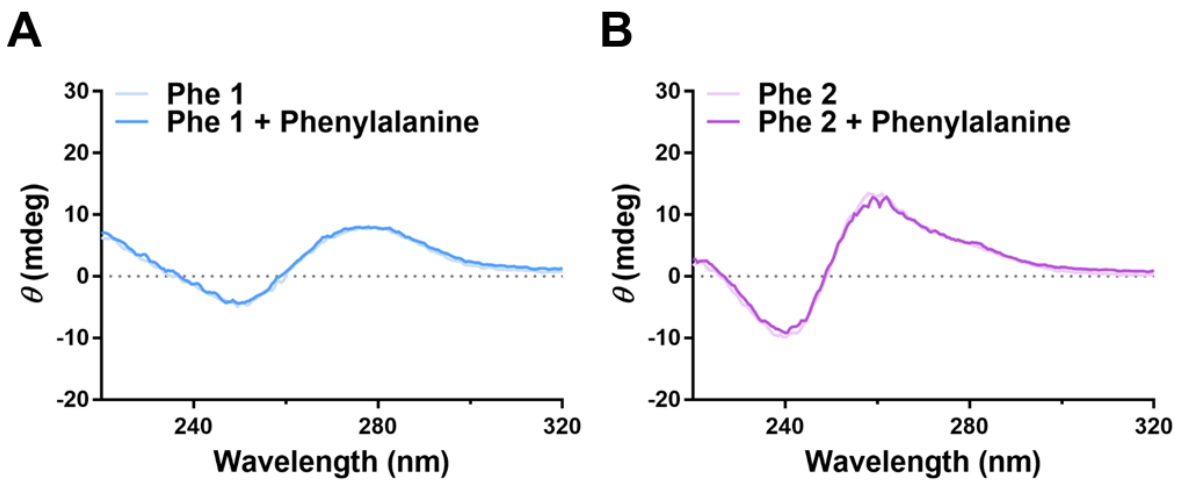

Figure VI.S11. (A-B) Circular dichroism spectra of Phe 1 and Phe 2 in 1× Ringer's solution before and after introduction of phenylalanine (2 μM). A peak at 280 nm for Phe 1 suggests the presence of B-DNA in the secondary structure, while a peak at 270 nm for Phe 2 suggests the presence of a parallel G-quadruplex.[30,45,46] Spectra shown in **(A-B)** are averages of N=2 spectra each.

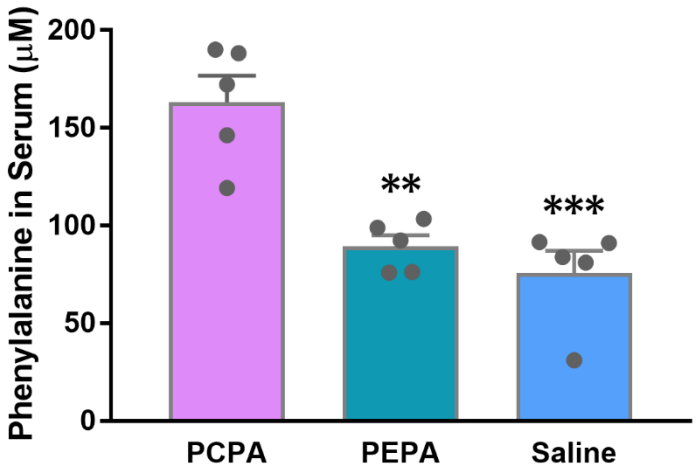

Figure VI.S12. High-performance liquid chromatography determination of phenylalanine levels in serum from mice treated with *para*-chlorophenylalanine (PCPA) or *para*-ethynylphenylalanine (PEPA) [F(2,12)=19.3; P<0.01]. Dots depict levels from individual animals. Error bars are standard errors of the means with *N*=5 per group. ***P*<0.01 *vs.* PCPA; ****P*<0.001 *vs.* PCPA; *ns* is not significant.

Aptamer	Strand	Sequence (5'→3')
Phe 1	**Sensor**	/56-FAM/CTC TCG GGA CGA CCG CGT TTC CCA AGA AAG CAA GTA TTG GTT GGT CGT CCC
	Capture	GGT CGT CCC GAG AG/3Dab/
Phe 2	**Sensor**	/56-FAM/CTC TCG GGA CGA CCG GTG GGG GTT CTT TTT CAG GGG AGG TAC GGT CGT CCC
	Capture	GTC GTC CCG AGA G/3Dab/
Phe 3	**Sensor**	/56-FAM/CTC TCG GGA CGA CGA GGC TGG ATG CAT TCG CCG GAT GTT CGA TGT CGT CCC
	Capture	GTC GTC CCG AGA G/3Dab/
Phe-Cp*Rh 2	**Sensor**	/56-FAM/CTC TCG GGA CGA CAC AGC GTG AGC CAA CTA ATT AGT GCG TAT TGT TCG TCC C
	Capture	TGT CGT CCC GAG AG/3Dab/
Phe-Cp*Rh 3	**Sensor**	/56-FAM/CTC TCG GGA CGA CCA CGG GAT ATC TTC AGG ATG GTG GTA ACT GGT CGT CCC
	Capture	GGT CGT CCC GAG AG/3Dab/

Table VI.S1. Previously unreported sequences of aptamers and associated complementary (capture) strands used for competitive fluorescence assays.

Aptamer	Strand	Sequence (5'→3')
Phe 1	**Thiolated**	/5ThioMC6-D/GA CCG CGT TTC CCA AGA AAG CAA GTA TTG GTT GGT C
	Stem Truncated	/5ThioMC6-D/AGC GTT TCC CAA GAA AGC AAG TAT TGG TTT
Phe 2	**Thiolated**	/5ThioMC6-D/GA CCG GTG GGG GTT CTT TTT CAG GGG AGG TAC GGT C
Phe 3	**Thiolated**	/5ThioMC6-D/CGA CGA GGC TGG ATG CAT TCG CCG GAT GTT CGA TGT CG
	Stem Truncated	/5ThioMC6-D/AGA GGC TGG ATG CAT TCG CCG GAT GTT CGA TT
	Scrambled	/5ThioMC6-D/ATT GCT ATT CAC CGG CGC GGG GCT GGG GCA TCG GTA AT
Phe-Cp*Rh 2	**Thiolated**	/5ThioMC6-D/CGA CAC AGC GTG AGC CAA CTA ATT AGT GCG TAT TGT CG

Table VI.S2. Sequences of shortened thiolated and further stem truncated aptamers used for field-effect transistor measurements. Stems were shortened based on previous studies of target induced stem closure.[59,60]

VI.F. References

(1) Blau, N.; van Spronsen, F. J.; Levy, H. L. Phenylketonuria. *Lancet* **2010,** *376*, 1417–1427.

(2) Friedman, P. A.; Kaufman, S.; Song Kang, E. Nature of the Molecular Defect in Phenylketonuria and Hyperphenylalaninaemia. *Nature* **1972,** *240*, 157–159.

(3) Mitchell, J. J.; Trakadis, Y. J.; Scriver, C. R. Phenylalanine Hydroxylase Deficiency. *Genet. Med.* **2011,** *13*, 697–707.

(4) Scriver, C. R.; Clow, C. L. Phenylketonuria: Epitome of Human Biochemical Genetics. *N. Engl. J. Med.* **1980,** *303*, 1336–1342.

(5) Scriver, C. R. The *PAH* Gene, Phenylketonuria, and a Paradigm Shift. *Hum. Mutat.* **2007,** *28*, 831–845.

(6) Penrose, L.; Quastel, J. H. Metabolic Studies in Phenylketonuria. *Biochem. J* **1937,** *31*, 266–274.

(7) Vockley, J.; Andersson, H. C.; Antshel, K. M.; Braverman, N. E.; Burton, B. K.; Frazier, D. M.; Mitchell, J.; Smith, W. E.; Thompson, B. H.; Berry, S. A. Phenylalanine Hydroxylase Deficiency: Diagnosis and Management Guideline. *Genet. Med.* **2013,** *16*, 188–200.

(8) Guttler, F. Hyperphenylalaninemia: Diagnosis and Classification of the Various Types of Phenylalanine Hydroxylase Deficiency in Childhood. *Acta Paediatr. Scand.* **1980,** *280*, 1–80.

(9) Fölling, A. Über Ausscheidung von Phenylbrenztraubensäure in den Harn als Stoffwechselanomalie in Verbindung mit Imbezillität. *Hoppe-Seyler's Z. Physiol. Chem.* **1934,** *227*, 169–176.

(10) Guthrie, R. Blood Screening for Phenylketonuria. *JAMA* **1961,** *178*, 863–863.

(11) Chace, D. H.; Millington, D. S.; Terada, N.; Kahler, S. G.; Roe, C. R.; Hofman, L. F. Rapid Diagnosis of Phenylketonuria by Quantitative Analysis for Phenylalanine and Tyrosine in Neonatal Blood Spots by Tandem Mass Spectrometry. *Clin. Chem.* **1993,** *39*, 66–71.

(12) Seashore, M. R.; Wappner, R.; Cho, S.; de la Cruz, F.; Wappner, R.; Cho, S.; Kronmal, R. A.; Schuett, V.; Seashore, M. R. Management of Phenylketonuria for Optimal Outcome: A Review of Guidelines for Phenylketonuria Management and a Report of Surveys of Parents, Patients, and Clinic Directors. *Pediatrics* **1999,** *104*, e68.

(13) Bickel, H.; Gerrard, J.; Hickmans, E. M. The Influence of Phenylalanine Intake on the Chemistry and Behaviour of a Phenylketonuria Child. *Acta Paediatr.* **1954,** *43*, 64–77.

(14) Armstrong, M. D.; Tyler, F. H. Studies on Phenylketonuria I. Restricted Phenylalanine Intake in Phenylketonuria. *J. Clin. Invest.* **1955,** *34*, 565–580.

(15) Walter, J. H.; White, F. J.; Hall, S. K.; MacDonald, A.; Rylance, G.; Boneh, A.; Francis, D. E.; Shortland, G. J.; Schmidt, M.; Vail, A. How Practical are Recommendations for Dietary Control in Phenylketonuria? *Lancet* **2002,** *360*, 55–57.

(16) Waisbren, S. E.; Mahon, B. E.; Schnell, R. R.; Levy, H. L. Predictors of Intelligence Quotient and Intelligence Quotient Change in Persons Treated for Phenylketonuria Early in Life. *Pediatrics* **1987,** *79*, 351–355.

(17) Longo, N.; Dimmock, D.; Levy, H.; Viau, K.; Bausell, H.; Bilder, D. A.; Burton, B.; Gross, C.; Northrup, H.; Rohr, F.; Sacharow, S.; Sanchez-Valle, A.; Stuy, M.; Thomas, J.; Vockley, J.; Zori, R.; Harding, C. O. Evidence- and Consensus-Based Recommendations for the Use of Pegvaliase in Adults with Phenylketonuria. *Genet. Med.* **2018**, DOI: 10.1038/s41436-41018-40403-z.

(18) Cleary, M.; Trefz, F.; Muntau, A. C.; Feillet, F.; van Spronsen, F. J.; Burlina, A.; Bélanger-Quintana, A.; Giżewska, M.; Gasteyger, C.; Bettiol, E.; Blau, N.; MacDonald, A. Fluctuations in Phenylalanine Concentrations in Phenylketonuria: A Review of Possible Relationships with Outcomes. *Mol. Genet. Metab.* **2013,** *110*, 418–423.

(19) Arnold, G. L.; Kramer, B. M.; Kirby, R. S.; Plumeau, P. B.; Blakely, E. M.; Cregan, L. S. S.; Davidson, P. W. Factors Affecting Cognitive, Motor, Behavioral and Executive Functioning in Children with Phenylketonuria. *Acta Paediatr.* **2007,** *87*, 565–570.

(20) Anastasoaie, V.; Kurzius, L.; Forbes, P.; Waisbren, S. Stability of Blood Phenylalanine Levels and IQ in Children with Phenylketonuria. *Mol. Genet. Metab.* **2008,** *95*, 17–20.

(21) Hood, A.; Grange, D. K.; Christ, S. E.; Steiner, R.; White, D. A. Variability in Phenylalanine Control Predicts IQ and Executive Abilities in Children with Phenylketonuria. *Mol. Genet. Metab.* **2014,** *111*, 445–451.

(22) Viau, K. S.; Wengreen, H. J.; Ernst, S. L.; Cantor, N. L.; Furtado, L. V.; Longo, N. Correlation of Age-Specific Phenylalanine Levels with Intellectual Outcome in Patients with Phenylketonuria. *J. Inherited Metab. Dis.* **2011,** *34*, 963–971.

(23) Markham, A. Pegvaliase: First Global Approval. *Biodrugs* **2018,** *32*, 391–395.

(24) Arroyo-Currás, N.; Ortega, G.; Copp, D. A.; Ploense, K. L.; Plaxco, Z. A.; Kippin, T. E.; Hespanha, J. P.; Plaxco, K. W. High-Precision Control of Plasma Drug Levels Using Feedback-Controlled Dosing. *ACS Pharmacol. Transl. Sci.* **2018,** *1*, 110–118.

(25) Cross, R. How Phenylketonuria, a Once-Neglected Disease, Became a Proving Ground for New Drugs *Chem. Eng. News*, July 2019, pp 24.

(26) Bilginsoy, C.; Waitzman, N.; Leonard, C. O.; Ernst, S. L. Living with Phenylketonuria: Perspectives of Patients and Their Families. *J. Inherited Metab. Dis.* **2005,** *28*, 639–649.

(27) Wendel, U.; Langenbeck, U. Towards Self-Monitoring and Self-Treatment in Phenylketonuria — A Way to Better Diet Compliance. *Eur. J. Pediatr.* **1996,** *155*, S105–S107.

(28) Clarke, S. F.; Foster, J. R. A History of Blood Glucose Meters and Their Role in Self-Monitoring of Diabetes Mellitus. *Br. J. Biomed. Sci.* **2012,** *69*, 83–93.

(29) Kim, J.; Rim, Y. S.; Chen, H.; Cao, H. H.; Nakatsuka, N.; Hinton, H. L.; Zhao, C.; Andrews, A. M.; Yang, Y.; Weiss, P. S. Fabrication of High-Performance Ultrathin In_2O_3 Film Field-Effect Transistors and Biosensors Using Chemical Lift-Off Lithography. *ACS Nano* **2015,** *9*, 4572–4582.

(30) Nakatsuka, N.; Yang, K.-A.; Abendroth, J. M.; Cheung, K. M.; Xu, X.; Yang, H.; Zhao, C.; Zhu, B.; Rim, Y. S.; Yang, Y.; Weiss, P. S.; Stojanović, M. N.; Andrews, A. M. Aptamer–Field-Effect Transistors Overcome Debye Length Limitations for Small-Molecule Sensing. *Science* **2018,** *362*, 319–324.

(31) Schöning, M. J.; Poghossian, A. Recent Advances in Biologically Sensitive Field-Effect Transistors (BioFETs). *Analyst* **2002,** *127*, 1137–1151.

(32) Allen, B. L.; Kichambare, P. D.; Star, A. Carbon Nanotube Field-Effect-Transistor-Based Biosensors. *Adv. Mater.* **2007,** *19*, 1439–1451.

(33) Curreli, M.; Zhang, R.; Ishikawa, F. N.; Chang, H.; Cote, R. J.; Zhou, C.; Thompson, M. E. Real-Time, Label-Free Detection of Biological Entities Using Nanowire-Based FETs. *IEEE Trans. Nanotechnol.* **2008,** *7*, 651–667.

(34) Li, B.-R.; Hsieh, Y.-J.; Chen, Y.-X.; Chung, Y.-T.; Pan, C.-Y.; Chen, Y.-T. An Ultrasensitive Nanowire-Transistor Biosensor for Detecting Dopamine Release from Living PC12 Cells under Hypoxic Stimulation. *J. Am. Chem. Soc.* **2013,** *135*, 16034–16037.

(35) So, H.-M.; Won, K.; Kim, Y. H.; Kim, B.-K.; Ryu, B. H.; Na, P. S.; Kim, H.; Lee, J.-O. Single-Walled Carbon Nanotube Biosensors Using Aptamers as Molecular Recognition Elements. *J. Am. Chem. Soc.* **2005,** *127*, 11906–11907.

(36) Green, N. S.; Norton, M. L. Interactions of DNA with Graphene and Sensing Applications of Graphene Field-Effect Transistor Devices: A Review. *Anal. Chim. Acta* **2015,** *853*, 127–142.

(37) Lung Khung, Y.; Narducci, D. Synergizing Nucleic Acid Aptamers with 1-Dimensional Nanostructures as Label-Free Field-Effect Transistor Biosensors. *Biosens. Bioelectron.* **2013,** *50*, 278–293.

(38) Vacic, A.; Criscione, J. M.; Rajan, N. K.; Stern, E.; Fahmy, T. M.; Reed, M. A. Determination of Molecular Configuration by Debye Length Modulation. *J. Am. Chem. Soc.* **2011,** *133*, 13886–13889.

(39) Nutiu, R.; Li, Y. *In Vitro* Selection of Structure-Switching Signaling Aptamers. *Angew. Chem. Int. Ed.* **2005,** *44*, 1061–1065.

(40) Yang, K.-A.; Pei, R.; Stefanovic, D.; Stojanović, M. N. Optimizing Cross-Reactivity with Evolutionary Search for Sensors. *J. Am. Chem. Soc.* **2012,** *134*, 1642–1647.

(41) Yang, K.-A.; Barbu, M.; Halim, M.; Pallavi, P.; Kim, B.; Kolpashchikov, D. M.; Pecic, S.; Taylor, S.; Worgall, T. S.; Stojanović, M. N. Recognition and Sensing of Low-Epitope Targets *via* Ternary Complexes with Oligonucleotides and Synthetic Receptors. *Nat. Chem.* **2014,** *6*, 1003–1008.

(42) Yang, K.-A.; Pei, R.; Stojanović, M. N. *In Vitro* Selection and Amplification Protocols for Isolation of Aptameric Sensors for Small Molecules. *Methods* **2016,** *106*, 58–65.

(43) Xiao, Y.; Uzawa, T.; White, R. J.; DeMartini, D.; Plaxco, K. W. On the Signaling of Electrochemical Aptamer-Based Sensors: Collision- and Folding-Based Mechanisms. *Electroanalysis* **2009,** *21*, 1267–1271.

(44) Neumann, O.; Zhang, D.; Tam, F.; Lal, S.; Wittung-Stafshede, P.; Halas, N. J. Direct Optical Detection of Aptamer Conformational Changes Induced by Target Molecules. *Anal. Chem.* **2009,** *81*, 10002–10006.

(45) Liu, W.; Fu, Y.; Zheng, B.; Cheng, S.; Li, W.; Lau, T.-C.; Liang, H. Kinetics and Mechanism of Conformational Changes in a G-Quadruplex of Thrombin-Binding Aptamer Induced by Pb^{2+}. *J. Phys. Chem. B* **2011,** *115*, 13051–13056.

(46) Nagatoishi, S.; Tanaka, Y.; Tsumoto, K. Circular Dichroism Spectra Demonstrate Formation of the Thrombin-Binding DNA Aptamer G-Quadruplex under Stabilizing-Cation-Deficient Conditions. *Biochem. Biophys. Res. Commun.* **2007,** *352*, 812–817.

(47) Kayser, B.; Altman, J.; Beck, W. Alkyne Bridged α- Amino Acids by Palladium Mediated Coupling of Alkynes with *N*-*t*-boc-4-Iodo-Phenylalanine Methyl Ester. *Tetrahedron* **1997,** *53*, 2475–2484.

(48) Lowary, T.; Meldal, M.; Helmboldt, A.; Vasella, A.; Bock, K. Novel Type of Rigid C-Linked Glycosylacetylene−Phenylalanine Building Blocks for Combinatorial Synthesis of C-Linked Glycopeptides. *J. Org. Chem.* **1998,** *63*, 9657–9668.

(49) Ishikawa, F. N.; Curreli, M.; Chang, H.-K.; Chen, P.-C.; Zhang, R.; Cote, R. J.; Thompson, M. E.; Zhou, C. A Calibration Method for Nanowire Biosensors to Suppress Device-to-Device Variation. *ACS Nano* **2009,** *3*, 3969–3976.

(50) Alexandre, C.; Popa, D.; Fabre, V.; Bouali, S.; Venault, P.; Lesch, K.-P.; Hamon, M.; Adrien, J. Early Life Blockade of 5-Hydroxytryptamine 1A Receptors Normalizes Sleep and Depression-Like Behavior in Adult Knock-Out Mice Lacking the Serotonin Transporter. *J. Neurosci.* **2006,** *26*, 5554–5564.

(51) Stokes, A. H.; Xu, Y.; Daunais, J. A.; Tamir, H.; Gershon, M. D.; Butkerait, P.; Kayser, B.; Altman, J.; Beck, W.; Vrana, K. E. *p*-Ethynylphenylalanine: A Potent Inhibitor of Tryptophan Hydroxylase. *J. Neurochem.* **2008,** *74*, 2067–2073.

(52) Kypr, J.; Kejnovská, I.; Renčiuk, D.; Vorlíčková, M. Circular Dichroism and Conformational Polymorphism of DNA. *Nucleic Acids Res.* **2009,** *37*, 1713–1725.

(53) Bongiovanni, R.; Yamamoto, B. K.; Jaskiw, G. E. Improved Method for the Measurement of Large Neutral Amino Acids in Biological Matrices. *J. Chromatogr. B: Biomed. Sci. Appl.* **2001,** *754*, 369–376.

(54) Guroff, G. Irreversible *in Vivo* Inhibition of Rat Liver Phenylalanine Hydroxylase by *p*-Chlorophenylalanine. *Arch. Biochem. Biophys.* **1969,** *134*, 610–611.

(55) Kilbey, M. M.; Harris, R. T. Behavioral, Biochemical and Maturation Effects of Early DL-*para*-Chlorophenylalanine Treatment. *Psychopharmacologia* **1971,** *19*, 334–346.

(56) Lipton, M. A.; Gordon, R.; Guroff, G.; Udenfriend, S. *p*-Chlorophenylalanine-Induced Chemical Manifestations of Phenylketonuria in Rats. *Science* **1967,** *156*, 248–250.

(57) Vorhees, C. V.; Butcher, R. E.; Berry, H. K. Progress in Experimental Phenylketonuria: A Critical Review. *Neurosci. Biobehav. Rev.* **1981,** *5*, 177–190.

(58) Koe, B. K.; Weissman, A. *p*-Chlorophenylalanine: A Specific Depletor of Brain Serotonin. *J. Pharmacol. Exp. Ther.* **1966,** *154*, 499–516.

(59) Kent, A. D.; Spiropulos, N. G.; Heemstra, J. M. General Approach for Engineering Small-Molecule-Binding DNA Split Aptamers. *Anal. Chem.* **2013,** *85*, 9916-9923.

(60) Yang, K.-A.; Chun, H.; Zhang, Y.; Pecic, S.; Nakatsuka, N.; Andrews, A. M.; Worgall, T. S.; Stojanovic, M. N. High-Affinity Nucleic-Acid-Based Receptors for Steroids. *ACS Chem. Biol.* **2017,** *12*, 3103-3112.

(61) Mocci, F.; Laaksonen, A. Insight into Nucleic Acid Counterion Interactions from Inside Molecular Dynamics Simulations is "Worth Its Salt". *Soft Matter* **2012,** *8*, 9268-9284.

(62) Bakker, E. So, You Have a Great New Sensor. How Will You Validate It? *ACS Sensors* **2018,** *3*, 1431–1431.

(63) Stein, W. H.; Moore, S. The Free Amino Acids of Human Blood Plasma. *J. Biol. Chem.* **1954,** *211*, 915–926.

(64) Jervis, G. A.; Drejza, E. J. Phenylketonuria: Blood Levels of Phenylpyruvic and ortho-Hydroxyphenylacetic Acids. *Clin. Chim. Acta* **1966,** *13*, 435–441.

(65) Huebert, N. D.; Schwach, V.; Richter, G.; Zreika, M.; Hinze, C.; Haegele, K. D. The Measurement of β-Phenylethylamine in Human Plasma and Rat Brain. *Anal. Biochem.* **1994,** *221*, 42–47.

(66) Clancy, B.; Kersh, B.; Hyde, J.; Darlington, R. B.; Anand, K. J. S.; Finlay, B. L. Web-Based Method for Translating Neurodevelopment from Laboratory Species to Humans. *Neuroinformatics* **2007,** *5*, 79–94.

(67) Workman, A. D.; Charvet, C. J.; Clancy, B.; Darlington, R. B.; Finlay, B. L. Modeling Transformations of Neurodevelopmental Sequences Across Mammalian Species. *J. Neurosci.* **2013,** *33*, 7368–7383.

(68) Larsen, D. D.; Callaway, E. M. Development of Layer-Specific Axonal Arborizations in Mouse Primary Somatosensory Cortex. *J. Comp. Neurol.* **2006,** *494*, 398–414.

(69) Lovenberg, W.; Jequier, E.; Sjoerdsma, A. Tryptophan Hydroxylation: Measurement in Pineal Gland, Brainstem, and Carcinoid Tumor. *Science* **1967,** *155*, 217–219.

(70) Somerville, A. R.; Whittle, B. A. The Interrelation of Hypothermia and Depletion of Noradrenaline, Dopamine and 5-Hydroxytryptamine from Brain by Reserpine, *p*-Chlorophenylalanine and α-Methylmetatyrosine. *Br. J. Pharmacol. Chemother.* **1967,** *31*, 120–131.

(71) Zimmer, L.; Luxen, A.; Giacomelli, F.; Pujol, J.-F. Short- and Long-Term Effects of *p*-Ethynylphenylalanine on Brain Serotonin Levels. *Neurochem. Res.* **2002,** *27*, 269–275.

(72) Hsia, D. Y. Y.; Driscoll, K. W.; Troll, W.; Eugene Knox, W. Detection by Phenylalanine Tolerance Tests of Heterozygous Carriers of Phenylketonuria. *Nature* **1956,** *178*, 1239–1240.

(73) Chen, H. In *Atlas of Genetic Diagnosis and Counseling*; Chen, H., Ed.; Springer New York: New York, NY, 2016.

(74) Stojanovic, M. N.; de Prada, P.; Landry, D. W. Aptamer-Based Folding Fluorescent Sensor for Cocaine. *J. Am. Chem. Soc.* **2001,** *123*, 4928-4931.

(75) Idili, A.; Gerson, J.; Parolo, C.; Kippin, T.; Plaxco, K. W. An Electrochemical Aptamer-Based Sensor for the Rapid and Convenient Measurement of L-Tryptophan. *Anal. Bioanal. Chem.* **2019,** *411*, 4629-4635.

(76) Ricci, F.; Vallée-Bélisle, A.; Simon, A. J.; Porchetta, A.; Plaxco, K. W. Using Nature's "Tricks" to Rationally Tune the Binding Properties of Biomolecular Receptors. *Acc. Chem. Res.* **2016,** *49*, 1884–1892.

(77) Zhao, C.; Xu, X.; Bae, S.-H.; Yang, Q.; Liu, W.; Belling, J. N.; Cheung, K. M.; Rim, Y. S.; Yang, Y.; Andrews, A. M.; Weiss, P. S. Large-Area, Ultrathin Metal-Oxide Semiconductor Nanoribbon Arrays Fabricated by Chemical Lift-Off Lithography. *Nano Lett.* **2018,** *18*, 5590–5595.

(78) National Institutes of Health Consensus Development Conference Statement: Phenylketonuria: Screening and Management, October 16–18, 2000. *Pediatrics* **2001,** *108*, 972–982.

(79) Kand'ár, R.; Žáková, P. Determination of Phenylalanine and Tyrosine in Plasma and Dried Blood Samples Using HPLC with Fluorescence Detection. *J. Chromatogr. B* **2009,** *877*, 3926–3929.

(80) Haghighi, F.; Talebpour, Z.; Amini, V.; Ahmadzadeh, A.; Farhadpour, M. A Fast High Performance Liquid Chromatographic (HPLC) Analysis of Amino Acid Phenylketonuria Disorder in Dried Blood Spots and Serum Samples, Employing C18 Monolithic Silica Columns and Photo Diode Array Detection. *Anal. Methods* **2015,** *7*, 7560–7567.

(81) Casey, C. N.; Campbell, S. E.; Gibson, U. J. Phenylalanine Detection Using Matrix Assisted Pulsed Laser Evaporation of Molecularly Imprinted Amphiphilic Block Copolymer Films. *Biosens. Bioelectron.* **2010,** *26*, 703–709.

(82) Zhang, K.; Yan, H.-T.; Zhou, T. Spectrofluorimetric Determination of Phenylalanine Based on Fluorescence Enhancement of Europium Ion Immobilized With Sol–Gel Method. *Spectrochim. Acta, Part A* **2011,** *83*, 155–160.

(83) Arakawa, T.; Koshida, T.; Gessei, T.; Miyajima, K.; Takahashi, D.; Kudo, H.; Yano, K.; Mitsubayashi, K. Biosensor for L-Phenylalanine Based on the Optical Detection of NADH Using a UV Light Emitting Diode. *Microchim. Acta* **2011,** *173*, 199–205.

(84) Girotti, S.; Ferri, E.; Ghini, S.; Budini, R.; Carrea, G.; Bovara, R.; Piazzi, S.; Merighi, R.; Roda, A. Bioluminescent Flow Sensor for L-Phenylalanine Determination in Serum. *Talanta* **1993,** *40*, 425–430.

(85) Thiessen, G.; Robinson, R.; De Los Reyes, K.; Monnat, R. J.; Fu, E. Conversion of a Laboratory-Based Test for Phenylalanine Detection to a Simple Paper-Based Format and Implications for PKU Screening in Low-Resource Settings. *Analyst* **2015,** *140*, 609–615.

(86) Robinson, R.; Wong, L.; Monnat, J. R.; Fu, E. Development of a Whole Blood Paper-Based Device for Phenylalanine Detection in the Context of PKU Therapy Monitoring. *Micromachines* **2016,** *7*, 28.

(87) Gouda, M. D.; Kumar, M. A.; Thakur, M. S.; Karanth, N. G. Enhancement of Operational Stability of an Enzyme Biosensor for Glucose and Sucrose Using Protein Based Stabilizing Agents. *Biosens. Bioelectron.* **2002,** *17*, 503-507.

(88) Naghib, S. M.; Rabiee, M.; Omidinia, E. Electrochemical Biosensor for L-Phenylalanine Based on a Gold Electrode Modified with Graphene Oxide Nanosheets and Chitosan. *Int. J. Electrochem. Sci.* **2014,** *9*, 2301–2315.

(89) Zaidi, S. A. Facile and Efficient Electrochemical Enantiomer Recognition of Phenylalanine Using β-Cyclodextrin Immobilized on Reduced Graphene Oxide. *Biosens. Bioelectron.* **2017,** *94*, 714–718.

(90) Reina, G.; González-Domínguez, J. M.; Criado, A.; Vázquez, E.; Bianco, A.; Prato, M. Promises, Facts and Challenges for Graphene in Biomedical Applications. *Chem. Soc. Rev.* **2017,** *46*, 4400–4416.

(91) Omidinia, E.; Shadjou, N.; Hasanzadeh, M. Aptamer-Based Biosensor for Detection of Phenylalanine at Physiological pH. *Appl. Biochem. Biotechnol.* **2014,** *172*, 2070–2080.

(92) Hasanzadeh, M.; Zargami, A.; Baghban, H. N.; Mokhtarzadeh, A.; Shadjou, N.; Mahboob, S. Aptamer-based Assay for Monitoring Genetic Disorder Phenylketonuria (PKU). *Int. J. Biol. Macromol.* **2018,** *116*, 735–743.

(93) Illangasekare, M.; Yarus, M. Phenylalanine-Binding RNAs and Genetic Code Evolution. *J. Mol. Evol.* **2002,** *54*, 298-311.

(94) Zhu, Q.; Shibata, T.; Kabashima, T.; Kai, M. Inhibition of HIV-1 Protease Expression in T Cells Owing to DNA Aptamer-Mediated Specific Delivery of siRNA. *Eur. J. Med. Chem.* **2012,** *56*, 396-399.

(95) Shedlovsky, A.; McDonald, J. D.; Symula, D.; Dove, W. F. Mouse Models of Human Phenylketonuria. *Genetics* **1993,** *134*, 1205-1210.

(96) Fraser, L. A.; Cheung, Y.-W.; Kinghorn, A. B.; Guo, W.; Shiu, S. C.-C.; Jinata, C.; Liu, M.; Bhuyan, S.; Nan, L.; Shum, H. C.; Tanner, J. A. Microfluidic Technology for Nucleic Acid Aptamer Evolution and Application. *Advanced Biosystems* **2019,** *3*, 1900012.

(97) Liao, W.-S.; Cheunkar, S.; Cao, H. H.; Bednar, H. R.; Weiss, P. S.; Andrews, A. M. Subtractive Patterning *via* Chemical Lift-Off Lithography. *Science* **2012,** *337*, 1517–1521.

(98) Xu, X.; Yang, Q.; Cheung, K. M.; Zhao, C.; Wattanatorn, N.; Belling, J. N.; Abendroth, J. M.; Slaughter, L. S.; Mirkin, C. A.; Andrews, A. M.; Weiss, P. S. Polymer-Pen Chemical Lift-Off Lithography. *Nano Lett.* **2017,** *17*, 3302–3311.

(99) Slaughter, L. S.; Cheung, K. M.; Kaappa, S.; Cao, H. H.; Yang, Q.; Young, T. D.; Serino, A. C.; Malola, S.; Olson, J. M.; Link, S.; Häkkinen, H.; Andrews, A. M.; Weiss, P. S. Patterning of Supported Gold Monolayers *via* Chemical Lift-Off Lithography. *Beilstein J. Nanotechnol.* **2017,** *8*, 2648–2661.

(100) Rim, Y. S.; Bae, S.-H.; Chen, H.; Yang, J. L.; Kim, J.; Andrews, A. M.; Weiss, P. S.; Yang, Y.; Tseng, H.-R. Printable Ultrathin Metal Oxide Semiconductor-Based Conformal Biosensors. *ACS Nano* **2015,** *9*, 12174–12181.

(101) Price, C. P.; Kricka, L. J. Improving Healthcare Accessibility Through Point-of-Care Technologies. *Clin. Chem.* **2007,** *53*, 1665–1675.

(102) Renaud de la Faverie, A.; Guédin, A.; Bedrat, A.; Yatsunyk, L. A.; Mergny, J.-L. Thioflavin T as a Fluorescence Light-Up Probe for G4 Formation. *Nucleic Acids Res.* **2014,** *42*, e65–e65.

(103) Zhu, J.; Yan, Z.; Zhou, W.; Liu, C.; Wang, J.; Wang, E. Lighting Up the Thioflavin T by Parallel-Stranded TG(GA)*n* DNA Homoduplexes. *ACS Sensors* **2018,** *3*, 1118–1125.

CHAPTER VII

Differentiating

Single-Nucleotide Polymorphisms

via Ultrathin-Film Field-Effect Transistors

VII.A. Introduction

Single nucleotide polymorphisms (SNPs), which are single base variations or substitutions in DNA, are the most common form of genetic variation in humans.[1-5] These SNPs occur on average once every *ca*. 1000 nucleotides in the human genome and contribute to individuality within humans (and other organisms).).[1-7] Single nucleotide polymorphisms can be found in coding and noncoding regions of DNA, and thus, in RNA (*e.g.*, mRNA, tRNA, miRNA).[8-13] The majority of SNPs have no noticeable effects on health or development. Nonetheless, a significant number of SNPs are known to be associated with disease susceptibility, cancers, and drug treatment responses. For example, a variety of SNPs have been suggested to be correlated with genetic susceptibility for common diseases such as asthma,[14] Alzheimer's disease,[15] β-thalassemia,[16] sickle cell disease,[17] different cancers,[11,18-21] and a variety of other diseases, as well as how certain populations respond to xenobiotics (both positively and negatively).[3,22] Thus, significant interest and efforts are aimed at identifying SNPs and their relationships with complex diseases and biological traits, and rapidly detecting specific SNPs in human patient populations to improve disease diagnostics, personalized healthcare, and precision medicine.[1-5]

Conventionally, SNPs are identified, detected, and profiled using techniques that require oligonucleotide amplification (*e.g.*, polymerase chain reaction, PCR)[5] and/or involve the use of fluorophore-labeled sequences (*e.g.*, molecular beacons, SNP microarrays).[5,23,24] These methods have had success in laboratory-based settings, but they are limited in terms of throughput, sensitivity, and accuracy,[5] impeding translation to clinical diagnostic applications. Alternately, techniques involving enzymatic reactions/digestions,[5] electrochemical detection,[25] nanopore sequencing,[26] mass spectrometry,[16,27] and high-

performance liquid chromatography[28] all show promise for SNP detection. Nonetheless, many of these latter methods also suffer from throughput issues, and are complex and labor intensive, and/or require the need for additional reagents, labeling, and/or amplification.

Applications in precision medicine and disease diagnostics, where analysis of large numbers of patient samples is needed, suggest that development of sensing platforms capable of direct, rapid, multiplexed, and label-free SNP detection without amplification would be useful. Field-effect transistor (FET) -based biosensors are platforms for electronic detection of biological analytes wherein target binding is transduced into electronic signals.[29-37] Transistor surfaces are typically modified with a receptor (*e.g.*, protein, antibody, nucleic acid) for molecular recognition of a variety of biologically relevant targets ranging from small molecules[29,30,37] to nucleic acids[38,39] and proteins,[40,41] with high sensitivity.

Previous examples of using FETs to detect DNA with specific sequences have established FET biosensors as promising platforms for electronic DNA detection.[42-47] Typically, FETs are functionalized with DNA or sometimes, peptide nucleic acids (PNAs)[48] to monitor DNA hybridization. Strategies to measure the kinetics of DNA hybridization have also been demonstrated using FETs, however these strategies focus on single (DNA) molecule detection,[49] which is inherently challenging. Many FET platforms for DNA detection involve the use of 1D or 2D materials (*e.g.*, graphene,[38,43,50] graphene oxide,[51] carbon nanotubes,[32] and semiconductor nanowires)[52] as their channel materials. However, these materials suffer from challenges associated with synthesis, material heterogeneity, device reproducibility, and robust functionalization.[35,53,54]

Here, we present a strategy for the differentiation of oligonucleotides towards the detection of SNPs, using ultrathin-film quasi-2D metal-oxide FETs. Previously, we demonstrated the use of this type of FET as biosensors for the sensitive and selective detection of a range of small molecules (*e.g.*, neurotransmitters, amino acids, sugars, and lipids) in complex biological fluids.[29,30,37] By functionalizing the semiconductor channel material of FETs with single-stranded DNA (ssDNA), we demonstrate the detection of complementary DNA hybridization. We distinguish FET responses associated with single base-pair mismatches of different types and locations in DNA to illustrate the potential for SNP genotyping. Investigating the mechanism of detection of ssDNA-FETS, we hypothesize that detection is contingent upon mismatch stability, and thus the degree of DNA hybridization (*i.e.*, density of dsDNA versus ssDNA) near the surface. Further, we show the potential of this platform for the detecting RNA with sequence variation at the single base level. The capability to differentiate nucleic acids that differ by a single base-pair using thin-film metal oxide FETs could enable development of electronic arrays for SNP genotyping.

VII.B. Experimental Methods

VII.B.1. DNA-Functionalized Field-Effect Transistor Fabrication and Assembly

Field-effect transistors were fabricated using ~4 nm In_2O_3 semiconductor films as channel materials to effect high surface-to-volume ratios.[29] Aqueous solutions (0.1 M) of indium(III) nitrate hydrate ($In(NO_3)_3 \bullet xH_2O$, 99.999%, Sigma 254215) were spin-coated at 3000 rpm for 30 s onto heavily doped silicon wafers (University Wafer, Boston, MA or WaferPro, San Jose, CA) having 100-nm thermally grown oxide layers. After In_2O_3 coating, substrates were pre-heated at 150 °C for 10 min followed by 3 h of annealing at 350 °C.[55] Source and drain

electrodes (10 nm Ti/30 nm Au) were deposited by electron-beam evaporation and patterned *via* standard photolithography.

To functionalize thin-film FETs with thiolated ssDNA, we first self-assembled mixed monolayers of (3-aminopropyl)trimethoxysilane and trimethoxy(propyl)silane (1:9 v/v ratio) using vapor-phase deposition on In_2O_3 surfaces at 40 °C for 1 h.[29,30,37] Substrates were then incubated with a 1 mM ethanolic solution of 1-dodecanethiol for 1 h to passivate Au electrodes *via* alkanethiol monolayer formation. After rinsing with ethanol, substrates were incubated with a 1 mM solution of 3-maleimidobenzoic acid *N*-hydroxysuccinimide ester (MBS) in a 1:9 (v/v) mixture of dimethyl sulfoxide and phosphate-buffered saline (1× PBS, pH 7.4, Fisher 10010023) for 30 min. Thiolated ssDNA (Integrated DNA Technologies, Coralville, IA) solutions were diluted to 1 μM in nuclease-free water and heated for 5 min at 95 °C followed by rapid cooling in an ice bath. Substrates were then incubated with ssDNA solutions in a humidified environment for 24 h, rinsed with deionized water, and dried under N_2 gas.

VII.B.2. DNA-Functionalized Field-Effect Transistor Measurements

Polydimethylsiloxane wells were sealed on individual FETs to hold target DNA solutions. Substrates had inter-FET distances that were ~2 mm and therefore, were large enough to enable isolation of single FET devices within the PDMS wells. Phosphate-buffered saline (0.1× PBS) was used as the electrolyte solution. The Ag/AgCl reference electrodes (World Precision Instruments, Inc., Sarasota, FL) were placed in sensing solutions in a top-gate (solution-gate) device configuration. Measurements were performed using a manual analytical probe station (Signatone, Gilroy, CA) equipped with a Keithley 4200A-SCS (Tektronix, Beaverton, OR) semiconductor parameter analyzer.

Solutions containing target DNA or RNA (1 μM; Integrated DNA Technologies, Coralville, IA) were incubated on top of single FETs. Sensing solutions were mixed with a pipet after addition of target oligonucleotides. Source-drain current (I_{DS}) transfer curves were obtained, wherein gate voltages (V_{GS}) were applied from 0 to 400 mV with a step voltage of 5 mV, every 5 min over a period of 30 min. The drain voltage (V_D) was held at 10 mV throughout. Five sweeps were averaged to determine each transfer curve. Calibrated responses were calculated by dividing the absolute sensor response (ΔI), which takes into account baseline subtraction, by the change in source-drain current with voltage sweep ($\Delta I_{DS}/\Delta V_G$).[56] Transistor responses at V_G=400 mV were used to calculate mean calibrated responses.

VII.B.3. DNA Melt Curves

To anneal oligonucleotides for melting temperature analysis, 2 μM solutions of probe DNA strands (the sequence that was functionalized to FET surfaces) and target sequences were prepared in a 1:1 ratio in 0.1x PBS buffer. Solutions were degassed with N_2 and incubated at 95 °C for 5 min before cooling slowly to room temperature using a programmable dry bath (ThermoFisher Scientific).

Measurements were conducted by first cooling solutions to 15 °C and subsequently ramping to 70 °C with a 6-s hold time at each 0.1 °C step. Absorption was recorded using a Hewlett-Packard HP8453 diode-array UV/Vis spectrophotometer (Palo Alto, CA, USA). Values were baseline corrected to absorption at 340 nm and normalized to relative absorption at 260 nm under fully denatured conditions.

VII.C. Results and Discussion

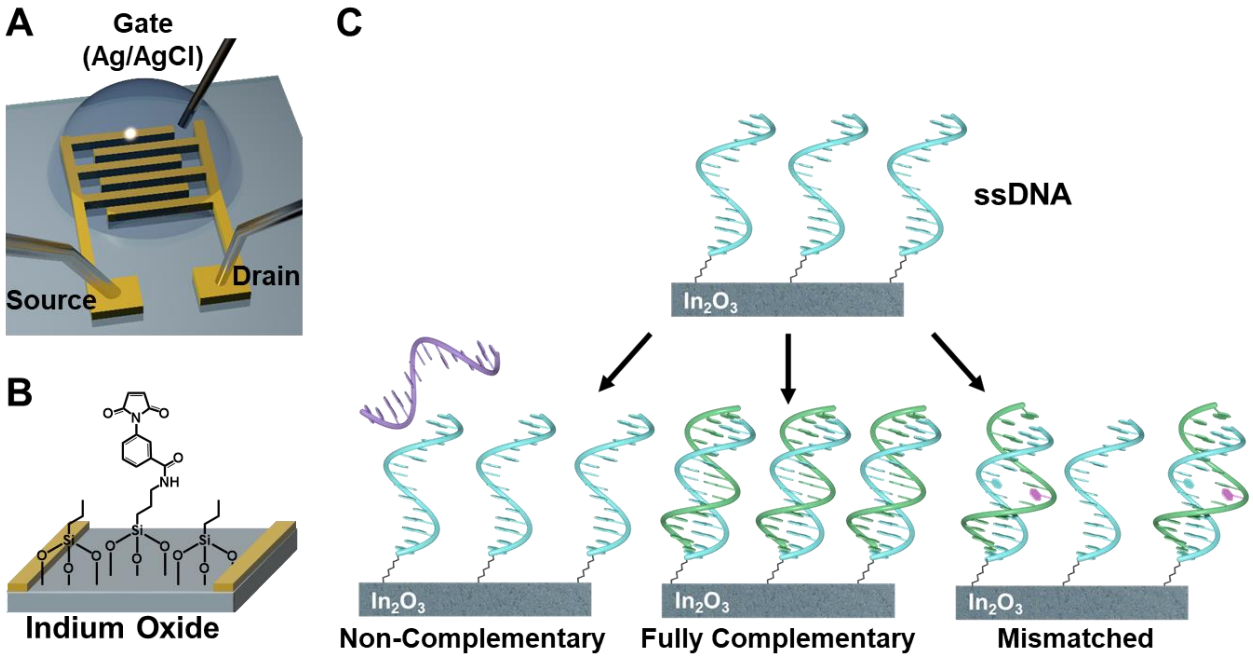

Figure VII.1. Experimental scheme for DNA detection *via* field-effect transistor (FET) measurements. (A) Transistors were composed of 4-nm thin-film In_2O_3 as the channel material, with 10-nm Ti adhesion and 30-nm top Au layers patterned as interdigitated electrodes. The FETs were operated in a solution-gated setup with a Ag/AgCl reference electrode as the gate electrode. **(B)** Thiolated single-stranded DNA (ssDNA) was tethered to amine-terminated silanes, co-assembled with methyl-terminated silanes on metal oxide surfaces using *m*-maleimidobenzoyl-*N*-hydroxysuccinimide ester as a linker. **(C)** Field-effect transistors functionalized with ssDNA were exposed to either non-complementary, fully complementary, or mismatched sequences.

The experimental scheme of the FET SNP detection platform is shown in **Figure VII.1**. Arrays of these transistors were fabricated using high-throughput cleanroom-free techniques with ultrathin In_2O_3 (*ca.* 4 nm), grown using a sol-gel method as the channel material.[29,30,37,57,58] Thiolated ssDNA was functionalized on FET surfaces *via* attachment to self-assembled silanes on the indium oxide channels of the FETs using an amine-thiol linker, 3-maleimidobenzoic acid *N*-hydroxysuccinimide ester (**Figure VII.1B**).[29,30] Individual ssDNA-functionalized FETs were then exposed to solutions containing target nucleic acids and FET responses were measured over a period of 30 min to allow time for hybridization

to occur (*vide infra*). Device responses were measured after exposure to ssDNA that was fully complementary, non-complementary, or had single base-pair changes in different locations with regard to the ssDNA sequences functionalized on FET surfaces.

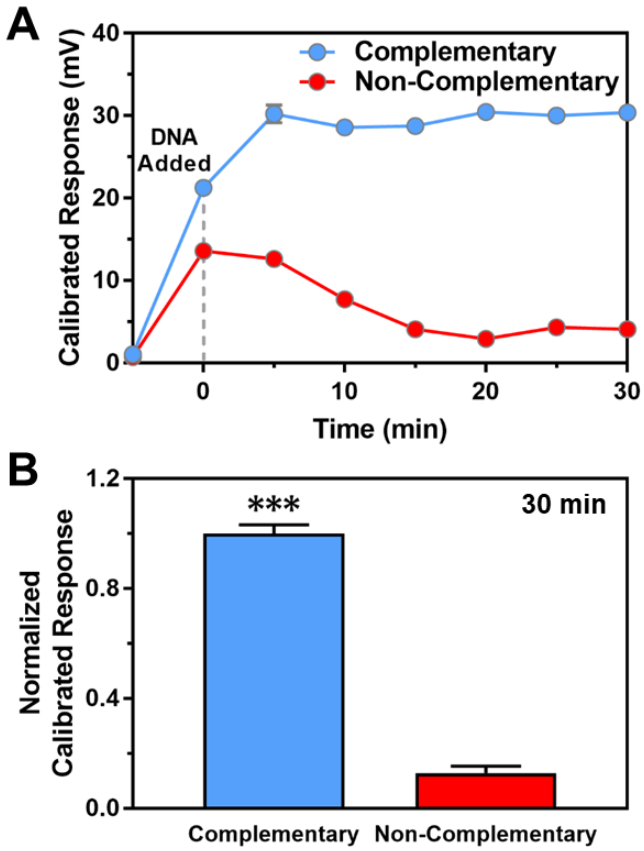

Figure VII.2. Detection of DNA hybridization *via* field-effect transistor (FET) measurements. (A) Representative FET responses over time after incubation with solutions of fully complementary *vs* non-complementary sequences (1 µM in 0.1× phosphate-buffered saline). Responses towards complementary sequences increased and remained stable over time while responses to non-complementary sequences showed an initial response; stabilized responses were negligible. **(B)** Normalized mean FET responses after 30 min of complementary *vs* non-complementary DNA incubation demonstrating detection of complementary DNA hybridization. Error bars are standard errors of the means with N=3 FETs per group. ***P<0.001 *vs* non-complementary DNA.

The measured FET responses differed for FETs exposed to complementary *vs* non-complementary DNA. The FETs incubated with DNA complementary to the ssDNA probe sequences on the In_2O_3 channel surfaces showed increases and stabilization of responses over 30 min. By contrast, FETs incubated with non-complementary DNA showed reduced initial responses that returned to near baseline (**Figure VII.2A**). We attribute this divergent behavior to DNA hybridization in the case of the fully complementary sequence, leading to the observed increases in FET conductances, and a lack of hybridization for the non-complementary sequences resulting in minimal responses after 30 min (**Figure VII.2B**).

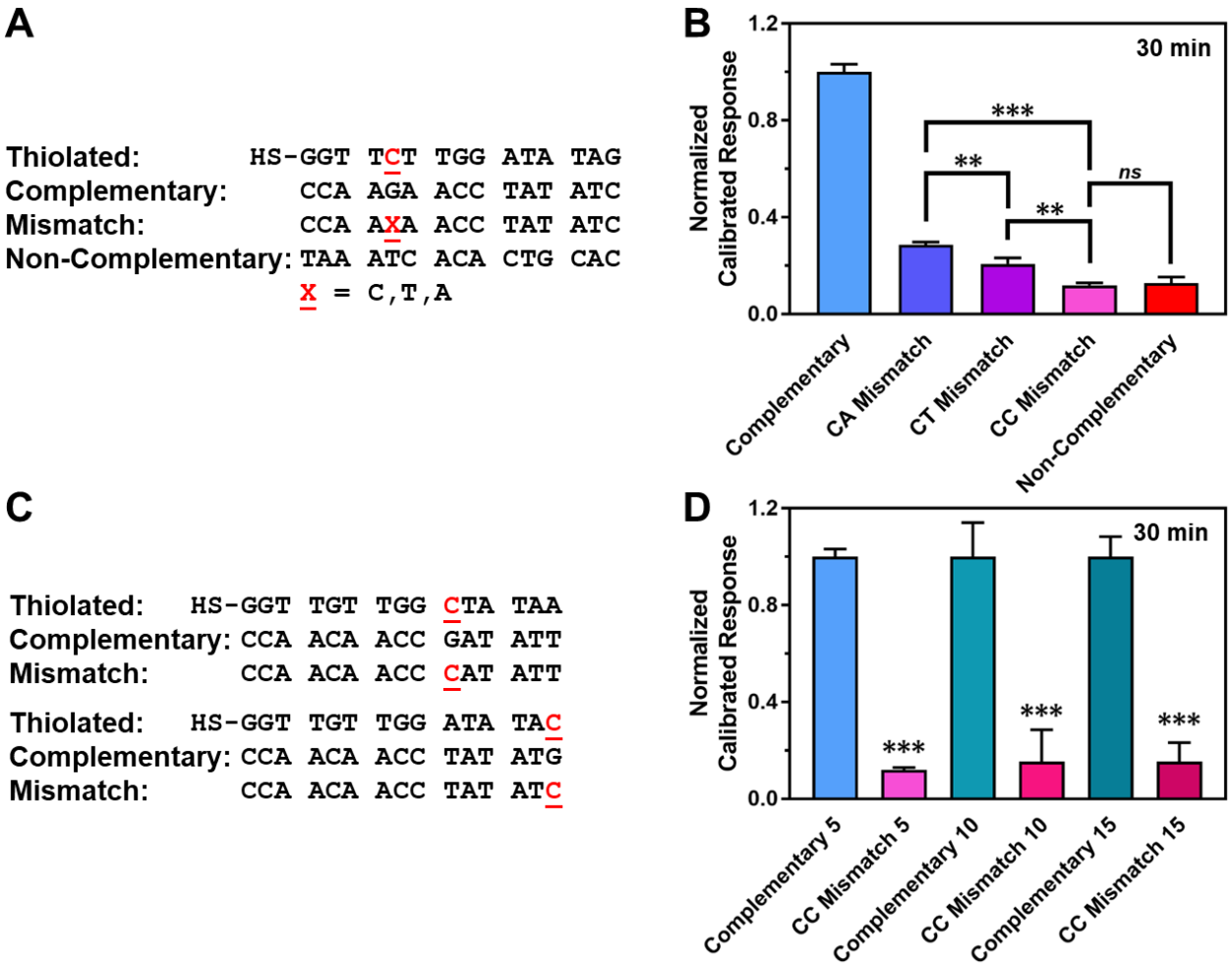

Figure 3. Detection and discrimination of single base-pair mismatches. (A) Sequences of DNA used for field-effect transistor (FET) measurements with different mismatches at the 5th position from the thiol modification. **(B)** Mean field-effect transistor (FET) responses after 30 min of target DNA incubation (1 μM in 0.1× phosphate-buffered saline, PBS) demonstrating detection and discrimination of sequences with single base-pair mismatches. Error bars are standard errors of the means with N=3 FETs per group. ***P<0.001, **P<0.01, *ns* is not significant. **(C)** Sequences of DNA FET measurements with different mismatches at the 10th and 15th position from the thiol modification. **(D)** Mean FET responses after 30 min of target DNA incubation (1 μM in 0.1× PBS) demonstrating detection of sequences with a CC mismatch at the 5th, 10th, or 15th base away from the thiolate attachment. Error bars are standard errors of the means with N=3 FETs per group. ***P<0.001 *vs* fully complementary DNA.

Sensor responses were determined after exposure to DNA sequences with different single base-pair mismatches (*e.g.*, CC, CT, CC mismatches at the 5th position distal to the thiolate attachment position, **Figure VII.3A**). These DNA sequences were designed to be short (*i.e.*, 15-mer) as single base-pair mismatches are less destabilizing in duplex formation as sequence length increases.[59] In all cases, FETs exposed to mismatched DNA sequences had significantly lower mean responses after 30 min compared to those of the fully complementary DNA sequence, showing the ability of these sensors to distinguish DNA sequences that differ from a single base compared to fully complementary DNA sequences (**Figure VII.3B**).

Mean sensor responses for the different mismatches significantly differed from one another (**Figure VII.3B**), demonstrating the capability of these sensors to discriminate sequences with different types of single base-pair mismatches. Sensor responses exposed to sequences with mismatches had stabilized responses after 30 min of incubation, thus mean responses were compared at this time point (**Figure VII.S1**).

The transfer characteristics (I-V curves) of the ssDNA-FETs after incubation with complementary, non-complementary, and (CC) mismatched DNA showed initial decreases in current (**Figure VII.S2**). There are two competing effects here – doubling negative charge due to hybridization (*i.e.*, one base *pair* for each base prior to hybridization) and negative charge moving away from the surface due to the increased stiffness of double-stranded DNA *vs* single-stranded. Hybridization increases the radius of gyration of DNA (*i.e.*, stiffens and extends DNA from *ca.* 1.5 nm to 5 nm for these sequences).[60] We conclude that the former effect dominates and that there is increased negative charge close to the surface, gating the

semiconductor channel. This observation is consistent with our previous findings that decreases in FET transfer characteristics for *n*-type In_2O_3 semiconductor materials are due to gating (*i.e.*, band bending)[61] *via* negatively charged DNA backbones.[30,37] We note that unlike our earlier experiments in which DNA was inserted into well-formed monolayers,[62] the functionalized ssDNA in the current configuration is less constrained and dsDNA may be able to lay across the surface, which would also increase the gating effect of the hybridized DNA.

In addition to DNA sequences with different types of single base-pair mismatches, the responses of ssDNA-functionalized FETs to DNA sequences with CC mismatches at different positions along the DNA backbone were determined. Sensors exposed to DNA sequences with CC mismatches at the 5^{th}, $10^{th,}$ or 15^{th} positions from the thiolate attachment showed significantly lower responses than those of the analogous complementary sequences (**Figure VII.3C,D**). The ability to detect changes at different positions along an oligonucleotide sequence further indicates that sequences that differ by as little as a single nucleotide, regardless of position, can be differentiated from perfectly matched complimentary sequences. These ssDNA-FETs (**Figure VII.3C**) showed comparable time responses to those in **Figures VII.2A** and **VII.S1** and had negligible responses to non-complementary sequences (**Figure VII.S3**).

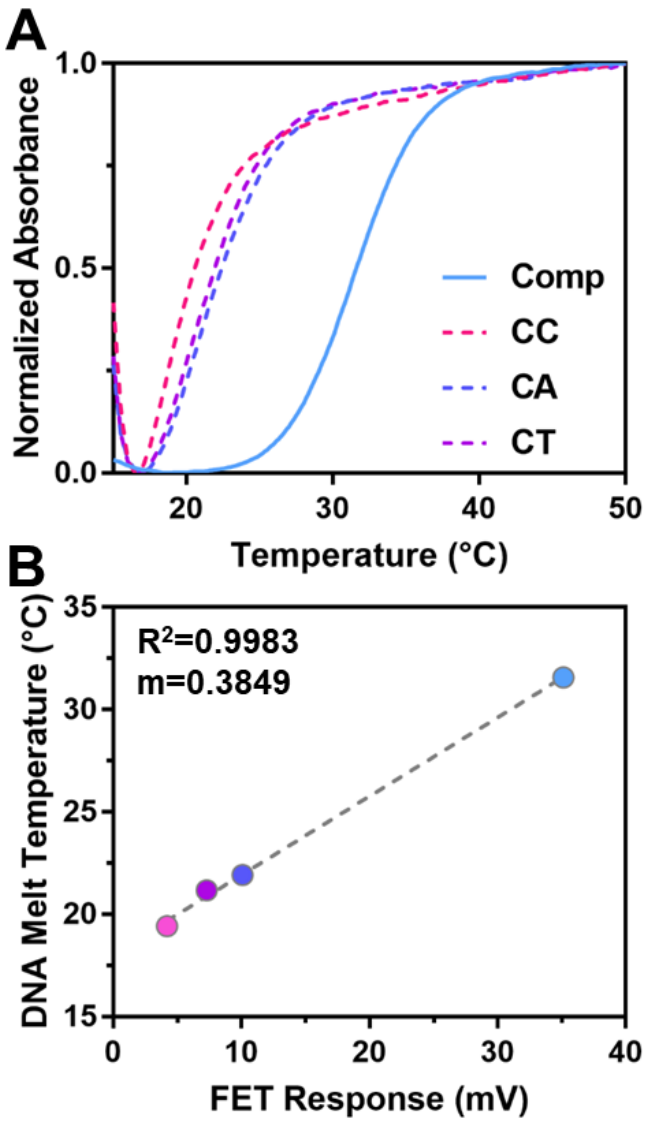

Figure VII.4. DNA melt analysis of mismatched duplexes. (A) DNA melt curves of sequences in **Figure VII.3A** showing relative stabilities of the different mismatches from least to most stable (*i.e.*, CC<CT<CA). **(B)** Correlation of field-effect transistor (FET) responses to sequences with different SNPs (**Figure VII.3B**) *vs* melt temperatures of those sequences. The corresponding linearity index (R^2) and regression slope (m) are indicated. Colors as defined in (A).

To investigate the effects of mismatch stability on DNA detection *via* ssDNA-FETs, DNA melt curves were determined for all sequences with mismatched bases at the 5th position (**Figure VII.3A**) from the thiolate modification (**Figure VII.4A**). The melting temperature of duplexed DNA is the temperature at which sequences dehybridize and thus, is indicative of the stability of the hybridized oligonucleotides (*i.e.*, less stable duplexes have *lower* melting temperatures).[63,64] The melt curves of the different duplexes indicated that the duplex with a CC mismatch has the lowest melt temperature, followed by the duplex with the CT mismatch, and then the CA mismatch. These data indicate the relative stabilities of the mismatched DNA duplexes. Sequences with CC mismatches at different positions also showed different melt temperatures compared to the fully complementary duplex (**Figure VII.S4**). Sensor responses to the different mismatched sequences were highly correlated to their corresponding melt temperatures (R^2>0.99; **Figure VII.4B**).

The correlation analysis suggests that differences in FET responses for various complementary DNA sequences with single base-pair mismatches are related to the relative stabilities of the hybridized DNA sequences. These results are consistent with the hypothesis that DNA detection *via* ssDNA-FETs at this time scale is based on the detection of differing amounts of DNA hybridization (*i.e.*, charge) on the surface. Mismatched DNA sequences that are thermodynamically less stable (*i.e.*, have lower melting temperatures) are less likely to hybridize with the surface-tethered ssDNA compared to that of more stable mismatched or complementary DNA sequences. Differing levels of DNA hybridization with the surface functionalized ssDNA sequences correspond to differing amounts of effective negative charge near the surface and thus the different observed FET responses to different mismatched DNA sequences.

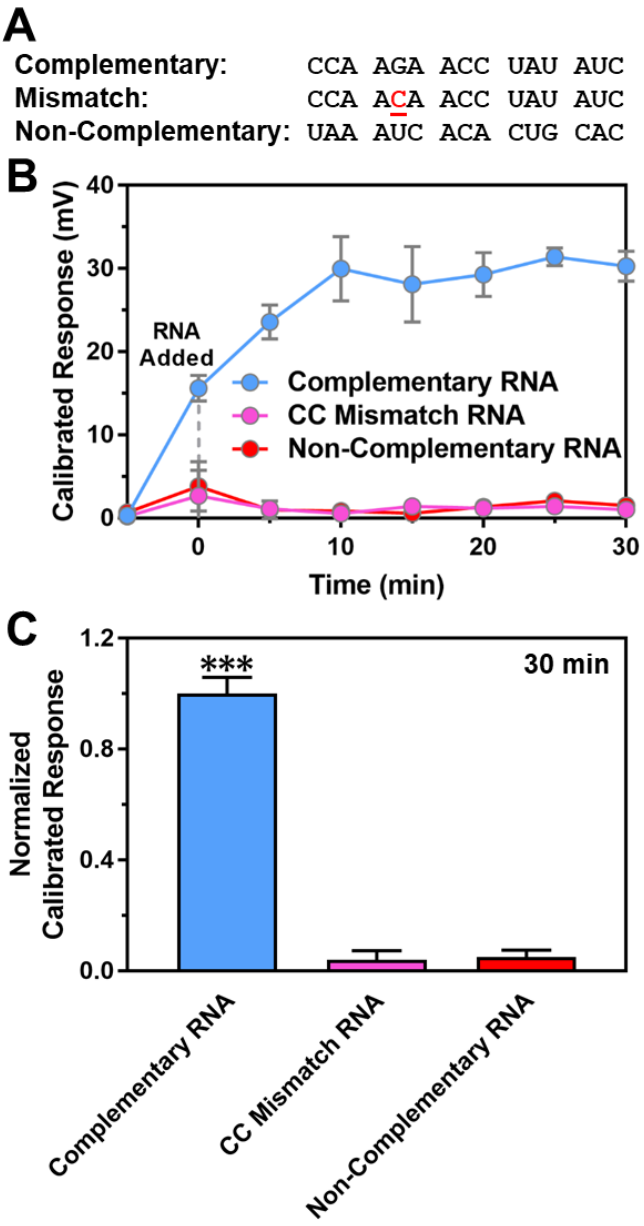

Figure VII.5. Single-nucleotide polymorphisms in RNA. (A) Sequences of RNA used for field-effect transistor measurements. **(B)** Representative field-effect transistor (FET) responses with respect to time after incubation with target RNA solutions (1 μM in 0.1× phosphate-buffered saline). Responses to complementary sequences increased and remained stable over time while responses to non-complementary and mismatched sequences were negligible. **(C)** Mean FET responses after 30 min of target RNA incubation demonstrating detection of complementary RNA *vs* CC mismatched and non-complementary RNA. Error bars are standard errors of the means with N=2 FETs per group. ***P<0.001 *vs* non-complementary and CC mismatch RNA.

To generalize our detection approach to other types of physiologically relevant nucleic acids, we tested our platform against complementary, (CC) mismatched, and non-complementary RNA sequences (**Figure VII.5A**). Single nucleotide polymorphisms also occur in RNA (*vide supra*), and similar to SNPs in DNA, have important implications in genetic diseases.[8-11] Genotyping SNPs in RNA *versus* DNA could be advantageous for applications such as noninvasive prenatal diagnostics, where RNA can be measured from maternal plasma samples.[9] DNA-RNA duplexes adopt a different conformation (*i.e.*, A-form helix).[65] Nonetheless, complementary, CC mismatched, and non-complementary RNA sequences showed responses similar to those of their DNA homologues when incubated on ssDNA-FET surfaces (**Figure VII.5**). Only in the case of the *fully* complementary RNA sequences were significant responses observed; with the mismatched and non-complementary sequences producing minimal signals (**Figure VII.5B**). Using FETs for RNA detection, we broaden the scope and applicability of our platform for the detection of SNPs.

VII.D. Conclusions and Prospects

Overall, we demonstrate a platform for the electronic detection of nucleic acids that differ by only a single pair using highly sensitive and solution processable ultrathin film FET sensors. The detection and discrimination of different types and locations of single base-pair mismatches in both DNA and RNA, shows the potential of this platform towards label-free and electronic SNP genotyping. Using DNA melt curve analyses, we posit that the detection mechanism of our ssDNA-FET platform is based on the detection of differences in nucleic acid hybridization near the surfaces of the transistors. Based on this detection scheme, the platform is not limited to the sequences explored herein; we expect that any nucleic acid

sequence with a SNP that results in differing hybridization stability compared to that of a fully complementary sequence could be discriminated. To detect specific SNPs, it will be necessary to have *multiple* sensor elements with different probe sequences in sensor arrays.[42] The fabrication methods used here are well suited to producing such sensor arrays.[29,37,57,66-68]

In this study, ssDNA sequences were functionalized onto FET surfaces to test the concept of utilizing mismatch destabilization and thus maximizing differential FET responses to perfect complimentary sequences *vs* those that differ by a single base. Longer ssDNA sequences can be tethered onto FET surfaces to engineer leniency into the sensing platform for the detection *multiple* mismatches along the same sequence.[69] Additionally, modulating the ionic strength of the sensing solution changes the charge screening distance near FET surfaces (*i.e.*, the Debye length).[30,37] This parameter enables a strategy for the detection and screening of SNPs that are either closer to the 3' or 5' end of the nucleic acid (*i.e.*, closer to or further away from the surface). Experiments comparing the gating of shorter complementary sequences that do not reach the bases closest to the surface *vs* those that do not reach the outermost tethered DNA bases will help elucidate the effects of charge *vs* changes in radius of gyration on FET responses. Functionalizing an array of FETs with ssDNA sequences that are perfect matches to each SNP allele will enable SNP genotyping in a mixture of nucleic acids and also, the measurement of other types of nucleotide mutations (*e.g.*, using wild-card bases).[70]

Compared with other FET-based detection platforms, our functionalized transistors can be straightforwardly and reproducibly fabricated at the wafer scale using soft-

lithographic techniques in arrays,[29,57,66-68] increasing the potential for translation towards clinical disease diagnostic and personalized healthcare type applications.[71] Moreover, device architectures and performances can be tailored for specific applications,[29,57,72] and ssDNA surface densities can be altered to tune FET responses.[30] Ultimately, further testing of clinical samples (*e.g.*, biobanked tissue samples) will be necessary for platform validation. The ssDNA-FETs investigated here demonstrate the potential for the versatile detection of SNPs in nucleic acids with broad implications in precision medicine.

VII.E. Supplementary Material

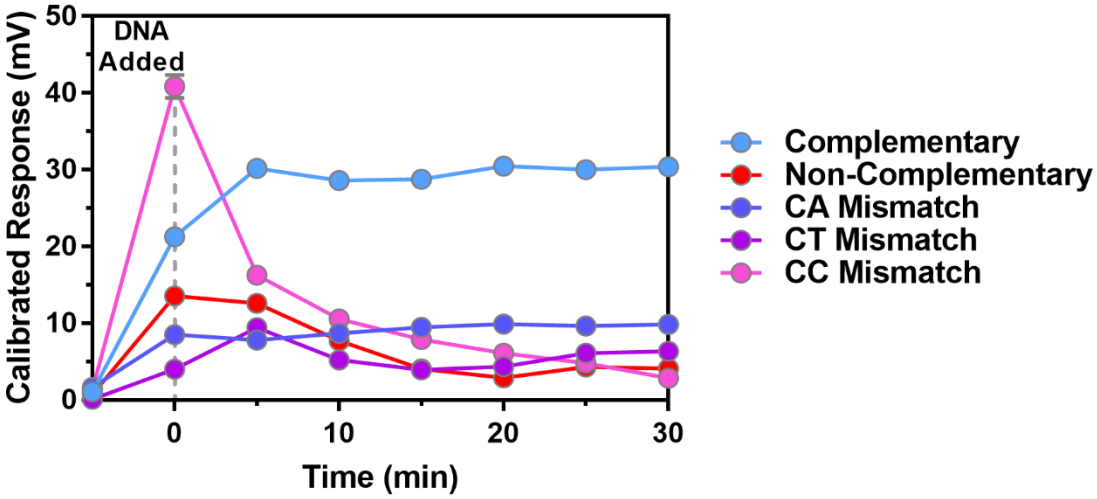

Figure VII.S1. Representative field-effect transistor responses with respect to time after incubation with solutions containing fully complementary *vs.* mismatched and non-complementary sequences (1 μM in 0.1× phosphate-buffered saline). Responses associated with complementary sequences increased and remained stable over time while responses of mismatched and non-complementary sequences showed varying degrees of initial increased responses followed by stabilized responses beginning at ~10 min.

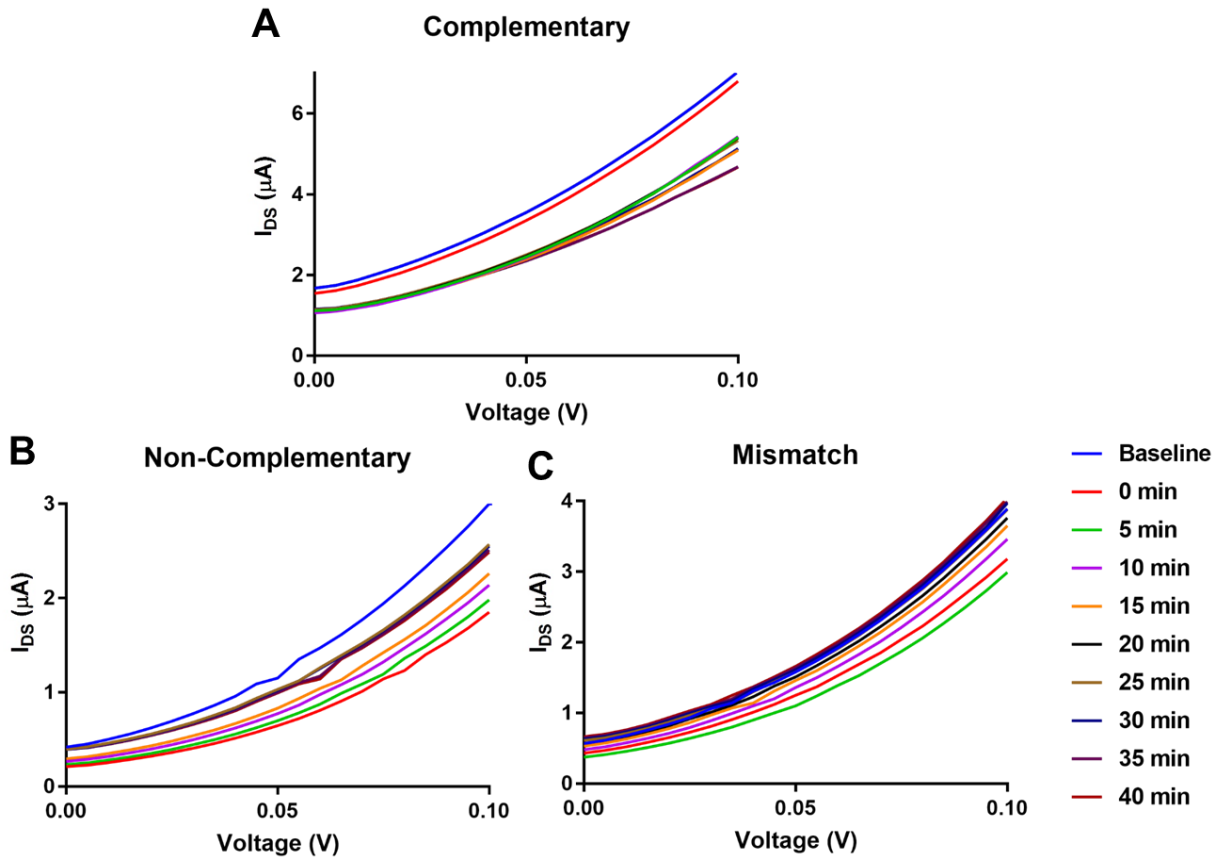

Figure VII.S2. (A-C) Representative field-effect transistor (FET) transfer curves (I-V curves) for FETs exposed to complementary, non-complementary, and CC mismatched sequences, respectively. Transfer characteristics showed a decrease and stabilization in current for the complementary sequence and a return to baseline current for the non-complementary and CC mismatched sequences.

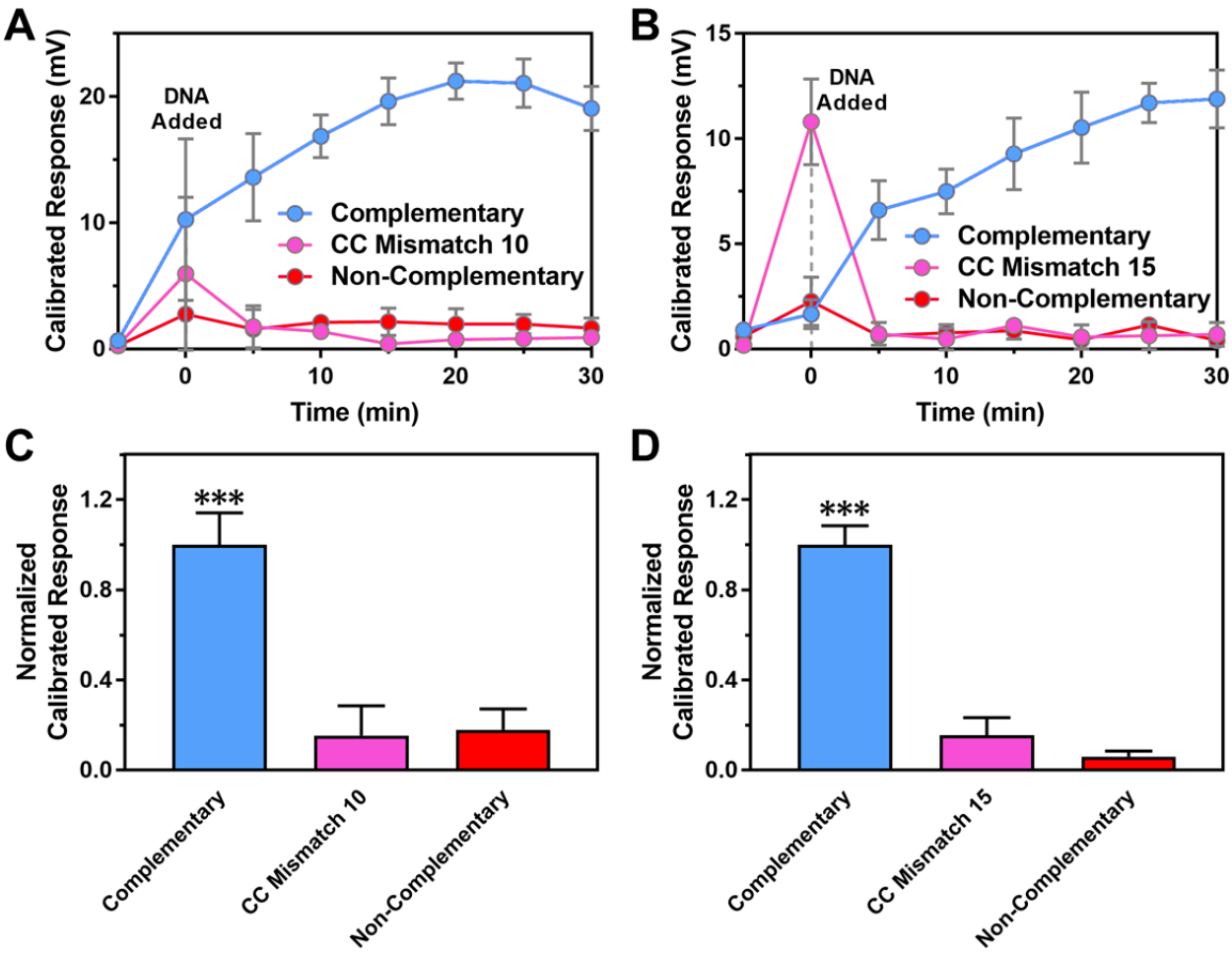

Figure VII.S3. (A,B) Representative field-effect transistor (FET) responses with respect to time after incubation with solutions of fully complementary *vs* non-complementary sequences and CC mismatched sequences at the 10th and 15th positions from the thiolate attachment, respectively (1 μM in 0.1× phosphate buffered saline). (Time-dependent responses for the 5th position CC mismatch are shown in **Figure VII.S1**) **(C,D)** Mean FET responses after 30 min of DNA incubation demonstrating discrimination of fully complementary DNA *vs* non-complementary sequences and CC mismatched sequences at the 10th and 15th positions away from the thiolate attachment, respectively. Error bars are standard errors of the means with N=3 FETs per group. ***P<0.001 *vs* CC mismatch and non-complementary DNA.

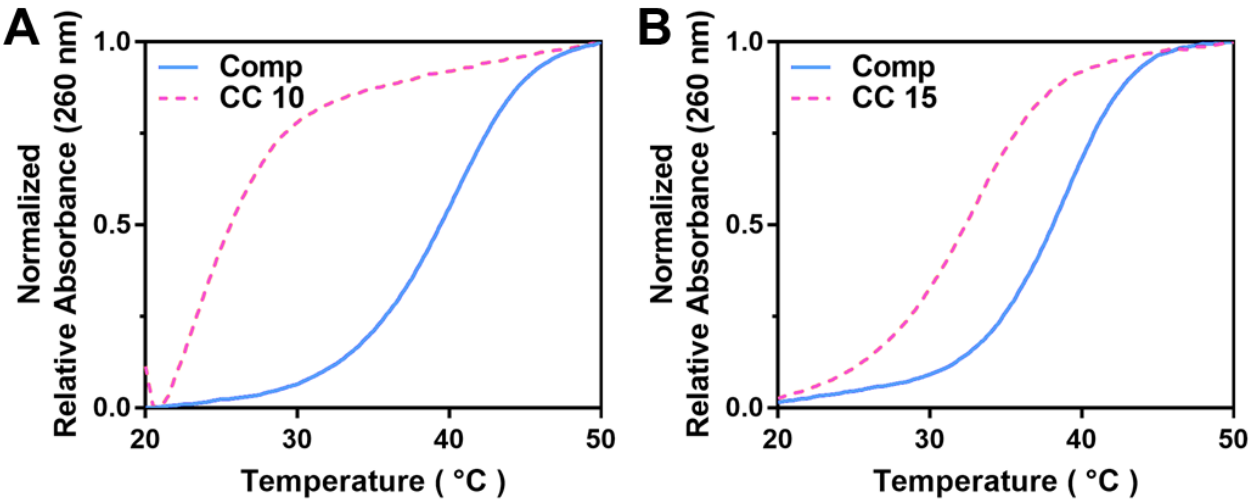

Figure VII.S4. DNA melt curves of sequences in main-text **Figure VII.3D** showing differences in melting temperatures between a fully complementary sequence and a sequence with a CC mismatch at the **(A)** 10th and **(B)** 15th position away from the thiolate modification.

VII.F. References

(1) Wang, D. G.; Fan, J.-B.; Siao, C.-J.; Berno, A.; Young, P.; Sapolsky, R.; Ghandour, G.; Perkins, N.; Winchester, E.; Spencer, J.; Kruglyak, L.; Stein, L.; Hsie, L.; Topaloglou, T.; Hubbell, E.; Robinson, E.; Mittmann, M.; Morris, M. S.; Shen, N.; Kilburn, D.; Rioux, J.; Nusbaum, C.; Rozen, S.; Hudson, T. J.; Lipshutz, R.; Chee, M.; Lander, E. S. Large-Scale Identification, Mapping, and Genotyping of Single-Nucleotide Polymorphisms in the Human Genome. *Science* **1998,** *280*, 1077–1082.

(2) Cargill, M.; Altshuler, D.; Ireland, J.; Sklar, P.; Ardlie, K.; Patil, N.; Lane, C. R.; Lim, E. P.; Kalyanaraman, N.; Nemesh, J.; Ziaugra, L.; Friedland, L.; Rolfe, A.; Warrington, J.; Lipshutz, R.; Daley, G. Q.; Lander, E. S. Characterization of Single-Nucleotide Polymorphisms in Coding Regions of Human Genes. *Nat. Genet.* **1999,** *22*, 231–238.

(3) Schork, N. J.; Fallin, D.; Lanchbury, J. S. Single Nucleotide Polymorphisms and the Future of Genetic Epidemiology. *Clin. Genet.* **2000,** *58*, 250–264.

(4) Sachidanandam, R.; Weissman, D.; Schmidt, S. C.; Kakol, J. M.; Stein, L. D.; Marth, G.; Sherry, S.; Mullikin, J. C.; Mortimore, B. J.; Willey, D. L.; Hunt, S. E.; Cole, C. G.; Coggill, P. C.; Rice, C. M.; Ning, Z.; Rogers, J.; Bentley, D. R.; Kwok, P.-Y.; Mardis, E. R.; Yeh, R. T.; Schultz, B.; Cook, L.; Davenport, R.; Dante, M.; Fulton, L.; Hillier, L.; Waterston, R. H.; McPherson, J. D.; Gilman, B.; Schaffner, S.; Van Etten, W. J.; Reich, D.; Higgins, J.; Daly, M. J.; Blumenstiel, B.; Baldwin, J.; Stange-Thomann, N.; Zody, M. C.; Linton, L.; Lander, E. S.; Altshuler, D. A Map of Human Genome Sequence Variation Containing 1.42 Million Single Nucleotide Polymorphisms. *Nature* **2001,** *409*, 928-933.

(5) Syvänen, A.-C. Accessing Genetic Variation: Genotyping Single Nucleotide Polymorphisms. *Nat. Rev. Genet.* **2001,** *2*, 930–942.

(6) Wade, C. M.; Daly, M. J. Genetic Variation in Laboratory Mice. *Nat. Genet.* **2005,** *37*, 1175-1180.

(7) Nishizaki, S. S.; Boyle, A. P. Mining the Unknown: Assigning Function to Noncoding Single Nucleotide Polymorphisms. *Trends Genet.* **2017,** *33*, 34-45.

(8) Shen, L. X.; Basilion, J. P.; Stanton, V. P. Single-Nucleotide Polymorphisms can Cause Different Structural Folds of mRNA. *Proct. Natl. Acad. Sci. U. S. A.* **1999,** *96*, 7871–7876.

(9) Go, A. T. J. I.; Visser, A.; Mulders, M. A. M.; Blankenstein, M. A.; van Vugt, J. M. G.; Oudejans, C. B. M. 44 Single-Nucleotide Polymorphisms Expressed by Placental RNA: Assessment for Use in Noninvasive Prenatal Diagnosis of Trisomy 21. *Clin. Chem.* **2007,** *53*, 2223–2224.

(10) Duan, R.; Pak, C.; Jin, P. Single Nucleotide Polymorphism Associated with Mature miR-125a Alters the Processing of pri-miRNA. *Hum. Mol. Genet.* **2007,** *16*, 1124–1131.

(11) Jupe, E. R.; Badgett, A. A.; Neas, B. R.; Craft, M. A.; Mitchell, D. S.; Resta, R.; Mulvihill, J. J.; Aston, C. E.; Thompson, L. F. Single Nucleotide Polymorphism in Prohibitin 3′Untranslated Region and Breast-Cancer Susceptibility. *The Lancet* **2001,** *357*, 1588–1589.

(12) Sun, G.; Yan, J.; Noltner, K.; Feng, J.; Li, H.; Sarkis, D. A.; Sommer, S. S.; Rossi, J. J. SNPs in Human miRNA Genes Affect Biogenesis and Function. *RNA* **2009,** *15*, 1640-1651.

(13) Parisien, M.; Wang, X.; Pan, T. Diversity of Human tRNA Genes from the 1000-Genomes Project. *RNA Biol.* **2013,** *10*, 1853-1867.

(14) Tantisira, K.; Klimecki, W. T.; Lazarus, R.; Palmer, L. J.; Raby, B. A.; Kwiatkowski, D. J.; Silverman, E.; Vercelli, D.; Martinez, F. D.; Weiss, S. T. Toll-Like Receptor 6 Gene (TLR6): Single-Nucleotide Polymorphism Frequencies and Preliminary Association with the Diagnosis of Asthma. *Genes Immun.* **2004,** *5*, 343–346.

(15) Li, H.; Wetten, S.; Li, L.; St. Jean, P. L.; Upmanyu, R.; Surh, L.; Hosford, D.; Barnes, M. R.; Briley, J. D.; Borrie, M.; Coletta, N.; Delisle, R.; Dhalla, D.; Ehm, M. G.; Feldman, H. H.; Fornazzari, L.; Gauthier, S.; Goodgame, N.; Guzman, D.; Hammond, S.; Hollingworth, P.; Hsiung, G.-Y.; Johnson, J.; Kelly, D. D.; Keren, R.; Kertesz, A.; King, K. S.; Lovestone, S.; Loy-English, I.; Matthews, P. M.; Owen, M. J.; Plumpton, M.; Pryse-Phillips, W.; Prinjha, R. K.; Richardson, J. C.; Saunders, A.; Slater, A. J.; St. George-Hyslop, P. H.; Stinnett, S. W.; Swartz, J. E.; Taylor, R. L.; Wherrett, J.; Williams, J.; Yarnall, D. P.; Gibson, R. A.; Irizarry, M. C.; Middleton, L. T.; Roses, A. D. Candidate Single-Nucleotide Polymorphisms From a Genomewide Association Study of Alzheimer Disease. *JAMA Neurology* **2008,** *65*, 45–53.

(16) Ding, C.; Chiu, R. W. K.; Lau, T. K.; Leung, T. N.; Chan, L. C.; Chan, A. Y. Y.; Charoenkwan, P.; Ng, I. S. L.; Law, H.-y.; Ma, E. S. K.; Xu, X.; Wanapirak, C.; Sanguansermsri, T.; Liao, C.; Ai, M. A. T. J.; Chui, D. H. K.; Cantor, C. R.; Lo, Y. M. D. MS Analysis of Single-Nucleotide Differences in Circulating Nucleic Acids: Application to Noninvasive Prenatal Diagnosis. *Proc. Natl. Acad. Sci. U. S. A.* **2004,** *101*, 10762–10767.

(17) Hoban, M. D.; Cost, G. J.; Mendel, M. C.; Romero, Z.; Kaufman, M. L.; Joglekar, A. V.; Ho, M.; Lumaquin, D.; Gray, D.; Lill, G. R.; Cooper, A. R.; Urbinati, F.; Senadheera, S.; Zhu, A.; Liu, P.-Q.; Paschon, D. E.; Zhang, L.; Rebar, E. J.; Wilber, A.; Wang, X.; Gregory, P. D.; Holmes, M. C.; Reik, A.; Hollis, R. P.; Kohn, D. B. Correction of the Sickle Cell Disease Mutation in Human Hematopoietic Stem/Progenitor Cells. *Blood* **2015,** *125*, 2597-2604.

(18) Gail, M. H. Discriminatory Accuracy From Single-Nucleotide Polymorphisms in Models to Predict Breast Cancer Risk. *J. Natl. Cancer Inst.* **2008,** *100*, 1037–1041.

(19) Manuguerra, M.; Saletta, F.; Karagas, M. R.; Berwick, M.; Veglia, F.; Vineis, P.; Matullo, G. XRCC3 and XPD/ERCC2 Single Nucleotide Polymorphisms and the Risk of Cancer: A HuGE Review. *Am. J. Epidemiol.* **2006,** *164*, 297–302.

(20) Horikawa, Y.; Wood, C. G.; Yang, H.; Zhao, H.; Ye, Y.; Gu, J.; Lin, J.; Habuchi, T.; Wu, X. Single Nucleotide Polymorphisms of microRNA Machinery Genes Modify the Risk of Renal Cell Carcinoma. *Clin. Cancer. Res.* **2008,** *14*, 7956–7962.

(21) Raghavan, M.; Lillington, D. M.; Skoulakis, S.; Debernardi, S.; Chaplin, T.; Foot, N. J.; Lister, T. A.; Young, B. D. Genome-Wide Single Nucleotide Polymorphism Analysis Reveals Frequent Partial Uniparental Disomy Due to Somatic Recombination in Acute Myeloid Leukemias. *Cancer Res.* **2005,** *65*, 375–378.

(22) Isla, D.; Sarries, C.; Rosell, R.; Alonso, G.; Domine, M.; Taron, M.; Lopez-Vivanco, G.; Camps, C.; Botia, M.; Nuñez, L.; Sanchez-Ronco, M.; Sanchez, J. J.; Lopez-Brea, M.; Barneto, I.; Paredes, A.; Medina, B.; Artal, A.; Lianes, P. Single Nucleotide Polymorphisms and Outcome in Docetaxel–Cisplatin-Treated Advanced Non-Small-Cell Lung Cancer. *Ann. Oncol.* **2004,** *15*, 1194–1203.

(23) Tyagi, S.; Kramer, F. R. Molecular Beacons: Probes that Fluoresce upon Hybridization. *Nat. Biotechnol.* **1996,** *14*, 303–308.

(24) Zhang, L.; Wu, C.; Carta, R.; Zhao, H. Free Energy of DNA Duplex Formation on Short Oligonucleotide Microarrays. *Nucleic Acids Res.* **2006,** *35*, e18.

(25) Xiao, Y.; Lou, X.; Uzawa, T.; Plakos, K. J. I.; Plaxco, K. W.; Soh, H. T. An Electrochemical Sensor for Single Nucleotide Polymorphism Detection in Serum Based on a Triple-Stem DNA Probe. *J. Am. Chem. Soc.* **2009,** *131*, 15311–15316.

(26) Venkatesan, B. M.; Bashir, R. Nanopore Sensors for Nucleic Acid Analysis. *Nat. Nanotechnol.* **2011,** *6*, 615–624.

(27) Haff, L. A.; Smirnov, I. P. Single-Nucleotide Polymorphism Identification Assays Using a Thermostable DNA Polymerase and Delayed Extraction MALDI-TOF Mass Spectrometry. *Genome Res.* **1997,** *7*, 378–388.

(28) Nairz, K.; Stocker, H.; Schindelholz, B.; Hafen, E. High-Resolution SNP Mapping by Denaturing HPLC. *Proct. Natl. Acad. Sci. U. S. A.* **2002,** *99*, 10575-10580.

(29) Kim, J.; Rim, Y. S.; Chen, H.; Cao, H. H.; Nakatsuka, N.; Hinton, H. L.; Zhao, C.; Andrews, A. M.; Yang, Y.; Weiss, P. S. Fabrication of High-Performance Ultrathin In_2O_3 Film Field-Effect Transistors and Biosensors Using Chemical Lift-Off Lithography. *ACS Nano* **2015,** *9*, 4572–4582.

(30) Nakatsuka, N.; Yang, K.-A.; Abendroth, J. M.; Cheung, K. M.; Xu, X.; Yang, H.; Zhao, C.; Zhu, B.; Rim, Y. S.; Yang, Y.; Weiss, P. S.; Stojanović, M. N.; Andrews, A. M. Aptamer–Field-Effect Transistors Overcome Debye Length Limitations for Small-Molecule Sensing. *Science* **2018,** *362*, 319–324.

(31) Schöning, M. J.; Poghossian, A. Recent Advances in Biologically Sensitive Field-Effect Transistors (BioFETs). *Analyst* **2002,** *127*, 1137–1151.

(32) Allen, B. L.; Kichambare, P. D.; Star, A. Carbon Nanotube Field-Effect-Transistor-Based Biosensors. *Adv. Mater.* **2007,** *19*, 1439–1451.

(33) Curreli, M.; Zhang, R.; Ishikawa, F. N.; Chang, H.; Cote, R. J.; Zhou, C.; Thompson, M. E. Real-Time, Label-Free Detection of Biological Entities Using Nanowire-Based FETs. *IEEE Trans. Nanotechnol.* **2008,** *7*, 651–667.

(34) So, H.-M.; Won, K.; Kim, Y. H.; Kim, B.-K.; Ryu, B. H.; Na, P. S.; Kim, H.; Lee, J.-O. Single-Walled Carbon Nanotube Biosensors Using Aptamers as Molecular Recognition Elements. *J. Am. Chem. Soc.* **2005,** *127*, 11906–11907.

(35) Green, N. S.; Norton, M. L. Interactions of DNA with Graphene and Sensing Applications of Graphene Field-Effect Transistor Devices: A Review. *Anal. Chim. Acta* **2015,** *853*, 127–142.

(36) Lung Khung, Y.; Narducci, D. Synergizing Nucleic Acid Aptamers with 1-Dimensional Nanostructures as Label-Free Field-Effect Transistor Biosensors. *Biosens. Bioelectron.* **2013,** *50*, 278–293.

(37) Cheung, K. M.; Yang, K.-A.; Nakatsuka, N.; Zhao, C.; Ye, M.; Jung, M. E.; Yang, H.; Weiss, P. S.; Stojanović, M. N.; Andrews, A. M. Phenylalanine Monitoring via Aptamer-Field-Effect Transistor Sensors. *ACS Sensors* **2019**, DOI:10.1021/acssensors.9b01963.

(38) Chen, T.-Y.; Loan, P. T. K.; Hsu, C.-L.; Lee, Y.-H.; Tse-Wei Wang, J.; Wei, K.-H.; Lin, C.-T.; Li, L.-J. Label-Free Detection of DNA Hybridization Using Transistors Based on CVD Grown Graphene. *Biosens. Bioelectron.* **2013,** *41*, 103–109.

(39) Chen, C.-P.; Ganguly, A.; Lu, C.-Y.; Chen, T.-Y.; Kuo, C.-C.; Chen, R.-S.; Tu, W.-H.; Fischer, W. B.; Chen, K.-H.; Chen, L.-C. Ultrasensitive in Situ Label-Free DNA Detection Using a GaN Nanowire-Based Extended-Gate Field-Effect-Transistor Sensor. *Anal. Chem.* **2011,** *83*, 1938–1943.

(40) Star, A.; Gabriel, J.-C. P.; Bradley, K.; Grüner, G. Electronic Detection of Specific Protein Binding Using Nanotube FET Devices. *Nano Lett.* **2003,** *3*, 459–463.

(41) Kim, D.-J.; Sohn, I. Y.; Jung, J.-H.; Yoon, O. J.; Lee, N. E.; Park, J.-S. Reduced Graphene Oxide Field-Effect Transistor for Label-Free Femtomolar Protein Detection. *Biosens. Bioelectron.* **2013,** *41*, 621–626.

(42) Ingebrandt, S.; Offenhäusser, A. Label-Free Detection of DNA Using Field-Effect Transistors. *Phys. Status Solidi A* **2006,** *203*, 3399–3411.

(43) Hwang, M. T.; Landon, P. B.; Lee, J.; Choi, D.; Mo, A. H.; Glinsky, G.; Lal, R. Highly Specific SNP Detection Using 2D Graphene Electronics and DNA Strand Displacement. *Proct. Natl. Acad. Sci. U. S. A.* **2016,** *113*, 7088–7093.

(44) Kim, D.-S.; Jeong, Y.-T.; Park, H.-J.; Shin, J.-K.; Choi, P.; Lee, J.-H.; Lim, G. An FET-Type Charge Sensor for Highly Sensitive Detection of DNA Sequence. *Biosens. Bioelectron.* **2004,** *20*, 69-74.

(45) Kergoat, L.; Piro, B.; Berggren, M.; Pham, M.-C.; Yassar, A.; Horowitz, G. DNA Detection with a Water-Gated Organic Field-Effect Transistor. *Org. Electron.* **2012,** *13*, 1-6.

(46) Uslu, F.; Ingebrandt, S.; Mayer, D.; Böcker-Meffert, S.; Odenthal, M.; Offenhäusser, A. Labelfree Fully Electronic Nucleic Acid Detection System Based on a Field-Effect Transistor Device. *Biosens. Bioelectron.* **2004,** *19*, 1723-1731.

(47) Lin, C.-H.; Hung, C.-H.; Hsiao, C.-Y.; Lin, H.-C.; Ko, F.-H.; Yang, Y.-S. Poly-Silicon Nanowire Field-Effect Transistor for Ultrasensitive and Label-Free Detection of Pathogenic Avian Influenza DNA. *Biosens. Bioelectron.* **2009,** *24*, 3019-3024.

(48) Cai, B.; Wang, S.; Huang, L.; Ning, Y.; Zhang, Z.; Zhang, G.-J. Ultrasensitive Label-Free Detection of PNA–DNA Hybridization by Reduced Graphene Oxide Field-Effect Transistor Biosensor. *ACS Nano* **2014,** *8*, 2632–2638.

(49) Sorgenfrei, S.; Chiu, C.-y.; Gonzalez Jr, R. L.; Yu, Y.-J.; Kim, P.; Nuckolls, C.; Shepard, K. L. Label-Free Single-Molecule Detection of DNA-Hybridization Kinetics With a Carbon Nanotube Field-Effect Transistor. *Nat. Nanotechnol.* **2011,** *6*, 126–132.

(50) Xu, S.; Zhan, J.; Man, B.; Jiang, S.; Yue, W.; Gao, S.; Guo, C.; Liu, H.; Li, Z.; Wang, J.; Zhou, Y. Real-Time Reliable Determination of Binding Kinetics of DNA Hybridization Using a Multi-Channel Graphene Biosensor. *Nat. Commun.* **2017,** *8*, 14902.

(51) Stine, R.; Robinson, J. T.; Sheehan, P. E.; Tamanaha, C. R. Real-Time DNA Detection Using Reduced Graphene Oxide Field Effect Transistors. *Adv. Mater.* **2010,** *22*, 5297–5300.

(52) Xie, P.; Xiong, Q.; Fang, Y.; Qing, Q.; Lieber, C. M. Local Electrical Potential Setection of DNA by Nanowire–Nanopore Sensors. *Nat. Nanotechnol.* **2011,** *7*, 119–125.

(53) Reina, G.; González-Domínguez, J. M.; Criado, A.; Vázquez, E.; Bianco, A.; Prato, M. Promises, Facts and Challenges for Graphene in Biomedical Applications. *Chem. Soc. Rev.* **2017,** *46*, 4400–4416.

(54) Yan, L.; Zheng, Y. B.; Zhao, F.; Li, S.; Gao, X.; Xu, B.; Weiss, P. S.; Zhao, Y. Chemistry and Physics of a Single Atomic Layer: Strategies and Challenges for Functionalization of Graphene and Graphene-Based Materials. *Chem. Soc. Rev.* **2012,** *41*, 97-114.

(55) Chen, H.; Rim, Y. S.; Wang, I. C.; Li, C.; Zhu, B.; Sun, M.; Goorsky, M. S.; He, X.; Yang, Y. Quasi-Two-Dimensional Metal Oxide Semiconductors Based Ultrasensitive Potentiometric Biosensors. *ACS Nano* **2017,** *11*, 4710-4718.

(56) Ishikawa, F. N.; Curreli, M.; Chang, H.-K.; Chen, P.-C.; Zhang, R.; Cote, R. J.; Thompson, M. E.; Zhou, C. A Calibration Method for Nanowire Biosensors to Suppress Device-to-Device Variation. *ACS Nano* **2009,** *3*, 3969-3976.

(57) Zhao, C.; Xu, X.; Bae, S.-H.; Yang, Q.; Liu, W.; Belling, J. N.; Cheung, K. M.; Rim, Y. S.; Yang, Y.; Andrews, A. M.; Weiss, P. S. Large-Area, Ultrathin Metal-Oxide Semiconductor Nanoribbon Arrays Fabricated by Chemical Lift-Off Lithography. *Nano Lett.* **2018,** *18*, 5590–5595.

(58) Chen, H.; Rim, Y. S.; Wang, I. C.; Li, C.; Zhu, B.; Sun, M.; Goorsky, M. S.; He, X.; Yang, Y. Quasi-Two-Dimensional Metal Oxide Semiconductors Based Ultrasensitive Potentiometric Biosensors. *ACS Nano* **2017,** *11*, 4710–4718.

(59) Pan, S.; Sun, X.; Lee, J. K. DNA Stability in the Gas versus Solution Phases: A Systematic Study of Thirty-One Duplexes with Varying Length, Sequence, and Charge Level. *J. Am. Soc. Mass. Spectrom.* **2006,** *17*, 1383–1395.

(60) Sim, A. Y. L. a. L., Jan and Herschlag, Daniel and Doniach, Sebastian. Salt Dependence of the Radius of Gyration and Flexibility of Single-Stranded DNA in Solution Probed by Small-Angle X-Ray Scattering. *Phys. Rev. E* **2012,** *86*, 021901.

(61) Weiss, P. S.; Trevor, P. L.; Cardillo, M. J. Gas–Surface Interactions on InP Monitored by Changes in Substrate Electronic Properties. *The Journal of Chemical Physics* **1989,** *90*, 5146-5153.

(62) Cao, H. H.; Nakatsuka, N.; Serino, A. C.; Liao, W.-S.; Cheunkar, S.; Yang, H.; Weiss, P. S.; Andrews, A. M. Controlled DNA Patterning by Chemical Lift-Off Lithography: Matrix Matters. *ACS Nano* **2015,** *9*, 11439–11454.

(63) Howley, P. M.; Israel, M. A.; Law, M. F.; Martin, M. A. A Rapid Method for Detecting and Mapping Homology Between Heterologous DNAs. Evaluation of Polyomavirus Genomes. *J. Biol. Chem.* **1979,** *254*, 4876–4883.

(64) Wallace, R. B.; Shaffer, J.; Murphy, R. F.; Bonner, J.; Hirose, T.; Itakura, K. Hybridization of Synthetic Oligodeoxyribonucleotides to Φ X 174 DNA: The Effect of Single Base Pair Mismatch. *Nucleic Acids Res.* **1979,** *6*, 3543–3558.

(65) Davis, R. R.; Shaban, N. M.; Perrino, F. W.; Hollis, T. Crystal Structure of RNA-DNA Duplex Provides Insight into Conformational Changes Induced by RNase H Binding. *Cell Cycle* **2015,** *14*, 668-673.

(66) Liao, W.-S.; Cheunkar, S.; Cao, H. H.; Bednar, H. R.; Weiss, P. S.; Andrews, A. M. Subtractive Patterning *via* Chemical Lift-Off Lithography. *Science* **2012,** *337*, 1517–1521.

(67) Slaughter, L. S.; Cheung, K. M.; Kaappa, S.; Cao, H. H.; Yang, Q.; Young, T. D.; Serino, A. C.; Malola, S.; Olson, J. M.; Link, S.; Häkkinen, H.; Andrews, A. M.; Weiss, P. S. Patterning

of Supported Gold Monolayers *via* Chemical Lift-Off Lithography. *Beilstein J. Nanotechnol.* **2017,** *8*, 2648–2661.

(68) Xu, X.; Yang, Q.; Cheung, K. M.; Zhao, C.; Wattanatorn, N.; Belling, J. N.; Abendroth, J. M.; Slaughter, L. S.; Mirkin, C. A.; Andrews, A. M.; Weiss, P. S. Polymer-Pen Chemical Lift-Off Lithography. *Nano Lett.* **2017,** *17*, 3302–3311.

(69) He, G.; Li, J.; Qi, C.; Guo, X. Single Nucleotide Polymorphism Genotyping in Single-Molecule Electronic Circuits. *Adv. Sci.* **2017,** *4*, 1700158.

(70) Nabel, C. S.; Manning, S. A.; Kohli, R. M. The Curious Chemical Biology of Cytosine: Deamination, Methylation, and Oxidation as Modulators of Genomic Potential. *ACS Chem. Biol.* **2012,** *7*, 20–30.

(71) Price, C. P.; Kricka, L. J. Improving Healthcare Accessibility Through Point-of-Care Technologies. *Clin. Chem.* **2007,** *53*, 1665–1675.

(72) Rim, Y. S.; Bae, S.-H.; Chen, H.; Yang, J. L.; Kim, J.; Andrews, A. M.; Weiss, P. S.; Yang, Y.; Tseng, H.-R. Printable Ultrathin Metal Oxide Semiconductor-Based Conformal Biosensors. *ACS Nano* **2015,** *9*, 12174–12181.

CHAPTER VIII

Conclusions and Prospects

VIII.A. Conclusions and Prospects for Chemical Lift-Off Lithography

In the first half of my dissertation I described my efforts to advance chemical lift-off lithography (CLL), a subtractive soft-lithographic technique used to pattern self-assembled monolayers (SAMs) of functionalized alkanethiolates on metal surfaces.[1,2] I demonstrated that by using arrays of polymer pens or DVD-templated polydimethylsiloxane (PDMS) stamps,[3,4] nanoscale patterns of SAMs on Au could be straightforwardly achieved. Additionally, I extended CLL to pattern a variety of different material surfaces including coinage and transition metals, as well as a semiconductor.[5] The patterns of SAMs on Au achieved *via* CLL are relatively well studied and have enabled a wide variety of applications ranging from small-molecule and biomolecule patterning to transistor fabrication.[1-4,6-15]

However, comparatively, the structure and function of the supported metal monolayer lifted-off onto PDMS stamps during CLL is much less studied.[2,16] As described in Chapter III, these supported-Au monolayers have sub-nanometer apparent heights, are optically transparent, yet retain the chemical functionality of bulk Au.[16] However, the properties and potential applications of this hybrid material have yet to be fully explored. In the following section, I describe prospects for supported Au monolayers including further characterization, patterning onto different substrates, and the use of these supported monolayers as templates for further structural growth.

VIII.A.1. Metal-Induced Fluorescence Enhancement *via* Supported Au Monolayers

Attempts to image and to measure the optical properties of supported Au monolayers directly proved challenging due to the small amount of Au that was removed onto PDMS stamps during CLL.[16] Alternatively, inspired by the technique of fluorescence-quenching microscopy (FQM),[17] which has been used to image two-dimensional (2D) materials

optically *via* quenching of proximal fluorophores, I developed a method to embed fluorescent dyes into the underlying PDMS substrates to visualize and to measure the influence of supported-Au monolayers on proximal fluorophores.

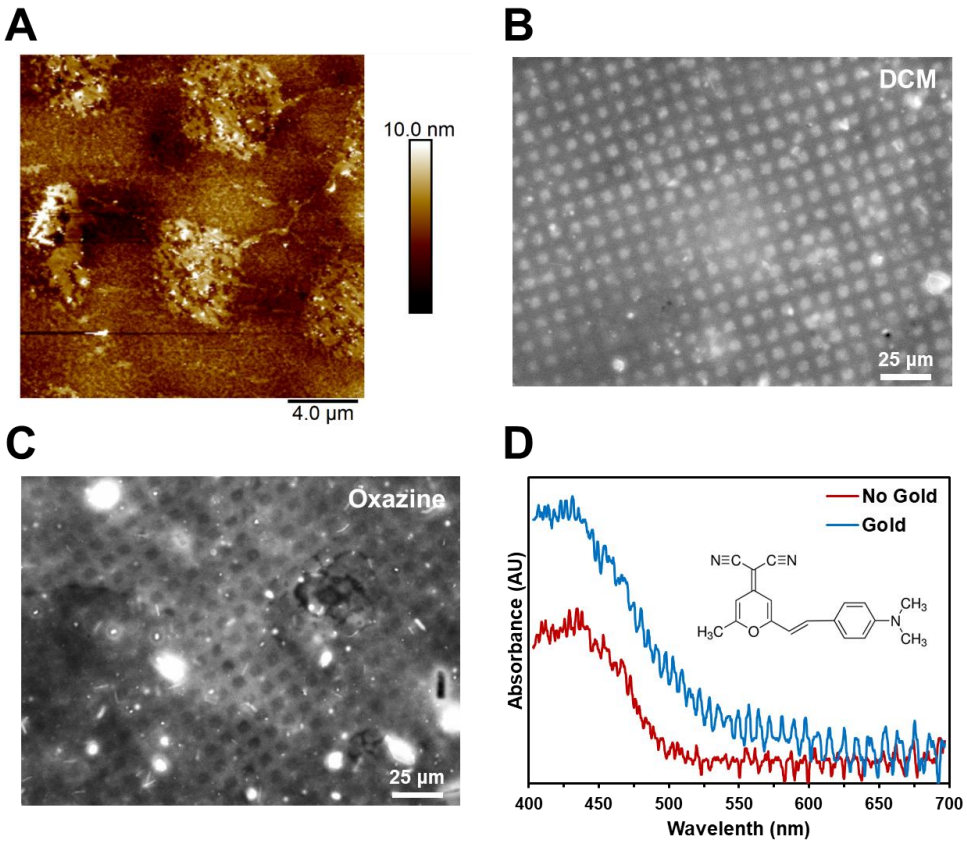

Figure VIII.1. Influence on proximal fluorophores by patterned-Au monolayers. **(A)** Atomic-force microscope image of supported-Au monolayers (5-μm squares) patterned on dye-embedded featureless polydimethylsiloxane (PDMS). **(B)** Fluorescence microscope image of 4-(dicyanomethylene)-2-methyl-6-(4-dimethylaminostyryl)-4*H*-pyran (DCM) dye-embedded PDMS patterned with supported-Au monolayers. Regions of brighter contrast (*i.e.*, fluorescence enhancement) correspond to areas of patterned Au. **(C)** Fluorescence microscope image of oxazine 170 dye-embedded PDMS patterned with supported Au monolayers. Regions of darker contrast (*i.e.*, fluorescence quenching) correspond to areas of patterned Au. **(D)** Ensemble UV-visible spectra of DCM dye-embedded PDMS with and without patterned-Au monolayers showing enhancement of absorbance for surfaces with Au. Inset depicts molecular structure of DCM.

Interestingly, for PDMS embedded with the dye 4-(dicyanomethylene)-2-methyl-6-(4-dimethylaminostyryl)-4*H*-pyran (DCM), regions of PDMS corresponding to patterned Au monolayers (**Figure VIII.1.A**) appeared brighter in contrast when imaged *via* fluorescence

microscopy, suggesting *enhancement* of fluorescence rather than quenching by the Au monolayers (**Figure VIII.1.B**), possibly by metal-induced fluorescence enhancement (MIFE).[18-20] For MIFE to occur, spectral overlap is needed between the optical properties of the metal and fluorophore.[18-20] The excitation and emission wavelengths of DCM are 450 nm and 650 nm, respectively. To probe the optical properties of the Au monolayers, two additional dyes, oxazine 170 and coumarine 6, were tested. For coumarine 6, which has a similar excitation but different emission wavelength compared to DCM, enhancement was also observed (data not shown). However, for oxazine 170, which has a different excitation wavelength, but similar emission wavelength to DCM, quenching was observed (**Figure VIII.1.C**), which is expected for fluorophores near metal surfaces.[18]

These data suggest that enhancement is contingent upon the excitation wavelength of the fluorophore and that the supported-Au monolayer may have a spectral feature around 450 nm, based on the absorption profiles of the dyes that exhibited MIFE. Additionally, absorbance spectra of DCM-dye-embedded PDMS with patterned-Au monolayers showed an increased absorption peak compared to that of PDMS without Au monolayers (**Figure VIII.1.D**), suggesting that excitation enhancement likely contributes to the observed MIFE.[19] Absorbance spectra for oxazine 170-embedded PDMS did not show increases in absorbance (data not shown). Ultimately, emission spectra, as well as florescence-lifetime and quantum-yield measurements will need to be performed to elucidate the mechanism of fluorescence enhancement *via* the Au monolayers. Additionally, a study using a library of dye molecules or quantum dots spanning the visible spectrum could be performed to probe the spectral properties of the supported-Au monolayer more precisely.

VIII.A.2. Patterning of Supported Au Monolayers onto Different Substrates

VIII.A.2.a. Fabrication of Ultrathin and Releasable Polydimethylsiloxane

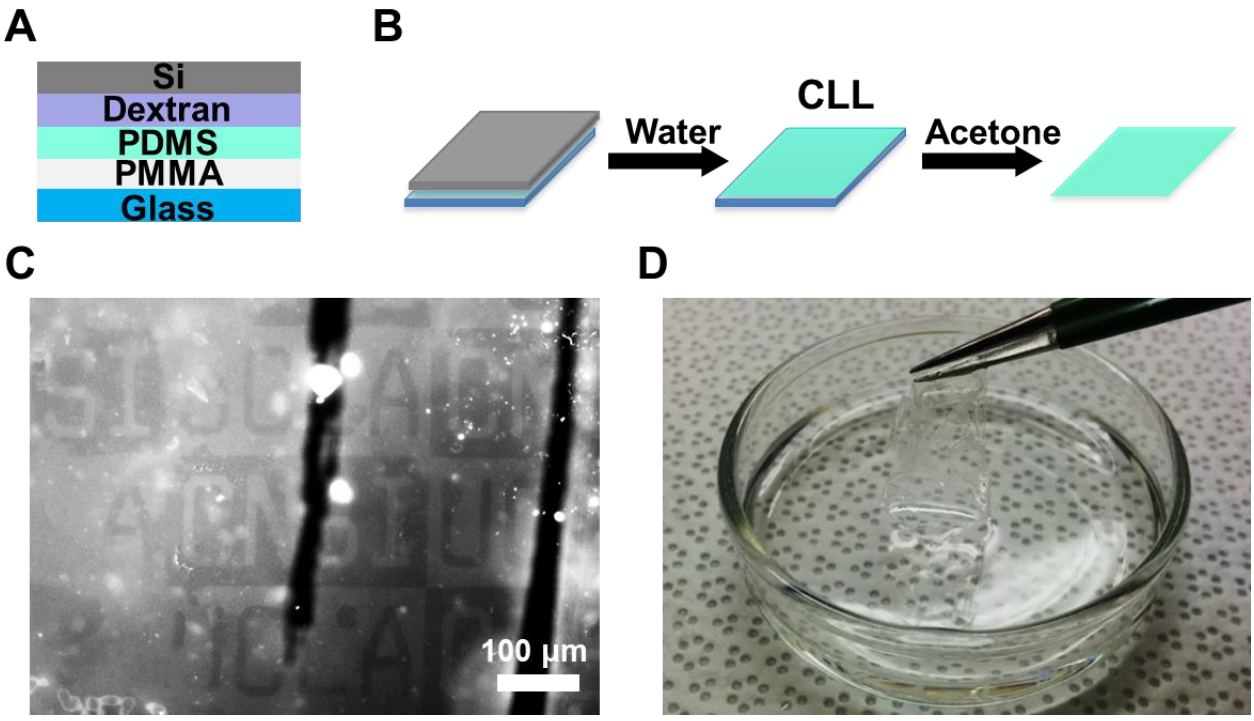

Figure VIII.2. Fabrication and characterization of ultrathin and releasable polydimethylsiloxane (PDMS). (A) Cross-sectional diagram of spin-coated ultrathin PDMS (*ca.* 30 μm thick) between dual sacrificial polymer layers of dextran and poly(methyl methacrylate) (PMMA). Here, Si was used as a flat template for the top surface of the PDMS, and glass was used as a solid, bottom support. **(B)** Experimental schematic of the sequential release process of ultrathin PDMS *via* dual sacrificial polymer layers. First, the dextran layer is dissolved in water. Then, the exposed PDMS surface can be patterned *via* chemical lift-off lithography (CLL). Finally, the PMMA layer is dissolved in acetone releasing the PDMS from the solid support. **(C)** Fluorescence microscope image of ultrathin 4-(dicyanomethylene)-2-methyl-6-(4-dimethylaminostyryl)-4*H*-pyran dye embedded PDMS patterned with Au monolayers. Bright regions correspond to regions with patterned Au. **(D)** Photograph of released PDMS after immersion in acetone.

In the fluorescence studies above, it was important to minimize the thickness of the PDMS substrate to reduce the amount of background fluorescence and to maximize the signal-to-noise of the measurements. Ultrathin and flat PDMS substrates were fabricated *via* spin-coating onto solid glass supports and templated with Si wafers. Substrates fabricated in this

manner had thicknesses of *ca.* 30 μm, measured *via* contact profilometry, and nanometer root-mean-squared roughnesses as measured *via* atomic force microscopy (AFM). Taking this method a step further, thin and releasable PDMS substrates were fabricated *via* the addition of sacrificial polymer layers to the spin-coating process (**Figure VIII.2.A**).[21] Dextran and poly(methyl methacrylate) (PMMA) were chosen as they are soluble in different solvents, enabling sequential release steps.

First, dextran was dissolved in water, releasing the glass-supported PDMS from the Si template (**Figure VIII.2.B**). Then, the PDMS was patterned with Au monolayers *via* CLL, and subsequently released from the glass support by immersion in acetone to dissolve the PMMA layer (**Figure VIII.2.B-D**). Patterning of supported-Au monolayers onto these substrates increases the versatility of this hybrid material, extending it to non-planar (*e.g.*, conformal) and releasable substrates. By controlling spin-coating speeds and diluting the PDMS with an organic solvent (*e.g.*, toluene) during the spin-coating process, even thinner PDMS substrates could be fabricated. Supported-Au monolayers patterned on ultrathin PDMS substrates might be more compatible with techniques like high-resolution transmission-electron microscopy,[22] which could enable visualization and characterization of the nanoscale structure of the Au monolayers.

VIII.A.2.b. Patterning Supported Au Monolayers on Si Substrates

Thus far, all investigations of Au monolayers have been performed on monolayers supported on PDMS substrates. The underlying PDMS support presented several issues that hindered the characterization of the Au monolayers. The deformability of PDMS could affect the accuracy of measured topographies of the Au layer *via* AFM, and the insulating nature of the PDMS was not compatible with techniques that could be used to characterize the nanoscale

electronic properties of the Au monolayer (*e.g.*, conductive AFM). Thus, patterning of Au monolayers on hard and conductive surfaces would enable further elucidation of the structure and electronic properties of the monolayer.

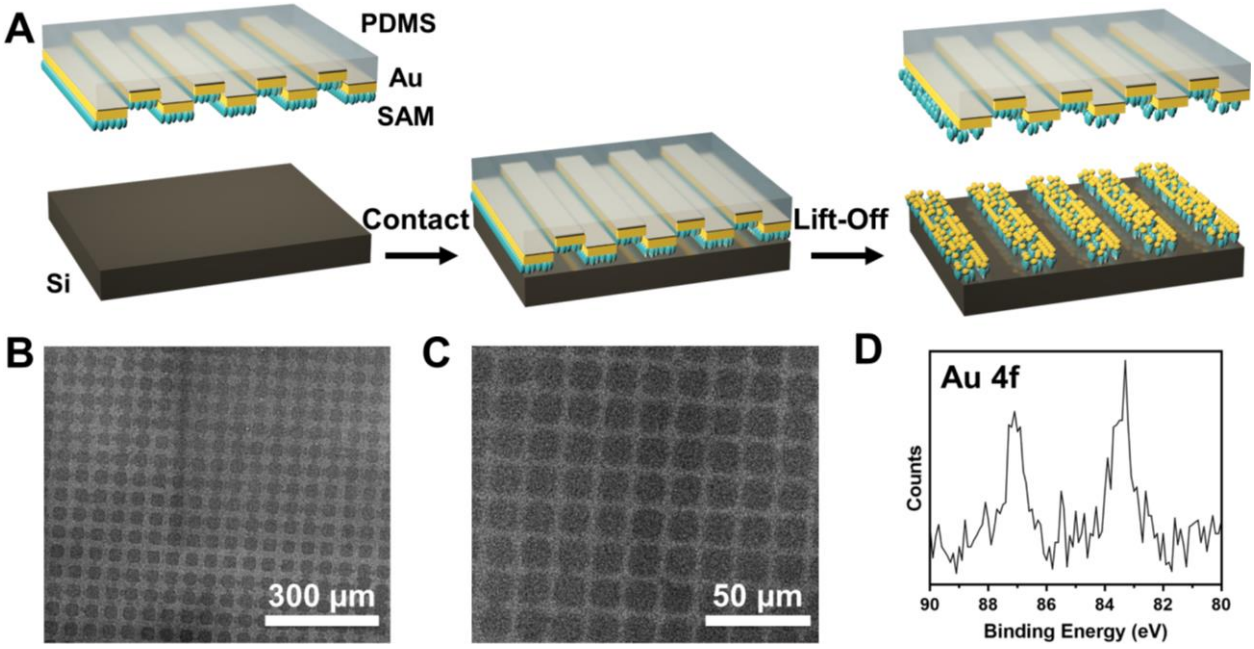

Figure VIII.3. Patterning of supported Au monolayers on Si surfaces *via* chemical lift-off lithography (CLL). (A) Experimental schematic showing the patterning of Au monolayers onto Si *via* CLL. Patterned polydimethylsiloxane stamps with evaporated Au overlayers functionalized with self-assembled monolayers of 11-mercapto-1-undecanol are brought into contact with oxygen-plasma-activated Si surfaces. Subsequent removal of PDMS stamps patterns the Si with Au monolayers in the contacted regions. **(B,C)** Scanning-electron microscope images of patterned-Au monolayers on Si. Regions of brighter contrast correspond to regions with Au. **(D)** X-ray photoelectron spectra of a Si surface after CLL, demonstrating the addition of Au onto the Si surface.

Using a reverse CLL strategy, where PDMS stamps with an evaporated 20-nm Au layer functionalized with SAMs of 11-mercapto-1-undecaol were brought into contact with oxygen-plasma-activated Si surfaces, Au monolayers were additively patterned on Si substrates (**Figure VIII.3.A**). These patterned-Au monolayers were visualized using scanning-electron microscopy (**Figure VIII.3.B,C**) and AFM (data not shown). X-ray photoelectron spectroscopy of Si surfaces after the CLL process confirmed the presence of

Au on the surfaces (**Figure VIII.3.D**). The patterning of Au monolayers onto Si substrates, a hard and conductive surface, increases the compatibility of this material towards characterization techniques such as conductive AFM or scanning-tunneling microscopy, which may enable the measurement of the nanoscale electronic properties and the molecular structure of the Au monolayer, respectively.[23,24]

VIII.A.3. Supported Au Monolayers as a Platform for Structural Growth

VIII.A.3.a. Supported Metal Bilayers

Taking advantage of the chemical functionality of supported Au monolayers towards thiols, a supported Au bilayer was formed by contacting an unpatterned supported Au monolayer on PDMS with a patterned SAM of 1,8-octanedithiol on Au. Removal of the PDMS patterned an additional layer of Au onto the first Au layer *via* bonding between the thiol tail group of the dithiol SAM and the first supported Au monolayer (**Figure VIII.4.A**). Atomic force microscopy of the patterned Au bilayer surface revealed minimal contrast in topography (**Figure VIII.4.B**). We have previously determined that a full monolayer of Au is not removed during CLL, thus using this Au monolayer as the surface for an additional lift-off step presumably results in an even lower yield for the second step. The sparse amount of Au removed after lift-off likely result in a lack of discernable topography measured *via* AFM. However, patterns were observed in the measured adhesion channel of the AFM, suggesting differences in composition and successful patterning of the second Au layer (**Figure VIII.4.C**).

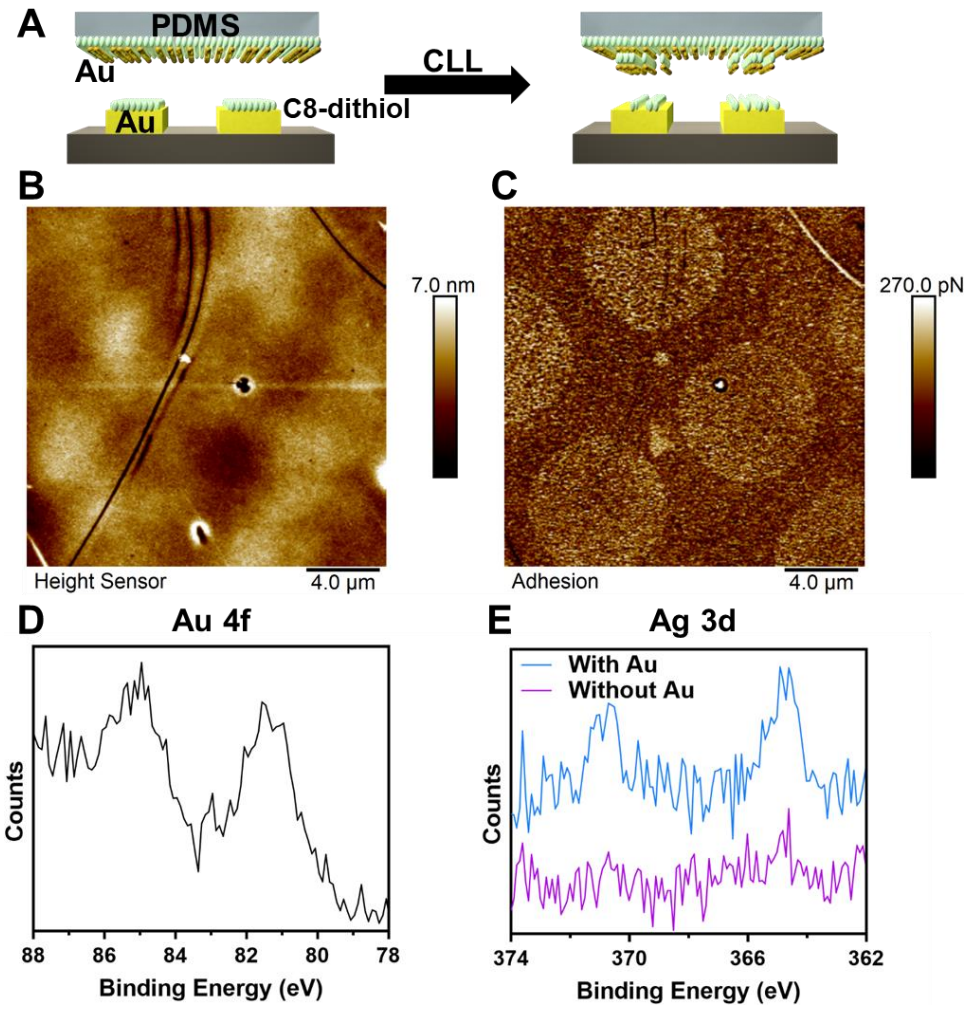

Figure VIII.4. Formation and characterization of supported metal bilayers. (A) Experimental schematic illustrating the formation of a supported Au bilayer on PDMS *via* chemical lift-off lithography. A supported Au monolayer on polydimethylsiloxane (PDMS) is brought into contact with a patterned 1,8-octanedithiol (C8-dithiol) self-assembled monolayer (SAM) on Au. Removal of the stamp additively patterns another layer of Au onto the contacted areas. Atomic force microscope **(B)** topography and **(C)** adhesion images of a patterned Au monolayer (7.5 μm circles) on top of an unpatterned Au monolayer. X-ray photoelectron spectroscopy **(D)** of a supported Au monolayer on PDMS and **(E)** of PDMS surfaces with and without a Au monolayer after contact and lift-off from a Ag surface with a C8-dithiol SAM. Peaks corresponding to Ag are present only in the case after contact with a PDMS stamp *with* a supported Au monolayer, demonstrating that the Ag is lifted-off onto the Au monolayer and not onto the PDMS surface itself.

Moreover, to test if the second layer of Au was actually removed onto the first Au layer and not removed onto the PDMS stamp itself *via* reaction of the thiol tail group with the active PDMS, activated PDMS stamps with and without Au monolayers were brought into

contact with Ag surfaces functionalized with 1,8-octaneditiol SAMs. X-ray photoelectron spectroscopy of both surfaces revealed that only in the case of the PDMS stamp with the Au monolayer were peaks corresponding to Ag observed (**Figure VIII.4.D,E**). This result suggests that the dithiol SAM is reacting specifically with the Au monolayer and not the PDMS stamp itself, and that the second layer of metal is likely removed onto the first layer. The ability to pattern bilayers and potentially, multilayers of metals using this method may have applications in the fabrication of new metamaterials,[25] however, the yield of CLL must be improved before this would be feasible.

VIII.A.3.b. Growth of Metal-Organic Multilayers

As proof-of-concept to demonstrate that three-dimensional structures could be grown using supported Au monolayers as templates, the layer-by-layer (LBL) growth of metal-organic multilayers was studied.[26] These layers consist of alternating organic molecules and metal ions, in this case 11-mercapto-1-undecanoic acid and Cu^{2+}, respectively. Atomic force microscopy of patterned Au monolayers after five and ten LBL deposition cycles showed qualitative increases in topography corresponding to the growth of these multilayers (**Figure VIII.5.A-C**). Additionally, changes in adhesion after the LBL deposition suggested differences in chemical composition from the original Au monolayer after multilayer growth (**Figure VIII.5.D-F**). The capability to grow three-dimensional nanostructures on surfaces could be translated to other systems that use similar metal coordination chemistry (*e.g.*, metal organic frameworks,[27] metal organic chalcogenolate assemblies),[28] which would enable the patterning of such materials on flexible transparent supports (*i.e.*, PDMS).

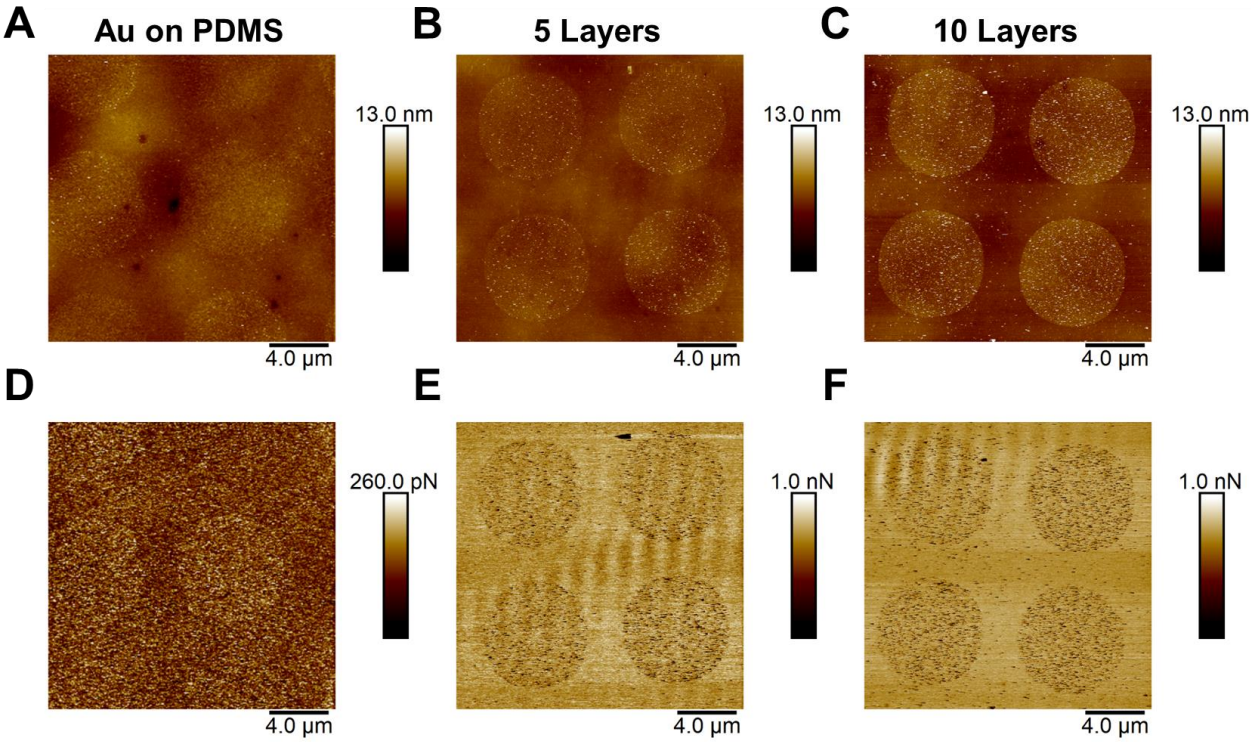

Figure VIII.5. Layer-by-layer (LBL) growth of metal-organic multilayers on patterned supported Au monolayers on polydimethylsiloxane. Atomic force microscope **(A-C)** topography and **(D-F)** adhesion images of **(A,D)** patterned Au monolayers (7.5 μm circles) after **(B,E)** five layers and **(C,F)** ten layers of multilayer growth. Each layer corresponds to a LBL deposition cycle of first Cu^{2+} and then 11-mercapto-1-undecanoic acid (MUDA), after an initial deposition of MUDA onto the Au monolayer.

VIII.A.3.c. Growth of Au Nanoparticles

In addition to Au-thiol chemistry, the functionality of the supported Au was also probed *via* the growth of Au nanoparticles using the Au monolayer as a seed layer. Patterned, supported Au monolayers on PDMS were incubated with solutions of chloroauric acid and cetyl trimethylammonium bromide to facilitate the growth of Au nanoparticles. Optical microscope images of PDMS surfaces after Au nanoparticle growth demonstrated the selective growth of nanoparticles in regions with patterned Au monolayers (**Figure VIII.6.A**). Atomic force microscopy of nanoparticle grown regions showed that *ca.* 50 nm

spherical nanoparticles were grown homogeneously over the patterned area (**Figure VIII.6.B-E**).

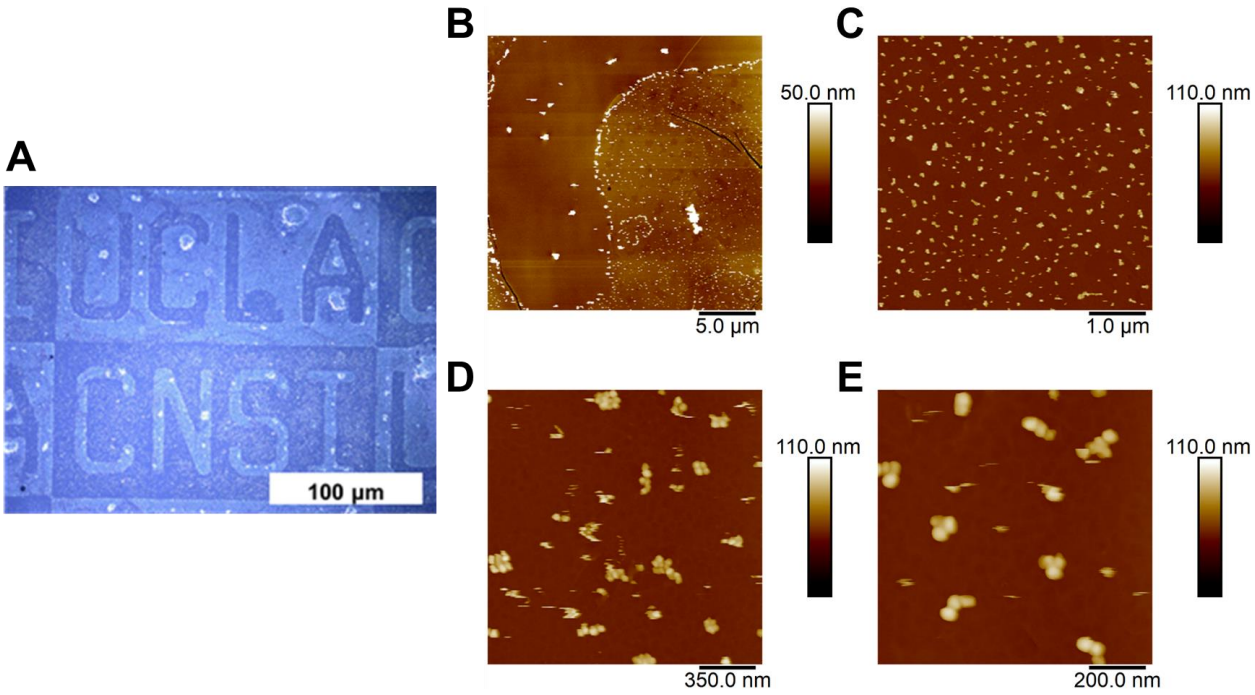

Figure VIII.6. Growth of Au nanoparticles on patterned supported Au monolayers on polydimethylsiloxane. (A) Optical microscope image of "UCLA/CNSI" patterned Au monolayers after nanoparticle growth. Regions of Au nanoparticles grown on Au monolayers appear brighter in contrast due to scattering of light by the nanoparticles. **(B)** Atomic force microscope (AFM) image of a "U"-shaped patterned region demonstrating selective Au nanoparticle growth in regions with supported Au monolayers. **(C-E)** Higher magnification AFM images demonstrating homogeneous growth of *ca.* 50 nm spherical nanoparticles.

The types of nanoparticles that can be patterned are not limited to the ones described herein. By changing reagents and growth conditions, the size, shape, and density of particles could be tuned. Using different metals as the supported template, nanoparticles of different compositions could also be grown. This method to pattern the growth of nanoparticles selectively on PDMS has potential for the fabrication of conformal plasmonic sensors.[29] Additionally, the ability of the supported Au to seed further metallic growth will enable

techniques like electroless deposition, which could be used to create more complete monolayers.[30]

Altogether, these experiments show the unexplored potential of supported-Au monolayers, both in terms of further characterization of structure and function, and also as a platform for further structural growth. Ultimately, additional experiments will be needed to elucidate the structure and quantity of the lifted-off Au monolayer.

VIII.B. Conclusions and Prospects for Aptamer-Field-Effect Transistor Sensors

In the latter half of my dissertation, I provided evidence for the use of field-effect transistors (FETs) as electronic sensors for the detection of a wide variety of biologically relevant targets.[31,32] Aptamer-FETs were used to detect small-molecule targets selectively in complex biological matrices over a wide range of concentrations.[31,32] Nonetheless, challenges remain for translating these sensors for clinical point-of-care applications and also towards measuring chemical signaling *in vivo*. For example, in the case of phenylalanine detection using aptamer-FET sensors, there were challenges in measuring in undiluted serum and whole blood; not because the sensors cannot function in these matrices, but rather because the concentration of phenylalanine in these samples was high compared to the dissociation constant of the aptamer-phenylalanine recognition (*i.e.*, saturating concentrations).[32] Additionally, the miniaturization and implantation of these sensors into living tissue to measure chemical flux presents challenges in fabrication and operation. In the following section, I discuss prospects for studying aptamer structure-function relationships to tune device sensitivities, and also initial experiments to measure serotonin *in vivo* in the brains of mice.

VIII.B.1. Structure-Function Relationships in Aptamer-Field-Effect Transistors

VIII.B.1.a. Rational Truncation of Aptamer Stems

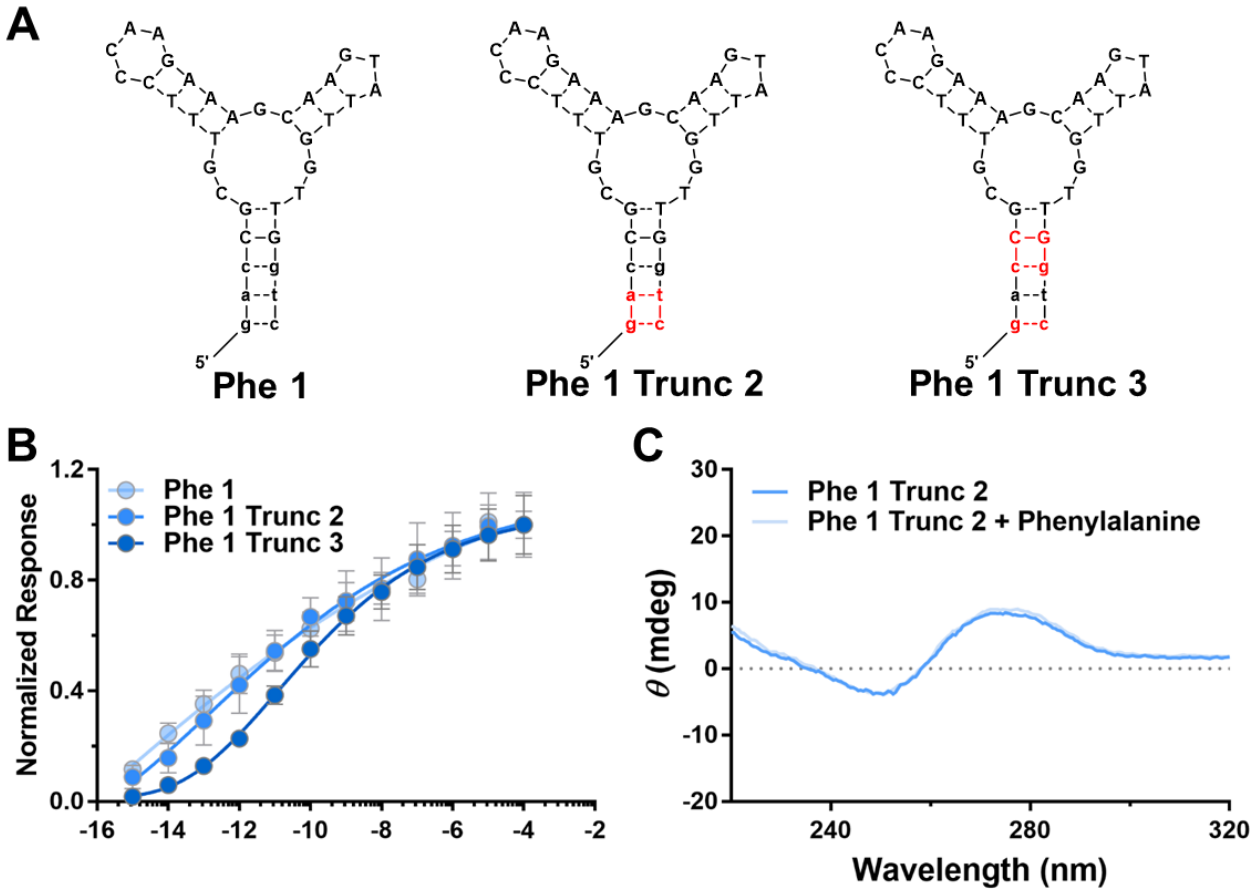

Figure VIII.7. Effects of stem truncation on aptamer-field-effect transistor (FET) responses. (A) Sequences of a phenylalanine specific aptamer (Phe 1) after indiscriminate stem truncation of two end base pairs (Phe 1 Trunc 2) and after rational deletion of CG base pairs (Phe 1 Trunc 3). Bases removed are highlighted in red. **(B)** Aptamer-FET responses of the three aptamer sequences in **(A)** to phenylalanine. **(C)** Circular dichroism spectra of Phe 1 Trunc 3 with and without incubation with phenylalanine.

Removing or truncating stem regions of rationally designed stem-loop aptamers is hypothesized to destabilize target-associated aptamer secondary structures, which increases the dissociation constant (K_d) of the aptamer.[33,34] The destabilization associated with stem truncation can result in larger aptamer conformational changes upon target binding.[33,35] Thus, this strategy is widely adopted for electrochemical aptamer-based (EAB)

sensors, which require large target-induced conformational rearrangements for signal transduction.[33,35,36] However, for EAB sensors, which are equilibrium-based sensors, truncating aptamers can decrease the overall sensitivity of the sensor.[37] In the case of aptamer-FETs, which have been shown to detect analytes several orders of magnitude below the K_d of the aptamer,[31,32] truncation of aptamer stems may enable the tuning of device sensitivities towards physiological concentration regimes.

To investigate the effects of stem truncation on aptamer-FET sensing, the stem of a phenylalanine-specific aptamer (Phe 1) was truncated indiscriminately by the two end-most base pairs (Phe 1 Trunc 2, **Figure VIII.7.A**). Aptamer-FET sensing using this particular truncated aptamer did not show differences in target sensitivity on FETs compared to that of the unmodified aptamer (**Figure VIII.7.B**). Circular dichroism spectroscopy of Phe 1 Trunc 2 with and without phenylalanine did not show differences in peak position or intensity (**Figure VIII.7.C**), indicating that no new secondary structural motifs were formed upon target binding. Based on these results, it is likely that the truncation performed was not destabilizing enough on the aptamer secondary structure.

We tested an alternate hypothesis—that by rationally removing GC base pairs, which form three hydrogen bonds, *versus* AT base pairs, which form two hydrogen bonds, we could destabilize the aptamer (**Figure VIII.7.A)**.[32] Aptamer-FET sensing using a phenylalanine-specific aptamer after removal of three GC base pairs from the stem (Phe 1 Trunc 3) showed a shift in device sensitivity towards higher phenylalanine concentrations (**Figure VIII.7.B**).[32] Thus, empirically modifying aptamer stems presents a potential strategy to tune device sensitivities toward target concentration ranges. However, this strategy is fundamentally limited by the number of base pairs in the stem region of the aptamer, and thus the amount

that the sensitivity can be shifted is also limited. Additional methods to tune device sensitivities (*e.g.*, changing aptamer surface densities[31] or device architectures)[4] could be performed in conjunction with stem truncation.

VIII.B.1.b. Field-Effect Transistor Sensing with Glucose Aptamer Variants

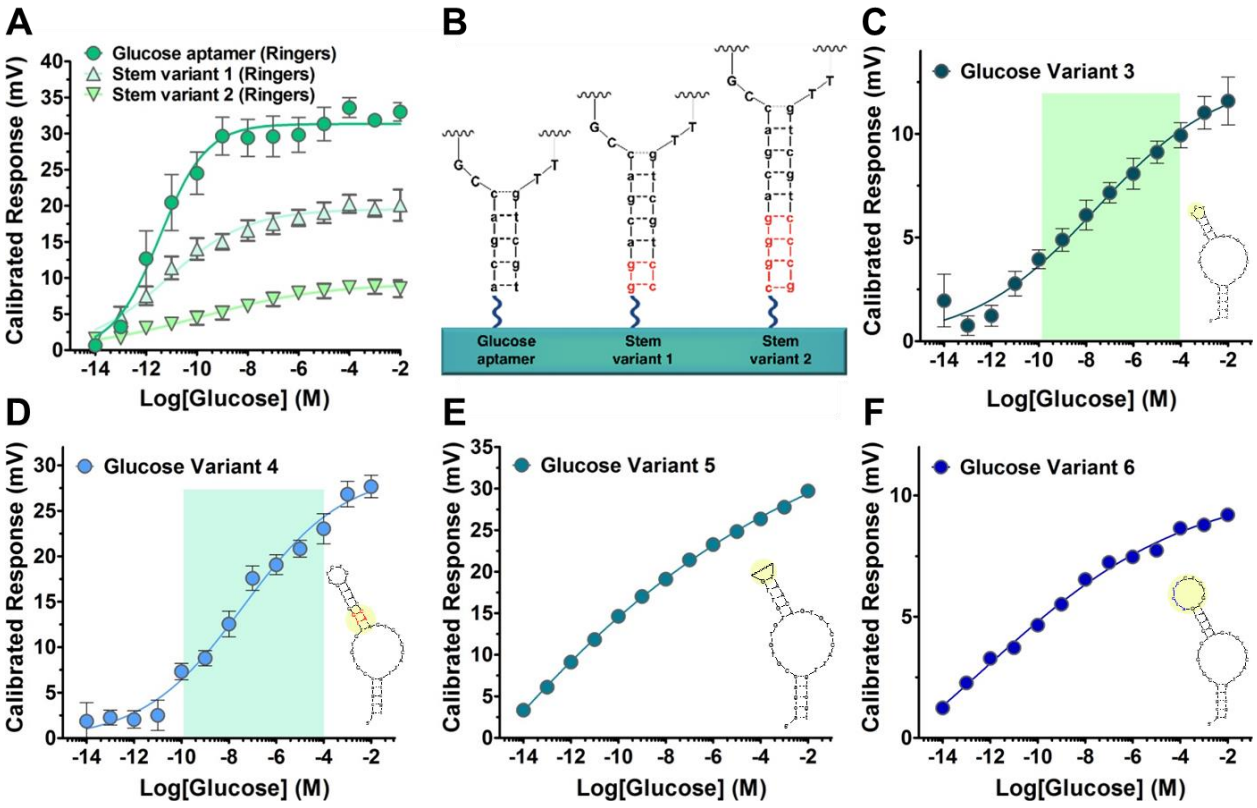

Figure VIII.8. Field-effect transistor (FET) sensing using glucose aptamer variants. (A) Aptamer-FET sensing of glucose using an unmodified glucose apatamer and aptamers with 2 (stem variant 1) and 4 (stem variant 2) additional base pairs in the stem. **(B)** Diagram showing additional base pairs added to the glucose aptamer sequence. **(C-F)** Aptamer-FET sensing using glucose aptamer variants where changes were made in the recognition loop regions of the aptamers. Insets show aptamer variants with changes to the sequence highlighted. (**A,B**) Reprinted (adapted) with permission from *Science*. Copyright 2018, American Association for the Advancement of Science.

We previously demonstrated the detection of glucose *via* a glucose-specific aptamer sequence and two other variant sequences with longer stems to demonstrate how the magnitude of sensor responses are contingent upon the distance of the aptamer from the

transistor surface (**Figure VIII.8.A,B**).[31] In this case, we hypothesized that the original glucose aptamer was already stem-stabilized, so increasing the stem-length had minimal effect on the sensitivity of the sensor, and thus effects of aptamer distances on sensor responses could be analyzed.[31] In addition to the two variant sequences with stem modifications, four other glucose variant sequences with varying modifications to the recognition loop region of the aptamer sequence were tested. Aptamer-FET sensing using these sequences showed varied responses with differences in both sensitivities and shapes of the sensing curves (**Figure VIII.8.C-F**).

Developing intuition regarding modifying recognition portions of aptamers by investigating how changes in structure relate to function could enable control over aptamer affinities beyond stem truncation. Changes to the recognition portion of the aptamer, however, may also change the selectivity of the aptamer. Thus, it will be important to reassess aptamer selectivity after such modifications are made.

VIII.B.2. Aptamer-Field Effect Transistors for *in Vivo* Serotonin Detection

We have miniaturized aptamer-FETs onto 150 μm × 150 μm Si microprobes for the ultimate goal of detecting neurotransmitters (*i.e.*, serotonin) *in vivo* in the brain (**Figure VIII.9.A**). Miniaturized aptamer-FETs responded to serotonin similarly to macroscale FETs when tested *ex vivo* in brain tissue homogenates from *Tph2* null mice (**Figure VIII.9.B**).[31] Moreover, FET microprobes were operational in gelatin, a solid matrix that mimics brain tissue, responding to the addition of 100 nM of serotonin (**Figure VIII.9.C**). After *in vitro* characterization of microprobes, we tested the implantation of a microprobe in the brain of an awake, head-fixed mouse for *in vivo* serotonin detection.

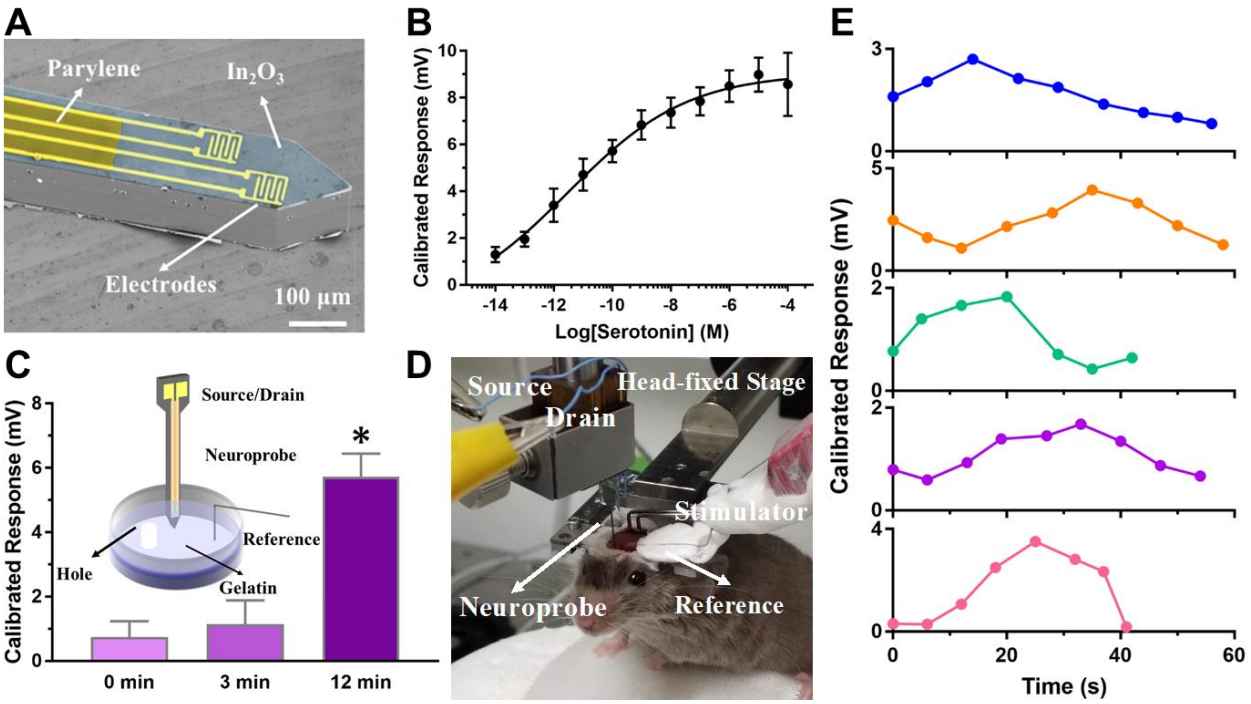

Figure VII.9. Serotonin sensing *via* aptamer-field-effect transistors (FETs) on implantable Si microprobes. (A) Representative scanning electron microscope image of two 50 µm × 50 µm FETs on a 150 µm × 150 µm Si microprobe with a parylene insulating layer. **(B)** Sensing of serotonin in brain tissue homogenates from *Tph2* null mice using aptamer-FET microprobes. **(C)** Aptamer-FET sensing in a solid gelatin matrix over time after introduction of 100 nM of serotonin into the gelatin. Inset shows the experimental sensing setup. **(D)** Photograph of the *in vivo* sensing setup showing the implanted microprobe, Ag/AgCl reference electrode, and electrical stimulator. **(E)** Five aptamer-FET responses collected over *ca.* 60 s from the same mouse immediately after 5 s of electrical stimulation for each measurement. Note, data collected were not time-locked between measurements.

Probes were implanted with a separate Ag/AgCl reference electrode as the gate electrode, and an electrical stimulator to stimulate serotonin release (**Figure VIII.9.D**). Aptamer-FET measurements were performed over a period of *ca.* 60 s after 5 s of electrical stimulation. Responses over time from 5 separate stimulations from the same mouse all showed similar behavior (*i.e.*, an increase and then a decrease in response over the measurement period, **Figure VIII.9.E**). These increases and subsequent decreases in response are suggestive of stimulated serotonin release and reuptake.

While promising, the calibration of FET sensors is challenging *in vivo*, as aptamer-FET responses have been previously shown to shift depending on the sensing matrix. Thus, pre- or post-calibration strategies may not representative of device sensitivities when implanted *in vivo*. Without a reliable calibration method, changes in response cannot be correlated to actual changes in serotonin concentrations. While measuring absolute concertation differences may be difficult, relative differences may be possible. Responses were collected from a single FET, and thus effects such as sensor drift or responses to nonspecific targets cannot be ruled out. Having an inactive FET (*i.e.*, functionalized with a scrambled sequence) that could be measured simultaneously will be opportune as an internal reference.

Overall, I have discussed opportunities for the translation of aptamer-FET sensors towards clinical point-of-care and *in vivo* applications. By empirically modifying aptamer sequences, either *via* stem truncation or modification of the recognition loops, device sensitivities can be shifted and possibly tuned towards specific target concentration ranges. Aptamer-FETs retain functionality when miniaturized and show promise towards *in vivo* neurotransmitter monitoring. Future work to characterize and to tune temporal responses (*i.e.*, aptamer kinetics) and to multiplex the detection of a variety of targets will be advantageous for *in vivo* applications.

VIII.C. References

(1) Liao, W.-S.; Cheunkar, S.; Cao, H. H.; Bednar, H. R.; Weiss, P. S.; Andrews, A. M. Subtractive Patterning *via* Chemical Lift-Off Lithography. *Science* **2012,** *337*, 1517.

(2) Andrews, A. M.; Liao, W.-S.; Weiss, P. S. Double-Sided Opportunities Using Chemical Lift-Off Lithography. *Acc. Chem. Res.* **2016,** *49*, 1449-1457.

(3) Xu, X.; Yang, Q.; Cheung, K. M.; Zhao, C.; Wattanatorn, N.; Belling, J. N.; Abendroth, J. M.; Slaughter, L. S.; Mirkin, C. A.; Andrews, A. M.; Weiss, P. S. Polymer-Pen Chemical Lift-Off Lithography. *Nano Lett.* **2017,** *17*, 3302-3311.

(4) Zhao, C.; Xu, X.; Bae, S.-H.; Yang, Q.; Liu, W.; Belling, J. N.; Cheung, K. M.; Rim, Y. S.; Yang, Y.; Andrews, A. M.; Weiss, P. S. Large-Area, Ultrathin Metal-Oxide Semiconductor Nanoribbon Arrays Fabricated by Chemical Lift-Off Lithography. *Nano Lett.* **2018,** *18*, 5590-5595.

(5) Cheung, K. M.; Stemer, D. M.; Zhao, C.; Young, T. D.; Belling, J. N.; Andrews, A. M.; Weiss, P. S. Chemical Lift-Off Lithography of Metal and Semiconductor Surfaces. *ACS Mater. Lett.* **2019,** *2*, 76-83.

(6) Cao, H. H.; Nakatsuka, N.; Serino, A. C.; Liao, W.-S.; Cheunkar, S.; Yang, H.; Weiss, P. S.; Andrews, A. M. Controlled DNA Patterning by Chemical Lift-Off Lithography: Matrix Matters. *ACS Nano* **2015,** *9*, 11439-11454.

(7) Kim, J.; Rim, Y. S.; Chen, H.; Cao, H. H.; Nakatsuka, N.; Hinton, H. L.; Zhao, C.; Andrews, A. M.; Yang, Y.; Weiss, P. S. Fabrication of High-Performance Ultrathin In2O3 Film Field-Effect Transistors and Biosensors Using Chemical Lift-Off Lithography. *ACS Nano* **2015,** *9*, 4572-4582.

(8) Abendroth, J. M.; Nakatsuka, N.; Ye, M.; Kim, D.; Fullerton, E. E.; Andrews, A. M.; Weiss, P. S. Analyzing Spin Selectivity in DNA-Mediated Charge Transfer *via* Fluorescence Microscopy. *ACS Nano* **2017,** *11*, 7516-7526.

(9) Cao, H. H.; Nakatsuka, N.; Liao, W.-S.; Serino, A. C.; Cheunkar, S.; Yang, H.; Weiss, P. S.; Andrews, A. M. Advancing Biocapture Substrates *via* Chemical Lift-Off Lithography. *Chem. Mater.* **2017,** *29*, 6829-6839.

(10) Zhao, C.; Xu, X.; Yang, Q.; Man, T.; Jonas, S. J.; Schwartz, J. J.; Andrews, A. M.; Weiss, P. S. Self-Collapse Lithography. *Nano Lett.* **2017,** *17*, 5035-5042.

(11) Cao, H. H.; Nakatsuka, N.; Deshayes, S.; Abendroth, J. M.; Yang, H.; Weiss, P. S.; Kasko, A. M.; Andrews, A. M. Small-Molecule Patterning *via* Prefunctionalized Alkanethiols. *Chem. Mater.* **2018,** *30*, 4017-4030.

(12) Chen, C.-Y.; Li, H.-H.; Chu, H.-Y.; Wang, C.-M.; Chang, C.-W.; Lin, L.-E.; Hsu, C.-C.; Liao, W.-S. Finely Tunable Surface Wettability by Two-Dimensional Molecular Manipulation. *ACS Appl. Mater. Interfaces* **2018,** *10*, 41814–41823.

(13) Chen, C.-Y.; Wang, C.-M.; Chen, P.-S.; Liao, W.-S. Surface Functional DNA Density Control by Programmable Molecular Defects. *Chem. Commun.* **2018,** *54*, 4100–4103.

(14) Chen, C.-Y.; Wang, C.-M.; Chen, P.-S.; Liao, W.-S. Self-Standing Aptamers by an Artificial Defect-Rich Matrix. *Nanoscale* **2018,** *10*, 3191–3197.

(15) Chen, C.-Y.; Wang, C.-M.; Li, H.-H.; Chan, H.-H.; Liao, W.-S. Wafer-Scale Bioactive Substrate Patterning by Chemical Lift-Off Lithography. *Beilstein J. Nanotechnol.* **2018,** *9*, 311–320.

(16) Slaughter, L. S.; Cheung, K. M.; Kaappa, S.; Cao, H. H.; Yang, Q.; Young, T. D.; Serino, A. C.; Malola, S.; Olson, J. M.; Link, S.; Häkkinen, H.; Andrews, A. M.; Weiss, P. S. Patterning of Supported Gold Monolayers *via* Chemical Lift-Off Lithography. *Beilstein J. Nanotechnol.* **2017,** *8*, 2648–2661.

(17) Kim, J.; Cote, L. J.; Kim, F.; Huang, J. Visualizing Graphene Based Sheets by Fluorescence Quenching Microscopy. *J. Am. Chem. Soc.* **2010,** *132*, 260-267.

(18) Xie, F.; Centeno, A.; Ryan, M. R.; Riley, D. J.; Alford, N. M. Au Nanostructures by Colloidal Lithography: From Quenching to Extensive Fluorescence Enhancement. *J. Mater. Chem. B* **2013,** *1*, 536-543.

(19) Geddes, C. D.; Lakowicz, J. R. Editorial: Metal-Enhanced Fluorescence. *J. Fluoresc.* **2002,** *12*, 121-129.

(20) Knoben, W.; Offermans, P.; Brongersma, S. H.; Crego-Calama, M. Metal-Induced Fluorescence Enhancement as a New Detection Mechanism for Vapor Sensing. *Sens. Actuators, B* **2010,** *148*, 307-314.

(21) Tseng, P.; Pushkarsky, I.; Di Carlo, D. Metallization and Biopatterning on Ultra-Flexible Substrates *via* Dextran Sacrificial Layers. *PLoS One* **2014,** *9*, e106091.

(22) Azubel, M.; Koivisto, J.; Malola, S.; Bushnell, D.; Hura, G. L.; Koh, A. L.; Tsunoyama, H.; Tsukuda, T.; Pettersson, M.; Häkkinen, H.; Kornberg, R. D. Electron Microscopy of Gold Nanoparticles at Atomic Resolution. *Science* **2014,** *345*, 909.

(23) Hamers, R. J.; Tromp, R. M.; Demuth, J. E. Scanning Tunneling Microscopy of Si(001). *Phys. Rev. B* **1986,** *34*, 5343-5357.

(24) Cui, X. D.; Primak, A.; Zarate, X.; Tomfohr, J.; Sankey, O. F.; Moore, A. L.; Moore, T. A.; Gust, D.; Harris, G.; Lindsay, S. M. Reproducible Measurement of Single-Molecule Conductivity. *Science* **2001,** *294*, 571.

(25) Wu, Z.; Chen, X.; Wang, M.; Dong, J.; Zheng, Y. High-Performance Ultrathin Active Chiral Metamaterials. *ACS Nano* **2018,** *12*, 5030-5041.

(26) Hatzor, A.; Weiss, P. S. Molecular Rulers for Scaling Down Nanostructures. *Science* **2001,** *291*, 1019.

(27) Lau, J.; Trojniak, A. E.; Maraugha, M. J.; VanZanten, A. J.; Osterbaan, A. J.; Serino, A. C.; Ohnsorg, M. L.; Cheung, K. M.; Ashby, D. S.; Weiss, P. S.; Dunn, B. S.; Anderson, M. E. Conformal Ultrathin Film Metal–Organic Framework Analogues: Characterization of Growth, Porosity, and Electronic Transport. *Chem. Mater.* **2019,** *31*, 8977-8986.

(28) Trang, B.; Yeung, M.; Popple, D. C.; Schriber, E. A.; Brady, M. A.; Kuykendall, T. R.; Hohman, J. N. Tarnishing Silver Metal into Mithrene. *J. Am. Chem. Soc.* **2018,** *140*, 13892–13903.

(29) Ashley, M. J.; Bourgeois, M. R.; Murthy, R. R.; Laramy, C. R.; Ross, M. B.; Naik, R. R.; Schatz, G. C.; Mirkin, C. A. Shape and Size Control of Substrate-Grown Gold Nanoparticles for Surface-Enhanced Raman Spectroscopy Detection of Chemical Analytes. *J. Phys. Chem. C* **2018,** *122*, 2307–2314.

(30) Miyake, H.; Ye, S.; Osawa, M. Electroless Deposition of Gold Thin Films on Silicon for Surface-Enhanced Infrared Spectroelectrochemistry. *Electrochem. Commun.* **2002,** *4*, 973-977.

(31) Nakatsuka, N.; Yang, K.-A.; Abendroth, J. M.; Cheung, K. M.; Xu, X.; Yang, H.; Zhao, C.; Zhu, B.; Rim, Y. S.; Yang, Y.; Weiss, P. S.; Stojanović, M. N.; Andrews, A. M. Aptamer–Field-Effect Transistors Overcome Debye Length Limitations for Small-Molecule Sensing. *Science* **2018,** *362*, 319.

(32) Cheung, K. M.; Yang, K.-A.; Nakatsuka, N.; Zhao, C.; Ye, M.; Jung, M. E.; Yang, H.; Weiss, P. S.; Stojanović, M. N.; Andrews, A. M. Phenylalanine Monitoring *via* Aptamer-Field-Effect Transistor Sensors. *ACS Sensors* **2019**, DOI:10.1021/acssensors.9b01963 10.1021/acssensors.9b01963.

(33) White, R. J.; Rowe, A. A.; Plaxco, K. W. Re-Engineering Aptamers to Support Reagentless, Self-Reporting Electrochemical Sensors. *Analyst* **2010,** *135*, 589-594.

(34) Kent, A. D.; Spiropulos, N. G.; Heemstra, J. M. General Approach for Engineering Small-Molecule-Binding DNA Split Aptamers. *Anal. Chem.* **2013,** *85*, 9916-9923.

(35) Idili, A.; Gerson, J.; Parolo, C.; Kippin, T.; Plaxco, K. W. An Electrochemical Aptamer-Based Sensor for the Rapid and Convenient Measurement of L-Tryptophan. *Anal. Bioanal. Chem.* **2019,** *411*, 4629-4635.

(36) Xiao, Y.; Uzawa, T.; White, R. J.; DeMartini, D.; Plaxco, K. W. On the Signaling of Electrochemical Aptamer-Based Sensors: Collision- and Folding-Based Mechanisms. *Electroanalysis* **2009,** *21*, 1267–1271.

(37) Baker, B. R.; Lai, R. Y.; Wood, M. S.; Doctor, E. H.; Heeger, A. J.; Plaxco, K. W. An Electronic, Aptamer-Based Small-Molecule Sensor for the Rapid, Label-Free Detection of Cocaine in Adulterated Samples and Biological Fluids. *J. Am. Chem. Soc.* **2006,** *128*, 3138-3139.